The State-to-State Dynamics of the Reactions of Oxygen Atoms with Hydrocarbons

Gillian Michelle Sweeney

A thesis presented for the degree
of Doctor of Philosophy in the Faculty
of Science at the University of Edinburgh
1997

Declaration

This thesis was composed by myself and is based on work carried out at the University of Edinburgh's Chemistry Department between October 1992 and December 1995.

Signed:

Date:

Michael and Samuel

Thanks for being here

The State-to-State Dynamics of the Reactions of Oxygen Atoms with Hydrocarbons

Pulsed laser photolysis-probe techniques have been used to investigate the nascent internal state distributions of $OH(X^2\Pi)$ produced in reactions of the type:

$$O(^3P) + RH \longrightarrow OH(X^2\Pi) + R$$

RH is a saturated hydrocarbon, which is chosen to contain representative primary, secondary or tertiary C-H bonds. Reactive superthermal $O(^3P)$ atoms are generated by photolysis of NO_2 at either 337, 308 or 248 nm. By changing the wavelength of photolysis of NO_2, the collision energy of the reaction can be effectively altered.

The OH product is detected in a state-specific manner by laser-induced fluorescence (LIF) on the $A^2\Sigma^+ \leftarrow X^2\Pi$ transition. The delay between the photolysis and probe pulses is kept short enough to allow the partitioning of the available energy amongst the possible vibrational, rotational and fine-structure states to be determined from collisionally unmodified OH LIF spectra.

The OH product, from the reaction between $O(^3P)$ and RH, is found to be rotationally cold. It is also apparent that the rotational distribution is largely independent of the nature of the R group. These findings have been interpreted as evidence that the reaction exhibits a strong preference for collinear approach of the $O(^3P)$ atom to the C-H bond from which the H atom is abstracted. In contrast, the degree of vibrational excitation depends strongly on both the type of C-H bond and the collision energy. These observations are consistent with the shift towards an "earlier" reaction

barrier with increasing reaction exothermicity, which occurs as the H atom being abstracted is changed from primary to secondary to tertiary. The OH spin-orbit state distribution is non-statistical. The correlations between the spin-orbit states of the $O(^3P)$ reactant and OH product have been clarified. A purely adiabatic correlation does not correctly predict the observed product spin-orbit state distribution but a model, which includes non-adiabatic coupling of surfaces with the same projection of total electronic angular momentum, gives much improved agreement. This model has interesting but as yet unstudied corollaries for the differential reactivity of the $O(^3P_j)$ states.

Preliminary studies have also been made on the reaction between $O(^1D)$, the first excited state of oxygen, and methane :

$$O(^1D) + CH_4 \longrightarrow OH(X^2\Pi) + CH_3$$

$O(^1D)$ is generated by the photolysis of N_2O at 193nm and the resultant OH is detected by LIF. It has been confirmed, in agreement with earlier observations, that the OH product is rotationally hot. This is indicative that the reaction proceeds via an insertion mechanism, to form chemically activated methanol, followed by prompt, unimolecular decomposition to produce non-statistical OH. Successful preparatory work was carried out into the resonance-enhanced-multi-photon-ionisation (REMPI) detection of CH_3. Photolysis of CH_3I was demonstrated to be a convenient source of CH_3. This work paves the way for future studies in which CH_3 will be detected as the nascent product of a bimolecular reaction.

Acknowledgements

I would now like to take the opportunity to acknowledge those who contributed, in a wide range of different ways, to this thesis. Firstly, I'd like to thank my supervisor, Kenneth McKendrick, for introducing me to the project and for his guidance and support throughout the course of this work. Special thanks are also owed to Allister Watson who helped me out in my first year, and to Neil Jackson who guided me through the I.T. maze. I'd also like to express my gratitude to the Carnegie Trust for the Universities of Scotland who generously funded this project.

In addition, I'd like to thank all members of the laser group for both technical assistance and good times. In particular I'd like to mention Cameron Watson, Trevor Ridley, Scott Wright, Graeme Maitland, Craig Redpath, Andy Cormack and Colin Randall. And special thanks to Robert McQuillan for keeping me company in Room 6.

The contribution of the technical staff is also greatly acknowledged. I would like to particularly thank Stuart Mains, Duncan Maclean and Derek Burgess for their help in building, mending and supplying various items of equipment in the duration of my studies.

On a more social note, I'd like to recommend Craig Sommerville, Tom Barlow, Mike McPherson and Eric McInnes as being "the best people to live with whilst carrying out postgraduate studies", surely the ultimate accolade. Thanks also to Lisa, Nicky, Dave D, Mel, Scott, Dave L, Lynda, Louise and Raymond for making life in Edinburgh (1992-1995) fun.

Thanks are also due to my family for all their support in both past and recent times.

Table of Contents

List of Figures

List of Tables

Chapter 1

Introduction to Reaction Dynamics

1.1 General Background

The field of molecular reaction dynamics provides a lens through which the mechanisms of elementary physical and chemical processes may be viewed. The subject probes and examines all types of intramolecular and intermolecular motions. In principle, an understanding of these molecular level dynamics should help to rationalise the macroscopic behaviour of bulk systems[1].

Collisions are fundamental to chemistry, serving as the microscopic mechanism on which all observed rate phenomena involving gases and liquids can be based. However, in spite of their central role in chemistry, it is only relatively recently that developments in experimental techniques and fundamental theory have progressed far enough to allow us to probe rate processes directly at the microscopic level. Over the last 30 years the emphasis of the branch of physical chemistry concerned with the kinetics of gas phase chemical reactions has progressed beyond the stage of determining macroscopic rate constants towards an understanding of reactions in terms of "chemical dynamics", the mechanics of molecular collisions. Advances in reaction dynamics have been made in both experimental and theoretical fields[2]. The advent of sophisticated new experimental procedures has generated a large amount of information relating to the dynamics of elementary chemical reactions. Development of theoretical methods has been aided by the rapid growth in computer technology, and it is now possible to attempt to understand chemical

dynamics from the classical or quantum mechanical motion of atoms or molecules on accurately calculated potential energy surfaces.

Simple chemical processes can be illustrated by generic exchange reactions as shown in Equation (1.1). Here A, B and C can either be atoms or groups of atoms.

$$A + BC \longrightarrow AB + C \qquad (1.1)$$

In Equation (1.1), which represents an exothermic system, the weak BC bond is broken and replaced by the stronger AB bond. The reaction thus liberates "chemical energy". It is also possible to make studies on endothermic processes by giving the reagents enough initial energy in some form. One principal question that reaction dynamics asks is, in what way is the energy released following the reactive collision between A and BC? Even if both products are formed in their electronic ground states, there are still three remaining modes available for energy disposal: vibration and rotation of AB or translation of AB and C. Using the microscopic approach of reaction dynamics the distribution of energy among these modes can be determined.

The main aim of reaction dynamics is to determine the motions of individual atoms or groups of atoms during the critical intermediary period which occurs as old chemical bond are broken and new ones formed, so that ultimately this behaviour can be explained in terms of the chemical forces acting between the fragments. Often, these motions are not observed directly but inferred by extrapolation of product state energy distributions, or from the effect of the motions of the reagent on the outcome of the collision[3].

1.2 Potential Energy Surfaces and Reaction Energetics

Energy is a factor of central importance in the dynamics of chemical change. It is the driving force of reactions, determines the reaction rate, governs the details of the collision trajectory and excess energy is released into the product species.

Potential energy surfaces (PES) are diagrammatic representations which show how the potential energy (and hence chemical forces) varies with the relative positions of the atoms in a colliding system[1]. The motivation for their development arose from the desire to model collisions and rationalise the subsequent energy distribution in the products. To gain a fuller understanding of colliding systems it is necessary to consider interatomic forces and motions: potential energy surfaces can be used to generalise the concept of an interatomic potential. The first PES was generated by London, Eyring and Polanyi[4] for the $H+H_2$ reaction; dynamical computations on the system were subsequently carried out by ~~Hirschfeld~~ Hirschfelder *et al*[5] a few years later.

To construct a PES plot[1] for a N atom system 3N-6 coordinates are required. Hence even in the simple case of three interacting atoms the potential energy is a function of three coordinates. In Figure 1.1 a possible combination of coordinates is shown: $V(R_1,R_2,\theta)$, where V is the potential energy, R_1 and R_2 the interatomic distances and θ is the angle between R_1 and R_2. Obviously it is not feasible to construct a simple plot which encompasses all features of the PES for a system with more than two atoms because at least four dimensions are required. This problem is resolved by fixing at least one coordinate and can be achieved by restricting consideration to limited geometries; for example, for the collinear (A-B-C) configuration shown in Figure 1.2 for which there are only two independent interatomic distances R_{AB} and R_{BC}. In this case the PES, treated as a function of two coordinates, is a potential contour map consisting of

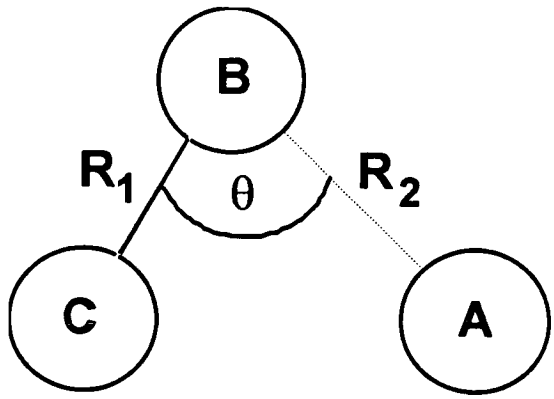

Figure 1.1: In the reactive system, A+BC, three coordinates are required to specify the potential: $V(R_1,R_2,\theta)$, where V represents the potential energy between the interacting atoms, R_1 and R_2 are the interatomic distances and θ is the angle between R_1 and R_2.

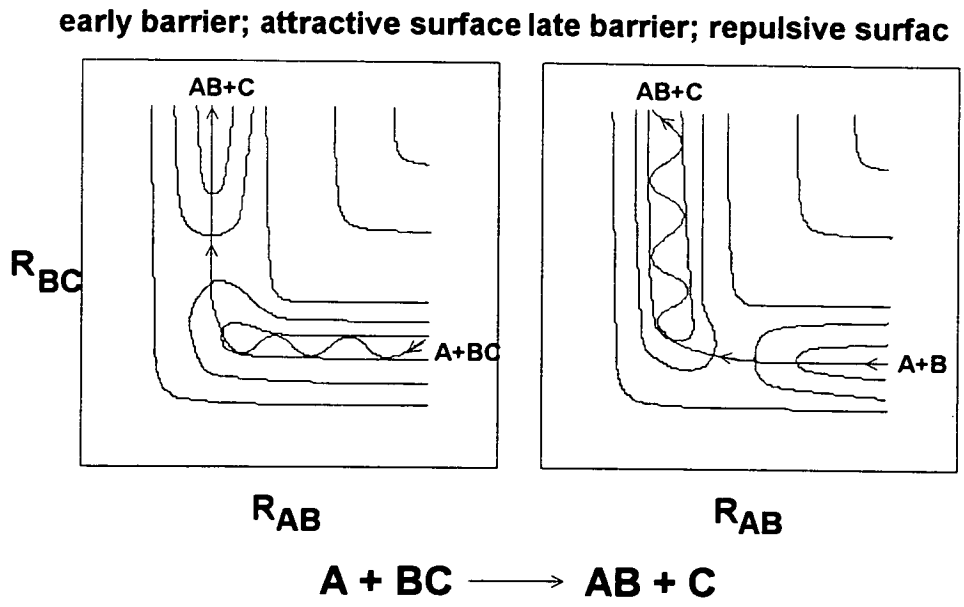

Figure 1.2: Diagrammatic representations of potential energy as a function of R for the reaction A+BC → AB+C, occurring on a collinear surface. If the reaction barrier is in the entrance channel (early), as shown in the left hand panel, then translational energy will promote the reaction. In this case A is accelerated towards B resulting in a vibrationally excited product (AB) manifested as exit channel oscillation. This surface is described as attractive. If the barrier is situated late, in the exit channel, as shown in the right hand panel, then vibrational energy is required to break the B-C bond. Translation of A → BC will be ineffective in promoting the reaction and energy release is termed repulsive: AB is accelerated away from C and the product is vibrationally cold. Energy is released as product translation exposed as a straight line trajectory down the exit channel. However, it is important to remember that θ is fixed at 180°. Hence neither impact parameter information nor rotational energy information is obtained here.

equipotential lines, its design similar to a topographical map with reactant and product "valleys" linked by a "pass". The forces on the atoms are equivalent to the slopes of the PES. The reaction path is the minimum energy route from the reactants to products and if the system in question has a barrier then its location along the reaction path is crucial in predicting product energy distributions.

Once the PES for a colliding system has been constructed and the initial conditions (such as relative positions, velocities and internal excitation of reactant species, impact parameters) specified it is then possible to calculate the outcome of a collision. Product energy distributions can be predicted by examining the minimum energy route through the PES from reactants to products. The surface can also be used to rationalise why internal excitation of reactants often enhances reactivity. The predictions can then be compared with experimental results as a direct test of the validity of the PES. The "perfect" PES will provide a complete description of a colliding system, serving to define a path from reactant to product configurations.

There are two main categories of chemical reactions: those with a barrier and those without. All endothermic processes must have a barrier; some exothermic systems may have a barrier. While barrierless reactions can occur at all collision energies, the energy consumption in reactions with a barrier is highly selective: the reactants must have sufficient collision energy to surmount the barrier and the nature of the energy available to the reactants controls the outcome of the reactions. There is a correlation between location of barrier along the reaction path and the form of initial energy most conducive to reaction. Figure 1.2 shows two extreme barrier positions. In the left picture an early barrier, situated in the entrance channel of the PES, is illustrated while the picture on the right shows a late reaction barrier located in the exit channel of the surface. **Translational** energy is most effective for passage across an **early** barrier whereas

vibrational energy is more efficient for surmounting **late** barriers. The reaction cross section, a parameter which controls the probability and rate of reaction, increases with translational energy once the barrier has been crossed.

Exoergic reactions can release energy in a number of different ways. Mechanisms for energy disposal include formation of electronically, vibrationally and rotationally excited products. The energy released can be supplied by replacement of a weaker bond by a stronger one, formation of a new bond or by external physical activation (for example, in photochemical reactions).

Energy disposal can be interpreted and discussed by analysis of classical trajectories on potential energy surfaces. Correlations can be made between the nature of the surface, position of the reaction barrier and the resulting mode of energy release. Polanyi *et al*[6] have shown that the efficiency of conversion of reaction exoergicity into product **vibration** is greater for a more **attractive** potential energy surface with an **early** barrier: vibrational state distributions in product fragments are sensitive to **where** the original bond breaks along the reaction coordinate. This can be illustrated by considering a simple generic system, as shown in Equation (1.1) and Figure 1.2. If energy is released early while the attacking atom A is still approaching species BC, then the attraction between A and B at close separation impels the exoergicity into product **vibration**. Alternatively, if the energy is released when atom A has approached BC and is almost at rest, then AB rebounds, is accelerated away from C and the energy is released as product **translation**. Hence, the correlation that can be drawn in this instance is that the efficiency of conversion of reaction exoergicity into product **translation** is greater for **repulsive** surfaces with **late** barriers.

Subsequently a useful, but not infallible, generalisation can be made on the correlation between surface properties and chemical reactions; as exothermicity increases the barrier height decreases and shifts to earlier locations (exit → entrance channel) within the PES, causing energy release to become more attractive. This generalisation works well for the H_2+X → HX+H (X = F,Cl,Br,I) system[1,7] where the barrier height increases, shifting to later positions, and the vibrational excitation of HX decreases with increasing molecular weight.

Kinematic (mass) effects on the PES must also be considered, becoming important when the masses of the atoms involved in the collision differ widely. When the system under study consists of disproportionate masses the motions in the coordinates are not independent; inertial coupling is observed. To account for differing masses the PES plot can be distorted; skewed and scaled[8,9]. Figure 1.3 illustrates a normal rectilinear surface and a skewed surface. Distorting the PES representation causes increased vibration of products. An example of a system where kinematic effects must be considered is the Cl+HI reaction[1,10-12], where the halogen atoms are "heavy" and the H atom is "light". In this system strong inertial coupling is observed and the PES is skewed. The light H atom is transferred between the two heavy atoms and I---H repulsion leads to relatively high HCl vibration. However if the light particle was on the "outside" and the heavy particle was in the middle, as in the H+Cl_2[1] system, there would be little internal coupling and Cl---Cl repulsion would result in only minimal HCl vibration; most of the available energy would be channeled into translation of HCl.

Hence, for simple atom-molecule exchange reactions the dynamical roles of translational and vibrational energy are relatively well understood[13,14], and their effects can be assessed by examining the topology of the potential energy surface of the system in question. However, no such clear

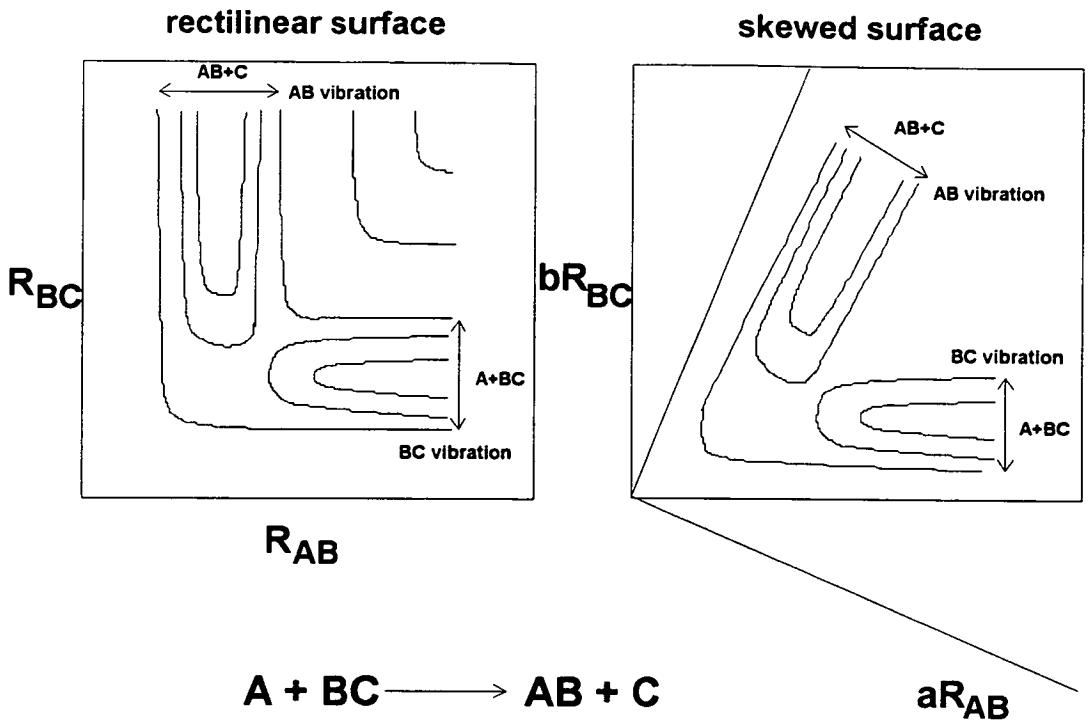

Figure 1.3: The left hand picture shows a rectilinear surface which is used when kinematic effects are negligible. On this surface there is little vibration of products. Vibration of AB is independent of R_{BC} and the BC vibration is independent of R_{AB}. The right hand panel illustrates a skewed surface, applicable when kinematic effects are important. On this surface products are vibrationally excited: the AB vibration is coupled to R_{BC} and the BC vibration is coupled to R_{AB}.

understanding exists for the role of rotational energy in reaction dynamics. In the study of rotational effects there are many factors which limit the experimentally obtainable resolution; rotational energy levels are very closely spaced and are rapidly equilibrated in inelastic, non-reactive collisions. Rotational energy effects are much more subtle than those which operate for translational and vibrational excitation as they depend on orientation and stereochemistry.

Reagent rotation can have a profound effect on the outcome of a collision, especially for direct reactions. An example is the Cl+HI reaction[10-12] where the amount of rotational energy in HI affects the probability of reaction. Initially rotational excitation causes the reaction rate to slow but as the level of rotational excitation is increased, the rate then also increases. The reaction is geometrically confined because the I atom is bulky and sterically hinders the H atom abstraction by Cl. This means that the approach geometry of the attacking atom has to be well defined and reaction can only occur at certain orientations. When J=0 collisions will occur and at a certain distance and preferred orientation a H-Cl bond will form. Then at low J (but when $J \neq 0$) there is a reduced probability of reaction and the Cl atom experiences repulsive potentials because the rotational motion twists the molecule away from the preferred reaction configuration. At high J, centrifugal distortion extends the H-I bond (the bond to be broken) and thus rotational energy enhances the reaction.

It has also been established that rotational excitation of the products, in the generic system illustrated in Equation (1.1), arises primarily from torque imparted to AB due to repulsion between the fragments in their intermediary state[15]. If the reaction occurs principally through a bent configuration then repulsion in the B-C bond produces a torque in AB and causes substantial rotational excitation. Conversely, if the reaction proceeds via a collinear intermediate then B-C repulsion produces only translational or vibration of

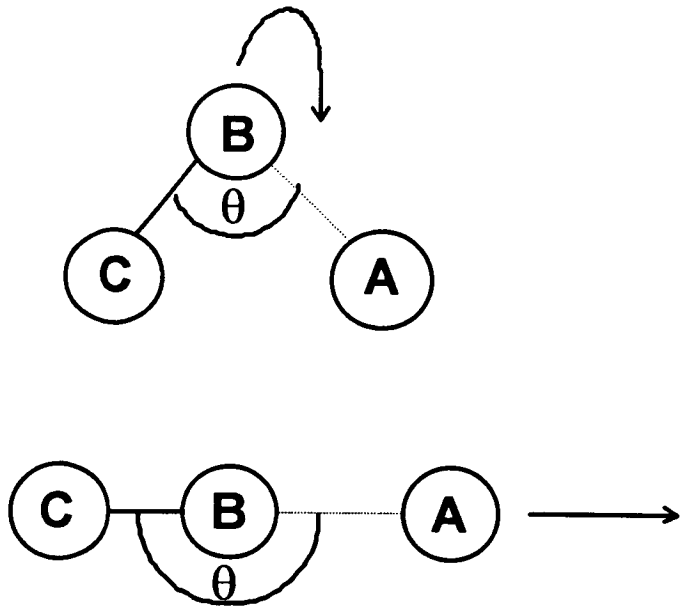

Figure 1.4: This figure illustrates why the degree of rotational excitation depends on the geometry of the intermediary state. Considering the generic system, A+BC → AB+C: if the reaction occurs through a bent configuration, as shown in the top panel, then repulsion between B and C causes A-B to spin off, rotationally excited. However if the reaction intermediate is collinear ($\theta = 180^{\circ}$) then any repulsion between B and C is channeled into product vibration or translation. This explains why the O+HBr produces rotationally hot OH product but the O+HR reaction produces rotationally cold OH.

AB with little excitation of rotational modes. These concepts are illustrated in Figure 1.4. Although the distribution of energy into rotational modes acts primarily as a probe of the preferred geometry in the exit channel of the reactive surface in question, similar geometries are expected to dominate the entrance channel. This is because the time taken for a molecule to rotate is longer than the time taken to pass through the critical intermediary configuration.

It is also possible to determine the degree of partitioning between product fine structure states, which can yield information on the preferred geometry and degree of electronic adiabaticity of a reaction. Obviously, though, this kind of analysis is only applicable to systems which have such states (for example, spin-orbit states and Λ-doublets).

To date, a number of experiments have been performed which have determined relatively complete rovibrational product state distributions[16], but few have examined the effect of reagent rotational excitation on reactivity[17]. Hence an ultimate goal in reaction dynamics is to determine the full correlation between reagent rovibrational excitation, reaction cross section and product state distribution, and although this objective has not yet been achieved, it is now beginning to be approached by workers in the field[18-25].

1.3 Theoretical Approaches to Reaction Dynamics

To fully describe the dynamics of chemical change, one would be required to carry out rigorous quantum mechanical calculations on the reaction(s) in question. For most reactive systems one must consider the motion of the nuclei on a given potential energy surface or set of surfaces. Thus, the most rigorous theoretical basis of reaction dynamics requires a knowledge of accurate potential energy surfaces and the ability to determine the

mechanics of the interacting particles. Ab initio calculations of reactive surfaces are improving with computer technology, however, even for the simplest systems, the level of accuracy is low. These techniques have been most rigorously applied to combinations involving hydrogen molecules, such as H + H_2[5,26-35] and F + H_2[36-40]. For systems containing heavier atoms, semi-empirical methods[4,9,12,41-46] are used to generate potential energy surfaces. An example is the London-Eyring-Polanyi-Sato (LEPS) scheme[4,9,12,43] which is widely used to estimate the potential function for three atom systems. Semi-empirical methods allow the PES to be systematically varied until the measured dynamics of a system are accurately simulated. Realistic surfaces can be generated for some systems using these techniques, but only if the parameters are chosen correctly.

Once the PES has been generated (by either semi-empirical or ab initio methods) the next phase in predicting the outcome of molecular collisions is to solve the equations of motion for the system of particles under study, assuming a form of the PES and knowing a set of initial conditions. The equations of motion can be solved using quantum, semi-classical or classical methods.

1.3.1 Quantum Mechanical Methods

A wavefunction contains all the necessary information pertaining to the system it represents. Quantum mechanical methods have been developed to allow this information to be extracted.

There are two approaches to solving the equations of motion using quantum methods. Firstly, solutions can be obtained by solving the time dependent Schrödinger equation. However this procedure has not until recently been frequently used due to the computational difficulties associated with such calculations, although it is now becoming more fashionable with

improvements in the algorithms for the calculation of propagation of wavepackets[47,48].

The second, and traditionally much more widely applied, approach relies on the assumption that the time dependence of the wavefunction can be neglected[47]. (Time independent methods are still exact in principle.) Much effort has been directed in recent years into solving the time independent quantum dynamics of small molecular systems. The $H+H_2$ reaction [33-35] and its isotopic variants have been studied using quantum scattering techniques at varying levels of approximation, exploiting the best ab initio potential energy surfaces[49,50]. Calculations have also been carried out on slightly more complex systems, such as the $O(^3P)+H_2$[51] and, of specific interest to this work, the $O(^3P)$ +HR[52] (HR representing neopentane and isobutane) reactions, by Clary *et al* who applied vibrationally adiabatic distorted wave (VADW) calculations[53] to extended London-Eyring-Polanyi-Sato (LEPS) potential energy surfaces. The VADW technique is just one of many approximation methods which can be used to predict the outcome of polyatomic collisions.

1.3.2 Semi-Classical Methods

Semi-classical methods provide a relatively easy (as compared with quantum methods) means of evaluating the outcome of collisions. This approach is essentially an extension of Bohr theory (periodic orbits) to unbound systems[54]. Here the concept of classical trajectories is retained but the wavemotion is associated with a phase. If only one trajectory occurs between each initial and final state then the semi-classical probability is equal to the classical probability. However, if more than one trajectory leads to the same outcome then the semi-classical result incorporates interferences between trajectories with different phases.

This approach is very useful in principle because it is computationally less intensive than quantum calculations and it corrects intuitive classical outcomes to non intuitive quantum predictions. It has, however, been applied more widely in practice in inelastic scattering than to reactive scattering.

1.3.3 Classical Methods

As a rapid and relatively simple alternative to quantum calculations, quasiclassical (QC) scattering methods may be used. This type of calculation has its basis in classical (Newtonian) mechanics but is usually written using Hamiltonian representation. The origin of the technique lies in the fact that very refined measurements are necessary to detect quantum effects, especially for systems with heavy atoms. This endorses the use of classical mechanics for "rough" calculations.

A particular example of a system which has been evaluated using quasiclassical (QC) methods is the $O(^3P)$+HR (HR represents saturated hydrocarbons) reaction. Andresen and Luntz used QC trajectory calculations on extended LEPS potential energy surfaces[55] to explain their experimental results[56]

Quasiclassical methods are simple, rapid and very useful for comparison with more rigorous quantum calculations. In addition, the match between theoretical predictions and experimental results tends to be good. However there are limitations to this technique; electronically non-adiabatic effects are neglected and genuine quantum effects, such as tunneling and interference, are absent.

Classical trajectory calculations are commonly used to aid the interpretation of experimental reaction dynamics[57]. In classical mechanics the trajectory

describes the motion of a particle and how it evolves with time. This method has been used, for both simple triatomic and more complicated polyatomic reaction systems, to rationalise the features of reaction dynamics with the characteristics of potential energy surfaces[58], and to explain observed experimental results. The main limitations of this technique are that quantum effects are approximated or neglected because continuous variables are used.

1.4 Experimental Approaches to Reaction Dynamics

The fundamental laws of mechanics should be able to provide detailed dynamical information for elementary chemical reactions: quantum mechanics provides a sufficiently accurate description of the motions of electrons, atoms and molecules participating in chemical reactions, and hence chemical dynamics is a mechanical problem which has the potential to be solved from first principles. However, technology and mathematics have not yet progressed far enough to provide quantitative solutions for many-particle systems. Hence the role of experimentalists in the field of reaction dynamics is crucial. Data obtained from experimental studies has not only explained observed macroscopic phenomena and facilitated the understanding of important chemical and kinematic features of chemical dynamics, but has also been used by theoreticians to rationalise their hypotheses.

There are two complementary experimental approaches to reaction dynamic studies: molecular beam scattering techniques and spectroscopic methods. These techniques have helped to shift the focus of experimental reaction dynamics from macroscopic kinetics and thermodynamics to the physics of chemical change at a molecular level. To understand the dynamics of a chemical reaction from experimental data it is necessary to obtain sufficient microscopic information in detail. Microscopic parameters, when used in

reference to a reactive system, imply reactant and product conditions such as molecular quantum state, relative velocity, orbital angular momentum (or impact parameter), orientation of reactant species, lifetimes of any collision complexes and distribution of reaction exoergicity into product energy/quantum states.

1.4.1 Molecular Beam Scattering Methods

In a molecular beam scattering experiment the reactant species are entrained into collimated beams (preferably with narrow velocity distributions and typically from a supersonic beam source). The beams are allowed to intersect (usually at right angles) and scattering occurs. The background pressure is kept low to minimise the chance of secondary collisions, and the collision energy can be varied by using different seeding ratios within the supersonic beam. A rotatable detector is used so that the angular distribution of the various scattered species, in the laboratory coordinate system, can be determined. At the same time the product speed distributions can be measured using time-of-flight methods. The limitations of this technique lie in that the product state energy distributions can only be inferred reliably by using energy conservation when the kinetic energy is well defined. The assumptions necessary to allow any product internal state information to be extracted from the experimental data can lead to erroneous results when a wide kinetic energy distribution characterises the initial conditions and when the energy dependence of the reactive cross section cannot be taken into account properly[2,59].

The first bimolecular reaction to be investigated using molecular beam scattering methods was the $Cs+CCl_4$ reaction[60]. Subsequently these techniques have been widely applied to a large number of reactive systems[61-76], in particular the reactions of alkali metals with hydrogen halides[61,62,72], molecular halogens[63,65] and methyl halides[66,73]. In such

molecular beam experiments the time-of-flight resolution is normally only sufficient to allow product vibrational state information to be obtained. However in special cases, such as for the reactions of $F+H_2$[74] and $F+D_2$[75], rotational resolution can be achieved indirectly through sufficiently high level translational energy measurements.

1.4.2 Spectroscopic Methods

The spectroscopic based approach to experimental reaction dynamics gained momentum with the advent of infra-red chemiluminescence. An important aspect of this technique was that the products were formed in their electronic ground state. Work in this field was concentrated on reactions which produced hydrogen halides due to the large cross section for infra-red emission of these molecules[77,78]. The use of lasers to probe reaction products was first introduced by Zare[79] and applied to metal atom+halide systems. Subsequently the laser based techniques of Laser-Induced Fluorescence[80] and Multiphoton Ionisation[81-85] were developed and have been used to detect a huge range of species.

Lasers can also be used to generate reagents from suitable precursor molecules[86]. Laser photolysis has proved extremely convenient for the production of H atoms[86,87] since conservation of momentum ensures that most of the available energy is channeled into the translation of H. Other atoms, such as $Cl(^2P)$[22,88,89], $O(^3P)$[90-95] and $O(^1D)$[21,96-104], have also been produced photolytically.

In spectroscopic experiments, high resolution spectroscopic detection methods are used to measure directly the product internal state distributions resulting from bimolecular reactions. These detection methods are often combined with laser photolytic generation of the necessary reagents. A

typical experimental strategy can be represented by the generic reaction system shown in Equations (1.2)-(1.5).

$$AR \xrightarrow{h\nu} A + R \qquad (1.2)$$

$$A + BC \longrightarrow AB + C \qquad (1.3)$$

$$AB \xrightarrow{n h\nu} AB^{*} \qquad (1.4)$$

$$AB^{*} \xrightarrow{m h\nu} AB^{+} \qquad (1.5a)$$

$$AB^{*} \longrightarrow AB + h\nu \qquad (1.5b)$$

In these equations A, R, B and C can either be atoms or groups of atoms. AB^{*} is an electronically excited fragment and AB^{+} represents a molecular ion. The reaction scheme (Equations (1.2)-(1.5)) illustrates how reagent A is photolytically generated and then participates in a bimolecular reaction. The product AB can then be spectroscopically probed by excitation with n photons to give the electronically excited fragment. This fragment can then be detected by either creating ions (Equation (1.5a)), or by measuring the fluorescence emitted from AB^{*} (Equation (1.5b)).

Modern spectroscopic methods used to investigate the dynamics of bimolecular reactions rely heavily on the use of laser based detection which offers high quantum state detection sensitivity and good resolution. In this work, pulsed laser photolysis was used to generate the necessary reagents and reaction products were detected using Resonance Enhanced Multiphoton Ionisation (REMPI) and Laser-Induced Fluorescence (LIF) techniques, described in the experimental section. The time delay between photolysis and probe lasers may be adjusted to ensure that genuinely nascent product state distribution(s) are observed, from which the dynamics of the reaction may be inferred.

By analysing the spectroscopy of the products of the reaction shown in Equation (1.3), suitable transitions can be identified from which reliable

information on populations can be deduced. Furthermore, if the reagents were also optically pumped, full state-to-state dynamics could be studied which would determine the influence of rovibrational state on reaction cross section and product state distributions.

1.4.3 Molecular Beam and Spectroscopic Methods: The Combined Approach

The conventional boundaries between molecular beam scattering techniques and spectroscopic approaches to experimental reaction dynamics have become increasingly blurred. Nowadays, spectroscopy and optical pumping are used in conjunction with molecular beams, and pulsed jets are employed in pump-probe experiments. An example is Molecular Beam Laser-Induced Fluorescence, a well established technique which has been often used to create and detect the products of metal atom+halide reactions[105-107]. Of particular relevance to this thesis, this experimental protocol has also been applied to the reactions of $O(^3P)$[56,108-115] and $O(^1D)$[116,117] with a variety of molecules, under both gas phase[56,108-113] and condensed medium (cluster)[114-117] conditions.

1.5 The Reactions of $O(^3P)$ and $O(^1D)$ with Hydrocarbons

The aim of this project was to investigate the reaction dynamics of fundamental, gas phase, bimolecular processes, using laser methods for the state selective preparation of reagents and state specific detection of products.

The particular chemical reactions selected for study were:

$$O(^3P) + RH \longrightarrow OH(X^2\Pi) + R \qquad (1.5)$$

$$O(^1D) + CH_4 \longrightarrow OH(X^2\Pi) + CH_3 \qquad (1.6)$$

$O(^3P)$ and $O(^1D)$ represent the ground electronic and first excited states of oxygen respectively. RH is a saturated hydrocarbon, which is chosen to contain representative primary, secondary or tertiary C-H bonds. Reactive superthermal $O(^3P)$ atoms are generated by photolysis of NO_2 at 337, 308 or 248nm. By changing the wavelength of photolysis of NO_2, the collision energy of the reaction is crudely altered. $O(^1D)$ is conveniently generated by photolysis of N_2O at 193nm.

In the following chapter the experimental apparatus and procedures used in this project are described. Chapter 3 provides a detailed account of the spectroscopy of OH and CH_3 radicals, with Chapters 4, 5 and 6 containing a study of the state-to-state dynamics of the reactions of $O(^3P)$ and $O(^1D)$ with hydrocarbons.

References

[1] R.D. Levine and R.B. Bernstein, *Molecular Reaction Dynamics and Chemical Reactivity* (Oxford University Press, 1987).

[2] J.M. Farrar and Y.T Lee, *Ann. Rev. Phys. Chem.*, **25**, 357 (1974).

[3] J.C. Polanyi, *Science*, **236**, 680 (1987).

[4] H. Eyring and M. Polanyi, *Z. Phys. Chem.*, B, **12**, 279 (1931).

[5] J.O. Hirschfelder, H. Eyring and B. Topley, *J. Phys. Chem.*, **4**, 170 (1936).

[6] J.C. Polanyi, *Acc. Chem. Res.*, **5**, 161 (1972).

[7] N. Agmon and R.D. Levine, *Isr. J. Chem.*, **19**, 330 (1980).

[8] F.T. Smith, *J. Chem. Phys.*, **31**, 1352 (1959).

[9] B.A. Hodgson and J.C. Polanyi, *J. Chem. Phys.*, **55**, 4745 (1971).

[10] K.G. Anlauf, P.E. Charters, D.S. Horne, R.G. McDonald, D.H. Maylotte, J.C. Polanyi, W.J. Skrlac, D.C. Tardy and K.B. Woodall, *J. Chem. Phys.*, **53**, 4091 (1970).

[11] D.H. Maylotte, J.C. Polanyi and K.B. Woodall, *J. Chem. Phys.*, **57**, 1547 (1972).

[12] C.A. Parr, J.C. Polanyi and W.H. Wong, *J. Chem. Phys.*, **58**, 5 (1973).

[13] R. Grice, *Farad. Diss. Chem. Soc.*, **67**, 16 (1979).

[14] C.B. Moore and I.W.M. Smith, *Faraday Discuss. Chem. Soc.*, **67**, 146 (1979).

[15] N.H. Hijazi and J.C. Polanyi, *Chem. Phys.*, **11**, 1 (1975).

[16] B.E. Holmes and D.W. Seter, *Physical Chemistry of Fast Reactions: Reaction Dynamics* (Ed. I.W.M Smith, Plenum Press, New York, 1980), Vol 2, Pages 83-214.

[17] N. Sathyamurthy, *Chem. Rev.*, **83**, 601 (1983).

[18] R. Altkorn, F.E. Bartoszek, J. DeHaven, G. Hancock, D.S. Perry and R.N. Zare, *Chem. Phys. Lett.*, **98**, 212 (1983).

[19] D.J. Rakestraw, K.G. McKendrick and R.N. Zare, *J. Chem. Phys.*, **87**, 7341 (1987).

[20] R. Zhang, D.J. Rakestraw, K.G. McKendrick and R.N. Zare, *J. Phys. Chem.*, **89**, 6283 (1985).

[21] M. Brouard, S. Duxon, P.A. Enriquez and J.P. Simons, *J. Chem. Soc. Faraday Trans.*, **89**, 1435 (1993).

[22] W.R. Simpson, A. Orr-Ewing and R.N. Zare, *Chem. Phys. Lett.*, **212**, 163 (1993).

[23] M. Brouard, H.M. Lambert, J. Short and J.P. Simons, *J. Phys. Chem.*, **99**, 13571 (1995).

[24] D.F. Varley and P.J. Dagdigian, *J. Phys. Chem.*, **100**, 4365 (1996).

[25] W.R Simpson, T.P. Rakitzis, S.A. Kandel, T. Lev-On and R.N. Zare, *J. Phys. Chem.*, **100**, 7938 (1996).

[26] F.T. Wall, F.A. Hiller and J. Mazur, *J. Chem. Phys.*, **29**, 255 (1958).

[27] F.T. Wall, F.A. Hiller and J. Mazur, *J. Chem. Phys.*, **35**, 1284 (1961).

[28] H. Conroy and B. Bruner, *J. Chem. Phys.*, **42**, 4047 (1965); **47**, 921 (1967).

[29] I. Shavitt, R.M. Minn and F.L. Karplus, *J. Chem. Phys.*, **48**, 2700 (1968).

[30] C. Edmiston and M. Krauss, *J. Chem. Phys.*, **49**, 192 (1968).

[31] B. Lui, *J. Chem. Phys.*, **58**, 1925 (1973).

[32] P. Seigbahn and B. Liu, *J. Chem. Phys.*, **68**, 2457 (1978).

[33] J.Z.H. Zhang and W.H. Miller, *Chem. Phys. Lett.*, **153**, 465 (1988).

[34] D.E. Manolopoulos and R.E. Wyatt, *Chem. Phys. Lett.*, **159**, 123 (1989).

[35] J.M. Launay and M. Le Dourneuf, *Chem. Phys. Lett.*, **163**, 178 (1989).

[36] C.F. Bender, P.K. Pearson, S.V. O'Neil and H.F. Schaefer III, *J. Chem. Phys.*, **56**, 4626 (1972).

[37] D. Neuhausser, R.S. Judson, R.L. Jaffe, M. Baer and D.J. Kouri, *Chem. Phys. Lett.*, **176**, 546 (1991).

[38] D.E. Manolopoulos, K. Stark, H.J. Werner, D.W. Arnold, S.E. Bradforth and D.M. Neumark, *Science*, **262**, 1852 (1993).

[39] S.E. Bradforth, D.W. Arnold, D.M. Neumark and D.E. Manolopoulos, *J. Chem. Phys.*, **99**, 6345 (1993).

[40] J.F. Castillo, D.E. Manolopoulos, K. Stark and H.J. Werner, *J. Chem. Phys.*, **104**, 6531 (1996).

[41] C.A. Parr and D.G. Truhlar, *J. Phys. Chem.*, **75**, 1844 (1971).

[42] J.T. Muckerman, *J. Chem. Phys.*, **54**, 1155 (1971).

[43] B.R. Johnson and N.H. Winter, *J. Chem. Phys.*, **66**, 4116 (1977).

[44] G.G. Balint-Kurti, *Mol. Phys.*, **25**, 393 (1973).

[45] P.A. Whitlock, J.T. Muckerman and E.R. Fisher, *J. Chem. Phys.*, **76**, 4468 (1982).

[46] I. Last and M. Baer, *J. Chem. Phys.*, **80**, 3246 (1984).

[47] G.C. Schatz, *J. Phys. Chem.*, **100**, 12839 (1996).

[48] A.H. Zewail, *J. Phys. Chem.*, **100**, 12701 (1996)

[49] J.Z.H. Zhang and W.H. Miller, *J. Chem. Phys.*, **91**, 1528 (1989).

[50] M. Zhao, D.G. Truhlar, D.W. Schwenke and D.J. Kouri, *J. Phys. Chem.*, **94**, 7074 (1990).

[51] D.C. Clary and J.N.L. Connor, *Mol. Phys.*, **41**, 689 (1980).

[52] D.C. Clary, J.N.L. Connor and W.J.E. Southall, *J. Chem. Phys.*, **84**, 2620 (1986).

[53] D.C. Clary and J.N.L. Connor, , *J. Chem. Phys.*, **75**, 3329 (1981).

[54] J.N. Murrell and S.D. Bosanac, *Introduction to the Theory of Atomic and Molecular Collisions*, (Wiley, 1989).

[55] A.C. Luntz and P. Andresen, *J. Chem. Phys.*, **72**, 5851 (1980).

[56] P. Andresen and A.C. Luntz, *J. Chem. Phys.*, **72**, 5842 (1980).

[57] D.L. Bunker, *Methods Comput. Phys.*, **10**, 287 (1971).

[58] J.C. Polanyi, *Accounts Chem. Res.*, **5**, 161 (1972).

[59] M.A.D. Fluendy and K.P. Lawley, *Chemical Applications of Molecular Beam Scattering* (Chapman and Hall, London, 1973).

[60] T.H. Bull and P.B. Moon, *Discuss. Faraday Soc.*, **17**, 54 (1954).

[61] E.H. Taylor and S. Datz, *J. Chem. Phys.*, **23**, 1711 (1955).

[62] E.F. Greene, R.W. Roberts and J. Ross, *J. Chem. Phys.*, **32**, 940 (1960).

[63] J.D. McDonald, P.R. LeBreton, Y.T. Lee and D.R. Herschbach, *J. Chem. Phys.*, **56**, 769 (1972).

[64] K.H. Kramer and R.B. Bernstein, *J. Chem. Phys.*, **42**, 767 (1965).

[65] K.T. Gillen, A.M. Rulis and R.B. Bernstein, *J. Chem. Phys.*, **54**, 2831 (1971).

[66] A.M. Rulis and R.B. Bernstein, *J. Chem. Phys.*, **57**, 5497 (1972).

[67] D.R. Herschbach, *Faraday Discuss. Chem. Soc.*, **55**, 233 (1973).

[68] D.D. Parrish and D.R. Herschbach, *J. Am. Chem. Soc.*, **95**, 6133 (1973).

[69] S.J. Riley and D.R. Herschbach, *J. Chem. Phys.*, **58**, 27 (1973).

[70] S. Stolte, A.E. Proctor, W.M. Pope and R.B. Bernstein, *J. Chem. Phys.*, **66**, 3468 (1977).

[71] J.J Valentini, Y.T. Lee and D.J. Auerbach, *J. Chem. Phys.*, **67**, 4866 (1977).

[72] C.H. Becker, P. Casavecchia, P.W. Tiedemann, J.J. Valentini and Y.T. Lee, *J. Chem. Phys.*, **73**, 2833 (1980).

[73] S.M. Hoffmann, D.J. Smith, A.G. Urena and R. Grice, *Chem. Phys. Lett.*, **107**, 99 (1984).

[74] A.M. Neumark, A.M. Wodtke, G.M. Robinson, C.C. Hayden and Y.T. Lee, *J. Chem. Phys.*, **82**, 3045 (1985).

[75] A.M. Neumark, A.M. Wodtke, G.M. Robinson, C.C. Hayden K. Shobatake, R.K. Sparks, T.P. Schafer and Y.T. Lee, *J. Chem. Phys.*, **82**, 3067 (1985).

[76] S.R. Gandhi, T.J. Curtiss, Q.X. Xu, S.E. Choi and R.B. Bernstein, *Chem. Phys. Lett.*, **132**, 6 (1986).

[77] D.H. Maylotte, J.C. Polanyi and K.B. Woodall, *J. Chem. Phys.*, **57**, 1547 (1972).

[78] K.G. Anlauf, P.J. Kuntz, D.H. Maylotte, P.D. Pacey and J.C. Polanyi, *Discuss. Faraday Soc.*, **44**, 183 (1967).

[79] A. Shultz, H.W. Cruse and R.N. Zare, *J. Chem. Phys.*, **57**, 1354 (1972).

[80] J.L. Kinsey, *Ann. Rev. Phys. Chem.*, **28**, 349 (1977).

[81] U. Boesl, *J. Phys. Chem.*, **95**, 2949 (1991).

[82] M.N.R. Ashfold, *Mol. Phys.*, **58**, 1 (1986).

[83] M.N.R. Ashfold, S.G. Clement, J.D. Howe and C.M Western, *J. Chem. Soc. Faraday Trans.*, **89**, 1153 (1993).

[84] P.M. Jonhson and C.E. Otis, *Ann. Rev. Phys. Chem.*, **32**, 139 (1981).

[85] P.M. Jonhson, *Acc. Chem. Res.*, **13**, 20 (1980).

[86] G.W. Flynn and R.E. Weston Jr., *Ann. Rev. Phys. Chem.*, **37**, 551 (1986).

[87] C.F. Wood, G.W. Flynn and R.E. Weston Jr., *J. Chem. Phys.*, **77**, 4776 (1982).

[88] J. Park, Y.Lee and G.W. Flynn, *Chem. Phys. Lett.*, **186**, 441 (1992).

[89] Y. Matsumi, K. Tonokura and M. Kawasaki, *J. Chem. Phys.*, **97**, 1065 (1992).

[90] C.R. Park, G.D. White and J.R. Wiesenfeld, *J. Phys. Chem.*, **92**, 152 (1988).

[91] K.G. McKendrick, D.J. Rakestraw, R. Zhang and R.N. Zare, *J. Phys. Chem.*, **92**, 5530 (1988).

[92] J. Miyawaki, T. Tsuchizawa, K. Yamanouchi and S. Tsuchiya, *Chem. Phys. Lett.*, **165**, 168 (1990).

[93] H.-G. Rubahn, W.J. Van Der Zande, R. Zhang, M.J. Bronikowski and R.N. Zare, *Chem. Phys. Lett.*, **186**, 154 (1991).

[94] F. Green, G. Hancock and A.J. Orr-Ewing, *Faraday Discuss. Chem. Soc.*, **91**, 1 (1991).

[95] A. Miyoshi, K. Tsuchiya, N. Yamauchi and H. Matsui, *J. Phys. Chem.*, **98**, 11452 (1994).

[96] P.M. Aker, J.J.A. O'Brien and J.J. Sloan, *J. Chem. Phys.*, **84**, 745 (1986).

[97] J.E. Butler, G.M. Jurisch, I.A. Watson and J.R. Wiesenfeld, *J. Chem. Phys.*, **84**, 5365 (1986).

[98] C.R. Park and J. R. Wiesenfeld, *J. Chem. Phys.*, **95**, 8166 (1991).

[99] G.K. Smith and J.E. Butler, *J. Chem. Phys.*, **73**, 2243 (1980).

[100] S.M. Singleton and R.D. Coombe, *J. Phys. Chem.*, **96**, 9865 (1992).

[101] A.A. Iogansen, O.M. Sarkisov, E.V. Zimont, J.A. Seetula, R.S. Timonen and S. Cheskis, *Chem. Phys. Lett.*, **212**, 604 (1993).

[102] T. Suzuki and E. Hirota, *J. Chem. Phys.*, **98**, 2387 (1993).

[103] J. Schluetter, R. Schott and K. Kleinermanns, *Chem. Phys. Lett.*, **213**, 262 (1993).

[104] R. Schott, J. Schluetter, M. Olzmann and K. Kleinermanns, *J. Chem. Phys.*, **102**, 8371 (1995).

[105] H.W. Cruse, P.J. Dagdigian and R.N. Zare, *Faraday Discuss. Chem. Soc.*, **55**, 277 (1973).

[106] A. Gupta, D.S. Perry and R.N. Zare, *J. Chem. Phys.*, **72**, 6237 (1980).

[107] A. Siegel and A. Schultz, *J. Chem. Phys.*, **72**, 6227 (1980).

[108] K. Kleinermanns and A.C. Luntz, *J. Chem. Phys.*, **77**, 3533 (1982).

[109] K. Kleinermanns and A.C. Luntz, *J. Chem. Phys.*, **77**, 3774 (1982).

[110] K. Kleinermanns and A.C. Luntz, *J. Chem. Phys.*, **77**, 3537 (1982).

[111] N.J. Dutton, I.W. Fletcher and J.C. Whitehead, *J. Phys. Chem.*, **89**, 569 (1985).

[112] N.J. Barry, I.W. Fletcher and J.C. Whitehead, *J. Phys. Chem.*, **90**, 4911 (1986).

[113] N.J. Dutton, I.W. Fletcher and J.C. Whitehead, *Mol. Phys.*, **52**, 475 (1984).

[114] Y. Rudich, S. Lifson and R. Naaman, *J. Am. Chem. Soc.*, **113**, 7077(1991).

[115] Y. Rudich, Y. Hurwitz, S. Lifson and R. Naaman, *J. Chem. Phys.*, **98**, 2936 (1993).

[116] Y. Rudich, Y. Hurwitz, G.J. Frost, V. Vaida and R. Naaman, *J. Chem. Phys.*, **99**, 4500 (1993).

[117] R.D. van Zee, J.C. Stephenson and M.P. Casassa, *Chem. Phys. Lett.*, **223**, 167 (1994).

Chapter 2

Experimental Techniques And Instrumentation

The following chapter outlines the experimental techniques and instrumentation used to perform the state-specific chemical reaction dynamic work described in the remaining chapters.

2.1 Experimental Techniques

There are two main experimental approaches to chemical reaction dynamics: molecular beam scattering techniques and spectroscopic based methods. In this work techniques belonging to the latter discipline, namely Laser-Induced Fluorescence (LIF) and Resonance Enhanced Multiphoton Ionisation (REMPI), were used to detect gas phase reaction products.

The reaction systems studied, as outlined in Chapter 1, were:

$$O(^3P) + RH \longrightarrow OH(X^2\Pi) + R \qquad (2.1)$$

$$O(^1D) + CH_4 \longrightarrow OH(X^2\Pi) + CH_3 \qquad (2.2)$$

$O(^3P)$ and $O(^1D)$ are the ground and first excited electronic states of oxygen respectively, and RH represents a saturated hydrocarbon molecule.

The OH radical can be readily detected by LIF and the CH_3 fragment is a suitable candidate for investigation by REMPI, as discussed in detail in Chapter 3. Hence both of these laser based techniques will be described.

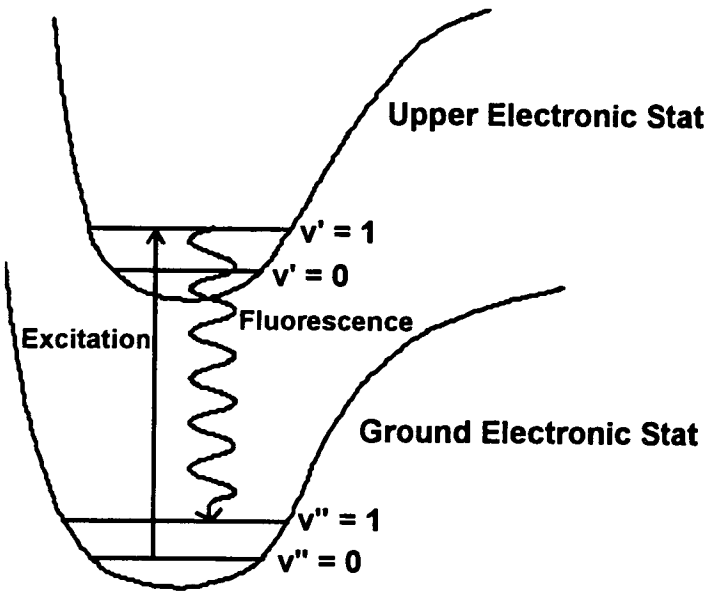

Figure 2.1: A simple LIF schematic. The lower curve represents the ground electronic state and the upper, an excited electronic state. The (1-0) band (for example) is excited by tunable laser light. Fluorescence is detected on the (1-1) band. In this work the excitation spectrum is scanned.

2.1.1 Laser-Induced Fluorescence (LIF)

Laser-Induced Fluorescence is a well established technique that is used for the detection of transient fragments produced by photodissociation or chemical reaction[1].

The basic concepts of LIF are simple[2]. The sample to be investigated is irradiated with tunable laser light. As the frequency of the laser is changed, molecules will be excited to fluoresce whenever the spectral envelope of the laser overlaps with an absorption line of the molecule. As implemented in this work and as most commonly used elsewhere, the light is in the visible/UV region and excites electronic transitions. Since the only molecules so excited are those in the specific lower level(s) of the corresponding transition, the excitation is selective for this state (or group of states). Fluorescence is spontaneously emitted as the molecules decay back down to lower-lying states. The excitation spectrum, obtained by recording the fluorescent intensity as a function of laser wavelength, will be proportional to the population of the state (or states) from which the fluorescence is excited. In summary LIF involves the observation of fluorescence from a selected excited state which has been populated by laser excitation from the ground electronic state. Figure 2.1 illustrates the LIF process.

To extract the relative product ground state populations (v″,J″) it is necessary to know the Franck-Condon factors and rotational line strengths of the system studied, or at least understand how these parameters vary over the spectral range investigated.

In the absence of alignment and saturation effects, the theoretical signal intensity, I_t, is given by[3,4]:

$$I_t = \frac{CP(v'',J'')q(v'',v')S(J'',J')}{(2J''+1)} \qquad (2.3)$$

In this expression P(v″,J″) is the population of the ground state molecules, q(v″,v′) is the Franck-Condon factor, S(J″,J′) is the rotational (Hoenl-London) line strength and C is an apparatus constant. The vibrational and total angular momentum quantum numbers of the ground state are v″ and J″ respectively; v′ and J′ are the corresponding quantum numbers for the resonantly excited state.

Hence LIF is a very useful experimental tool because ground state populations can be directly abstracted from spectra. However to be LIF active the fragment being examined must have an appreciable fluorescence quantum yield, Φ_f[2]. The OH radical fits this criterion, but CH_3, which does not fluoresce, cannot be detected by LIF.

Line Broadening Effects in LIF

The most dramatic and detrimental factor influencing the appearance and resolution of LIF spectra is a manifestation of saturation effects. In LIF experiments lines can be power broadened as a result of reduced excited state lifetimes, due to rapid optical pumping rates at high laser intensities. If present, saturation affects the interpretation of results which are based on the assumption that the observed intensity relates only to a product of line strength and population factors[5]. Hence, unless the difficult task of analysing partially saturated spectra is to be attempted, caution must be exercised when recording LIF spectra to ensure that low power regimes are used as this will limit the possibility of saturation and hence line broadening.

2.1.2 Resonance Enhanced Multiphoton Ionisation (REMPI)

One of the most recent and useful developments in molecular spectroscopy has been the ability to observe transitions where more than one photon is absorbed simultaneously[6-8]. Such processes provide the basis for REMPI.

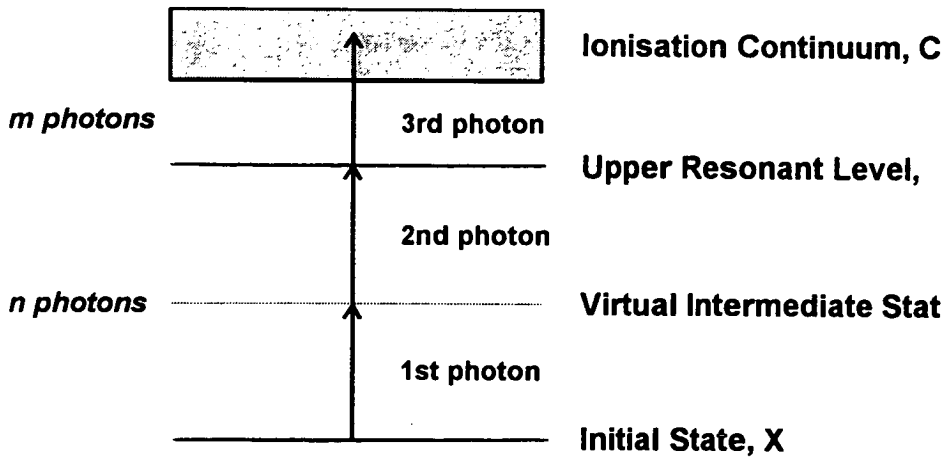

Figure 2.2: A typical (2+1) REMPI scheme. The species of interest is coherently excited from the ground state X, by simultaneous absorption of two photons (*n* photons) via an intermediate (virtual) state, up into the electronically excited state A. A further photon (*m* photons) excited the system above its ionisation potential. The generic REMPI example is an (*n*+*m*) photon system.

Resonance Enhanced Multiphoton Ionisation is a non-linear optical technique which has proved to be extremely useful as a spectroscopic probe of the electronic structure of many diatomic and polyatomic molecules[9].

Figure 2.2 demonstrates the principles of the REMPI process. The molecule in electronic state X (usually the ground electronic state) undergoes simultaneous absorption of *n* photons to reach the resonant intermediate electronic state A. Absorption of a further *m* photons takes the molecule into the ionisation continuum C. The (*n*+*m*) photons may come from either a single laser beam passing through the absorbing sample or from two or more beams emitted from one or several lasers. The success of the multiphoton ionisation lies in that the probability of ionisation is enhanced when an integral multiple of the laser photon energy is resonant with an allowed molecular transition to a bound state (for example, state A in Figure 2.2) lying below the ionisation potential.

There are several advantages to using multiphoton processes as a spectroscopic probe of transient species:

- Multiphoton selection rules allow access to states which are forbidden in single photon absorption. Table 3.1 in Chapter 3 lists single and multiphoton selection rules, and illustrates how much more flexible the rules are for multiphoton transitions. In addition, the spectra resulting from these multiphoton transitions often display quite different characteristics from single photon experiments because of the altered selection rules and transition probabilities.
- The absorption of more than one photon allows transitions that would be too large energetically to be attempted conveniently in single photon experiments. This is especially relevant for species which have their first excited states lying in the UV or VUV. REMPI studies using two or more

photons of visible or UV radiation are much easier to perform than single photon VUV experiments.

- REMPI can be a very sensitive technique due to the efficiency of ion collection.

The simplest and most common REMPI experiment consists of a tunable dye laser focused into a low pressure gas. Electrons or ions created by the laser pulse are collected, the current amplified and the resultant signals recorded as a function of laser wavelength.

Once the REMPI spectra have been recorded it should then be possible to extract the ground state populations. An equation similar to Equation (2.3) is used, except that with multiphoton studies the expression for S(J",J') is more complicated: rotational line strengths for multiphoton transitions (for example, for two photon transitions the calculated Bray and Hochstrasser transition probabilities[10]) are used. Another difference is that in some cases the Franck-Condon factors will not apply because there is a chance of overlap with real (even dissociative) states at the intermediate "virtual" level.

(2+1) REMPI (shown in Figure 2.2) is the most commonly used multiphoton ionisation detection protocol, but any combination of (n+m) photons is theoretically possible. However the main drawback to using large numbers of photons to access excited states is that the cross section for absorption falls as n increases. Typical cross sections are 10^{-50} cm^4s for a two photon absorption and 10^{-82} cm^6s^2 for a three photon process[6]. From these small numbers it is apparent that very high light fluxes are necessary to achieve a significant transition probability. Modern pulsed dye lasers, with powers of approximately 10^5 W in 10^{-8} s pulses, are the only real choice as light sources for REMPI.

Line Broadening Effects in REMPI

The focused high laser intensities used in REMPI experiments can cause saturation effects which drastically affect spectral resolution.

Saturation line broadening arises due to the fact that the excitation and ionisation processes must take place within the duration of a single laser pulse. For a 5ns pulse, uncertainty broadening limits the linewidth to a minimum of 200MHz. However, as the ionisation step tends to be much more probable than the excitation step (because it is usually a single photon process), when reasonable signal levels are attained the excited state lifetime is considerably shortened and the energy of the state effectively broadened. This results in a broadening of spectral lines[11]. For an (*n*+*m*) process the degree of lifetime broadening is a function of *n*/*m*, thus spectral lines for (3+1) REMPI are expected to be broader than for a (2+1) process.

Another cause of line broadening is the quadratic AC Stark effect[12,13] which can promote extensive broadening even at moderate laser powers. This type of broadening is so called because the energy level shift (Stark shift) depends quadratically on the electric field strength. The AC Stark shift depends purely on the laser intensity and can arise from both temporal and spatial effects within the laser pulse. However under normal REMPI experimental configurations conically focused beams are used which causes the spatial effects to dominate.

The quadratic AC Stark shift predicts that the shift in the resonant frequency is proportional to the radiation intensity. Consider two identical species at positions A and B within the focused beam, where intensity at A is greater than at B. The line shift at A will therefore be greater than at B, and this results in a broadening of the transition. In the presence of an AC Stark effect the order of the non-linear dependence on intensity for a multiphoton

process may differ considerably from a simple-minded prediction based on the number of photons absorbed in each step.

2.1.3 Time-of-Flight (TOF) / Mass Spectrometric (MS) Analysis

Time-of-flight analysis, coupled with mass spectrometric detection, is a method of collecting and detecting ion counts and is often used in tandem with REMPI.

The physical basis for TOF analysis is that ions of equal charge, subjected to the same accelerating electric field, will travel at different speeds according to their respective masses. Hence, in a REMPI experiment, ions are created via a laser pulse and then accelerated through a fixed potential into a field free drift tube (TOF tube). All ions are extracted, to a first approximation, with the same kinetic energy. This means that ions of different masses will travel at different velocities through the drift tube and will be separated in time before reaching the detector. The flight time, t, depends on the ion mass as shown in Equation (2.4). K is a proportionality constant determined by the particular design parameters of the instrument.

$$t = K(m)^{1/2} \qquad (2.4)$$

Light, fast moving ions reach the detector before heavy, slow moving species. By recording the ion intensity as a function of time, a time-of-flight spectrum is generated, and spectral features (peaks or lines) can be assigned according to their mass. To record the REMPI spectrum of a particular species the appropriate mass is gated and the relevant transition scanned.

2.2 Experimental Instrumentation

In this section the instrumentation necessary to experimentally investigate the gas phase, bimolecular, chemical processes outlined in Equations (2.1) and (2.2) will be described. The apparatus, which has also been discussed in previous work[14,15], was designed to incorporate both REMPI-TOF and LIF detection techniques.

The experimental apparatus can be categorised into two main groups which will be discussed separately: lasers and the vacuum system. The instrumentation belonging to each category will be described, methods of generation of reactive species outlined and the data acquisition process explained.

2.2.1 The Laser System

In this work experiments were performed with a view to achieving two main objectives:

- Firstly, laser spectroscopic methods (namely LIF and REMPI) were developed to detect OH and CH_3 / R reaction products. These radicals were generated simply, by either microwave discharge (Section 2.3.1) or laser photolysis (Section 2.3.2) of suitable precursor molecules, and then spectroscopic investigations were performed to identify transitions from which reliable population information could be deduced. The experimental procedures used to develop and enhance LIF and REMPI detection techniques tended to be relatively simple and required only one laser. In all such experiments a Nd:YAG pumped dye laser system was used to generate (where applicable) and probe the radical species. Such experiments are termed one colour experiments.

- Secondly, and most importantly, LIF and REMPI were applied, in conjunction with pulsed laser photolytic generation of reagents, to investigate the gas-phase reactions specified in Equations (2.1) and (2.2). Such experiments required the use of two laser systems: one to photolytically generate active reagents and the other to probe the nascent product molecules. A gas-discharge laser was used to achieve the first objective while a Nd:YAG pumped dye laser system was used for the spectroscopic detection of products.

2.2.1.1 Questek Series 2000 Gas-Discharge Laser

The gas-discharge (excimer) laser was used to photolytically generate reactive species from suitable precursor molecules. Different gas mixtures could be used to achieve a number of output frequencies. In this work the laser was operated using the following mixtures:

1. 5% F_2 in He + Kr + He to generate 248nm radiation (KrF laser).
2. 5% F_2 in He + Ar + He to generate 193nm radiation (ArF laser).

The laser required a 5V trigger pulse for external operation. There was a 1μs delay between the sending of the trigger pulse and observed laser light output. This corresponds to the time taken for the thyratron to fire and initiate discharge in the laser cavity. The temporal jitter of the laser pulse, relative to the input trigger, was measured to be ±2ns.

The excimer laser was thyratron-switched, and the high voltage discharge operated between 0 and 30kV. At the maximum voltage output energies of 200mJ, in a 10ns pulse, could be achieved at 248nm and 120mJ/pulse at 193nm. The final output energy could be altered by adjusting the control voltage setting.

The emergent beam was rectangular (approximately 30mm by 15mm) and unpolarised. A f=50cm quartz lens, which had a diameter of 25mm, was used to focus the photolysis beam into the vacuum system. This lens was estimated to transmit and focus approximately 85% of the beam energy.

2.2.1.2 Spectron Nd:YAG Laser-Pumped Dye Laser System

The Spectron Laser System comprised of a Q-switched, pulsed Nd:YAG laser (SL803S), a dye laser (SL4000G) , a scan controller (SL4000SC) and a wavelength extension unit (SL4000EX). The combined laser system could provide tunable laser radiation from 200 to 700nm.

Spectron SL803S Nd:YAG Laser

The Nd:YAG laser contained two Neodymium doped YAG rods which operated as an oscillator/amplifier pair, with the lasing occurring between the electronic levels of the Nd^{3+} ions. Each rod was pumped by its own flashlamp. The oscillator and amplifier flashlamps could be triggered internally or from an external source. In either operational mode the triggering initiated the charging of the Q-switch capacitors. Then once the specified flashlamp to Q-switch delay (200μs) had elapsed the high voltage relay supplying the Pockels Cell was activated. This resulted in the production of short (approximately 10ns FWHM) pulses with energies of approximately 800mJ at the laser's fundamental wavelength of 1064nm. The Nd:YAG laser was optimised at a 10Hz repetition rate.

For this work, the fundamental 1064nm output from the oscillator/amplifier unit was frequency doubled using a KDP crystal and the resulting 532nm radiation (second harmonic) was separated from the residual 1064nm beam using a dichroic beam splitter. The optimised pulse energy at 532nm was approximately 300mJ and the beam was horizontally polarised. The remaining 1064nm radiation was either collected by a beam dump or used

for frequency mixing in the SL4000EX wavelength extension unit. The 532nm beam was used to pump the SL4000G dye laser.

Spectron SL4000G Dye Laser

The function of the dye laser was to provide a tunable source of laser light which could either be used directly or doubled and/or mixed in the wavelength extension unit.

This laser comprised of an oscillator and two amplifier stages. The oscillator was pumped using only a small amount (approximately 10%) of the 532nm output from the Nd:YAG laser. The remainder of the pump beam was split equally to drive the two amplifier modes.

The oscillator consisted of a transversely pumped flowing dye cell, an output coupler, a diffraction grating, a wavelength tuning mirror and a prism beam expander. The grating was operated in a grazing incidence configuration and wavelength tuning was achieved using a separate mirror mounted on a stepper motor sine drive arrangement. The sine drive contained a mechanical counter and two proximity switches to detect the limits of the drive travel.

The amplifier section comprised of two longitudinally pumped dye cells set at Brewster's angle. The pump light for each of the amplifiers was supplied by the main pump beam via two beam splitters; one for each dye cell.

The dye circulator contained two separate reservoirs; one each for the oscillator and amplifier dye cells. Each reservoir held approximately one litre of dye solution with the oscillator solution typically being significantly more concentrated than the amplifier.

A large number of laser dyes could be utilised to achieve a wide range of wavelengths (550-700nm). The dyes used were generally rhodamine and coumarin salts, dissolved in methanol. The final output from the dye laser was horizontally polarised, and the beam energy was highly dependent on the dye used.

Spectron SL4000EX Wavelength Extension Unit

To perform the majority of the experiments in this work, wavelengths between 250 and 350nm were required. This range was achieved by either doubling the output from the dye laser or by doubling then mixing this light with the residual Nd:YAG fundamental of 1064nm.

The wavelength extension unit comprised of a delay line for the Nd:YAG beam, a doubling unit for the dye beam and a mixing unit to sum frequency mix the doubled dye and 1064nm beams. The doubling and mixing components had separate stepper motor drives and heaters.

The SL4000EX system utilised parallel faced non-linear KDP crystals for harmonic generation and sum frequency mixing, with axial effects being corrected for by plain quartz compensating blocks. All crystals were temperature controlled to maintain stability and prevent absorption of water from the atmosphere. To preserve the correct phase matching conditions in the chosen doubling or mixing crystals, small fractions of the doubled and mixed beams were diverted onto two separate photodiodes with local head amplifiers and adjustable gain. A linked BBC microcomputer monitored the respective doubled and mixed power outputs via analogue to digital converters. As the dye wavelength was scanned the orientations of the crystals were continually updated to ensure the correct phase matching conditions, and hence maintain the maximum power output. The crystals were rotated in one angular plane by stepper motors, whose drivers had limit

switches to detect and prevent excessive rotation of the crystals. Different crystals were used to generate a range of UV wavelengths.

When the required UV wavelengths could be produced by doubling only, the frequency mixing crystal was removed and the 1064nm radiation prevented from entering the unit. The doubled UV radiation typically had pulse energies of 2-4mJ, depending on the dye tuning curve and the efficiency of doubling at a particular wavelength. The frequency doubled beam was vertically polarised. If mixing was necessary, both doubling and mixing crystals were mounted in the unit and the 1064nm beam was directed around an optical delay line incorporating a beam diameter reducing telescope. The mixed UV radiation generally had pulse energies less than 2.5mJ, again dependent on the dye tuning curve and the efficiency of the doubling and mixing crystals. The frequency doubled/mixed beam was horizontally polarised. The desired beam was separated from the unwanted beams by a pair of Pellin-Broca prisms, which also compensate for the angular dependence of the beam on the wavelength.

Spectron SL4000SC Scan Controller

The Spectron SL4000SC scan controller was used to control the diffraction grating position of the dye laser. The scan controller was connected to a PC (Section 2.4.3) via a RS-232 serial port. This configuration enabled the dye laser wavelength to be directed by computer.

Laser Radiation Power Meters

Laser powers were measured using either a Scientech 372 power meter or a Molectron J3-09 Pyroelectric Joulemeter. The Scientech meter was a good general purpose instrument, whereas the Molectron was particularly useful for determining powers of less than 1mJ.

2.2.2 The Vacuum System

The vacuum system (constructed by Vacuum Generators UK Ltd. to a custom design) could be configured for both REMPI-TOF and LIF detection schemes. In this section the experimental apparatus required for each technique will be described.

2.2.2.1 REMPI-TOF Detection

The vacuum system, shown in Figure 2.3, consisted of two differentially pumped chambers (a reaction chamber and a detection chamber) linked by a flight tube. All sections of the apparatus had a nominal 101.52mm (4″) internal diameter components. The pressure in the system was monitored via a number of Pirani (Edwards PR10K) and ion (Vacuum Generators VIG 8) gauges connected to analogue controllers (Vacuum Generators VIG 17F). Additionally a MKS Baratron (Type 127) capacitance manometer was used to monitor pressures too high for the reaction chamber ion gauge (that is, pressures in the range 0.1mTorr to 1Torr). Typical steady-state background pressures, with no gas flowing, were 1×10^{-6} mbar in the reaction chamber and 5×10^{-8} mbar in the detection chamber.

The reaction chamber was separated from the flight tube and detection chamber via a small aperture incorporated into a component labeled the "top hat" flange, which is shown in Figure 2.3. This aperture, of variable dimension, allowed a pressure differential between the reaction and TOF tube/detection chambers and ensured that the relatively high pressures (typically 10^{-4} mbar) required at the reaction zone for bimolecular dynamic studies were achievable whilst maintaining the necessary high vacuum (below 10^{-6} mbar) needed for ion detection. A low pressure was required in the TOF tube/detection chamber for two reasons: to protect the Microchannel Plate detector from electrical breakdown and to provide a collision free region for the ions to travel along.

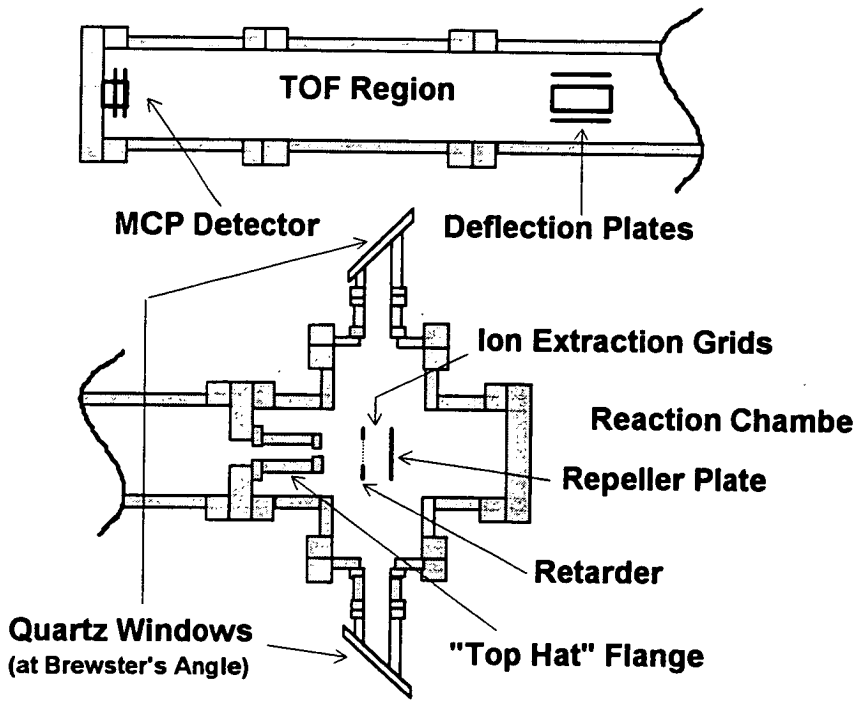

Figure 2.3: Schematic of the vacuum system, showing a generic set up incorporating REMPI detection. The ion extraction grids, composed of a repeller, retarder and ground plate are arranged in the Wiley-McLaren[16] configuration. With this experimental apparatus it was found to be convenient to use the "top hat" flange as the ground plate.

The reaction and detection chambers were separately evacuated by two cryotrapped 101.52mm (4") oil diffusion pumps (Edwards 100/300M), backed by rotary pumps (Edwards E2M8). The rotary pump which served the reaction chamber was further protected from corrosive gases by a cryotrap. The flight tube was principally evacuated via the detection chamber diffusion pump although some flow could occur via the reaction chamber pump, made possible by the "top hat" hole. Vacuum conditions were aided by the use of Viton O-rings and copper or rubber gaskets between vacuum connections.

The main body of the reaction chamber was a six way cross. Two limbs of the cross could potentially be used to let gases into the system, one limb was attached to the diffusion pump and another housed the "top hat" flange. Inset into the final two opposing faces were quartz windows allowing entry and exit of the laser beams. As the radiation from the probe beam was of a single polarisation (either vertical or horizontal depending on whether the output was doubled or mixed) the windows were set at Brewster's angle and ~~orientated~~ oriented to ensure the maximum transmission of light.

2.2.2.2 Ion Extraction

The UV light from the probe laser was typically focused into the reaction chamber using a f=30cm quartz lens. This produced a focused beam with a diameter of approximately 100 μm. The ions formed at the laser focus were extracted using one of two arrangements, depending on the REMPI experiment. For the REMPI detection of OH following the photolysis of formic acid (Chapter 3 Section 3.1.4) a modified Wiley-McLaren[16] configuration was used. However for the REMPI detection of CH_3, following photolysis of CH_3I (Chapter 3 Section 3.2.3) or in a bimolecular study (Chapter 6), an ion extraction set-up with an electrostatic lens was used.

(a) The modified Wiley-McLaren ion extraction arrangement

The classic Wiley-McLaren double field linear ion extraction configuration[16] consists of a repeller, a retarder and a ground plate as illustrated in Figure 2.3. With the available experimental apparatus, it was found to be convenient to use the "top hat" flange as the ground plate as this lessened the distance traveled by the ions before entering the high vacuum TOF region, thus improving the overall sensitivity[14].

However, while this configuration gave perfectly good signals for simple REMPI spectroscopy experiments, it was deemed necessary to alter the optics for bimolecular dynamics experiments. In dynamics experiments the concentrations of nascent products available for probing is greatly reduced as compared with spectroscopic experiments. Hence to extract nascent ions the retarder plate was discarded and the "top hat" flange repositioned so that its front face was located at the previous retarder position. An insulating spacer, bolted between the flight tube and the "top hat" flange, allowed the "top hat" to be electrically floated. The idea behind these changes was to minimise the path through the relative high density of gases in the reaction chamber necessary in a bimolecular experiment and maximise the number of ions that could be extracted. With this configuration the "top hat" acted as the retarder and subsequently the mass spectrometer was only a single field system. No great loss in the resolution of the spectrometer was observed in changing from the double to single field design. This is mainly because the focused spot size is very small and the principal effect of the Wiley-McLaren arrangement is to provide "space-focusing" to reduce the spread in flight times for an extended source. The modified single field ion extraction configuration is shown in Figure 2.4.

All the ion optic components were built by the technical support staff at Edinburgh University and fabricated from stainless steel. The repeller plate

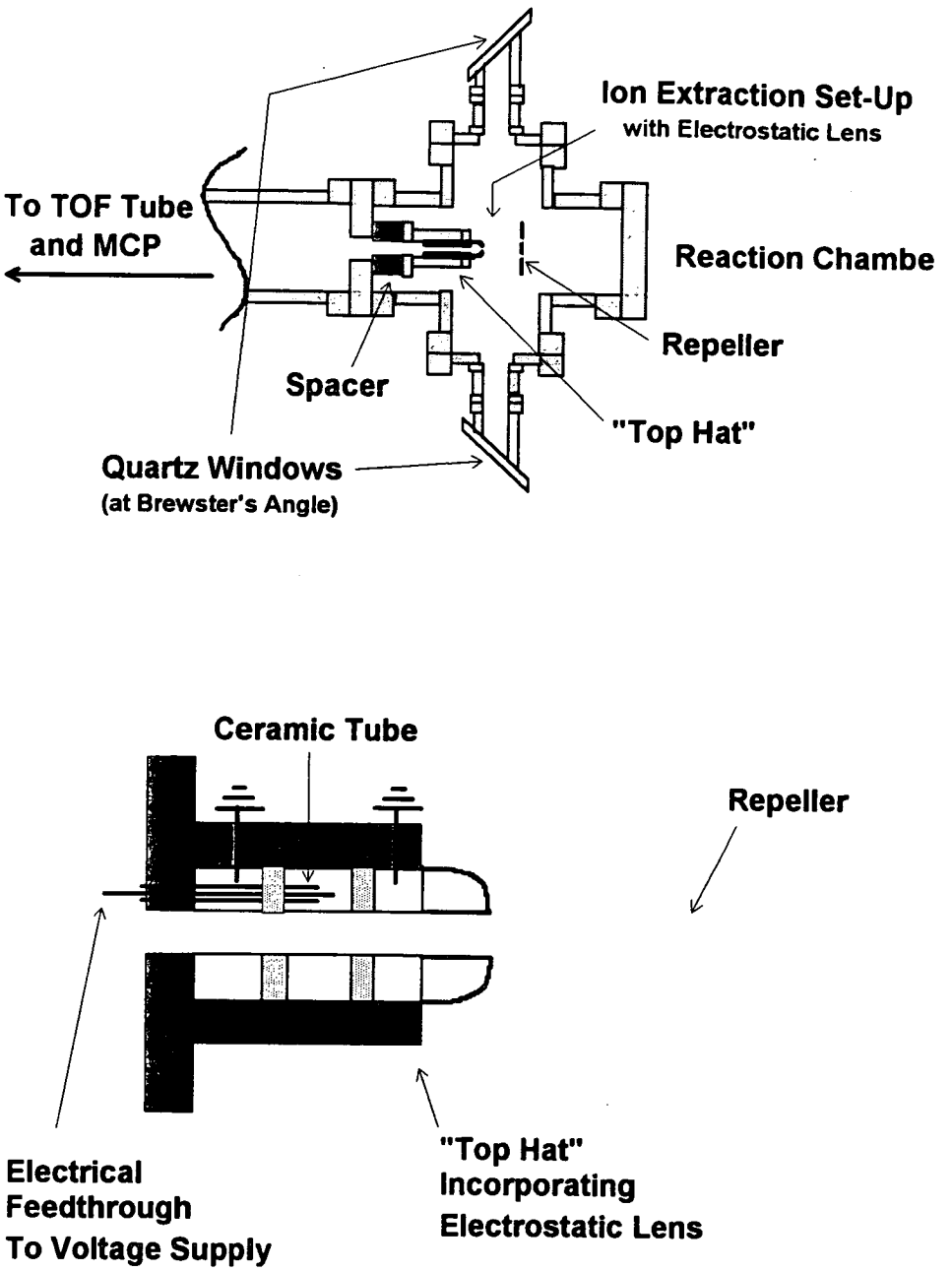

Figure 2.5: The top panel shows a schematic of the reaction chamber, incorporating REMPI detection. Here, the ion extraction components are bullet shaped and include an electrostatic lens. The bottom panel shows a close-up of the component mounted within the "top hat" (i.e. the electrostatic lens) and the repeller.

was 75mm in diameter and 0.5mm thick. The voltages to the grids were supplied by two high voltage power supplies (Bertan 353, 0-3kV).

Despite the modifications made to the grid system, this configuration was not used in the bimolecular reaction dynamic study. Detecting nascent products from a bimolecular reaction by REMPI can be a tricky procedure and more radical alterations to the ion extraction arrangement were discovered to be necessary (refer to (b)). This set-up was used, however, in the detection of OH following photolysis of formic acid.

(b) Ion extraction arrangement incorporating an electrostatic lens

A number of changes to the ion extraction arrangement, described in (a), were deemed necessary.

1. A critical experimental factor in reaction dynamic studies is the proximity of the gas inlet to the focus of the laser beam(s). With REMPI detection pulsed molecular beam valves (or nozzles) are often used as a means of introducing gases into the reaction chamber, for the reasons outlined in Section 2.2.3.2. An important improvement to the ion extraction set-up was to allow the gas inlet (that is, the nozzle) to be brought closer to the laser beam(s). This, in theory, could be achieved by reducing the size of the repeller plate and "top hat" flange. In practice, a solid stainless steel bullet shaped component, with a maximum diameter of 10mm, was screwed on to the centre of the existing repeller plate and electrical feedthroughs attached. A similarly shaped stainless steel bullet, with an aperture of variable dimensions, was also designed and incorporated into the "top hat" flange. These changes illustrated in Figure 2.5 allowed the bulky repeller plate and "top hat" flange, which had previously served as the extraction grids, to be moved further from the laser focus and hence the gas inlet (a bullet shaped nozzle) could be moved closer to the reaction zone at the centre of the reaction chamber. The bullet shaped

components, affixed to the repeller plate and "top hat" flange, could now serve as the ion extraction optics. The "top hat" aperture was located 6.5mm from the laser focus[1] and the position of the repeller could be varied with respect to the centre of the reaction chamber. Voltages to the grids were supplied by the two high voltage power supplies (Bertan 353, 0-3kV). An advantage to using bullet shaped grids is that the fields between the repeller and "top hat" flange are flatter, thus enabling the nozzle (also bullet shaped) to be brought closer to the laser focus with less chance of voltage trips. Additionally, the signal was found to be improved (and the fields flattened) by having a rectangular slot (10mm×2mm) rather than a hole (5mm diameter) in the "top hat".

2. The bullet shaped component affixed to the "top hat" flange is not merely a retarder with an aperture, but was designed, based on theory from Harting and Read[17], to act as an electrostatic lens. The component is not solid like the bullet attached to the repeller, but comprises of three cylindrical sections. The two outer cylinders are grounded but the component was designed so that a potential could be applied to the cylinder in the middle; the voltage is supplied to this cylinder by an electrical feedthrough, insulated by a ceramic tube. These features are illustrated in the bottom panel of Figure 2.5. The electrostatic lens was designed to focus ions, and by applying the correct voltages a significantly greater proportion of ions, as compared with conventional Wiley-McLaren extraction methods, should reach the detector thereby improving the signal to noise ratio.
3. As previously mentioned, pulsed molecular beam valves were often used to introduce gases into the reaction chamber in REMPI experiments. The nozzles conventionally comprise of a neck and flange which are relatively bulky. For this work, however, bullet shaped nozzles were used which were smaller and could be brought closer to the laser focus, but with less

[1] To get the "top hat" this close to the centre of the reaction chamber, a spacer, 10mm thick, was placed between the flight tube and "top hat" flange.

likelihood of voltage trips. In addition, with these nozzles, there is less distortion of the fields which would prevent the ions from passing through the aperture and reaching the detector. The nozzles are discussed in more detail in Section 2.2.3.2.

(c) Deflection Plates

Once the ions have been accelerated through the aperture in the "top hat" flange they enter into the high vacuum, field free, time-of-flight (TOF) region. This region contained a two dimensional deflection plate arrangement, designed to allow horizontal and vertical adjustment of the ion trajectories and thus maximise the ion flux at the detector. Positive or negative d.c. voltages could be applied independently to each set of plates via a dual power supply (Kingshill, variable 0-150V). The electrical connections were fed through a flange situated above the deflection plates.

2.2.2.3 Microchannel Plate Detector

The ion signals were monitored using a Microchannel Plate (MCP) detector (R.M. Jordan) located at the end of the TOF region. The detector consisted of two parallel microchannel plates (Galileo MCP-18B), each having an active area of 2.5cm^2. A maximum potential difference of 2kV could be applied between the front and rear surfaces of each plate. Additionally, an accelerating potential of approximately 1kV was applied between the rear of the first plate and the front of the second plate. In this configuration each plate had a gain of 10^3 resulting in a net gain of 10^6. The voltages to the plates were supplied by a high voltage power supply (Bertan, 0-5kV) and a voltage divider chain. The output from the MCP detector was amplified (Stanford Research Systems SR240) and then collected using the data acquisition system described in Section 2.4.

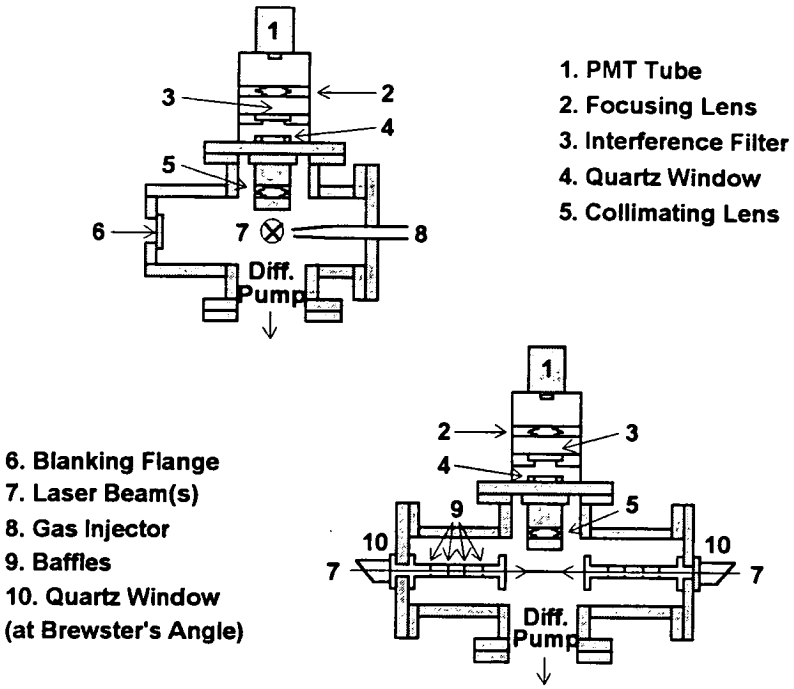

Figure 2.6: Schematic of the experimental arrangement within the reaction chamber used for LIF detection. The upper diagram is a view perpendicular to the laser beam(s) while the lower diagram shows a view parallel to the laser beam(s).

2.2.2.4 LIF Detection

Figure 2.6 shows how the vacuum system was adapted to accommodate LIF experiments. The flight tube and detection chamber are redundant in fluorescence experiments, so to convert from REMPI to LIF detection protocol the first major step was to remove the "top hat" flange and replace it with a blank flange. This served to isolate the reaction chamber from the detection chamber and was a very necessary procedure because the high pressures used in LIF experiments would have damaged the MCP detector. In an LIF experiment the detector is situated external to the vacuum system and is obviously insensitive to the pressure inside the reaction chamber. Hence the pressure constraints, inherent to REMPI detection, are avoided. It must be noted though, that the pressure must not be too high if detection of nascent products is required. Typical total pressures in an LIF experiment could be up to 300mTorr.

The reaction chamber was evacuated using a 101.52mm (4") cryobaffled diffusion pump (Edwards 100/300M) and backed by a cryotrapped rotary pump (Edwards E2M8). However because relatively high pressures were required, the diffusion pump was isolated and the chamber pumped solely by the rotary pump whilst experiments were carried out (that is, when gases were allowed into the chamber). The rotary pump could maintain a base pressure of 10^{-3} mbar with no gas flowing.

For the LIF experiments the main body of the reaction chamber was utilised in a slightly different way as compared with the arrangement used for REMPI detection. Only one face of the six way cross could be used to let reactants into the system because the detector was mounted on top of the reaction chamber. Two of the opposing faces housed quartz windows set at Brewster's angle, which allowed the laser beams to access the chamber.

In a typical experiment the UV light from the probe beam entered the reaction chamber, unfocused, and the resulting fluorescence was directed in the Photomultiplier Tube (PMT) detector placed above and perpendicular to the laser beam(s).

The lens assembly, shown in Figure 2.6, was used to focus the fluorescence onto the detector. The plate at the base of the lens assembly contained a rectangular hole (10mm×5mm) cut through it's centre to allow light to enter. The first lens, placed at a distance equal to it's focal length from the laser beam(s), produced a collimated beam of light which then passed through an interference filter, chosen to transmit only the desired fluorescence. A second lens imaged the light onto the PMT photocathode. Both lenses were mounted so that their positions could be altered to ensure the maximum signal.

A key factor in the success of LIF experiments is maintaining low levels of scattered light. Several measures were taken to ensure that the amount of stray light seen by the detector was minimal:

1. The laser beams were directed through long (25cm), internally baffled entrance and exit arms. The baffles were arranged so as to best trap any scattered light generated at the windows.
2. The interior of the reaction chamber, the baffles, the entrance and exit arms and the lens assembly were all coated with matt black paint.
3. An appropriate bandpass interference filter was placed in the lens assembly between the focusing lens and PMT detector. This effected the most significant reduction in scattered light. The filter was chosen to transmit radiation over the wavelength region of the desired vibronic transition, whilst blocking out the wavelengths of both the photolysis and probe lasers. Two bandpass interference filters were used in this work; an Ealing 35-8044, centred at 310nm with a bandwidth of 10nm and a

Melles Griot O3FIM018, centred at 280nm and with a bandwidth also of 10nm.

2.2.2.5 The Photomultiplier Tube (PMT) Detector

Photomultiplier detectors provide an efficient means of capturing fluorescent signals. Photons enter the tube and impinge on a metal surface, such as caesium. The electrons (photoelectrons) emitted are subjected to an accelerating voltage and they fall onto a secondary surface, releasing more electrons. This process is repeated several times, resulting in a large current amplification[18].

The photomultiplier tube (Thorn EMI 9789QB) used to detect fluorescence in this work had a relatively high response in the wavelength region of interest. The response time of the detector was 10ns and the pulse width at normal operating temperatures was 20ns FWHM. The tube had a 13 stage venetian blind dynode chain and the CsSb photocathode had a working diameter of 10mm. This relatively small photocathode diameter produced low dark currents at low light levels. The output from the PMT was amplified (Stanford Research Systems SR240) and collected using the data acquisition system described in Section 2.4.

2.2.3 Gas Handling

Reagents of interest were introduced into the reaction chamber via a gas inlet network connected to the vacuum system. There were two separate lines leading to the reaction chamber: one for photolysis precursor regents and the other for molecular target reagents. Gases were kept, prior to use, in stainless steel reservoirs (Whitey) and could be purified by freeze-pump-thaw cycles. Liquid reagents could also be used and were stored in stainless steel "fingers". Reagents could enter the reaction chamber either as effusive sources or using pulsed molecular beam valves.

2.2.3.1 Effusive Sources

The simplest way to generate an effusive source was to bleed gas in via inlets in the rear flange of the reaction chamber. This method proved sufficient for some spectroscopic studies where the transition being studied was fairly intense and the number density of the species was high. However, sometimes the signal was weaker and a more direct inlet source was required. In these instances glass or quartz injectors, with various outlet hole sizes, were used to feed the reagents into the reaction chamber. The number density at the reaction zone was highly dependent on the distance between the injector tip and the laser focus, and dramatic increases in the signal intensity were observed when this distance was small.

The injector method proved to be very useful for LIF experiments, however in REMPI measurements ion extraction was problematic. In REMPI experiments the tip of the injector was often located within the fixed extraction field defined by the draw-out-grids. This problem could be resolved by coating the injector tip with a conductive material, connecting it to a separate power supply and tuning its voltage to optimise the ion signal. However this arrangement proved susceptible to voltage trips and it was difficult to maintain a steady signal.

2.2.3.2 Pulsed Molecular Beam Valve Sources

A major problem in gas phase bimolecular studies, especially with effusive sources, is in obtaining sufficient density of species at the laser focus without greatly overloading the pumping system. The gas number density at this point can be greatly increased by using a pulsed molecular beam valve (nozzle) to introduce gas into the vacuum system.

There are several advantages to using nozzles in such experiments:

- Firstly the nozzle is movable and can be brought close to the laser beam, thus increasing the gas density at the laser focus. A manifestation of this effect is that the signal to noise ratio is increased in nozzle experiments as compared with continuous flow systems. The distance between the bottom of the nozzle and the laser focus depends on the detection protocol. In LIF experiments the nozzle could be brought very close (approximately 10mm) to the laser focus but with REMPI detection the nozzle could sit only at a minimum distance of 20mm from the laser; bringing it any closer caused distortion of the extraction fields.
- The second advantage of using nozzles is that the reagents are pulsed into the vacuum system in short bursts. Typically the valve is only open for 200-500μs every 100ms. This leads to a high transient density for a given apparent steady-state pressure recorded on the ion gauge. So, despite the high density of gas at the laser focus, the background pressure in the reaction ~~pressure~~ chamber, and hence the detection chamber, remains low, allowing the use of higher MCP detection voltages.
- Additionally, the downward flow of the reagents, as they pass out of the nozzle into the chamber, aids the pumping capacity of the vacuum system.

The pulsed molecular beam valve used in this work was supplied by the General Valve Corporation (Series 9). The valve consisted of an iron actuator "neck" piece screwed onto a "body" part, which housed an orifice of variable dimension, although in this work 0.5mm diameter holes, only, were used. The "body" of the nozzle was either flange or bullet (snub nosed) shaped. For LIF experiments the conventional flange shaped nozzle was used but for REMPI detection it was found to be much more advantageous to use a bullet shaped nozzle as this design lessened distortion in the ion extraction fields as the nozzle was brought close to the laser focus. A Teflon plunger, attached to the actuator, sealed against the orifice at the bottom of the valve.

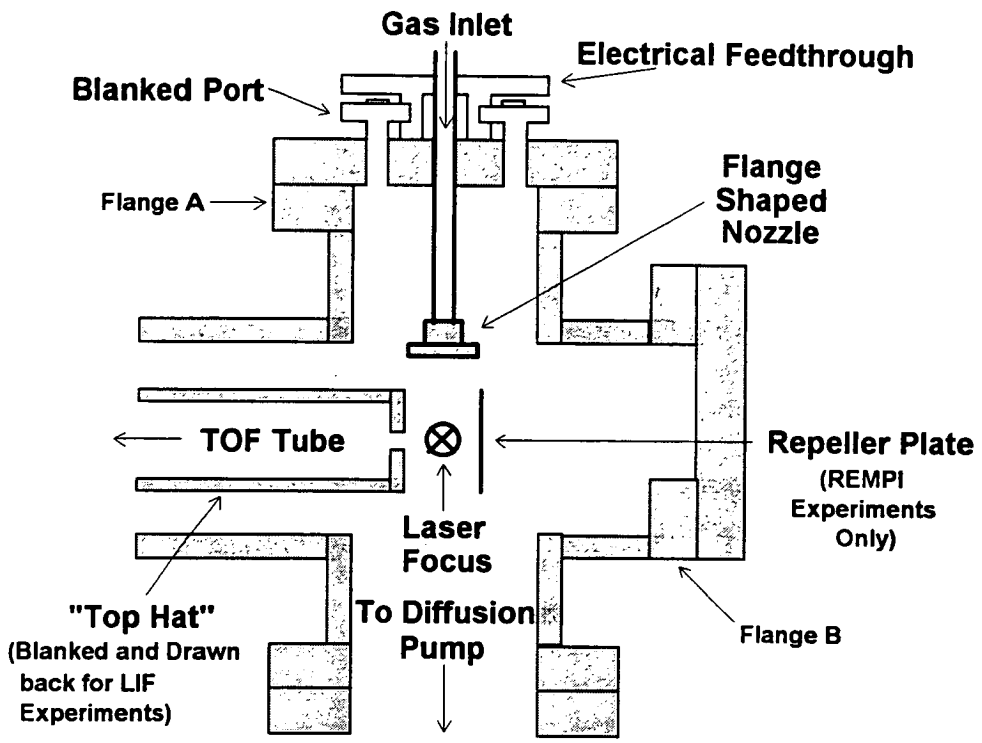

Figure 2.7(a): Reaction chamber with the flange shaped nozzle, set up for REMPI experiments. Here the valve is mounted on top of the chamber and attached to flange A. However for LIF experiments the valve would be attached to flange B, at the side of the reaction chamber, because the PMT and lens assembly needs to be mounted on flange A.

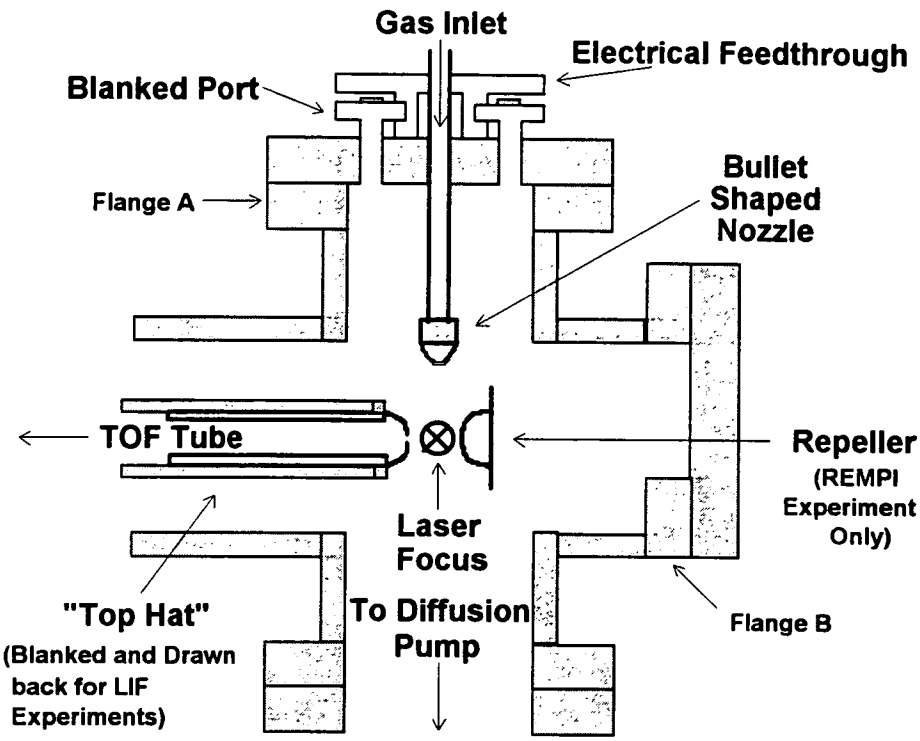

Figure 2.7(b): Reaction chamber with the bullet shaped nozzle, set up for REMPI experiments, with the valve attached to flange A. For LIF experiments the valve would be transferred to flange B.

The valve was opened by the application of a current pulse to a solenoid, which pulled back the actuator (and plunger) and opened the nozzle. The resultant gas pulse duration was determined by the length of time that the current was applied. The current pulse was supplied by an Iota One (General Valve Corporation) valve driver.

Figures 2.7(a) and (b) show how the valve was arranged within the reaction chamber. Figure 2.7(a) shows the flange shaped nozzle while Figure 2.7(b) illustrates the bullet shaped (snub nosed) nozzle. The valve was mounted on a custom built flange supplied by Vacuum generators, UK Ltd., and connected to the gas inlet inset in the centre of the flange via stainless steel tubing. Vertical adjustment of the valve was possible.

This single valve configuration was intended for use in bimolecular experiments where the precursor and reactant gases were unreactive and could be mixed prior to entering the reaction chamber.

2.3 Production of Radical and Atomic Species

To carry out both spectroscopic and bimolecular reaction dynamic studies radical and atomic sources were necessary. Two methods of production of these reactive species were available.

1. Microwave discharge of suitable precursor molecules.
2. Laser photolysis of suitable precursor molecules.

2.3.1 Microwave Discharge of Suitable Precursor Molecules

Microwave discharge was used in this work as a source of thermal OH, necessary for spectroscopic studies on this system. The OH was produced by microwave discharge-induced dissociation of water (no carrier gas was necessary) and subsequently probed by LIF.

The apparatus used for microwave discharge experiments was as follows. An EMS Microtron (Mk 3) power supply was used to produce microwaves at 2450Mhz[19]. The air cooled discharge cavity (EMS 214L) was operated at approximately 50W and the reflected power was measured using an EMS reflected power meter, incorporated within the power supply. The discharge injector was made of quartz and internally coated with ortho-phosphoric acid to reduce heterogeneous loss of radicals. The injector, set in the rear flange of the vacuum system and attached to the gas lines, could be moved relative to the laser beam.

2.3.2 Laser Photolysis of Suitable Precursor Molecules

Laser photolysis of suitable precursors is a very useful way of providing radical and atomic sources, necessary for spectroscopic and bimolecular reaction dynamic studies, for a variety of reasons[15]:

- A high density of species is produced effectively instantaneously
- The resulting collisions between the atoms (produced by photolysis) and target reagent molecules are highly energetic due to the non-thermal atomic translational energy distributions produced.
- Polarised laser photolysis creates an anisotropic distribution of fragment recoil velocities and hence collision velocities.

The degree of molecular dissociation following laser photolysis depends on the molecular extinction coefficient at a particular photolysis wavelength and on the intensity of the photolysis beam.

Figures 2.8 and 2.9 illustrate how the combined laser and vacuum hardware was arranged for pump (photolysis) and probe experiments, incorporating LIF (Figure 2.8) and REMPI (Figure 2.9) detection.

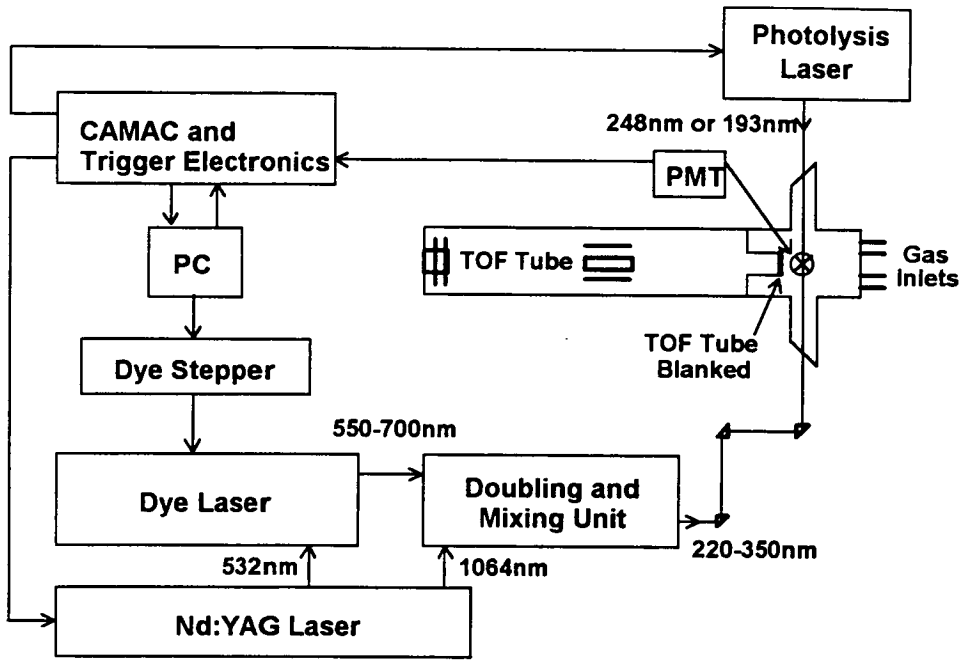

Figure 2.8: Schematic of photolysis/probe apparatus incorporating LIF detection.

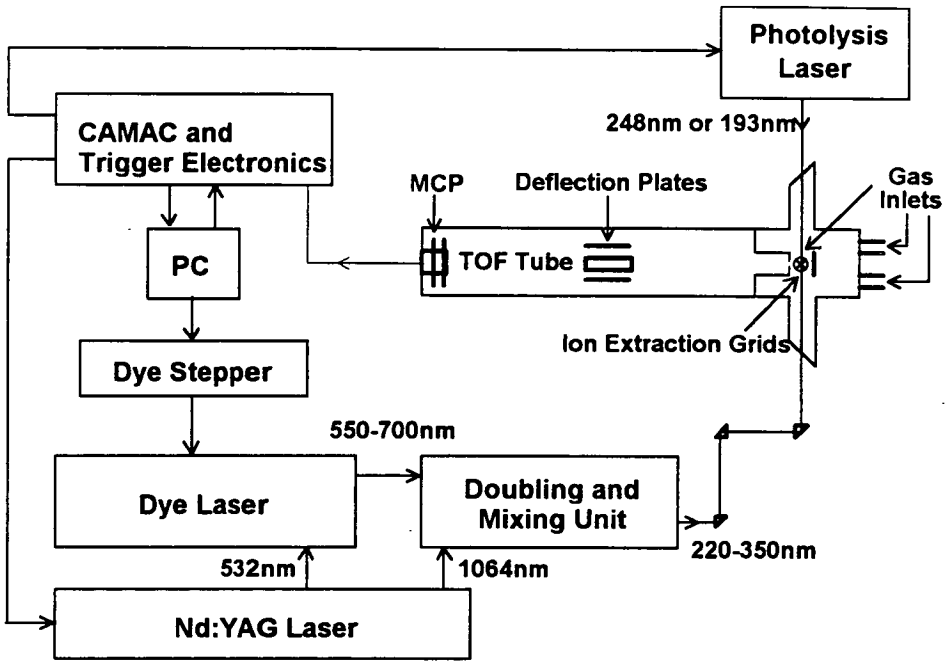

Figure 2.9: Schematic of photolysis/probe apparatus incorporating REMPI detection.

2.4 Experimental Control and Data Acquisition

Previous work[14] describes how a computer based, data acquisition system was designed and developed to control the experimental parameters and to enable collection, processing and analysis of the experimental data obtained.

The whole experiment was driven by software written by a predecessor[14]. This software controlled experimental timings and captured experimental data via a CAMAC system interfaced to an IBM compatible PC-AT. In the following sub-sections a brief outline of the experimental cycle, instrumentation and computer hardware, necessary to control the experimental system, will be given.

2.4.1 The Experimental Cycle

To control the experimental apparatus the PC-AT periodically sent signals via a CAMAC dataway to trigger a pulse generator. The pulse generator then delivered trigger pulses to various items of experimental hardware in an appropriate sequence.

The most complicated timing sequence controlled the triggers necessary for a two laser experiment incorporating a pulsed molecular beam valve. A timing schematic for this set-up is shown in Figure 2.10. With this arrangement 3 separate variable time delays are required:

1. Δt_1 is the time delay between the nozzle opening and the Q-switch (that is, the probe laser) firing.
2. Δt_2 is the time delay between the gas-discharge laser firing and the Q-switch firing. This is the delay between the pump and probe lasers.

3. Δt_3 is the time delay between the start and stop pulses of the transient digitiser (TD). This delay ensures that the correct (probe-induced) data is collected.

The flashlamps and the Q-switch of the probe laser were initiated at a fixed time because this delay had to be at an optimum for maximum gain. The timings of the molecular beam valve and gas-discharge laser triggers, and stop pulse to transient digitiser could be varied.

In summary, the experimental cycle for a two laser process was initiated by the firing of the pulsed molecular beam valve. After a delay the probe laser's flashlamps were charged. More time elapsed before the gas-discharge laser was fired and then, after another delay, the Q-switch was triggered, initiating the probe laser pulse. The signal generated was detected, amplified and then channeled into the transient digitiser. A stop pulse was then sent which prompted the TD to digitise the ion or fluorescence signals. In between experimental cycles the digitised data stored by the TD was downloaded into a temporary buffer file in the PC-AT for processing.

2.4.2 CAMAC Instrumentation

CAMAC is an international standard of modularised electronics, defining a common dataway to which a wide range of instruments can be interfaced, which in turn can be interfaced to a computer.

All the CAMAC instruments were located in a crate (Optima 860) whose backplane provided data communication and power lines to each module. Information and commands were directed to and from the crate via software implemented on the PC-AT. Figure 2.11 is a schematic of the CAMAC based experimental control system used in the work. In the following sub-sections the CAMAC instrumentation will be described.

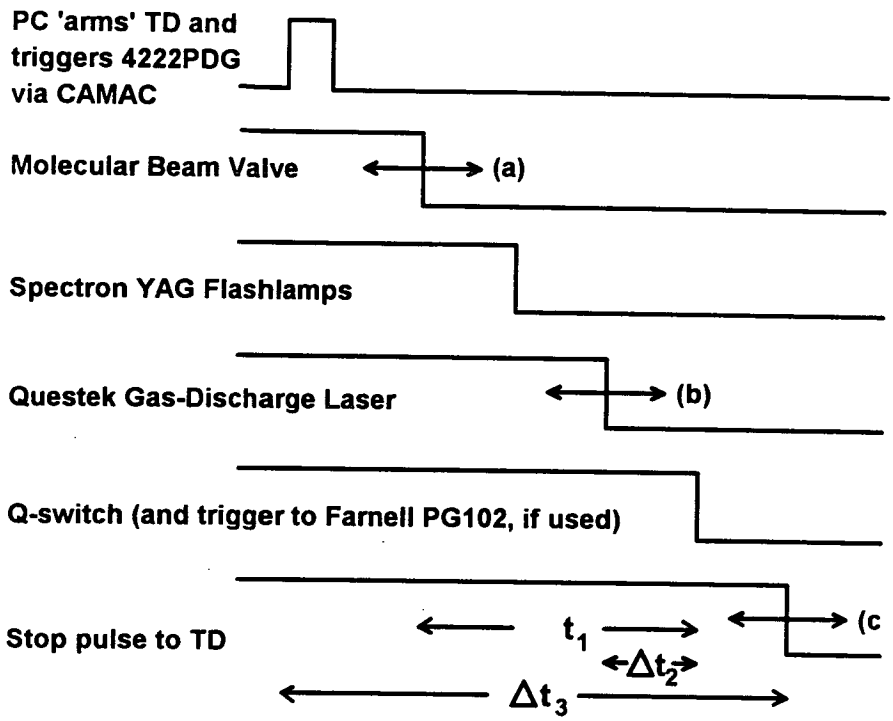

Figure 2.10: Schematic of the timing sequence for a two laser experiment, incorporating a molecular beam valve. The arrows at positions (a), (b) and (c) represent channels whose time delays could be varied.

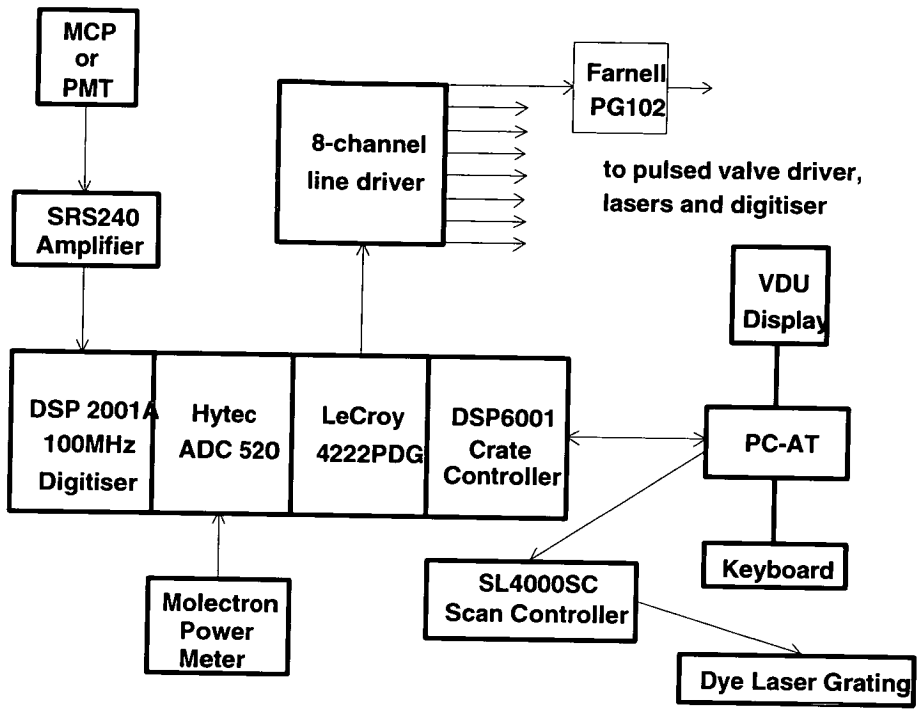

Figure 2.11: Schematic of the CAMAC based experimental control system. The Farnell PG102 is not connected directly to the CAMAC system, but can be triggered by the LeCroy 4222PDG via the line driver.

DSP6001 Crate Controller

The controller mounted in the Optima 860 crate was a DSP Technologies 6001 model. The controller was connected to the PC via a DSP PC004 interface card. Commands were accepted from the computer software and then passed onto the appropriate modules within the crate. The controller also sent data, collected by the modules, back to the PC for processing.

Pulse Delay Generators (PDG)

Two pulse delay generators were used to provide the necessary trigger pulses: a LeCroy 4222PDG and a Farnell PG102.

The LeCroy PDG comprised of 4 channels each with the capability to produce a range of outputs including the 100ns FWHM TTL pulses (with an accuracy of ±1ns) used in this work. It was triggered by commands sent through the dataway from the PC. This PDG had a very low pulse jitter and hence was used to trigger devices where very accurate control of timing was required.

The Farnell PG102 was not CAMAC controlled. It had two channels which could also produce 100ns FWHM TTL pulses. Consequently it was used to trigger devices which required less precise timing control. Often the output from one of the channels on the LeCroy was shared; a trigger would be sent directly to one device, delayed through the Farnell, and then sent to another device.

Some of the CAMAC modules required higher or longer trigger levels than those supplied by the pulse generators. The PDG outputs were boosted by a custom built 8 channel line driver, housed in a NIM bin, which could generate 5V;10μs, 15V;50μs or 20V;50μs pulses.

DSP2001A Transient Digitiser (TD)

Digitisation of the ion or fluorescence signal required a fast sampling device. The DSP2001A TD, with a digitising rate between 1Hz and 100MHz and a maximum record length of 4096 samples, fitted this description.

The arrival of ions at the MCP or photons at the PMT generated a waveform which was digitised by the TD. The input signal was continuously sampled and stored until the TD received an external stop trigger pulse from the PDG. The captured data was subsequently collected by the PC via the dataway. In this way a mass spectrum or LIF fluorescent decay signal was generated.

Hytec ADC520 Analogue to Digital Convertor

The ADC520 was used to monitor and collect data from sources other than the detection devices. For example, often the laser power was monitored during an experiment. This would allow the signal to be normalised and was useful because the power often fluctuated during the course of a scan.

2.4.3 IBM PC-AT Microcomputer

During the course of the work two microcomputers (an 80286 and an 80486) conforming generally to the IBM PC-AT specification were used. The PC used had to have a machine operating system compatible with the CAMAC Crate Controller (DSP6001).

2.4.4 Control Software

The control software, written and described in detail by a former colleague[14], performed several functions:

- Provided a means of setting the experimental parameters.

- Controlled the input to and output from the experimental apparatus.
- Synchronised all the relevant, active modes while the dye laser was scanning.
- Allowed specific, selected signals to be recorded.
- Enabled spectra to be recorded at different delay settings simultaneously.
- Aided data and spectral analysis.

References

[1] R.B. Bernstein, *Chemical Reaction Dynamics Via Molecular Beam and Laser Techniques*, (Oxford University Press, 1982).

[2] J.L. Kinsey, *Ann. Rev. Phys. Chem.*, **28**, 349 (1977).

[3] G. Herzberg, *Molecular Spectra and Molecular Structure, I. Spectra of Diatomic Molecules*, (Van Nostrand, Princeton, 1950).

[4] Y. Xie, P.T.A. Reilly, S. Chilukuri and R.J. Gordon, *J. Chem. Phys.*, **95**, 854 (1991).

[5] K.D. Rinnen, D.A.V. Kliner and R.N. Zare, *J. Chem. Phys.*, **91**, 7514 (1989).

[6] P.M. Johnson and C.E. Otis, *Ann. Rev. Phys. Chem.*, **32**, 139 (1981).

[7] P.M. Johnson, *Acc. Chem. Res.*, **13**, 20 (1980).

[8] M.N.R. Ashfold, S.G. Clement, J.D. Howe and C.M. Western, *J. Chem. Soc. Faraday Trans.*, **89**, 1153 (1993).

[9] D.H. Parker, *Ultra Sensitive Laser Spectroscopy*, (Academic Press, New York, 1983), Chapter 4.

[10] R.G. Bray and R.M. Hochstrasser, *Mol. Phys.*, **31**, 1199 (1976).

[11] P.W. Atkins, *Physical Chemistry*, (Oxford University Press, 1986), 3rd edition, P. 436.

[12] J. Morellec, D. Normand and G. Petite, *Phys. Rev.*, **A14**, 300 (1976).

[13] R.E. Demaray, C.E. Otis and P.M. Johnson, *J. Chem. Phys.*, **72**, 5772 (1980).

[14] G. Maitland, *Spectroscopic Studies For State-To-State Reaction Dynamics*, Ph.D. Thesis, University of Edinburgh, 1993.

[15] A. Watson, *State-Specific Reaction Dynamics*, Ph.D. Thesis, University of Edinburgh, 1994.

[16] W.C. Wiley and I.H. McLaren, *Rev. Sci. Instrumen.*, **26**, 1150 (1955).

[17] Harting and Read, *Electrostatic Lenses*, (Elsevier Scientific Publishing Company, 1976).

[18] J.M. Hollas, *Modern Spectroscopy*, (John Wiley & Sons, 1987), Ch.3.

[19] F.C. Frehsenfeld, K.M. Evenson and H.P. Broida, *Rev. Sci. Instrumen.*, **36**, 294 (1965).

Chapter 3

The Spectroscopy of OH and CH_3 Radicals

3.1 The Spectroscopy and Detection of the OH Radical

The OH radical is one of the most exhaustively studied reactive species in the gas phase, playing an important role in a wide variety of chemical and physical phenomena. It is of prime importance to combustion and atmospheric chemistry and occurs in an array of environments ranging from liquid solutions to interstellar space[1-4]. The detection of OH by spectroscopic methods and the analysis of the spectra resulting from low-lying states are well developed[5,6], and hence it is a much detected product in reaction dynamic studies[7-14].

The ground electronic state of the OH radical has the dominant configuration $(1\sigma)^2(2\sigma)^2(3\sigma)^2(1\pi)^3$ which is labelled $X^2\Pi$. The A, B and C states, illustrated in Figure 3.1(a), are $^2\Sigma^+$ valence states[15]. Rydberg states are formed, in this case, by adding electrons in σ Rydberg orbitals to the OH^+ ground state ion core. The $D^2\Sigma^-$ state is the lowest of such states and was first observed by Douglas[16] via one-photon absorption. Its dominant electronic configuration is $(1\sigma)^2(2\sigma)^2(3\sigma)^2(1\pi)^2(3p\sigma)$. The $3^2\Sigma^-$ state also possesses predominant Rydberg character and is of slightly higher energy than the D state. Figure 3.1(b) shows the $D^2\Sigma^-$ and $3^2\Sigma^-$ Rydberg states of OH[15].

3.1.1 LIF Detection of the OH Radical

Photofragmentation processes and bimolecular experiments resulting in production of OH usually adopt an LIF detection scheme, utilising the $A^2\Sigma^+$

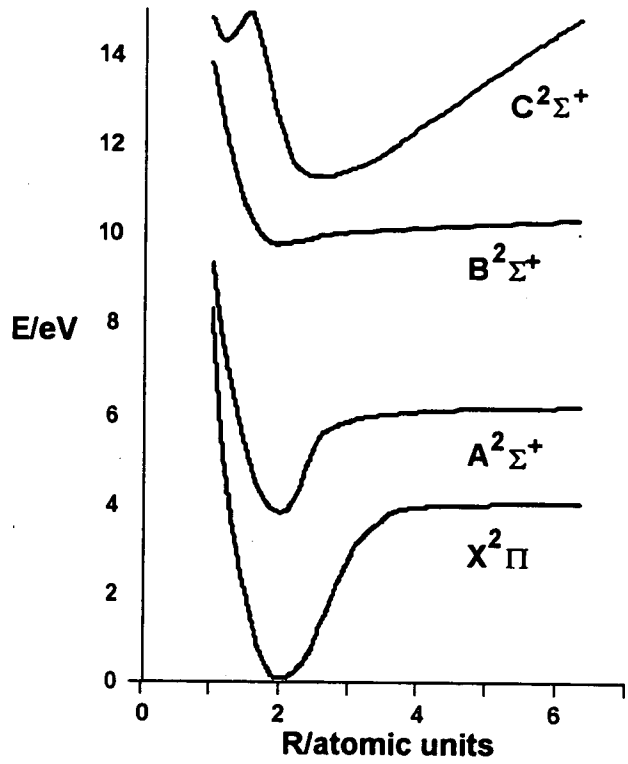

Figure 3.1(a): Potential energy curves for the ground and $^2\Sigma^+$ valence states of OH. The curves were redrawn from Reference [15].

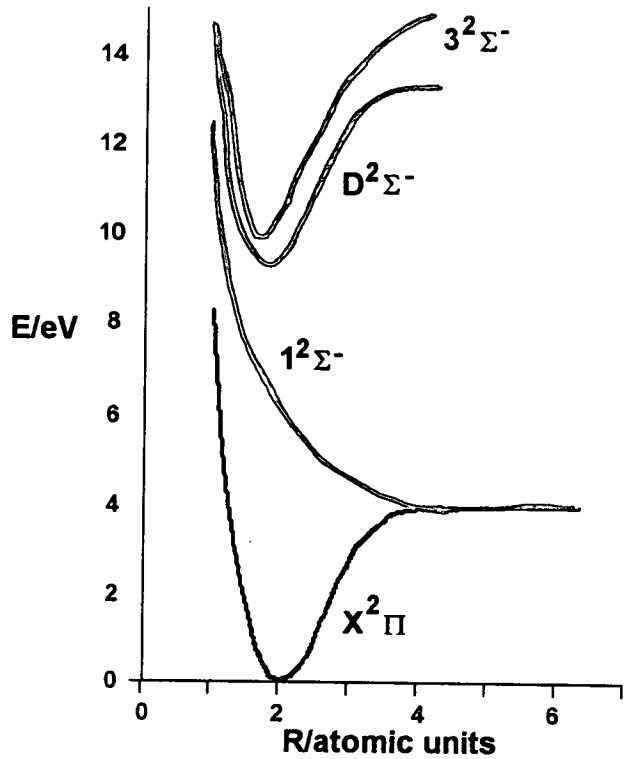

Figure 3.1(b): Potential energy curves for the ground and $^2\Sigma^-$ Rydberg states of OH. The curves were redrawn from Reference [15].

$\leftarrow X^2\Pi$ electronic transition[7-14]. To be able to extract dynamical information from the LIF spectra an understanding of the spectroscopy of the system is necessary.

$^2\Sigma^+$ States of the OH Radical

For the description of the rotational states of OH the quantum number N, which defines the angular momentum excluding the spin contribution, is commonly used[6]. The associated nomenclature is appropriate for Hund's case (b). This is the most convenient way to describe a Σ state where the orbital angular momentum, Λ, along the internuclear axis is zero. Hence the $A^2\Sigma^+$ state of OH can be classified as belonging to Hund's case (b). There is no resulting orbital angular momentum along the internuclear axis so the electronic spin must be coupled to the rotation axis. This magnetic coupling of the spin and momentum, created by the rotation of the nuclei, causes the rotational levels of the upper electronic state to split into two doublet components. Figure 3.2 shows the energy level structure of the OH $A^2\Sigma^+$ state.

$^2\Pi$ States of the OH Radical

The orbital angular momentum,Λ, for a Π state is equal to ± 1. When $\Lambda \neq 0$ both Hunds' cases (a) and (b) must be considered to find the correct spectroscopic description for the system. In case (a) the spin (S) is coupled through the orbital angular momentum (L) to the internuclear axis. L and S thus have projection quantum numbers on the internuclear axis of Λ and Σ respectively. The resultant $|\Lambda+\Sigma|$ forms the projection quantum number Ω. This situation applies where the rotation is slow enough not to affect this coupling. The rotational energy is approximately BJ(J+1), where J is the total angular momentum of the molecule. Hund's case (b) exists where the rotation of the system is so strong that the spin is coupled to the rotation axis. There are two possible states: J = N+1/2 and J = N-1/2, where N is the total angular momentum excluding the electronic spin. Most real $^2\Pi$ states,

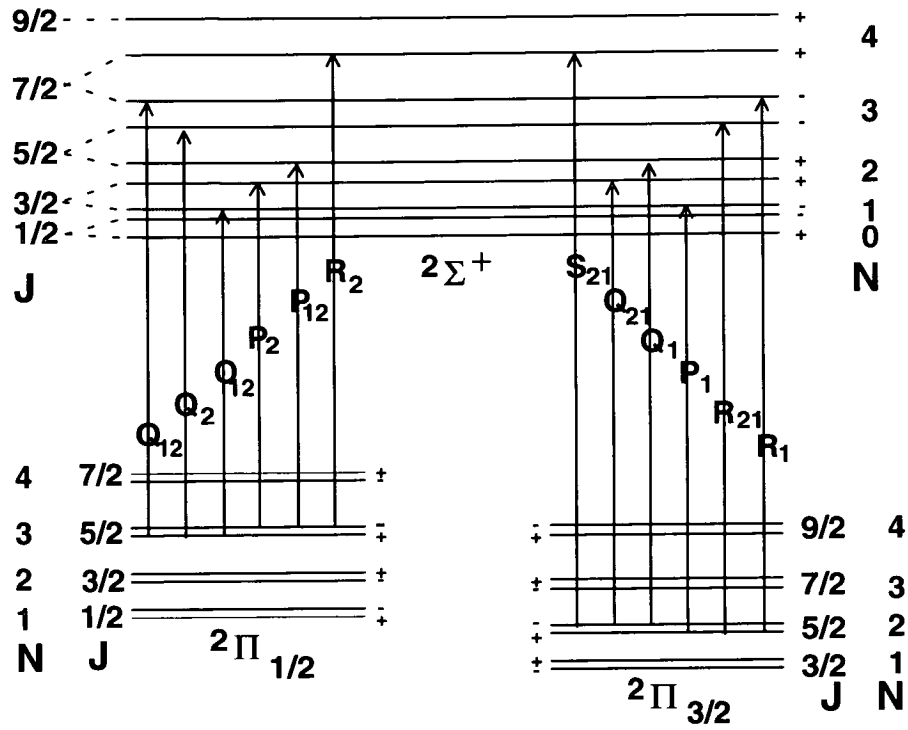

Figure 3.2: Energy level diagram for the $^2\Sigma^+ \leftarrow {}^2\Pi$ transition. The Π ground state is split into two widely separated stacks, $^2\Pi_{1/2}$ and $^2\Pi_{3/2}$, due to spin-orbit coupling. In the $^2\Sigma^+$ upper state, levels with the same N are split into J = N±1/2 by the spin-rotation interaction. Branches are labelled according to Hund's case (a) with each transition resulting from a change in ΔN_{F2F1}. In the OH radical the electronic spin has the value 1/2 which produced the doublets. The two components of the doublet can be characterised by subscripts 1 and 2 so that $F_1(N)$; $f_1(N)$: J = N +1/2 and $F_2(N)$; $f_2(N)$: J = N-1/2. F_1 and F_2 are used for the rotational levels of the $^2\Sigma$ state, f_1 and f_2 for those of the $^2\Pi$ state[6].

including the OH ground state, $X^2\Pi$, are close to Hund's case (a) for slow rotation and case (b) for fast rotation, and it is often necessary to consider an intermediary case. The low rotational levels of OH conform to a coupling scheme intermediate between Hund's case (a) and (b). For higher rotational levels the spin decouples from the internuclear axis and the coupling approximates Hund's case (b).

The structure of the ground state rotational levels of OH is shown in Figure 3.2. Spin-orbit interactions cause the $^2\Pi$ state to split into a pair of spin-doublets, $^2\Pi_{3/2}$ and $^2\Pi_{1/2}$ (where Ω = 3/2,1/2), separated by approximately 125cm^{-1}[6]. The degeneracy of the levels within each spin-doublet is removed due to coupling of the total electronic angular momentum (the sum of the orbital and spin contributions) to the nuclear framework. The two resulting Λ-doublet components are distinguished by symmetry with respect to reflection in the plane of rotation. This Λ-doubling arises because the OH ground state is a Π state and in the limit of high rotational angular momentum the Π orbital can lie either in the plane, $\Pi(A')$, or perpendicular to the plane, $\Pi(A'')$, of rotation. Hence OH has four fine structure levels for each (v,N) level.

$^2\Sigma^+ \leftarrow {}^2\Pi$ Transitions

Figure 3.2 shows the transitions between the $A^2\Sigma^+$ and $X^2\Pi$ states of OH, commonly utilised in LIF studies. Each vibronic band of the $^2\Sigma^+ \leftarrow {}^2\Pi$ transition is divided into two sub-bands, $^2\Sigma^+ \leftarrow {}^2\Pi_{3/2}$ and $^2\Sigma^+ \leftarrow {}^2\Pi_{1/2}$, which are separated approximately by the amount of the spin-orbit splitting of the $^2\Pi$ state.

The rotational selection rules for a one-photon transitions are $\Delta J = 0, \pm 1$. Changes in parity are also constrained to (+ $\leftrightarrow$ -) and (- $\leftrightarrow$ +). For pure Hund's case (b) there is also the selection rule $\Delta N = 0, \pm 1$. In Hund's case

(a) the quantum number N is not defined and hence the selection rules for ΔN do not apply. Transitions between the $^2\Pi$ and $^2\Sigma^+$ states that satisfy both selection rules form strong branches but those that violate the ΔN rule are weak, except for small values of N where the coupling is intermediate between Hund's case (a) and (b). From each J, within each sub-band in the ground electronic state, there will be six possible transitions giving rise to twelve branches in total.

3.1.2 LIF Spectrum of the OH Radical - Microwave Discharge of Water

A description of the LIF technique and instrumentation was given in Chapter 2 (Sections 2.1.1 and 2.2.2.4). Figure 2.8 is a schematic of the apparatus used in a LIF experiment. To obtain a simple thermal OH spectrum, for spectroscopic analysis, the following procedure was used.

The OH radical was generated via microwave discharge of distilled water in a quartz glass discharge tube external to the vacuum chamber. The discharge tube was terminated by a 1mm orifice through which the gas expanded to form an effusive jet. The injector tip was located 25mm from the centre of the region probed by the LIF excitation beam. The pressure in the reaction chamber was typically 50mTorr.

The $A^2\Sigma^+(v'=1) \leftarrow X^2\Pi(v''=0)$ transition in the OH radical was excited by tunable ultraviolet radiation from the probe laser beam. The appropriate wavelengths were generated by frequency-doubling the output from the Nd:YAG pumped dye laser. Available output energies from the doubled dye (R590/R610 mixture, Exciton) beam were typically 2mJ/pulse, which is far in excess of the energy required to cause appreciable optical saturation in OH, so the laser power was reduced by using a pair of Glan-Taylor prisms which allowed variable attenuation of the probe beam whilst maintaining a fixed linear polarisation axis.

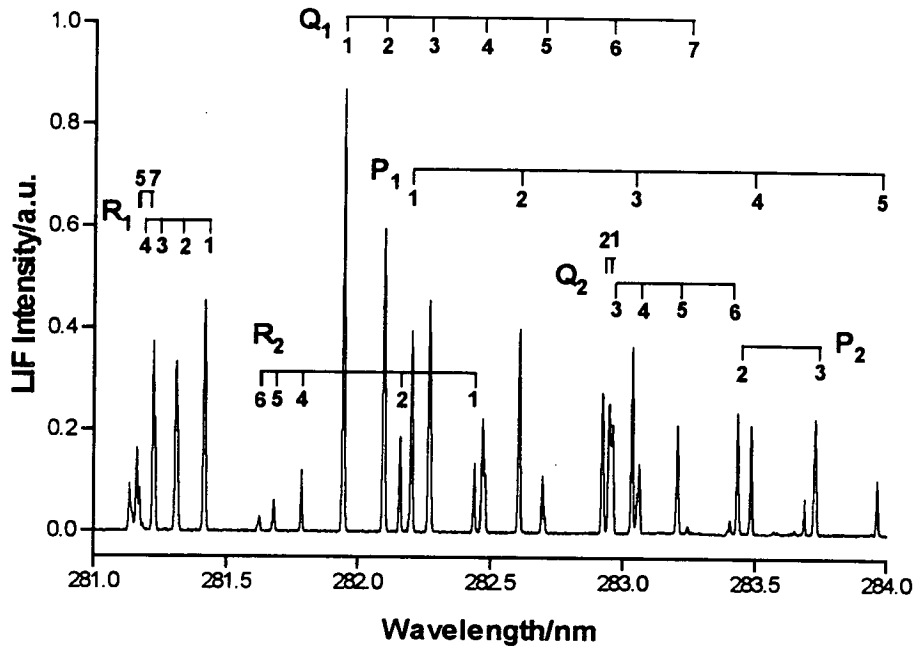

Figure 3.3: LIF excitation spectrum of the OH $^2\Sigma^+(v'=1) \leftarrow X^2\Pi(v''=0)$ band. Fluorescence was selectively detected on the (1-1) band. The OH was produced by microwave discharge of water. The rotational lines originating in levels N″ of the $X^2\Pi$ ground state have been assigned[6].

Fluorescence was detected in the vertical direction, perpendicular to the laser beam axis. A combination of fused silica lenses focused the fluorescence through a suitable interference filter, chosen to transmit radiation at the wavelength of the desired OH $A^2\Sigma^+ \leftarrow X^2\Pi$ vibronic transition, onto the photocathode of the photomultiplier tube. Signals were captured and digitised in a 1.5μs gate (which corresponds to approximately twice the OH $A^2\Sigma^+ \leftarrow X^2\Pi$ fluorescence lifetime) approximately 20ns after the probe pulse to discriminate against scattered light.

Figure 3.3 shows the LIF excitation spectrum of the OH $A^2\Sigma^+(v'=1) \leftarrow X^2\Pi(v''=0)$ band. Fluorescence was detected on the (1-1) band. This spectrum was obtained at a reaction chamber pressure of 35mTorr and with a laser energy of 350μJ/pulse (at 282nm). As can be seen from this spectrum only low rotational states of OH (up to N″=7) are populated. This is as expected since the OH produced by microwave discharge of water will be thermalised by the time it reaches the observation zone in the chamber. The rotational lines were assigned using Dieke and Crosswhite's data[6]. It should be noted that only the principal branches are labelled: the weaker satellites are not shown.

3.1.3 REMPI Detection of the OH Radical

OH has conventionally been detected by LIF via the $A^2\Sigma^+ \leftarrow X^2\Pi$ transition. However, whilst LIF provides a very effective and sensitive means of detecting the hydroxyl radical under many circumstances, the low transition moment and long lifetime (τ = 0.7μs) combine with efficient electronic quenching to reduce sensitivity. Furthermore, it is often necessary to exploit off-diagonal LIF excitation schemes ($\Delta v \neq 0$) to obtain information on the population of OH $X^2\Pi$ due to strong predissociation of successively lower rotational states with increasing v of the A state by the repulsive $1^2\Sigma^-$ state[17-

[19] (shown in Figure 3.1(b)). REMPI can provide an alternative detection technique which may be convenient where LIF is inadequate[20-22].

The A state (exploited in LIF) is not a suitable state for REMPI since it is a valence state and requires three additional photons of the same colour for ionisation after initial excitation. Low-lying Rydberg states, such as the $D^2\Sigma^-$ and $3^2\Sigma^-$ Rydberg states of OH, are much preferable and suitable candidates for REMPI. However, according to the calculations of Van Dishoeck and Dalgarno[15] both the $D^2\Sigma^-$ and $3^2\Sigma^-$ Rydberg states should be subject to a heterogeneous (J' dependent) predissociation by the repulsive $2^2\Pi$ state. If this predissociation were strong then this would affect the ability to extract ground state populations from the observed spectra and would rule out the use of these transitions in a dynamical study. Observed spectra of these transitions, however, show no evidence for strong predissociation of either state[20]. Therefore the interaction is concluded to be weak, and the spectral lines should not be seriously affected by the predissociation.

$^2\Sigma^-$ Rydberg States of the OH Radical

The $D^2\Sigma^- \leftarrow X^2\Pi$ and $3^2\Sigma^- \leftarrow X^2\Pi$ transitions can be probed by (2+1) REMPI using laser wavelengths of approximately 246 and 228nm respectively[20]. To deconvolute the REMPI spectra an understanding of the spectroscopic nature of these transitions is necessary. The coupling case for the $X^2\Pi$ electronic ground state of OH has been discussed in Section 3.1.1. Lower-lying states of Σ symmetry generally conform to Hund's case (b) because Λ=0, hence the description pertaining to the Σ^+ valence states (Section 3.1.1) also applies to the Σ^- Rydberg states.

$^2\Sigma^- \leftarrow {}^2\Pi$ Two-Photon Transitions

In the electric dipole approximation the rotational selection rules for two-photon transitions are $\Delta J = 0, \pm1, \pm2$. For pure Hund's case (b) the constraint $\Delta N = 0, \pm1, \pm2$ also exists. In Hund's case (a) the N quantum

number is not defined and hence the ΔN rules do not hold. Transitions between $^2\Pi$ and $^2\Sigma^-$ states satisfying both ΔJ and ΔN rules will give rise to twelve strong branches and transitions not obeying the ΔN selection rule should only have appreciable probability where the coupling is intermediate between Hund's case (a) and (b).

3.1.4 REMPI Spectrum of the OH Radical - Photolysis of Formic Acid

A description of the REMPI technique and necessary instrumentation is given in Chapter 2 (Sections 2.1.2 and 2.2.2.1). The OH radical was generated by the one-photon laser photolysis of formic acid (HCOOH) and detected using (2+1) REMPI via the $D^2\Sigma^-(v'=0) \leftarrow X^2\Pi(v''=0)$ and $3^2\Sigma^-(v'=0) \leftarrow X^2\Pi(v''=0)$ transitions at laser wavelengths of approximately 244 and 228nm respectively. This one laser, photolysis/probe experiment has been described in previous work[23].

The required one photon laser wavelengths were generated by doubling the output of the dye laser (DCM dye (Lambda Physik) for the D $\leftarrow$ X transition and a R590/R610 dye mixture (Exciton) for the 3 $\leftarrow$ X transition) then mixing the doubled output with the 1064nm fundamental of the Nd:YAG laser. The final output beam had an energy of approximately 1mJ per pulse and was horizontally polarised.

The formic acid (Fisons, 98% purity) entered the vacuum system effusively via the rear flange of the reaction chamber. Typical reaction and detection chamber pressures of 1mTorr and 1×10^{-6}mbar, respectively, were employed.

The photolysis of formic acid and subsequent probing of the OH product required the absorption of four photons from a single laser beam; one photon for photolysis and three for (2+1) REMPI. Hence it was necessary to use a short focal length lens to increase the photon density at the

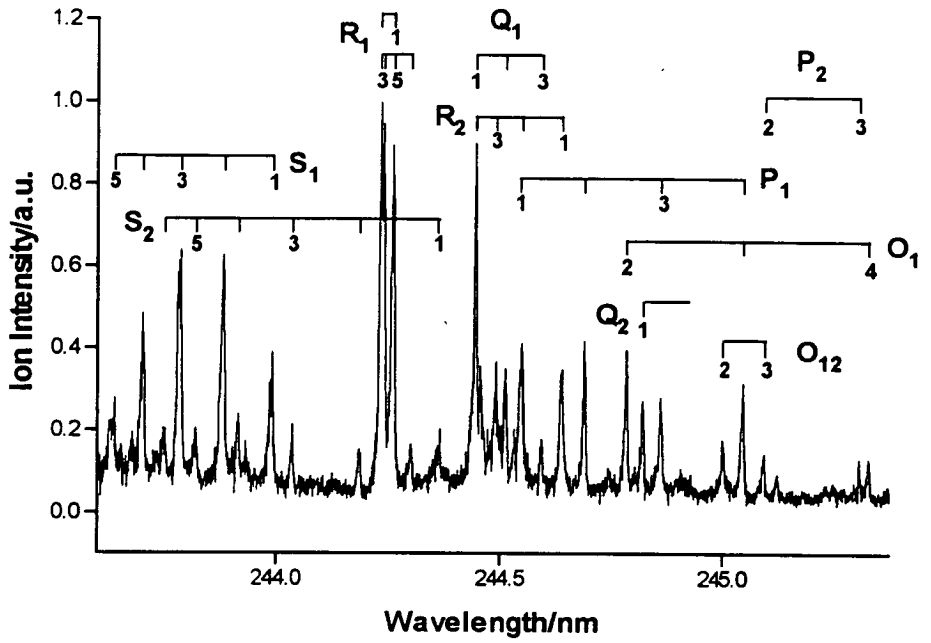

Figure 3.4: (2+1) REMPI spectrum of the $D^2\Sigma^-(v'=0) \leftarrow X^2\Pi(v''=0)$ band of the OH product resulting from the photodissociation of formic acid. The rotational lines (N″) of the $X^2\Pi$ ground state have been assigned[20].

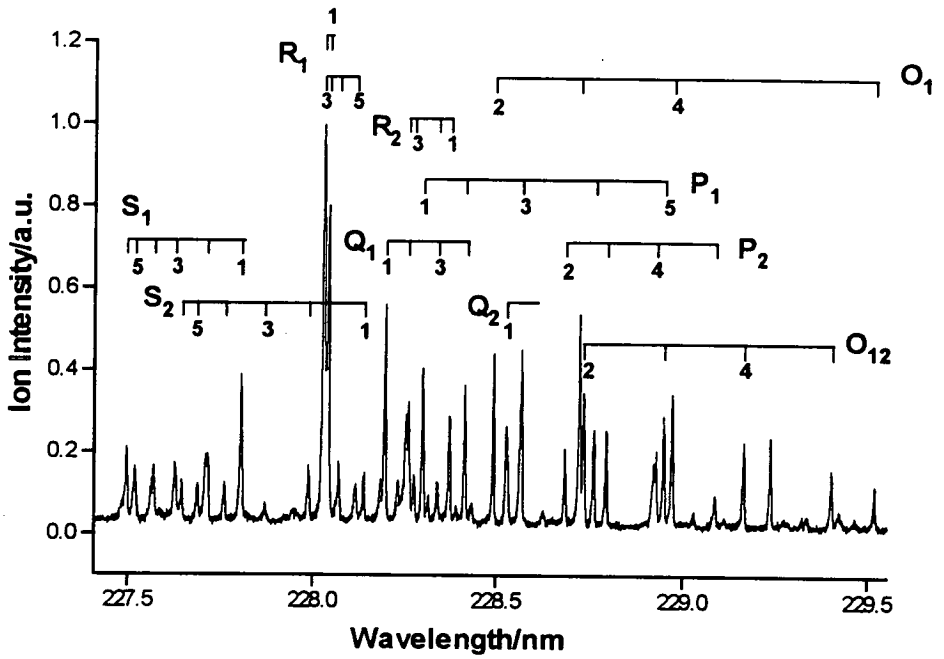

Figure 3.5: (2+1) REMPI spectrum of the $3^2\Sigma^-(v'=0) \leftarrow X^2\Pi(v''=0)$ band of OH resulting from the photodissociation of formic acid. The rotational lines (N″) of the $X^2\Pi$ ground state have been assigned.

observation zone. A f=6cm quartz lens was mounted internally within the reaction chamber and used to focus the laser beam. The resultant ions were extracted using the modified Wiley-McLaren[24] configuration described in Chapter 2 (Section 2.2.2.2) and illustrated in Figure 2.4.

Figures 3.4 and 3.5 show the (2+1) REMPI spectra of the OH $D^2\Sigma^-(v'=0) \leftarrow X^2\Pi(v''=0)$ and $3^2\Sigma^-(v'=0) \leftarrow X^2\Pi(v''=0)$ transitions. The rotational lines were assigned using the (2+1) REMPI spectra of de Lange *et al*[20]. In both spectra rotational levels up to N″=6 are populated indicating that the OH fragment is rotationally cold. This is in agreement with the results obtained by Ebata *et al*[25], who measured the internal state distributions of OH by LIF following the photolysis of formic acid at 246nm. In that study the OH fragment was observed to be both vibrationally and rotationally cold with only v″=0 up to N″=5 populated.

The signal to noise ratio observed for the $3^2\Sigma^-(v'=0) \leftarrow X^2\Pi(v''=0)$ (Figure 3.5) transition is evidently better than for the $D^2\Sigma^-(v'=0) \leftarrow X^2\Pi(v''=0)$ transition (Figure 3.4). This can be rationalised to a certain extent by examining the wavelength dependence of the extinction coefficient of formic acid which is $2dm^3mol^{-1}cm^{-1}$ at 244.44nm (approximately the wavelength of the $Q_1(1)$ line of the D ← X (0-0) band) and $30dm^3mol^{-1}cm^{-1}$ at 227.95nm (approximately the wavelength of the $Q_1(1)$ line of the 3 ← X (0-0) band)[23]. Hence assuming that the laser intensity and beam radius are the same for each transition, it is expected that more formic acid molecules will be dissociated at the wavelength of the 3 ← X (0-0) transition as compared with the D ← X (0-0) band.

3.1.5 Optimum Detection of the OH Radical: LIF versus REMPI

The OH radical can potentially be investigated using both LIF and REMPI detection methods in tandem. However, a previous study into the relative

merits of LIF and REMPI, with respect to OH detection, found that the detection sensitivity using LIF was always better than that of REMPI, with the available experimental apparatus and under the typical conditions of a dynamical experiment[23]. On comparing Figure 3.3 (LIF detection of OH) with Figures 3.4 and 3.5 (REMPI detection of OH) it is clearly evident that the signal to noise in the spectrum obtained using LIF detection methods to probe OH is far superior than that observed in the REMPI spectra. Also several other factors encourage the preferential use of LIF:

- In a REMPI experiment the pressure constraints, imposed by the microchannel plate detector, limit the ability to detect the small quantities of nascent product resulting from bimolecular reactions. However in LIF experiments, the detector is external to the vacuum system and greater pressures can be used to enhance the probability of finding product signals.
- REMPI detection of OH requires the use of a short focal length lens. This could introduce practical problems in a hot atom dynamics experiment since the much increased (focused) laser intensities created can promote undesirable probe-induced photolysis and ionisation of the reactants.
- Converting measured spectral intensities to populations is considerably more complicated for REMPI than LIF. The one-photon absorption line-strength formulae and selection rules necessary to deconvolute OH LIF spectra are extremely well documented[6]. However, the two-photon line-strength formulae for transitions involving states of differing Hund's case coupling, as occurs in transitions of the OH radical, are not well known and are complex due to the combined effect of spin-orbit splitting and the generosity of two-photon selection rules. This situation is exacerbated by incompletely characterised predissociation.

For these reasons, in this work LIF has been used, solely, to detect OH as the product of bimolecular reactions.

3.2 The Spectroscopy and Detection of the CH_3 Radical

Most of the understanding of the electronic structure of the methyl radical originates from the ultraviolet and vacuum ultraviolet absorption spectra recorded by Herzberg[26] over thirty years ago, and a crucial finding of his work, since confirmed by others[27-31], was that the ground state of the radical must be planar.

3.2.1 REMPI Detection of the CH_3 Radical

Assuming D_{3h} symmetry, ground state CH_3 has the electronic configuration $(1a'_1)^2(2a'_1)^2(2e')^4(2a''_2)^1$. This state is labelled X^2A_2''. As a consequence of the planar structure most excited states of the methyl radical cannot be accessed by one-photon spectroscopy: one-photon selection rules permit only $^2A_1' \leftarrow {}^2A_2''$ and $^2E'' \leftarrow {}^2A_2''$ transitions. Many more states are accessible via two- and three-photon transitions, because the selection rules are more relaxed and thus REMPI is a convenient tool for probing the electronic states of CH_3 and retrieving ground state information. Table 3.1 lists the selection rules for single and multiphoton transitions from the methyl radical's $^2A_2''$ ground state.

REMPI spectroscopy has enabled new information on excited Rydberg states of the radical to be gained. The CH_3 radical cannot be detected by LIF because it effectively does not fluoresce. Hudgens *et al*[32] detected and identified a np^2A_2'' Rydberg series for both CH_3 and CD_3 using (2+1) REMPI. Members of this series, in particular the $3p_z{}^2A_2''$ and $4p_z{}^2A_2''$ states, have

Transition	One-Photon	Two-Photon	Three-Photon
$^2A_1' \leftarrow {}^2A_2''$	$\Delta K = 0$ $K = 0;\ \Delta N = \pm 1$ $K \neq 0;\ \Delta N = 0, \pm 1$	forbidden	$\Delta K = 0$ $K = 0;\ \Delta N = \pm 1, \pm 3$ $K \neq 0;\ \Delta N = 0, \pm 1, \pm 2, \pm 3$
$^2A_1'' \leftarrow {}^2A_2''$	forbidden	$\Delta K = 0$ $K = 0;\ \Delta N = \pm 1$ $K \neq 0;\ \Delta N = 0, \pm 1, \pm 2$	$\Delta K = \pm 3$ $K'' = 0;\ \Delta N = \pm 1, \pm 3$ $K'' \neq 0;\ \Delta N = 0, \pm 1, \pm 2, \pm 3$
$^2A_2' \leftarrow {}^2A_2''$	forbidden	forbidden	$\Delta K = 0$ $K = 0;\ \Delta N = 0, \pm 2$ $K \neq 0;\ \Delta N = 0, \pm 1, \pm 2, \pm 3$
$^2A_2'' \leftarrow {}^2A_2''$	forbidden	$\Delta K = 0$ $K = 0;\ \Delta N = 0, \pm 2$ $K \neq 0;\ \Delta N = 0, \pm 1, \pm 2$	$\Delta K = \pm 3$ $K'' = 0;\ \Delta N = 0, \pm 2$ $K'' \neq 0;\ \Delta N = 0, \pm 1, \pm 2, \pm 3$
$E' \leftarrow {}^2A_2''$	forbidden	$\Delta K = \pm 1$ $\Delta N = 0, \pm 1, \pm 2$	$\Delta K = \pm 2$ $\Delta N = 0, \pm 1, \pm 2, \pm 3$
$E'' \leftarrow {}^2A_2''$	$\Delta K = \pm 1$ $\Delta N = 0, \pm 1$	$\Delta K = \pm 2$ $\Delta N = 0, \pm 1, \pm 2$	$\Delta K = \pm 1$ $\Delta N = 0, \pm 1, \pm 2, \pm 3$

Table 3.1: Optical selection rules for transitions from the vibrationless CH_3 ground state, X^2A_2'', to higher excited states. This table is redrawn from ref. [32]. Hund's case (b) notation is used. For symmetric tops J is the quantum number of the total angular momentum, **J**; N is the angular momentum excluding the spin contribution and K is the quantum number of the component of **J** in the direction of the top axis. K takes values 0, 1, 2, ... and J = K, K+1, K+2, ... The change in N determines whether an O, P, Q, R or S branch is formed: each branch then consists of K sub-structure. The prime and double prime indicate symmetry and antisymmetry with respect to the plane of the molecule.

since been probed spectroscopically and the $3p_z{}^2A_2'' \leftarrow X^2A_2''$ and $4p_z{}^2A_2'' \leftarrow X^2A_2''$ transitions, accessed by laser wavelengths of approximately 330 and 280nm respectively[32-36], could prove useful for population extraction in a bimolecular experiment[37]. The two-photon selection rules for these vibronic transitions allow for parallel $\Delta K = 0$, $\Delta N = 0, \pm 1, \pm 2$ rotational branches.

3.2.2 Predissociation of the CH_3 Radical

Quite frequently potential energy curves (surfaces) cross and these crossings have very important consequences. The simplest form of curve crossing is predissociation and can occur when a bound state is crossed by a repulsive state leading to dissociation[38]. Severe predissociation can be detected in spectra as a loss in vibrational structure which may be resumed at higher frequencies. Weaker predissociation may have similar effects on the rotational structure of vibronic bands.

There are two main mechanisms for predissociation: homogeneous and heterogeneous. Homogeneous predissociation occurs when a bound state is predissociated by a state of the same symmetry, which allows the states to couple. With this mechanism the degree of predissociation is independent of rotational level. This form of predissociation affects all excited state rotational levels equally. It will always be present, even if the system is rotationally cold and thus confers on all spectral lines a width, ω_o[33,39]. Conversely, the heterogeneous mechanism results in a predissociative rate proportional to some varying content of excited state rotational energy or angular momentum[39]. This means that the degree of heterogeneous predissociation is dependent on the amount of rotational excitation of the system: when the system is rotationally cold the rates of heterogeneous predissociation will be suppressed.

Spectroscopic studies of the methyl radical have shown that whilst CD_3 is affected by homogeneous predissociation, the main mechanism for predissociation in CH_3 is heterogeneous. The rotational linewidths (FWHM) of resolved CD_3 spectral lines for the $4p_z \leftarrow X$ (0-0) transition were measured by Powis and Black[33] and found to be constant: the apparent invariance of the linewidths as the rotational energy increases indicated that any responsible predissociation mechanism must be homogeneous. However, for the same transition in CH_3, the measured linewidths were found to be rotational level dependent, clearly indicating that a significant heterogeneous predissociation channel was operative.

Hence, a major impediment to the acquisition of resolved rovibronic data for the methyl radical is the rapid predissociation of the excited states, particularly for undeuterated species. However, the $3p_z\,^2A_2''$ state has been shown to be somewhat more resistant to predissociative effects and as a result has been much more frequently probed in dynamics experiments[34,35,37]. Extensive studies have been made of the internal state and velocity distributions of methyl fragments resulting from the photodissociation of methyl iodide, where the CH_3 fragment is state-selectively ionised using (2+1) REMPI via the $3p_z$ Rydberg state[34,35,40-44]. Hudgens *et al*[32] showed that only the $3p_z\,^2A_2''$ state shows vibrational structure: most of the vibrational activity occurs in the ν_2 out-of-plane bending ("umbrella") mode. The rotational structure and predissociation dynamics of the $4p_z$ ($v'=0$) state were examined by Powis and Black[33] following photolysis of CH_3I/CD_3I at 286nm. For CD_3 they observed O, P, Q, R and S branches with resolved K sub-structure for the higher N lines. However, for CH_3, virtually no well resolved sub-structure was seen due to increased predissociation in CH_3.

The impact of these findings is that predissociation could impede the attainment of well resolved REMPI spectra for the methyl radical and prevent

the measurement of ground state populations, necessary for dynamical studies. However, recently, Kleinermanns *et al*[37] managed to extract a modest level of information on the rotational distribution from the REMPI spectra of CH_3 following reaction between $O(^1D)$ and saturated hydrocarbons. In this study[37] the product CH_3 was probed via the $3p_z \leftarrow X$ transition. Since the $3p_z$ Rydberg state is suspected to be more resistant to predissociation than the $4p_z$ state it would be sensible, in any reaction dynamic study, to utilise the $3p_z \leftarrow X$ transition to probe CH_3. An additional measure, to increase spectral resoultion, would be to use deuterated samples because the excited electronic states of CD_3 are less predissociative than those of CH_3[43].

3.2.3 REMPI Spectrum of the CH_3 Radical - Photolysis of Methyl Iodide

A simple way to generate the CH_3 radical for the purpose of developing REMPI as a spectroscopic probe is to photolyse CH_3I. In Chapter 2 (Sections 2.1.2 and 2.2.2.1) a description of the REMPI technique and instrumentation is given. Figure 2.9 is a schematic of the apparatus used in a REMPI experiment.

The photodissociation of CH_3I is an extensively studied process[33-36,40-44] where both the CH_3 radical and I atom products have been probed using REMPI. Photolysis and detection can be achieved by using either one or two laser beams depending on the photolysis wavelength used and transition of CH_3 excited. Methyl iodide has an absorption spectrum, labelled the A-band, in the ultraviolet[45] ranging from approximately 220 - 340nm with a λ_{max} at 257.6nm. Photolysis within this range results in prompt fragmentation to a methyl radical and an iodine atom and hence has been widely exploited in photodissociation experiments.

(a) Photolysis of methyl iodide and REMPI detection of CH_3 in a one laser experiment:

The laser wavelength required for two-photon excitation of the $4p_z$ Rydberg level of CH_3, via the $4p_z{}^2A_2''(v'=0) \leftarrow X^2A_2''(v''=0)$ transition at approximately 286nm, falls within the CH_3I A-band continuum. Hence when methyl iodide is irradiated at this wavelength with a tightly focused laser beam one-photon dissociation is followed by (2+1) REMPI of the methyl photofragment: a single colour laser pulse serves for both photolytic generation and spectroscopic probing of the radicals. A brief description of the procedure used to carry out such an experiment follows.

The frequency doubled output of a Nd:YAG pumped dye laser was focused into the reaction chamber with a f=30cm lens. Output energies from the doubled dye (R590/R610 mixture, Exciton) beam were typically 500μJ - 1mJ/pulse. Degassed CH_3I (Merck, 99%) was admitted to the vacuum system via two methods. In the initial tests on the system, the CH_3I entered the reaction chamber effusively. The spectra shown in Figures 3.6 and 3.7 were recorded with this experimental arrangement. Then in later experiments, the CH_3I was seeded in He (BOC, 99.99%) and a pulsed nozzle (0.5mm diameter hole) used to admit the reagent normal to the laser beam direction. The spectra shown in Figures 3.8 and 3.9 were obtained in this fashion. The measured pressure in the reaction chamber ranged from 1×10^{-4} to 1×10^{-5} mbar. For the effusive experiments this was the "true" pressure. However for the jet experiments this represented the "steady-state background" since the density, and hence the pressure, at the interaction region is much higher than the pressure in the rest of the chamber and at the ion gauge.

There is a dual advantage to using nozzles in REMPI experiments. Firstly the nozzle is movable and can be brought close to the laser beam, increasing the gas density at the laser focus. This allows more species to be

ionised. A manifestation of this effect is that the signal to noise ratio is increased in nozzle experiments (Figures 3.8 and 3.9) as compared with continuous flow experiments (Figures 3.6 and 3.7). In these experiments the nozzle was approximately 2cm from the laser beam. A second advantage of using nozzles is that the reagents are pulsed into the vacuum system in short bursts (in these experiments lasting approximately 200μs) leading to a high transient density for a given apparent "steady-state" pressure on the ion gauge. This helps to reduce the pressure in the reaction and hence detection chambers which allows the use of higher MCP detection voltages. The downward flow of the reagents also aids the pumping capacity of the vacuum system.

The reaction chamber housed the REMPI ion extraction set-up with electrostatic lens illustrated in Chapter 2 Figure 2.5. For the jet experiments a bullet shaped nozzle (Chapter 2 Figure 2.7(b)) was used which helped to reduce distortion of the extraction fields. The reaction and detection chambers were separated by a small aperture which maintained the low pressure required in the TOF tube/detection chamber. For the effusive experiments the aperture was a 5mm diameter hole. With the pulsed nozzle a 10mm×2mm slot was used to maintain the pressure differential between the two chambers while maximising the number of ions extracted from the narrow strip irradiated by the focused probe beam. Ions formed at the laser focus were extracted along the flight tube to the MCP detector and the signals digitised as described in Chapter 2 Section 2.4.

Figures 3.6 - 3.9 are (2+1) REMPI spectra of the methyl radical, which was ionised via $4p_z{}^2A_2''(v'=0) \leftarrow X^2A_2''(v''=0)$ transition. These spectra were obtained with laser energies of approximately 750μJ/pulse (at 286nm). The spectra shown in Figures 3.6 and 3.7 were obtained by admitting methyl iodide to the reaction chamber effusively. Figures 3.8 and 3.9 were recorded under molecular beam conditions, using a pulsed nozzle to

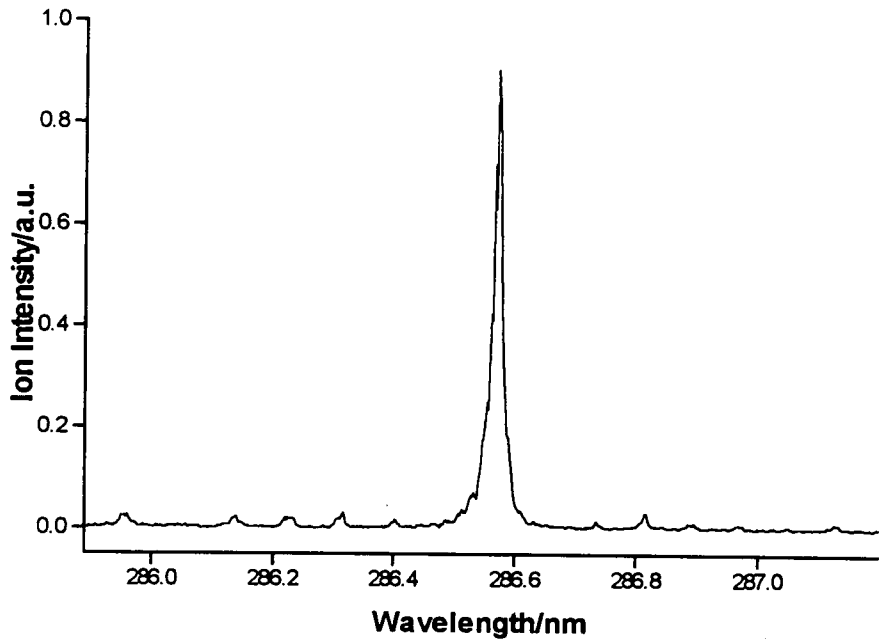

Figure 3.6: Low sensitivity (2+1) REMPI scan of the $4p_z{}^2A_2'' \leftarrow X^2A_2''$ band origin for CH_3. The Q branch dominates the spectrum. The methyl radical was generated by laser photolysis of CH_3I at 286nm. The CH_3I was admitted into the reaction chamber effusively. This spectrum was recorded with a reaction chamber pressure of 6.5×10^{-5}mbar.

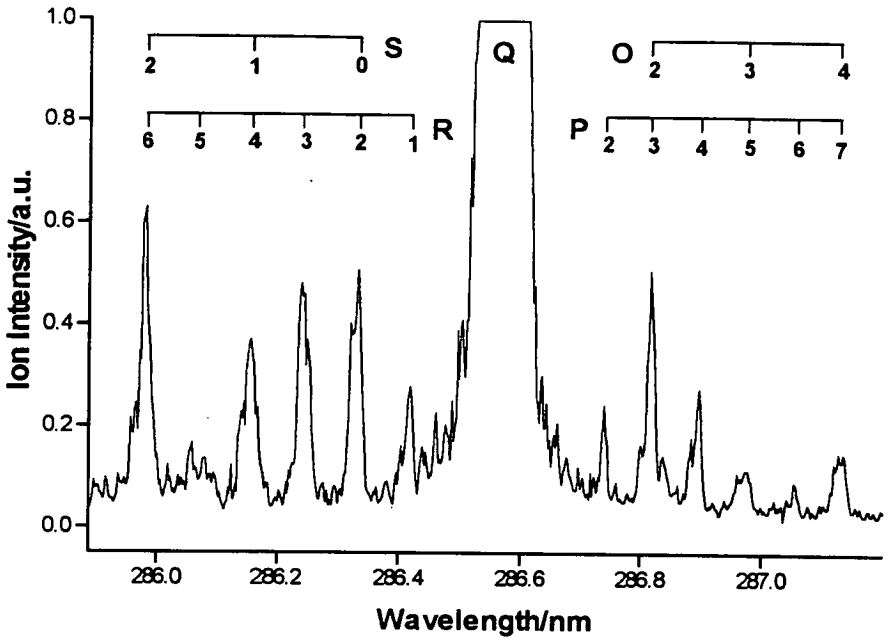

Figure 3.7: Higher sensitivity (2+1) REMPI scan of the $4p_z{}^2A_2 \leftarrow X^2A_2''$ band origin for CH_3. In this spectrum the O, P, R and S branch structure is seen. For each transition (ΔN, N") the predicted position for the maximum permissible K" is marked[33]. The photolysis precursor, methyl iodide, entered the reaction chamber effusively and was photolysed at 286nm. This spectrum was recorded with a reaction chamber pressure of 6.5×10^{-5}mbar.

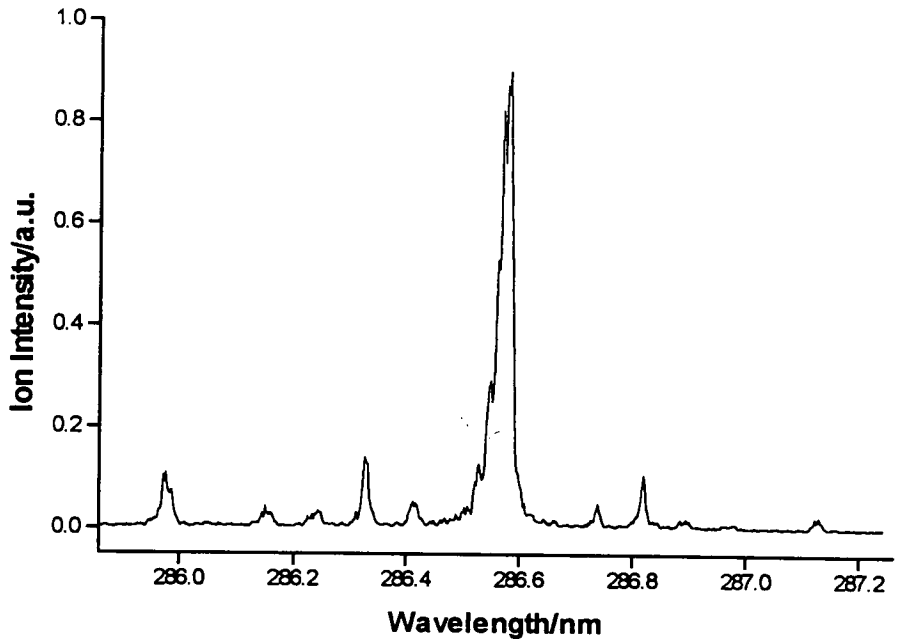

Figure 3.8: Low sensitivity (2+1) REMPI scan of the $4p_z{}^2A_2'' \leftarrow X^2A_2''$ band origin for CH_3. The intense Q branch dominates the spectrum. The methyl radical was generated by laser photolysis of CH_3I at 286nm. The CH_3I, seeded in He (1/5:4/5 mixture of CH_3I:He), was admitted into the reaction chamber using a pulsed molecular beam valve. The backing pressure was approximately 3bar above atmosphere.

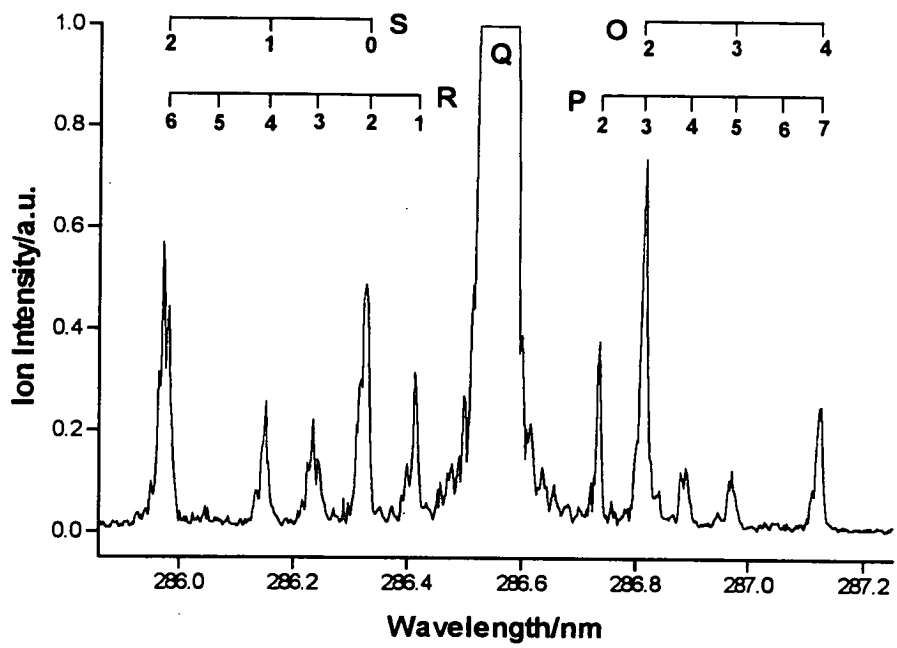

Figure 3.9: Higher sensitivity (2+1) REMPI scan of the $4p_z{}^2A_2'' \leftarrow X^2A_2''$ band origin for CH_3. In this spectrum the O, P, R and S branch structure is seen. For each transition (ΔN, N") the predicted position for the maximum permissible K" is marked[33]. This spectrum is very similar to the one shown in Figure 3.7, but here the photolysis precursor, methyl iodide (seeded in He), was introduced into the reaction chamber via a pulsed nozzle. The seeding ratio and backing pressure is the same as for the spectrum shown in Figure 3.8

introduce the CH_3I (20%CH_3I : 80%He) to the reaction system. In these experiments the backing pressure was approximately 3bar above atmosphere.

Figures 3.6 and 3.8 show the CH_3 $4p_z$ 0-0 resonance recorded at low sensitivity. In these scans the dominance of the intense Q branch is unmistakable, but weaker features to the red and blue are also visible. Higher sensitivity spectra, illustrated in Figures 3.7 and 3.9, were obtained by increasing the detector voltage. In these scans the O, P, R and S branches can be seen, but there is virtually no well resolved K substructure. The lack of resolution can be attributed to predissociation. The spectra shown in Figures 3.7 and 3.9 were assigned using the transition frequencies given by Powis and Black[33]. The two-photon selection rules for the $4p_z{}^2A_2'' \leftarrow X^2A_2''$ 0-0 transition allow for parallel $\Delta K = 0$, $\Delta N = 0, \pm1, \pm2$ rotational branches, but an additional selection rule is the rovibronic symmetry requirement for the D_{3h} point group which forbids $\Delta K = 0$, $\Delta N = \pm1$ transitions for K = 0 levels. The absence of the R(0) line is a manifestation of this rule. The signal to noise ratio is enhanced in Figures 3.8 and 3.9 as compared with Figures 3.6 and 3.7, thus illustrating the advantages of using pulsed nozzles in REMPI experiments.

(b) Photolysis of methyl iodide and REMPI detection of CH_3 in a two laser experiment:

Methyl iodide has a very broad absorption spectrum and can be photolysed at 248nm to yield a CH_3 radical and an I atom[46]. Then, the $3p_z{}^2A_2'' \leftarrow X^2A_2''$ transition of CH_3 can be probed by (2+1) REMPI using laser wavelengths of approximately 330nm. A brief account of this experiment follows. A fuller but generic description of the instrumentation can be found in Chapter 2.

The methyl radical was generated by excimer laser photolysis (KrF, 100mJ/pulse) of CH_3I at 248nm. The photolysis laser was focused into the

reaction chamber with an f=50cm lens which was estimated to transmit and focus approximately 85% of the beam energy. The frequency doubled output of the dye laser was then used to probe the $3p_z \leftarrow X$ transition in the methyl photofragment. The time delay between the photolysis and probe lasers firing was approximately 100ns. Output energies from the doubled dye (DCM (Lambda Physik)/trace LDS 698 (Exciton)) beam were extremely low; typically 200-400μJ/pulse. This is primarily because the dye optics do not work well in the extreme red.

Degassed CH_3I (Merck, 99%) was seeded in He (BOC, 99.99%) to give a CH_3I:He ratio of 20%:80%, and introduced into the reaction chamber, via a pulsed nozzle, normal to the laser beam direction. The nozzle (bullet shaped, 0.5mm diameter hole, Chapter 2 Figure 2.7(b)) was situated approximately 1cm from the laser beam axis. The measured "steady-state background" pressure was relatively constant at 1×10^{-5} mbar and the backing pressure was approximately 3bar above atmosphere. Ions formed at the laser focus were extracted, by the ion optic arrangement illustrated in Chapter 2 Figure 2.5, to the MCP detector and the signals digitised. The reaction and detection chambers were separated by a 10mm×2mm slot which maintained the pressure differential between them.

Power Normalisation

To probe the $3p_z \leftarrow X$ transition of CH_3, one-photon laser wavelengths of approximately 333nm were required. These wavelengths were generated by frequency doubling the output of the dye laser (Chapter 2 Section 2.2.1.2). Unfortunately, the dye optics did not work well in this extreme red range and this caused severe power fluctuations in the recorded spectra. Power normalisation was used to remove these fluctuations. Firstly, however, the form of normalisation required had to be established.

The signal, S, is typically expected to be related to the power, P, by the relationship specified in Equation (3.1):

$$S = kP^n \Leftrightarrow \ln S = \ln k + n \ln P \qquad (3.1)$$

Hence a plot of ln S against ln P will have gradient n, which is representative of the form of normalisation which needs to be applied to the signal to correct power fluctuations.

To determine the power normalisation experimentally the following procedure was used. Methyl Iodide (20% CH_3I : 80% He) was photolysed at 248nm and the resultant CH_3 probed by REMPI via the $3p_z \leftarrow X$ transition at a fixed wavelength resonant with the Q branch. Simultaneously, the corresponding spontaneous fluctuations in the probe laser power were recorded.

The data from these spectra was analysed and **ln S** plotted against **ln P** as shown in Figure 3.10. Linear regression carried out on this plot yielded a gradient of approximately 4 indicating that in this wavelength range (~333nm) the REMPI spectra of CH_3, recorded following photolysis of CH_3I at 248nm, need to be 4-photon normalised.

REMPI of the CH_3 $3p_z \leftarrow X$ transition is not four-photon dependent; it is a (2+1) REMPI process[37]. However the four-photon normalisation procedure seemed necessary because the probe power output was extremely low and unstable in this wavelength range. This is not really a satisfactory explanation of the behaviour of the system but the observed empirical power dependence will be used nonetheless.

In subsequent experiments the probe power was monitored by passing the doubled dye output through the Molectron Joulemeter (Chapter 2 Section

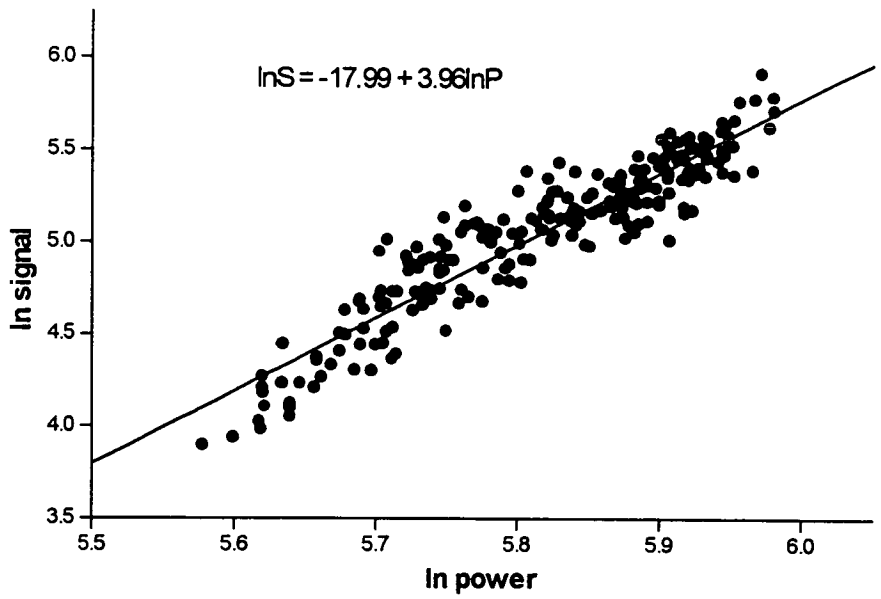

Figure 3.10: A plot of ln signal against ln power for CH_3 (probed by REMPI) obtained following photolysis of CH_3I. The gradient of this plot is approximately 4 indicating that the signal can be normalised by dividing by $(power)^4$.

2.2.1.2) prior to entering the reaction chamber. Only a very small fraction of the beam is reflected onto the detector element; the remainder is transmitted to the experiment. The power measured by the Molectron was collected by the ADC520 analogue-to-digital convertor module (Chapter 2 Section 2.4.2). A "spectrum" of the probe laser power was thus recorded in coincidence with the REMPI scan of CH_3. This scan could then be normalised by dividing the signal by (power)^4. REMPI of the CH_3 $3p_z \leftarrow X$ transition is not four- photon dependent; it is a (2+1) REMPI process[37].

Results

Figure 3.11 shows (2+1) REMPI spectra of the $3p_z{}^2A_2''(v'=0) \leftarrow X^2A_2''(v''=0)$ transition of the CH_3 radical. These spectra were obtained with photolysis and probe laser energies of 145mJ and 300μJ, respectively. The main picture in Figure 3.11 is a high sensitivity scan. Inset is the same $3p_z$ 0-0 resonance recorded using a lower detector voltage. In this scan only the dominant Q branch is obvious. These spectra exhibit oscillatory features which can be attributed to the fluctuations in the probe laser power output in this wavelength region. These spectra require power normalisation to correct the fluctuations in signal.

Figure 3.12 shows the same spectra as in Figure 3.11 but here the signal has been normalised by dividing by (power)^4. Again, the main picture in Figure 3.12 is a high sensitivity scan. In this spectrum a rough structure is seen and has been assigned as O, P, R and S branches. Inset is the $3p_z$ 0-0 resonance exhibiting only the dominant Q branch. In these scans power normalisation has been effective in removing the severe signal oscillations.

Clearly, these scans are not well resolved and spectral assignment is difficult. The reasons for this are two-fold. Firstly the $3p_z{}^2A_2''$ electronic state

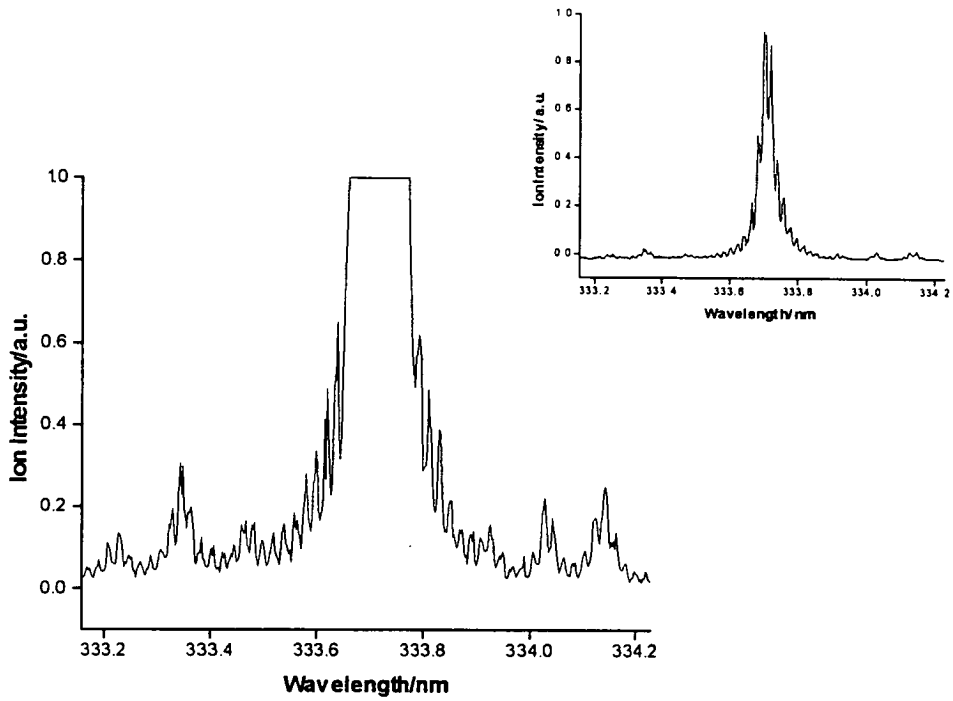

Figure 3.11: In the main frame a high sensitivity (2+1) REMPI scan of the $3p_z{}^2A_2''(v'=0) \leftarrow X^2A_2''(v''=0)$ transition of the CH_3 radical is shown. Inset is a low sensitivity scan showing the dominance of the Q branch. The methyl radical, probed in both these spectra, was obtained by excimer laser photolysis (KrF) of CH_3I at 248nm. The CH_3I (seeded in He) entered the reaction chamber via a pulsed molecular beam valve. The probe power ouput during the recording of these scans was extremely low; this accounts for the fluctuations in the signal. These spectra require power normalisation (refer to Figure 3.12).

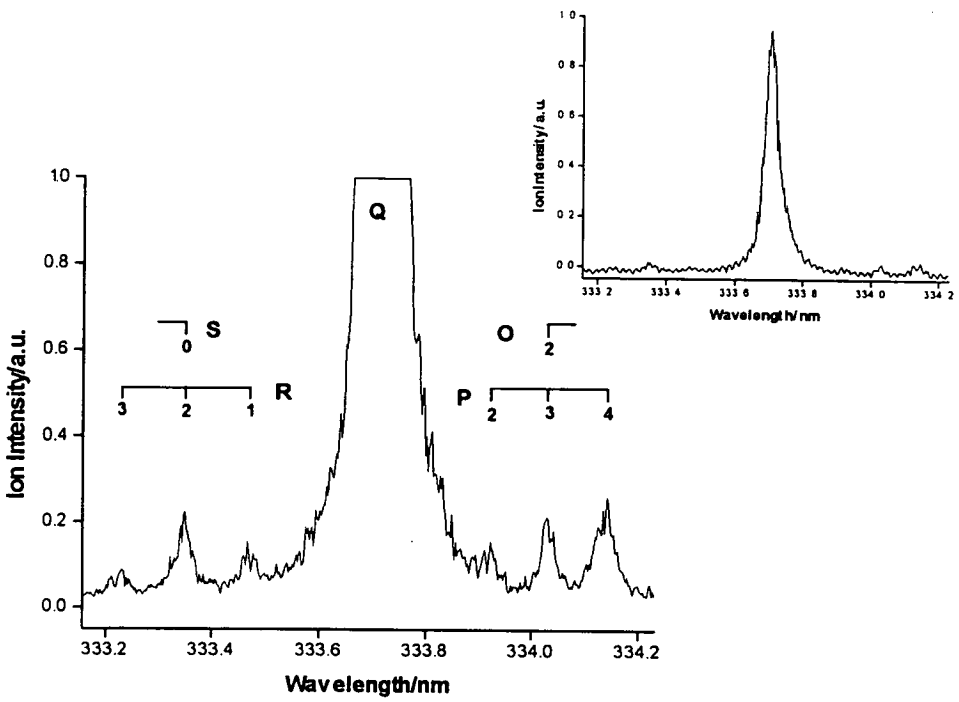

Figure 3.12: Here the spectra shown in Figure 3.11 have been power normalised as described in the text. In the main frame a high sensitivity (2+1) REMPI scan of the $3p_z{}^2A_2''(v'=0) \leftarrow X^2A_2''(v''=0)$ transition of the CH_3 radical is shown. The O, P, R and S branch structure was assigned by comparison with similar spectra obtained by Chandler and Parker *et al*[42]. Inset is a low sensitivity scan showing the dominance of the Q branch. The methyl radical, probed in both these spectra, was obtained by excimer laser photolysis (KrF) of CH_3I at 248nm.

of CH_3 is predissociative, which results in broadened rovibronic transitions and correspondingly weak REMPI spectra. Secondly, as described, the probe laser power in the extreme red is very unstable and weak, affecting the quality of spectra obtained. To solve this problem an alternative laser probing scheme would have to be used. This option was not available at the time of the experiment.

(c) The photolysis of methyl iodide - concluding remarks

In conclusion, the photolysis of CH_3I, using either a one or two laser experimental scheme yields CH_3 which can be probed by REMPI. Spectra of both the $3p_z{}^2A_2''(v'=0) \leftarrow X^2A_2''(v''=0)$ and $4p_z{}^2A_2''(v'=0) \leftarrow X^2A_2''(v''=0)$ transitions of the CH_3 radical have been obtained and analysed: an insight into the spectroscopy of the methyl radical has been gained. This kind of study is very useful in that it paves the way for future studies in which CH_3 will be detected as the product of a bimolecular reaction.

References

[1] E.J. Llewellyn and B.H. Long, *Can. J. Phys.*, **56**, 581 (1978).

[2] D.J.W. Kendall and T.A. Clark, *J. Quant. Spectrosc. Radiat. Transfer*, **21**, 511 (1979).

[3] J.A. Coxon and S.C. Foster, *Can. J. Phys.*, **60**, 41 (1982).

[4] W.J. Wilson and A.H. Battett, *Science*, **161**, 778 (1968).

[5] G. Herzberg, *Molecular Spectra and Molecular Structure, I. Spectra of Diatomic Molecules* (D. Van Nostrand Reinhold, 1950).

[6] H.M. Crosswhite and G.H. Dieke, *J. Quant. Spectrosc. Radiat. Transfer*, **2**, 97 (1962).

[7] P. Andresen and A.C. Luntz, *J. Chem. Phys.*, **72**, 5842 (1980).

[8] A.C. Luntz, *J. Chem. Phys.*, **73**, 1143 (1980).

[9] P.M. Aker, J.J.A. O'Brien and J.J. Sloan, *J. Chem. Phys.*, **84**, 745 (1986).

[10] D.J. Rakestraw, K.G. McKendrick and R.N. Zare, *J. Chem. Phys.*, **87**, 7341 (1987).

[11] M. Brouard and J. O'Mahony, *Chem. Phys. Lett.*, **149**, 45 (1988).

[12] J. August, M. Brouard and J.P. Simons, *J. Chem. Soc. Faraday Trans. 2*, **84**, 587 (1988).

[13] C.R. Park and J.R. Wiesenfeld, *J. Chem. Phys.*, **95**, 8166 (1991).

[14] M. Brouard, S. Duxon, P.A. Enriquez and J.P. Simons, *J. Chem. Soc. Faraday Trans.*, **89**, 1435 (1993).

[15] E.F. Van Dishoeck and A. Dalgarno, *J. Chem. Phys.*, **79**, 873 (1983).

[16] A.E. Douglas, *Can. J. Phys.*, **52**, 318 (1974).

[17] W.H. Smith, *J. Chem. Phys.*, **53**, 792 (1970).

[18] R.A. Sutherland and R.A. Anderson, *J. Chem. Phys.*, **58**, 1226 (1973).

[19] K.R. German, J. *Chem. Phys.*, **63**, 5252 (1975).

[20] E. De Beer, M.P. Koopmans, C.A. De Lange, Y. Wang and W.A. Chupka, *J. Chem. Phys.*, **94**, 7634 (1991).

[21] R. Forster, H. Hippler, K. Hoyermann and G. Rohde, *Chem. Phys. Lett.*, **183**, 465 (1991).

[22] M. Collard, P. Kerwin and A. Hodgson, *Chem. Phys. Lett.*, **179**, 422 (1991).

[23] A. Watson, *State-Specific Reaction Dynamics*, Ph.D Thesis, University of Edinburgh, 1994.

[24] W.C. Wiley and I.H. McLaren, *Rev. Sci. Instrumen.*, **26**, 1150 (1955).

[25] T. Ebata, A. Fujji, T. Amano and M. Ito, *J. Phys. Chem.*, **91**, 6095 (1987).

[26] G. Herzberg, *Proc. R. Soc. London Ser. A*, **262**, 291 (1961).

[27] J. Dyke, N. Jonathon, E. Lee and A. Morris, *J. Chem. Soc. Faraday Trans. 2*, **72**, 1385 (1976).

[28] R.W. Fesenden, *J. Phys. Chem.*, **71**, 74 (1967).

[29] M.E. Jacox, *J. Mol. Spectrosc.*, **66**, 272 (1977).

[30] A. Snelson, *J. Phys. Chem.*, **74**, 537 (1970).

[31] C. Yamada, E. Hirota and K. Kawaguchi, *J. Chem. Phys.*, **75**, 5256 (1981).

[32] J.W. Hudgens, T.G. DiGuiseppe and M.C. Lin, *J. Chem. Phys.*, **79**, 571 (1983).

[33] J.F. Black and I. Powis, *J. Chem. Phys.*, **89**, 3986 (1988).

[34] R. Ogorzalek-Loo, G.E. Hall, H.-P. Haerri and P.L. Houston, *J. Phys. Chem.*, **92**, 5 (1988).

[35] R. Ogorzalek-Loo, G.E. Hall, H.-P. Haerri and P.L. Houston, *J. Chem. Phys.*, **90**, 4222 (1989).

[36] P. Chen, S.D. Colson, W.A. Chupka and J.A. Berson, *J. Phys. Chem.*, **90**, 2319 (1986).

[37] R. Schott, J. Schluetter, M. Olzmann and K. Kleinermanns, *J. Chem. Phys.*, **102**, 8371 (1995).

[38] P.W. Atkins, *Physical Chemistry, 3rd edition* (Oxford University Press, 1988) p.475.

[39] M.N.R. Ashfold, J.M. Bayley and R.N. Dixon, *Can. J. Phys.*, **62**, 1806 (1984).

[40] J. Danon, H. Zacharias, H. Rottke and K.H. Welge, *J. Chem. Phys.*, **76**, 2399 (1982).

[41] D.H. Parker, Z.W. Wang, M.H.M. Janssen and D.W. Chandler, *J. Chem. Phys.*, **90**, 60 (1989).

[42] D.W. Chandler, J.W. Thoman Jr., M.H.M. Janssen and D.H. Parker, *Chem. Phys. Lett.*, **156**, 151 (1989).

[43] D.W. Chandler, M.H.M. Janssen, S. Stolte, R.N. Strickland, J.W. Thoman Jr. and D.H. Parker, *J. Phys. Chem.*, **94**, 4839 (1990).

[44] M.H.M. Janssen, D.H. Parker, G.O. Sitz, S. Stolte and D.W. Chandler, *J. Phys. Chem.*, **95**, 8007 (1991).

[45] J.C. Calvert and J.N. Pitts, *Photochemistry*, p.523.

[46] M.D. Barry and P.A. Gorry, *Mol Phys.*, **52**, 461 (1984).

Chapter 4

The Reactions of $O(^3P)$ with Hydrocarbons

4.1 Introduction

The reactions of the electronic ground state of oxygen, $O(^3P)$, with simple organic molecules are of primary importance to combustion and atmospheric chemistry. Consequently, much time has been devoted to measuring the rates and studying the kinetics of $O(^3P)$ reactions[1-10]. Many of these reactions had been assumed to proceed via hydrogen abstraction, but it is only relatively recently that the detailed chemical dynamics of such reactions with organic molecules have been elucidated.

The dynamics of these processes were first investigated by Andresen and Luntz[11,12] who used the technique of molecular beam laser-induced fluorescence to determine product internal state distributions. They studied the OH fragment produced in the reactions of $O(^3P)$ with a series of saturated hydrocarbons (namely neopentane, cyclohexane and isobutane), chosen to contain abstractable primary, secondary and tertiary hydrogens. This work was soon afterward enhanced by Kleinermanns and Luntz[13-15] and the Whitehead group[16-19] who used similar techniques to examine the OH distribution following reaction of $O(^3P)$ with a range of organic compounds. Subsequently, laser photolytic generation of $O(^3P)$ was introduced and the work into the reactions of $O(^3P)$ has now been extended to include the organic hydrides, HBr and HCl[20-23], silanes[24,25] and GeH_4[26]. Related reactions with hydrocarbon clusters have been studies by Naaman and co-workers[27,28].

In all these studies, with the exception of the cluster experiments, the hydrogen abstraction mechanism inferred by kinetic experiments has been confirmed. Gas-phase systems can be used to gain an insight into the dynamics of corresponding liquid-phase reactions. However, for the $O(^3P)$ + (saturated) hydrocarbon reaction, the products of the gas-phase and condensed medium reactions differ. Naaman *et al*[27,28] showed that the reaction between O atoms and hydrocarbon clusters mimics the mechanism in the liquid phase: when cyclohexane clusters react with $O(^3P)$, the OH product is suppressed. Instead alcohol (cyclohexanol) is obtained via an insertion mechanism. The hydrogen abstraction is blocked.

Detailed dynamical information on the gas-phase $O(^3P)$ reactions was obtained from the nascent internal state distribution of the product OH(v,N,f), where v is the vibrational quantum number, N is the rotational quantum number (excluding spin) and f refers to one of the four OH fine-structure levels. Spin-orbit interactions in the OH radical cause a spin doubling and this results in two manifolds of (v,N) levels. Each spin doublet is further spilt by Λ-doubling. Hence OH has four fine-structure states for each (v,N) level. A detailed discussion of the spectroscopy of OH was given in Chapter 3.

The main conclusions drawn from the (monomeric) saturated hydrocarbon investigations were that the degree of vibrational excitation in the OH product is determined by the strength of the C-H bond broken during the course of the reaction: the vibrational state distribution of OH depends markedly on the type of hydrogen being abstracted, the degree of excitation increasing dramatically across the series primary to secondary to tertiary, reflecting the decreasing bond strength. This can be interpreted as a shift from a repulsive towards a more attractive potential energy surface across the series, as discussed in Chapter 1 Section 1.2. However, in all cases the amount of OH rotational excitation is low, indicating that the reaction

dynamics are direct and a collinear approach of the oxygen atom to the bond under attack is favoured.

Similar results were obtained for the reactions between $O(^3P)$ and unsaturated hydrocarbons[13], aldehydes[14], amines[15], ethanol[16] and benzene[17], studied by Luntz *et al* and Whitehead *et al*. For all these systems the degree of rotational excitation in OH was low indicative of direct reaction dynamics and a preferentially collinear (O---H---C) transition state. In the reactions of $O(^3P)$ with unsaturated molecules[13] addition pathways, leading to products other than OH, are also very important.

In the $O(^3P)$ + HR reaction Luntz *et al*[11] reported that the lower OH spin doublet ($^2\Pi_{3/2}$) was almost two times more populated than the upper spin doublet ($^2\Pi_{1/2}$). Whitehead *et al*[19] also noted a preference, this time threefold, for the population of the $OH(^2\Pi_{3/2})$ state following the reaction between $O(^3P)$ and cyclohexane. Andresen and Luntz proposed that the source of the spin-orbit state selectivity lay in reactant to product surface correlations and concluded that the reaction was neither fully adiabatic nor wholly statistical with respect to mixing between the surfaces linking the entrance and exit channels. Whitehead *et al*[19] agreed with this conclusion.

The energy disposal in the $O(^3P)$+HBr(HCl) reaction, however, was found to be different[20-23]. The OH product had a highly inverted vibrational distribution, resulting from an early barrier in the entrance channel and "corner cutting" trajectories in which the H atom is transferred at relatively large internuclear distances[21]. This system differs substantially from the $O(^3P)$ + hydrocarbon reaction in that the OH was found to be rotationally hot. This high rotational excitation presumably derives from repulsive Br(Cl)---H interactions acting off the line of centres in a bent (O---H---Br(Cl)) intermediate.

The reaction between $O(^3P)$ and the simplest hydrocarbon, CH_4, was not studied in the original experiments by Luntz *et al*[11]. This omission was undoubtedly due to the difficulty in surmounting the barrier to the reaction: the barrier height in these reactions is correlated with the strength of the C-H bond which is greatest for CH_4[29]. An additional factor is that the kinematics do not cooperate to promote reaction between $O(^3P)$ and methane. If HR is heavy with respect to the O atom, then the centre-of-mass collision energy is high because O is moving fast relative to HR in the lab frame. However, in the $O(^3P)/CH_4$ system, the O atom velocity in the lab frame leads to a smaller centre-of-mass collision energy because the HR collision partner is light.

The $O(^3P)+CH_4$ reaction has escaped detailed scrutiny, though it was briefly mentioned in a recent publication by Suzuki and Hirota[30] who applied the technique of tunable infra-red diode laser kinetic absorption spectroscopy to oxygen atom reactions. Their primary interest was in the reaction between $O(^1D)$ and methane, but they also measured the ν_2 out-of-plane "umbrella" mode vibrational distribution for CH_3 produced in the $O(^3P)$ + methane reaction. The ν_2 mode was found to be moderately excited with a non-inverted distribution which was slightly hotter than expected on statistical grounds. This discrepancy was accounted for by a broadening in the collision energy caused by the thermal motion of the reactants, resulting in a number of collisions occurring at higher energy than the average collision energy.

Suzuki and Hirota also noted significant CH_3 rotational excitation but the relatively high pressure required for adequate signal-to-noise ratios prevented the measurement of any nascent rotational distributions. This result is surprising considering that Luntz and other workers in the field have assigned a collinear approach geometry to related reactions. If the reaction occurred through a collinear intermediate then very little torque would be imparted to CH_3 and the fragment would be rotationally cold. The

observation of rotational excitation in CH_3 contradicts the previously noted trends, based on examination of the distribution within the OH product, and it would be of interest to either confirm Luntz's predictions, that all saturated hydrocarbons should react in a similar manner, or Suzuki and Hirota's results.

Independent results obtained for the reactions of Cl atoms with hydrocarbon molecules should probably be discussed at this point. These reactions can be considered to be analogous to the reactions of $O(^3P)$+HR because the product HCl and OH bond dissociation energies are comparable[31] which leads to very similar reaction exothermicities. Accordingly, conclusions reached for the more comprehensively studied $Cl(^2P)$+HR reactions may potentially be applied to the reactions of $O(^3P)$.

The internal state distributions of HCl (and DCl) have been determined following the reactions of Cl with a range of hydrocarbon species, in particular CH_4[32-40]. The general conclusion from these studies is that the product HCl is rotationally cold, confirming the similarity between the reactions of $O(^3P)$ and $Cl(^2P)$. Much effort has been concentrated on measuring product time-of-flight profiles and determining the angular scattering distributions of HCl[32,34-37,39,40]. From this kind of analysis it has been established that reactants in the vibrational ground state yield predominantly backward scattered products. This result is consistent with a collinear abstraction mechanism. However, the situation is more complex if the CH_4 reactant is vibrationally excited[34-37]. In this instance, although the HCl(v=0) product is still principally backward scattered, the rotationally cold HCl(v=1) product is scattered in the forward direction. An explanation for this rather surprising result has been proposed by Zare *et al*[37]. It is thought that the geometry of the transition state becomes less constrained to collinearity and that the cone of acceptance widens following vibrational excitation of CH_4. Hence, even though the dynamics of $O(^3P)$ + hydrocarbon

reactions seem to conform to a strictly collinear geometry, this conclusion should not be taken for granted until further data have been obtained.

The main drawback to studying the $O(^3P)+CH_4$ reaction is in obtaining sufficiently energetic O atoms to overcome the barrier to the reaction. $O(^3P)$ can be generated by the photolysis of NO_2 between 243.9 and 397.8nm[41,42], but is most conveniently produced between 300 and 350nm where the absorption cross-section, and hence yield of $O(^3P)$, is high[43-47]. However at these wavelengths, the photolytically generated reactants do not have enough energy to surmount the reaction barrier. Alternative routes include microwave discharge of O_2[11,19,28] and photolysis of SO_2[48,49] and O_3[50]. However, in a recent paper by Polanyi *et al*[51] the photodissociation dynamics of NO_2 at 248nm were studied. This wavelength is just above the energetic threshold for production of $O(^1D)$, the first excited electronic state of oxygen. The nascent NO photofragment was probed by (1+1) REMPI and the relative populations of the rovibrational states of NO determined. A bimodal vibrational distribution in NO (peaking at v"=0 and v"=5) was seen. If the NO produced is vibrationally cold then, by inference, the $O(^3P)$ atom will be translationally hot. Similarly, if the NO is vibrationally hot then the $O(^3P)$ is translationally cold. Hence, from the vibrational distribution seen by Polanyi *et al*, it can be inferred that the translational distribution of $O(^3P)$, following photolysis of NO_2 at 248nm, is also bimodal. The fast $O(^3P)$ atoms formed are sufficiently energetic to overcome the $O(^3P)+CH_4$ barrier, hence photolysis of NO_2 at 248nm provides an energetically viable route to this reaction.

4.2 The $O(^3P)$/HR Reaction: Specific Aims

A series of experiments was designed to investigate the gas phase bimolecular process specified in Equation (4.1), using laser methods for the

state-selective preparation of $O(^3P)$ and for the state-specific detection of the nascent OH fragment.

$$O(^3P) + HR \longrightarrow OH + R \qquad (4.1)$$

HR is a saturated hydrocarbon, chosen to represent primary, secondary or tertiary C-H bonds. Translationally excited $O(^3P)$ atoms were generated by photolysis of NO_2 at either 337nm, 308nm or 248nm: changing the wavelength of photolysis effectively alters the collision energy of the reaction. The kinetic energy of the $O(^3P)$ atoms increases with the photolysis energy.

This system had been previously studied by a colleague[52], who probed the OH product following photolysis of NO_2 at 337nm and 308nm. This work concentrates principally on photolysis at 248nm, but the earlier results will also be presented so that the system can be fully described over a range of collision energies.

4.3 Experimental Procedure

4.3.1 The Reaction Between $O(^3P)$ and HR Following 248nm Photolysis of NO_2

Nascent OH internal state distributions resulting from the reaction specified in Equation (4.1) were measured using the two laser photolysis-probe scheme described in Chapter 2 and illustrated in Figure 2.8. $O(^3P)$ was generated by excimer laser photolysis (KrF) of NO_2 at 248nm[51] and subsequently reacted with a range of saturated hydrocarbon molecules. Nascent conditions were ensured by maintaining NO_2/HR pressures less than 250mTorr and the time delay between the photolysis and probe lasers was kept short. The $OH(v'=0)$[53] product was then detected by LIF (as

described in Section 2.2.2.4 and illustrated in Figure 2.6) via the $A^2\Sigma^+(v=1) \leftarrow X^2\Pi(v=0)$ and $A^2\Sigma^+(v=0) \leftarrow X^2\Pi(v=0)$ transitions. This involved generating laser wavelengths in the region 282nm and 307nm respectively, achieved by doubling the output of the dye laser. To probe OH via the (1-0) band R590 dye (Exciton) was used. DCM dye (Lambda Physik) was used for the (0-0) band.

The photolysis beam (~30mJ/pulse) was loosely focused (with a f=50cm lens) to give a spot size of approximately 2mm in the interaction region. The probe beam (~1mJ/pulse) remained unfocused. The typical output energy of the doubled dye beam was far in excess of the energy required to excite fluorescence in OH. Hence to minimise saturation the probe beam was passed through a pair of Glan-Taylor prisms which allowed the laser power to be attenuated whilst still maintaining a fixed (vertical) polarisation axis. The resultant beam entering the reaction chamber typically had pulse energies between 100 and 500μJ. For investigation of potential polarisation effects, a photoelastic modulator (Hinds PEM-80) was used.

As mentioned previously, OH(v'=0) was detected via two different bands. In the initial experiments fluorescence was excited on the A-X (1-0) band and observed on the (1-1) band. In later experiments fluorescence was both excited and detected on the (0-0) band. An interference filter (Ealing 35-8044), centred at 310nm with a bandwidth of 10nm, was placed in the lens assembly between the focusing lens and PMT detector. Its purpose was to block out the wavelengths from the photolysis and probe lasers whilst transmitting radiation over the wavelength region of the desired vibronic transition

The saturated hydrocarbons used in this study were isobutane (chosen to represent tertiary abstraction), cyclohexane (secondary abstraction), ethane (primary abstraction) and methane. Non-condensable contaminants were

removed from the reactants by freeze-pump-thaw cycling at liquid N_2 temperatures. The sources and manufactures' stated purities were as follows: NO_2 (Distillers MG, 98%), isobutane (Matheson, 99.0%), cyclohexane (Fisons, >99%), ethane (Matheson, 99.0%) and methane (Distillers MG 99.5%). The reagent flow was controlled by needle valves and gases entered the reaction chamber effusively via a glass injector (hole diameter ~2mm) which was painted black to minimise scattered light. The injector tip was located approximately 10mm from the laser focus. A "steady-state" pressure of around 250mTorr during the experiment was achieved by partially throttling the reaction chamber diffusion pump.

4.3.2 The Reaction Between $O(^3P)$ and HR Following 337 and 308nm Photolysis of NO_2

The experimental details for the detection of the OH product of the reaction between $O(^3P)$ and HR, following photolysis of NO_2 at 337 and 308nm, have been discussed in great depth elsewhere[52]. A brief outline of the procedure is given below.

The techniques and instrumentation used to carry out these experiments are described in Chapter 2. $O(^3P)$ atoms were generated by excimer laser (Lambda Physik EMG102E) photolysis of NO_2 (Distillers MG, 98%) at 337nm (N_2) and 308nm (XeCl). The photolysis beam was loosely focused to a spot size of ~2mm. Typical pulse energies entering the reaction chamber were 3mJ/pulse at 337nm and 25mJ/pulse at 308nm.

In this study both OH(v'=0) and OH(v'=1)[53], resulting from the reactions between $O(^3P)$ and isobutane, cyclohexane, ethane and methane, were probed. The procedures used were similar to those described above for the reactions initiated at 248nm.

4.4 Results - Rotational Distributions

Firstly the OH LIF spectra resulting from the reaction between $O(^3P)$ and HR, following 337 and 308nm photolysis of NO_2[52], will be presented and discussed. Then the results from the 248nm photolysis will be given.

Each photolysis wavelength generated a variety of interfering signals, which affected the choice of OH A ← X vibronic band on which to excite and detect LIF signals. The problems which were encountered in obtaining the OH spectra will be discussed prior to the results.

4.4.1 Rotational Distributions: 337 and 308nm Photolysis

As mentioned previously this work was carried out principally by a colleague and is fully described elsewhere[52]. Given below is a brief summary of the pertinent features of the work, since the experiments at 248nm photolysis are an extension of this work.

Following photolysis at 337nm OH(v'=0) was detected by exciting on the (1-0) and observing the resulting fluorescence on the (1-1) band. Conversely OH(v'=1) was excited on (1-1) and observed via (1-0). These detection protocols were chosen because the photolysis wavelength (337nm) does not overlap with any of the OH A ← X vibronic bands. The principal problem at this wavelength was relatively weak signal intensities due to the low photolysis energy.

For 308nm photolysis the situation was slightly more complicated. Despite precautionary measures to reduce scattered light from both lasers, it was not possible to observe the emission from the OH A ← X diagonal bands because of the substantial signal from scattered photolysis laser light. Hence OH(v'=0) was probed by both exciting and detecting on the (1-0)

band. Detection of OH(v'=1) was more straightforward as it could be excited on (1-1) and observed on (1-0).

At both photolysis wavelengths there were background contributions to the signal which had to be removed before the nascent OH spectra could be analysed. The source and subsequent removal of undesirable signals are described in ref. [52].

Figure 4.1 shows typical LIF excitation spectra for OH(v'=0) produced in the reactions of $O(^3P)$ with isobutane, cyclohexane and ethane, following 308nm photolysis of NO_2. Comparable, but slightly noisier, spectra were obtained at 337nm. Figures 4.2(a) and 4.2(b) compare the respective OH(v'=0) and OH(v'=1) spectra obtained from the $O(^3P)$+isobutane reaction following photolysis of NO_2 at 308nm. In all these spectra the rotational lines, originating in levels N'[53] of the $X^2\Pi$ ground state, have been assigned using the data collected by Dieke and Crosswhite[54]..

A few details pertaining to the reactive systems and subsequent spectra need to be clarified. Firstly, isobutane, $(CH_3)_3CH$, is chosen to exemplify tertiary abstraction, but out of the 10 hydrogens, 9 are primary and only one is tertiary. Hence, it is possible that both tertiary and primary hydrogens could simultaneously be abstracted, thus confusing the results. However, it has been noted[52] that at 337nm the OH(v'=0) from the $O(^3P)$+ethane reaction was substantially more difficult to detect relative to cyclohexane and isobutane. This provides support for the conclusion[11] based on isotopic substitution that the signal from isobutane is dominated by the contribution from the tertiary C-H only, at least at the relatively low collision energies characteristic of 337nm photolysis.

It should also be noted that the spectra resulting from the $O(^3P)$+cyclohexane reaction always had better signal to noise ratios,

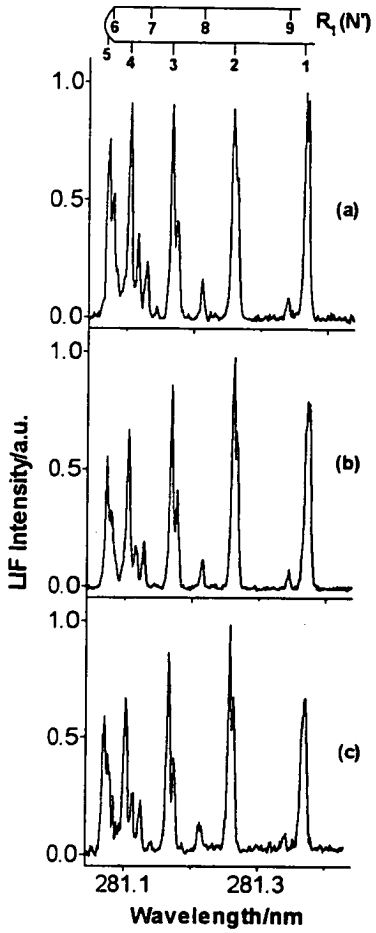

Figure 4.1: LIF excitation spectra of the R_1 branch region of the OH(v'=0) A←X (1-0) band, probed following reaction between $O(^3P)$ with (a) isobutane, (b) cyclohexane and (c) ethane. The $O(^3P)$ was generated by excimer laser photolysis of NO_2 at 308nm. The photolysis power was typically ~25mJ/pulse and the probe power 100μJ/pulse. In all cases the total pressure was 100mTorr and Δt=200ns. Minor contributions to the signal from photolysis of impurities have been removed as described in ref. [52]. The rotational lines, originating in levels N'[53] of the $X^2\Pi$ ground state, have been assigned[54].

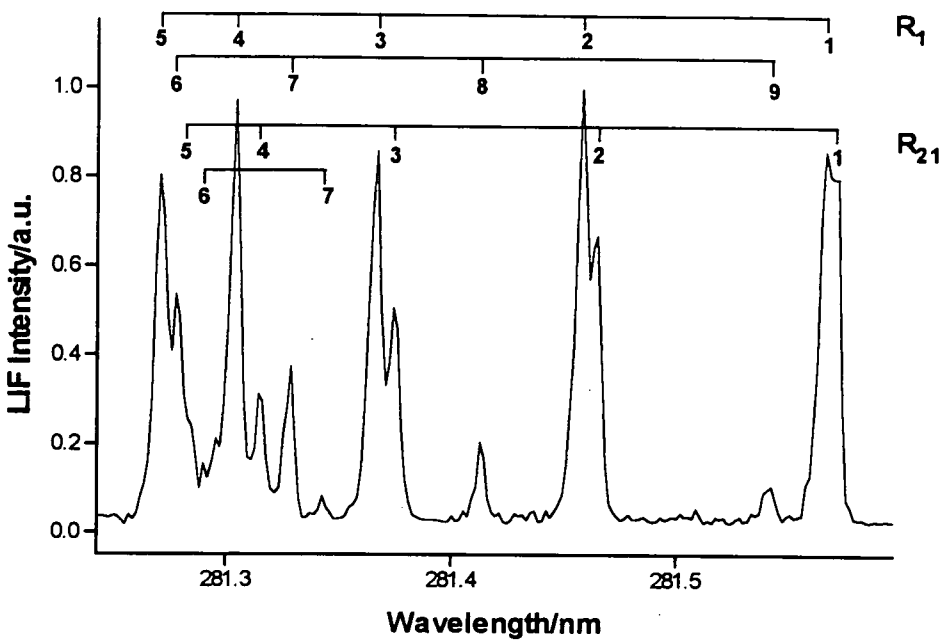

Figure 4.2(a): The OH(v'=0) product resulting from the reaction between $O(^3P)$ and isobutane. $O(^3P)$ was generated by photolysis at 308nm. The photolysis and probe laser powers were 25mJ/pulse and 100μJ, respectively. The total gas pressure was 100mTorr. Background contributions to the OH signal were removed as described in the text. The time delay between the photolysis and probe sequences was 200ns, ensuring that nascent products were detected.

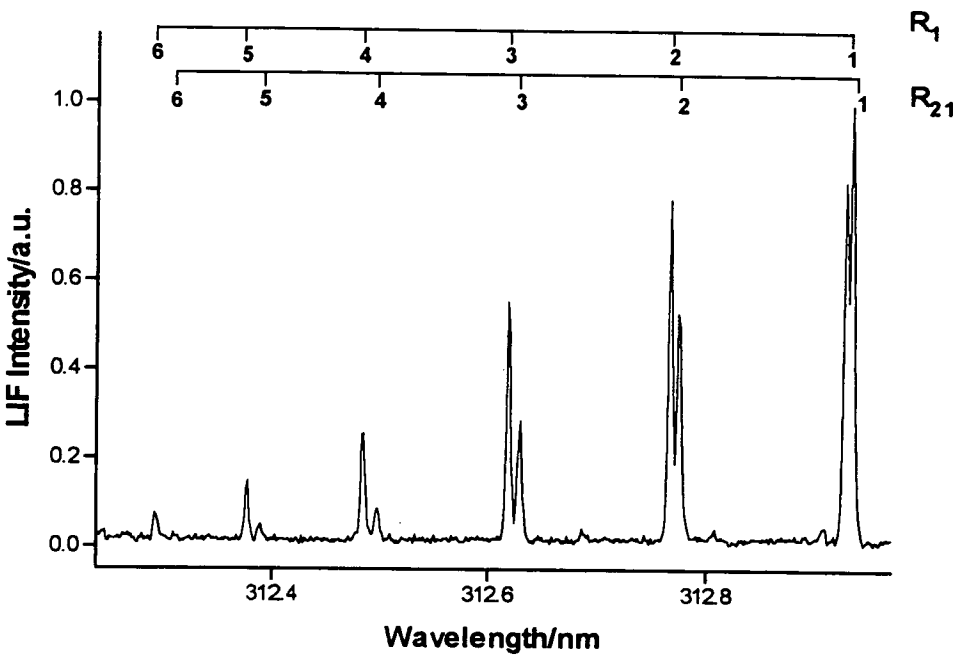

Figure 4.2(b): The OH(v'=1) product resulting from the reaction between $O(^3P)$ and isobutane. $O(^3P)$ was generated by photolysis at 308nm. The photolysis and probe laser powers were 25mJ/pulse and 20μJ, respectively. The total gas pressure was 80mTorr. Background contributions to the OH signal were removed as described in the text. The time delay between the photolysis and probe sequences was 200ns, ensuring that nascent products were detected.

irrespective of the collision energy. This is a slightly unusual result considering that tertiary abstraction should be easier than secondary abstraction. However, this was probably due to the fact that in isobutane only one tertiary hydrogen was available for abstraction whereas in cyclohexane there are twelve secondary hydrogens.

The reaction between $O(^3P)$ and methane is expected to be energetically unfeasible[29] and, accordingly, OH(v'=0) was not detected at all as a reactive product at 337nm. However signal was just discernible above the background noise at 308nm. At this point though, this specific reaction was not fully investigated and rotational populations were not obtained. Similarly, OH(v'=1) was not detected at 337nm from the ethane reaction, whereas at 308nm the v'=1 product was observed for HR=isobutane, cyclohexane and ethane. However, no firm conclusions can be drawn about the photolysis energy dependence of the v'=0/v'=1 branching ratio: a more detailed examination of the system is required before any qualitative conclusions can be made.

The LIF excitation spectra were analysed[52] to yield the relative populations over the rotational levels of OH by making use of the known transition probabilities[54-56]. This involved assessment of the contributions to each signal from individual returning A-X lines. The resultant populations were corrected for the measured (wavelength dependent) transmission functions of the interference filters used to isolate the emission and for the manufacturer's quoted PMT response. Account was also taken of the minor effects of the anisotropy of the LIF signal excited and observed on specific lines using a known probe laser linear polarisation[57].

The resulting rotational populations in the $^2\Pi_{3/2}$ spin-orbit state of OH(v'=0), determined by converting the intensities of lines in the R_1 branch into populations, are shown in Figures 4.3(a) and 4.3(b) for 337nm and 308nm

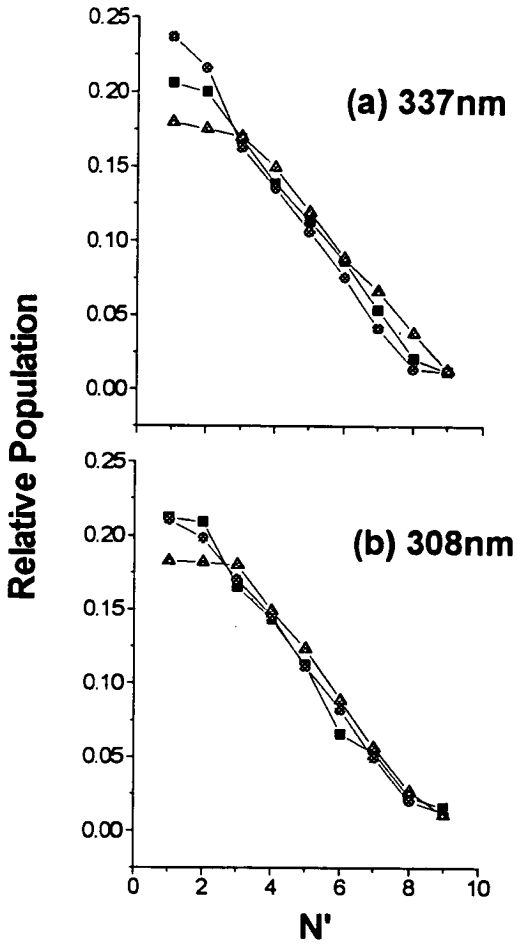

Figure 4.3: Rotational distributions in OH $^2\Pi_{3/2}$ (v'=0) from reactions of O(^{3}P) with hydrocarbons, following photolysis of NO_2 at (a) 337nm and (b) 308nm.

Hydrocarbon reactants:

(■) - isobutane

(●) - cyclohexane

(▲) - ethane

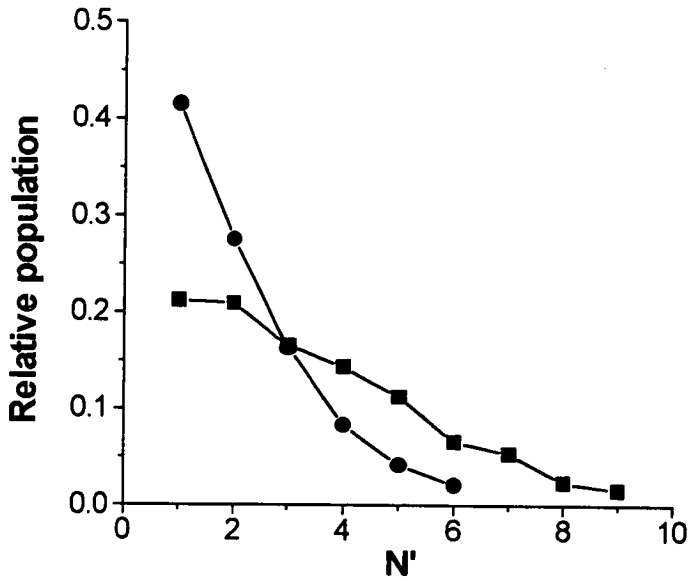

Figure 4.4: Rotational populations in OH v'=0 (■) and v'=1 (●) vibrational levels of OH $^2\Pi_{3/2}$ produced in the O(^{3}P)+isobutane reaction, following 308nm photolysis of NO_2.

photolysis, respectively. It is clearly evident that only a few rotational levels (N′) are populated and thus the distributions are cold, irrespective of the nature of HR or of the collision energy. Figure 4.4 compares the distributions obtained for v′=0 and v′=1, for the reaction between $O(^3P)$ and isobutane, following photolysis at 308nm. This figure shows that the rotational partitioning within v′=1 is even colder than that for v′=0.

4.4.2 Features of the Spectra Recorded Following 248nm Photolysis

Photodissociation of NO_2 at 248nm proved to be very beneficial because very fast $O(^3P)$ atoms were created which reacted easily with the hydrocarbon reagents. Fortunately this wavelength does not overlap with any of the OH A-X vibronic bands and thus allowed v′=0 to be probed by both the (1-0) and (0-0) bands. In the initial experiments on the system fluorescence was excited on the (1-0) band and observed on the (1-1) band. Later experiments, also probing v′=0, utilised the (0-0) band for both excitation and detection. However, there were complications associated with this photolysis wavelength which are described below.

In the resultant OH LIF excitation scans, there were two rogue contributors to both signal and background noise, which obviously had to be removed before quantitative analysis of the spectra could be carried out. Firstly, the photolysis laser alone excited a strong, prompt emission which shall be labelled the background fluorescent signal. Secondly, but more problematic, was the existence of an OH signal at all photolysis laser - probe laser time delays; a background OH signal.

The background fluorescent signal, observed in the absence of the probe laser, has been attributed to a previously identified[58,59] NO A-X fluorescent signal. It is the result of secondary absorption by nascent NO (v=6) in its ground electronic state, formed by photolysis of NO_2 at 248nm, on the

accidentally resonant NO A-X (3,6) band. Unfortunately, the emission from the NO $A^2\Sigma^+$ v=3 has quite a broad Franck-Condon envelope extending throughout the region containing the conveniently detectable OH A-X bands.

Figure 4.5 shows the waveform of the background fluorescent signal obtained when only the photolysis laser (KrF excimer) laser is allowed into the reaction chamber. The main problem with the photolysis-induced signal is that it occurs at the time at which the photolysis laser fires. We require nascent product and must therefore collect spectra at short photolysis-probe laser time delays. Hence the photolysis-induced emission interferes greatly with the signal to noise ratio and most of the spectra recorded show the signal sitting on a background, which must be subtracted out before analysis.

The second problematic interference in the recorded OH LIF spectra was the presence of a background OH signal when both lasers are operated. Figure 4.6 shows the waveform obtained with both the photolysis and probe lasers firing (with a time delay of 1000ns), and with NO_2 and isobutane in the reaction chamber. Here the earliest LIF signal is the fluorescent emission resulting from excited NO, and the later one is the OH A-X $Q_1(1)$ line. An OH signal was continually observed at all photolysis-probe laser time delays, indicating that parallel mechanisms are responsible for producing OH; not all the OH observed in the spectra recorded following 248nm photolysis is the nascent product resulting from the bimolecular reaction. This problem was encountered previously, at 337nm and 308nm, but unfortunately the relative yield of prompt OH from photolysis of the unknown impurity is considerably higher at 248nm than at the two longer wavelengths. We tentatively assign the background signal as being the result of photolysis of HONO (a suspected impurity in NO_2 gas) at 248nm, yielding rotationally excited OH, observed in the spectra at all time delays. In Figure 4.6 the OH signal comprises of two components: nascent OH resulting from the

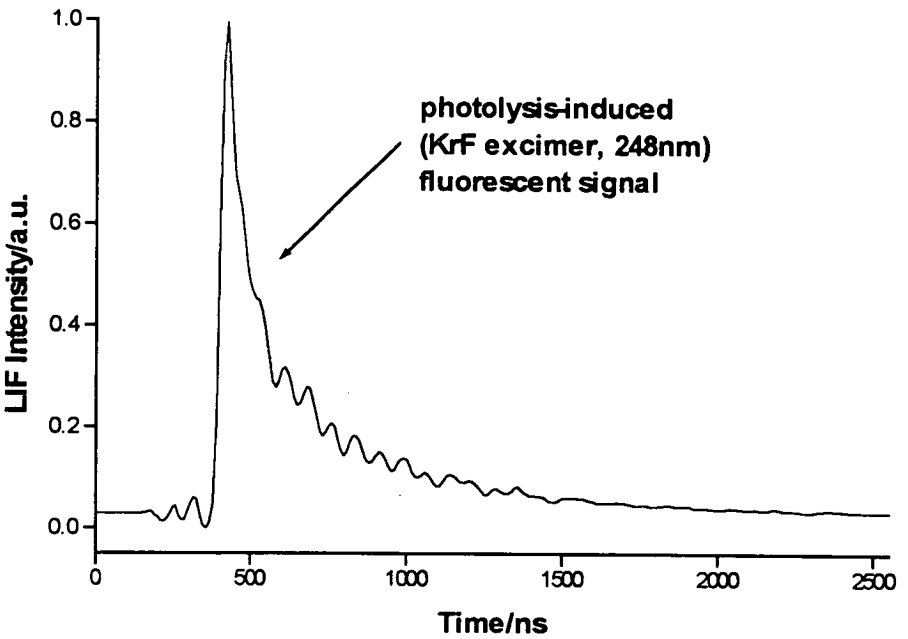

Figure 4.5: Background fluorescent signal obtained when the photolysis laser (KrF excimer, 248nm) **only** passes through a mixture of NO_2 and isobutane in the reaction chamber. This signal occurs promptly as the photolysis laser fires and is thought to be due to fluorescent emission from excited NO. 64 shots were averaged for this waveform. The "ringing" on the signal is an artefact due to electrical noise from the firing of the excimer laser.

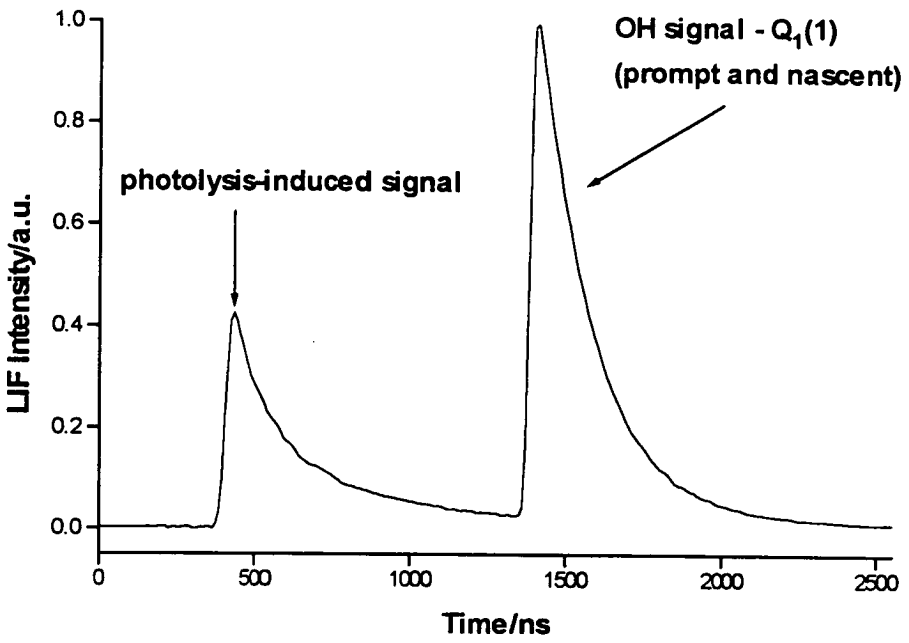

Figure 4.6: The waveform obtained when the OH(v'=0) product of the $O(^3P)$/isobutane reaction is probed via exciting fluorescence on the A-X (1-0) band. The NO_2 was photolysed at 248nm and the time delay between the photolysis and probe laser firing was 1000ns. 64 shots were averaged for this waveform. The first LIF signal has been attributed to decay from an excited NO state and the second signal is the OH signal.

$O(^3P)$/isobutane reactions and prompt OH from the photolysis of an impurity in the gas mixture.

The most direct approach to eliminating the background OH signal would be to remove the source. We tried passing the NO_2 gas through KOH pellets to remove any acidic impurities (i.e. HONO) but unfortunately this had no effect on the prompt signal. Unsuccessful attempts were also made to remove impurities by selective trapping at various temperatures.

A roundabout, yet more effective way of removing the unwanted OH signal is to subtract it out. The prompt OH signal remains essentially constant in intensity over a reasonable range of photolysis-probe laser time delays, whereas the nascent signal grew in, on top of the prompt OH, as Δt increased. This is illustrated in Figures 4.7(a) and 4.7(b). The OH signal resulting from photolysis of an impurity yields rotationally excited OH whereas the OH from the $O(^3P)$+HR reaction yields rotationally cold OH[11,52]. Hence a low N′ line should be composed of prompt and nascent OH while a high N′ line should only be due to prompt OH. In Figure 4.7(a) the laser has been set at the wavelength of the $R_2(10)$ line (a high N′ line composed of prompt OH only) and the waveform has been recorded at different photolysis-probe laser pulse time delays. The area under each LIF decay has been measured and it is apparent that the signal is relatively constant. In Figure 4.7(b) the laser has been moved to the wavelength of the $Q_1(1)$ line (a low N′ line composed of both prompt and nascent OH) and again the waveform has been recorded at different Δt's. This time the area under each LIF decay increases with Δt. This is because the nascent signal grows in with time. In both 4.7(a) and 4.7(b) there are actually two waveforms at each Δt. The early signal is the photolysis-induced background and the later is the OH signal. At early time delays it is impossible to separate the two signals and the area under both was always measured. Fortunately though, the photolysis-induced signal is invariant with Δt.

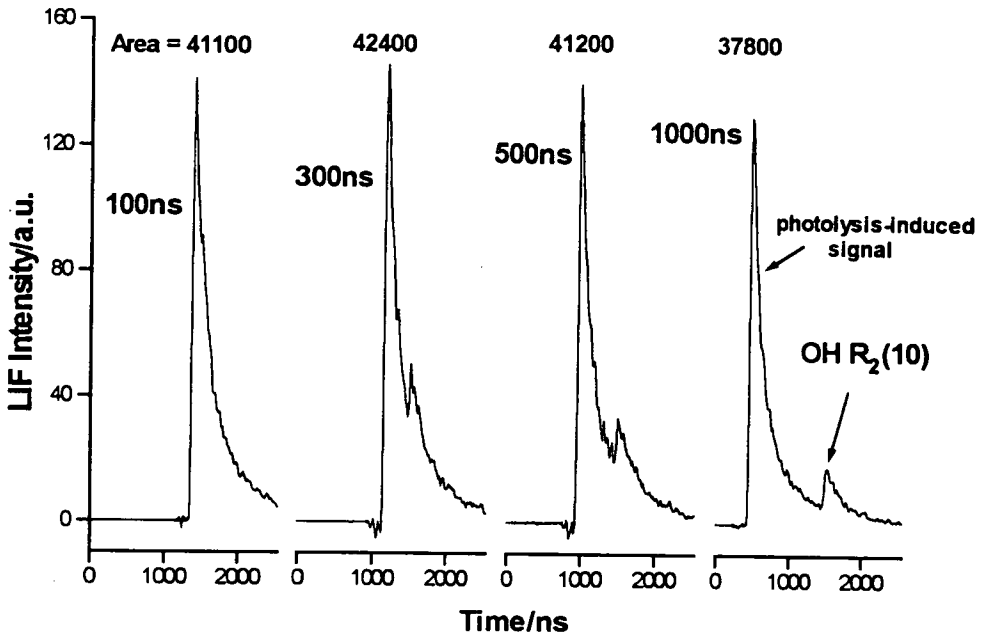

Figure 4.7(a): This figure shows how the area under the $R_2(10)$ line, of the OH A-X (1-0) band, is affected by changing the photolysis-probe laser pulse time delay, Δt. The $R_2(10)$ line is assumed to result only from prompt OH, arising from the photolysis of impurities at 248nm. The area remains roughly constant with Δt. At each Δt two LIF decay signals are recorded. The earlier is photolysis-induced and the later is the probe-induced OH signal. However the area under both signals has been measured because the photolysis-induced signal is invariant with Δt. These waveforms were obtained with NO_2 and isobutane in reaction chamber.

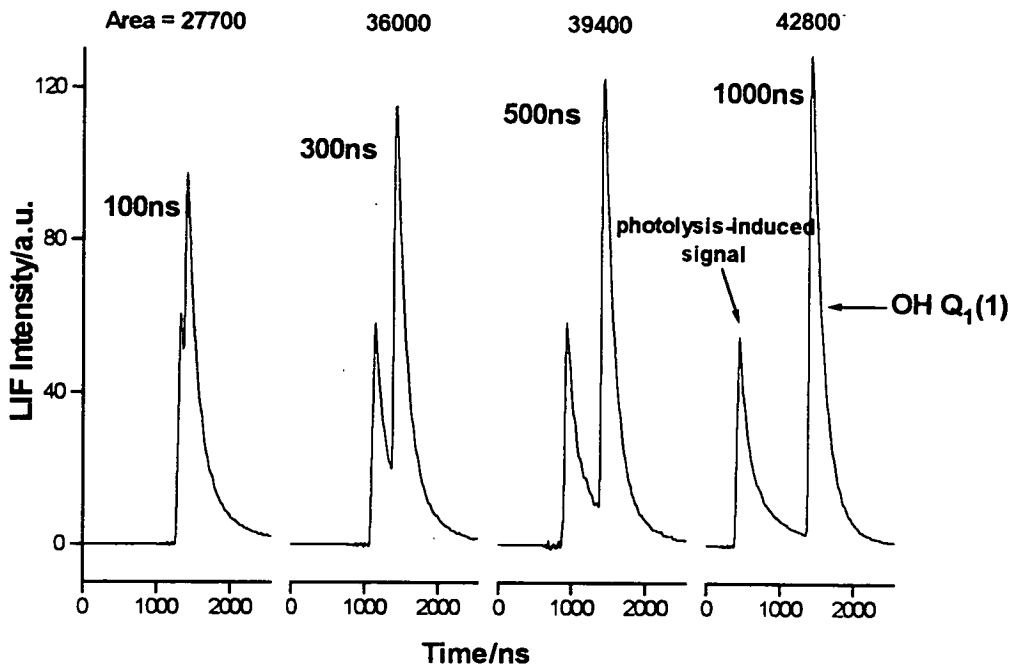

Figure 4.7(b): This figure shows how the area under the $Q_1(1)$ line, of the OH A-X (1-0) band, is affected by changing the photolysis-probe laser pulse time delay, Δt. The $Q_1(1)$ line is composed of prompt and nascent OH. The area increases with Δt indicating that the nascent OH signal grows in with Δt. At each Δt two LIF decay signals are recorded. The earlier is photolysis-induced and the later is the probe-induced OH signal. However the area under both signals has been measured because the photolysis-induced signal is invariant with Δt. These waveforms were obtained with NO_2 (photolysed at 248nm) and isobutane in reaction chamber.

Hence, knowing that the prompt signal remains constant with time allows it to be subtracted in the following way. If two spectra are simultaneously recorded at different Δt's (though still within a collisionally unmodified range) and one is subtracted from the other, then the resultant spectrum should contain only the OH product from the bimolecular reaction: the constant prompt OH background will have been removed and all that will remain is the nascent OH that has been formed in the time difference of the two spectra chosen to be subtracted.

The photolysis-induced background could also be removed by a, in this case simpler, subtraction procedure. Since this component occurs as the photolysis laser fires and signal must be collected at short Δt's, the resultant OH lines sit on top of the background, which is simply subtracted off before any further spectral manipulations are carried out.

An example of the combined subtraction procedure is illustrated in Figure 4.8:

1. Two spectra are simultaneously recorded at different photolysis-probe laser pulse time delays. In this instance, Δt's of 100 and 300ns were chosen. These spectra are shown in Figures 4.8(a) and 4.8(b).
2. The photolysis-induced background, that the OH signal sits on, is subtracted off. The resultant spectra are shown in Figures 4.8(c) and 4.8(d).
3. The scan obtained with a Δt of 100ns (4.8(c)) is then subtracted from the scan obtained with a Δt of 300ns (4.8(d)). The resultant subtraction spectrum is shown in Figure 4.8(e).

In Figures 4.8(a)-(e) the $R_1(1)$, $Q_1(1)$, $P_1(1)$, $R_1(10)$ and $R_2(10)$ lines are marked on the spectra. It is clearly evident that the $R_1(10)$ and $R_2(10)$ lines, which are assumed to arise solely from photolysis of impurities within the reactive system, subtract out: these high N′ lines are not seen in Figure

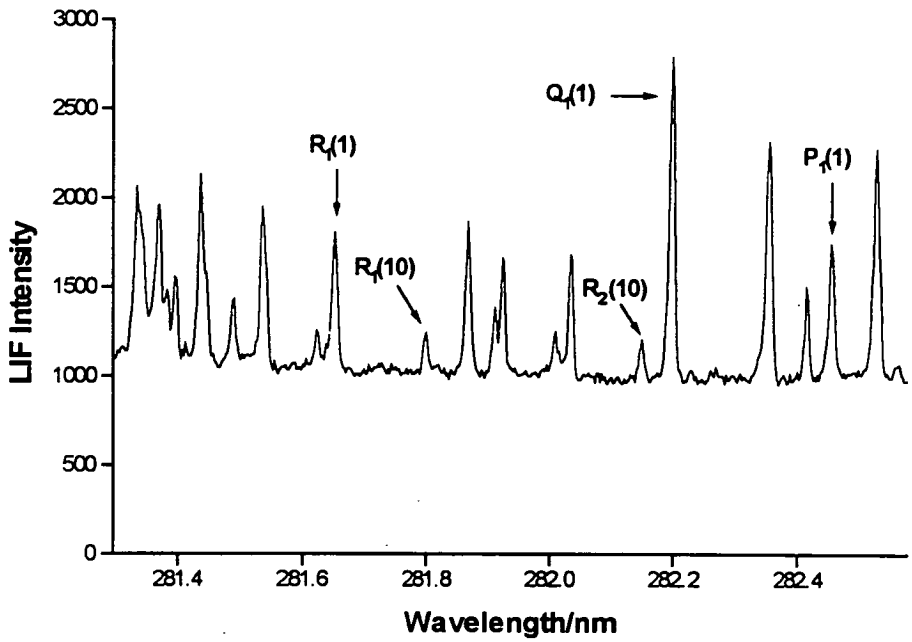

Figure 4.8(a): The OH(v'=0) product of the $O(^3P)$+isobutane reaction has been probed by LIF via the (1-0) band of the A-X transition. Some of the rotational lines, originating in levels N'[53] of the $X^2\Pi$ ground state, have been assigned[54]. This figure shows the raw, unsubtracted data. The OH signal is sitting on a photolysis-induced background and is composed of both prompt and nascent contributions.

Δt=100ns and $\lambda_{photolysis}$ = 248nm

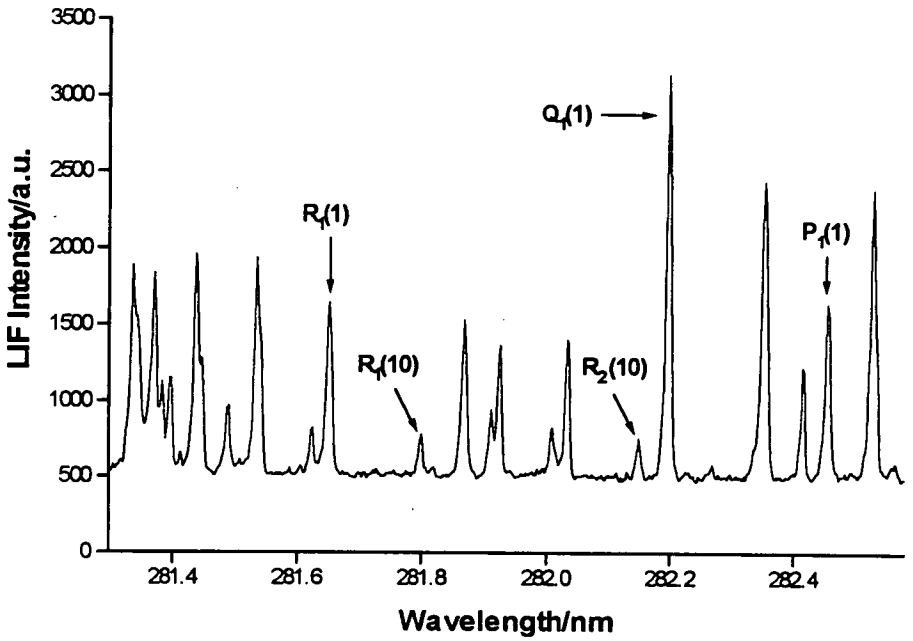

Figure 4.8(b): The OH(v'=0) product of the $O(^3P)$+isobutane reaction has been probed by LIF via the (1-0) band of the A-X transition. This figure shows the raw, unsubtracted data. The OH signal is sitting on a photolysis-induced background and is composed of both prompt and nascent contributions. In this scan the background is less than that observed in Figure 4.8(a) because here Δt=300ns and thus the distance between the two LIF decays is greater.

$\lambda_{photolysis}$ = 248nm

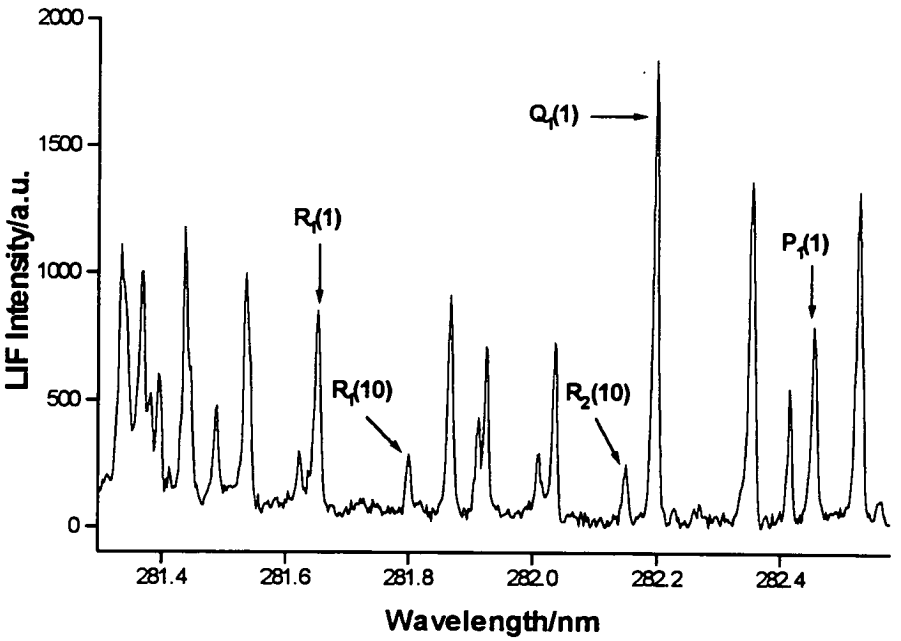

Figure 4.8(c): The OH(v'=0) product of the $O(^3P)$+isobutane reaction has been probed by LIF via the (1-0) band of the A-X transition. The photolysis-induced background has been subtracted from the scan shown in Figure 4.8(a) to obtain this spectrum. The resultant OH signal is composed of both prompt and nascent contributions. The presence of prompt OH is manifested in high N' lines in the spectrum.

Δt=100ns and $\lambda_{photolysis}$ = 248nm

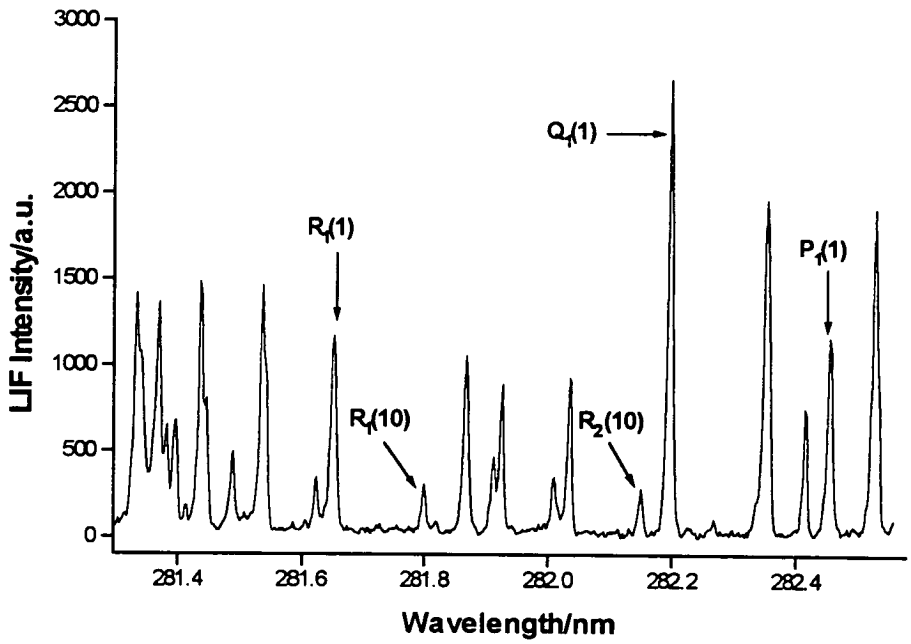

Figure 4.8(d): The OH(v'=0) product of the $O(^3P)$+isobutane reaction has been probed by LIF via the (1-0) band of the A-X transition. The photolysis-induced background has been subtracted from the scan shown in Figure 4.8(b) to obtain this spectrum. The resultant OH signal is composed of both prompt and nascent contributions. The presence of prompt OH is manifested in high N' lines in the spectrum.

Δt=300ns and $\lambda_{photolysis}$ = 248nm

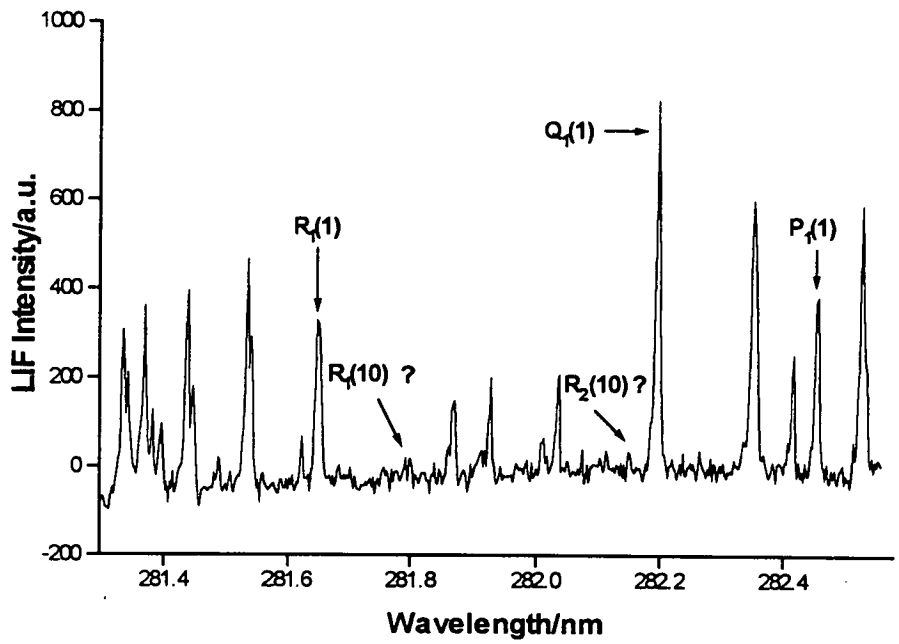

Figure 4.8(e): The OH(v'=0) product of the $O(^3P)$+isobutane reaction has been probed by LIF via the (1-0) band of the A-X transition. $O(^3P)$ was generated by 248nm photolysis of NO_2. This spectrum was obtained by subtracting Figure 4.8(c) from Figure 4.8(d): i.e. Δt=300ns spectrum – Δt=100ns spectrum. The resultant spectrum now ought to be composed of nascent OH signal only. This is exemplified by the near complete removal of high N' lines, such as $R_1(10)$ and $R_2(10)$, which are assumed to associated with the prompt OH signal. These lines were clearly evident in the unsubtracted scans (Figures 4.8(a)-(d)).

4.8(e). In contrast, the $R_1(1)$ line, a low N' line composed of contributions from both prompt and nascent OH, decreases in intensity but is still significant. This is consistent with the prompt contribution being removed upon subtraction.

The experimental strategy in the 248nm experiments was specially modified to help limit and remove these background interferences at short Δt. Sequences of OH LIF excitation spectra were recorded from Δt=100 to 500ns, generally in increments of 100ns. In addition a scan was taken at a much longer delay (typically Δt=100μs). All these spectra were recorded in parallel by looping through the time delays at each probe laser wavelength on a shotwise basis. This technique ensured that any long term drifts in the experimental conditions (e.g. changes in gas pressure, changes in the laser power, wavelength dependent differences in the transmission through interference filter and PMT response) affect each spectrum equally. It was established that spectra recorded with Δt's between 10 and 100μs are statistically invariant, hence we concluded that the spectrum obtained at a long time delay represented a fully thermalised OH rotational distribution. An example of such a scan is shown in Figure 4.9, which was obtained following the reaction between $O(^3P)$+isobutane with Δt set at 100μs. The signal to noise at large Δt was very good because a substantial yield of OH had accumulated and the NO A-X interference was absent.

The next step was to convert the raw spectra obtained into a format that could be easily analysed, thus allowing the OH rotational populations to be extracted. The combined populations evolved slightly due to rotational relaxation in the timescale of detection. Firstly the photolysis-induced background was removed from each time delay spectrum. Then it was concluded that the best approach would be to subtract the integrated OH LIF signal at Δt=100ns from each of the signals at later times. In this way contributions to the OH signal, from anything other than the bimolecular

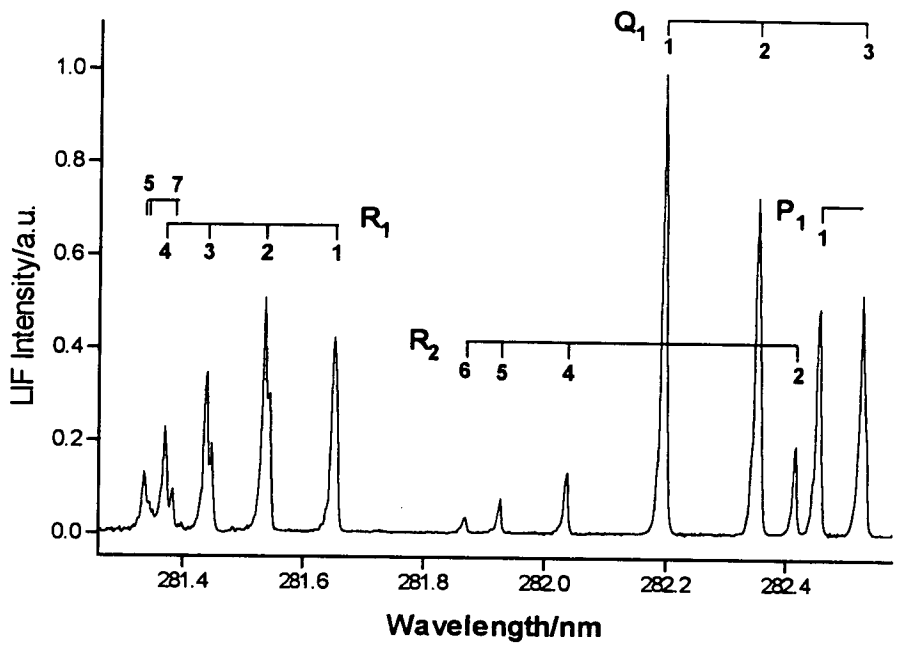

Figure 4.9: The OH(v'=0) product following reaction between $O(^3P)$ and isobutane. The photolysis wavelength was 248nm. Fluorescence was excited on the A-X (1-0) band and detected on the (1-1) band. This scan was obtained by setting the time delay between the photolysis and probe laser pulses to 100μs, thus obtaining a thermalised rotational distribution. The total gas pressure was 250mTorr. The photolysis and probe laser powers were ~120mJ/pulse and ~300μJ/pulse respectively. The rotational lines, originating in levels N'[53] of the $X^2\Pi$ ground state, have been assigned[54].

reaction, are effectively removed in one step. In theory it might have been better to subtract a $\Delta t \sim 0$ spectrum from the others but the photolysis-induced background was greatest at this minimal Δt, and the signal to noise was extremely bad in such subtractions.

As mentioned previously OH v'=0 was probed via excitation on the A-X (1-0) and (0-0) bands. Attempts were also made to examine the OH v'=1 product but the signal to noise in the region of the (1-1) band was extremely poor. While v'=0 could be distinguished from the background interferences, the v'=1 signal was not strong enough to be clearly seen. However this was not regarded as too much of a set back since the characteristics of the vibrational partitioning had been clearly established in previous work[11,52]. In this work we endeavored to obtain rotational and fine-structure populations within the v'=0 vibrational level.

Figures 4.10 - 4.13 are the OH LIF (v'=0) excitation spectra obtained for the reactions of $O(^3P)$ with isobutane, cyclohexane, ethane and methane respectively. Fluorescence was excited on the (1-0) band and observed on the (1-1) band. In these figures the product recorded with a Δt of 100ns (Δt=300ns for Figure 4.13) has been subtracted from the Δt=300ns (Δt=500ns for Figure 4.13) scan, so that what is seen is the OH product formed in a 200ns period starting 100ns after the photolysis laser.

Figures 4.14 - 4.17 are also OH LIF (v'=0) excitation spectra obtained from reaction of $O(^3P)$ with isobutane, cyclohexane, ethane and methane respectively, but in these scans fluorescence was both excited and detected on the (0-0) band. In these figures the product recorded with a Δt of 100ns (Δt=300ns for Figure 4.17) has been subtracted from the Δt=300ns (Δt=500ns for Figure 4.17) scan. For comparison Figure 4.18 is representative of a thermal rotational distribution, recorded with a Δt of

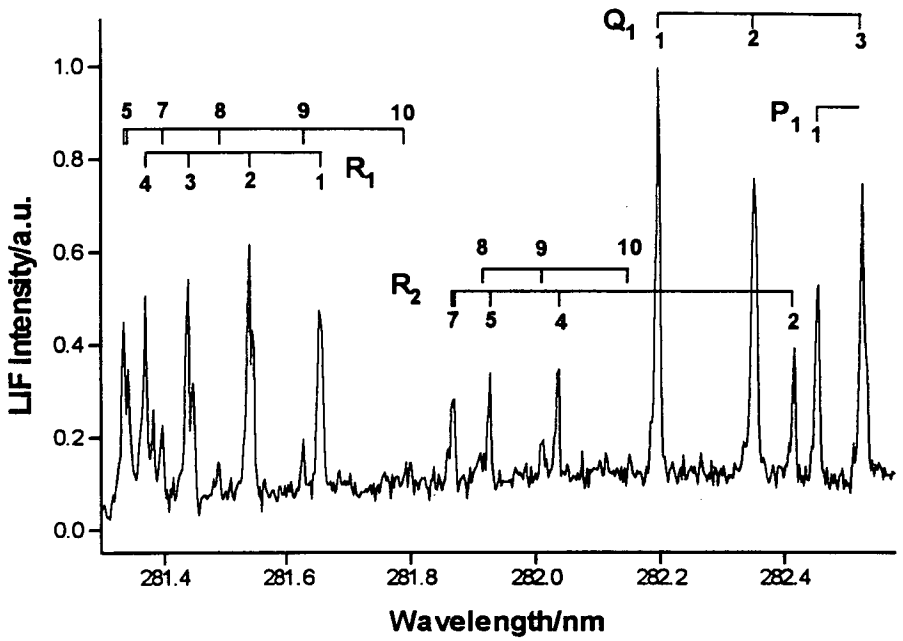

Figure 4.10: The OH(v'=0) product following reaction between $O(^3P)$ and isobutane. The photolysis wavelength was 248nm. Fluorescence was excited on the A-X (1-0) band and detected on the (1-1) band. This figure was obtained by subtracting the spectrum obtained with Δt=100ns from the spectrum with Δt=300ns. The total gas pressure was 250mTorr. The photolysis and probe laser powers were ~120mJ/pulse and ~300μJ/pulse respectively. The rotational lines, originating in levels N'[53] of the $X^2\Pi$ ground state, have been assigned[54].

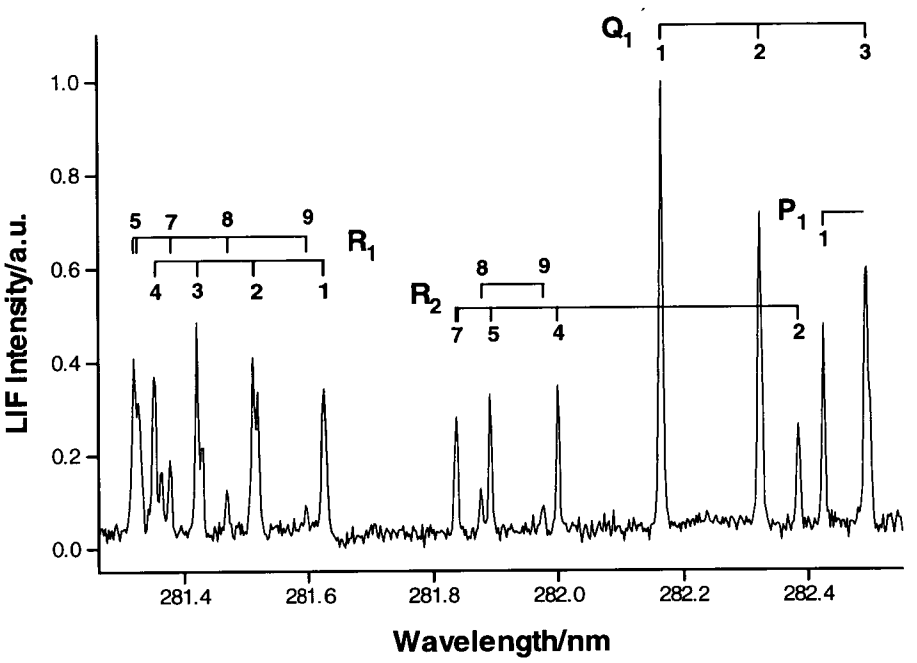

Figure 4.11: The OH(v'=0) product following reaction between $O(^3P)$ and cyclohexane. The experimental conditions and subtraction procedures were the same as for Figure 4.10.

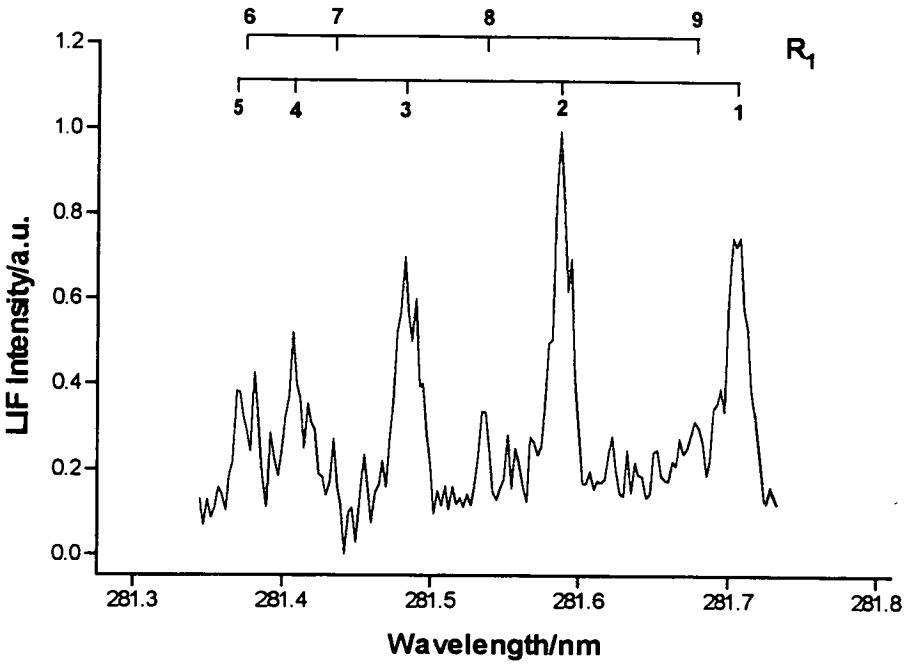

Figure 4.13: The OH(v'=0) product following reaction between $O(^3P)$ and methane. The experimental conditions were the same as for Figure 4.10. This figure was obtained by subtracting the spectrum obtained with Δt=300ns from the spectrum with Δt=500ns.

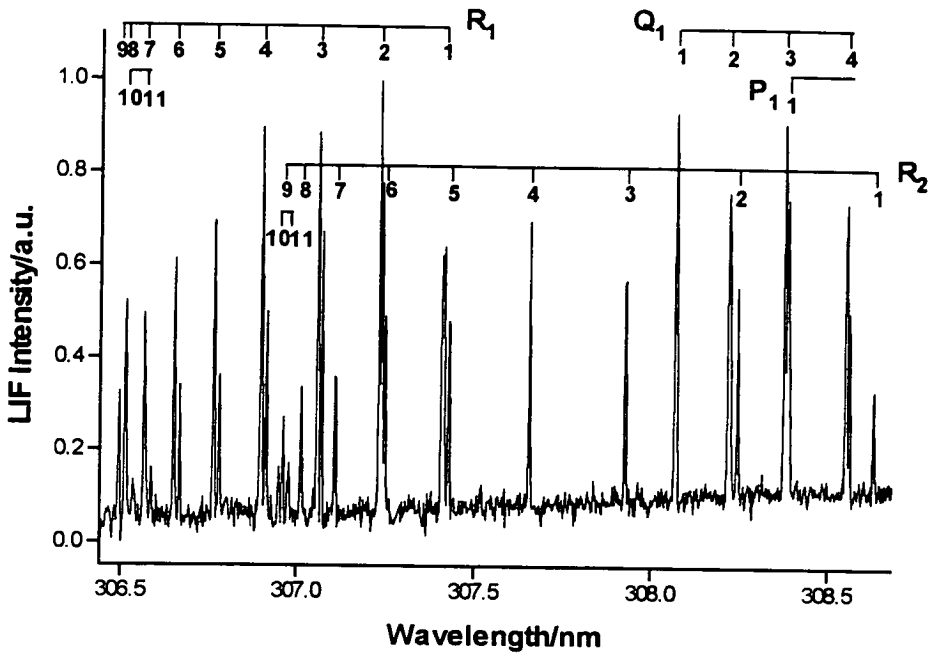

Figure 4.14: The OH(v'=0) product following reaction between $O(^3P)$ and isobutane. The photolysis wavelength was 248nm. Fluorescence was excited and detected on the A-X (0-0) band. This figure was obtained by subtracting the spectrum obtained with Δt=100ns from the spectrum with Δt=300ns. The total gas pressure was 250mTorr. The photolysis and probe laser powers were ~60mJ/pulse and <100μJ/pulse respectively. The rotational lines, originating in levels N'[53] of the $X^2\Pi$ ground state, have been assigned[54].

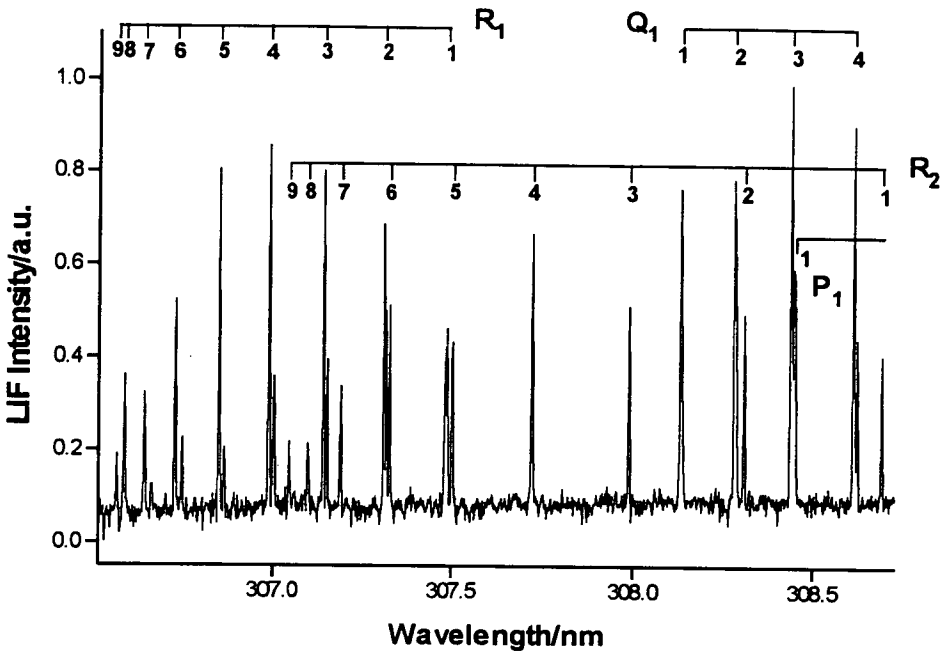

Figure 4.15: The OH(v'=0) product following reaction between $O(^3P)$ and cyclohexane. The experimental conditions and subtraction procedures were the same as for Figure 4.14.

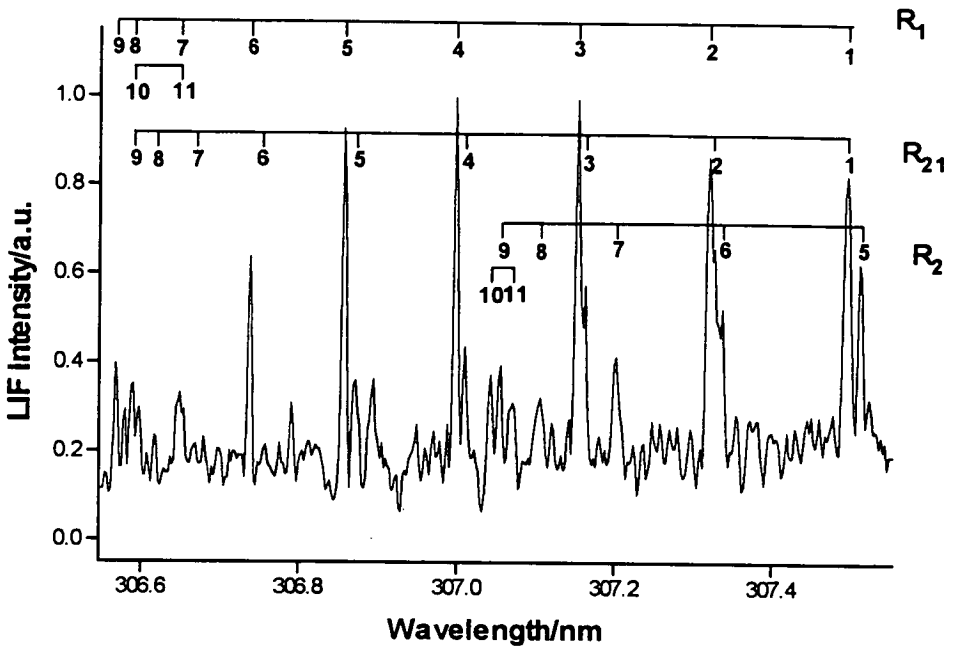

Figure 4.16: The OH(v'=0) product following reaction between $O(^3P)$ and ethane. The experimental conditions and subtraction procedures were the same as for Figure 4.14.

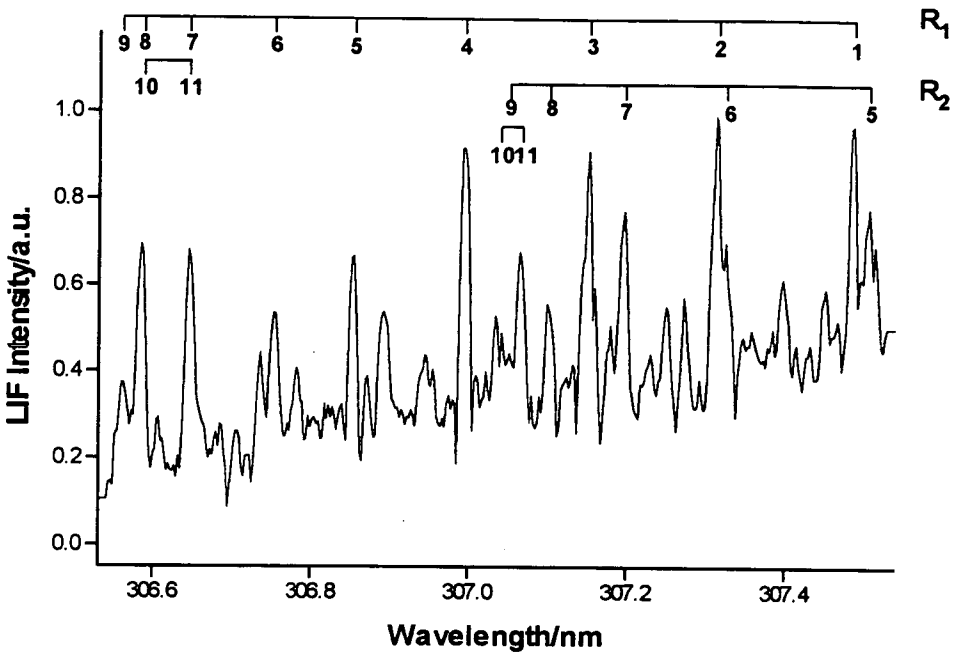

Figure 4.17: The OH(v'=0) product following reaction between $O(^3P)$ and methane. The experimental conditions were the same as for Figure 4.14. This figure was obtained by subtracting the spectrum obtained with Δt=300ns from the spectrum with Δt=500ns.

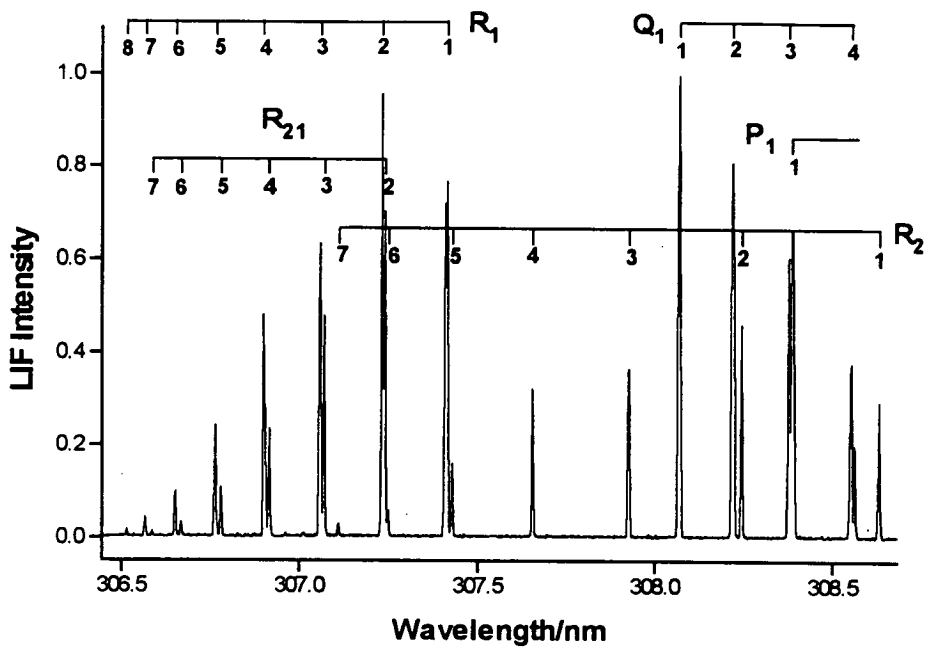

Figure 4.18: The OH(v'=0) product following reaction between $O(^3P)$ and isobutane. The photolysis wavelength was 248nm. Fluorescence was excited and detected on the A-X (0-0) band. This scan was obtained by setting the time delay between the photolysis and probe laser pulses to 100μs, thus obtaining a thermalised rotational distribution. The total gas pressure was 250mTorr. The photolysis and probe laser powers were ~60mJ/pulse and <100μJ/pulse respectively. The rotational lines, originating in levels N'[53] of the $X^2\Pi$ ground state, have been assigned[54].

100μs following the reaction between $O(^3P)$ and isobutane. In all spectra the rotational lines, originating in levels N'[53] of the $X^2\Pi$ ground state, have been assigned using the data collected by Dieke and Crosswhite[54]..

The spectra shown in Figures 4.13 and 4.17 are of particular interest as, in the scans, the OH product following reaction between $O(^3P)$ and methane has been detected. This is the first time that nascent product has been detected from this reaction. Obviously the signal to noise in these spectra is not very good and for aesthetic reasons Δt=500ns - Δt=300ns subtractions are shown. It is still clearly evident, though, that some degree of nascent product is present.

4.4.3 Rotational Analysis of the 248nm Spectra

An analytical procedure was devised which eliminated the need to correct spectra for variable parameters, such as gas pressure, laser power, transmission through interference filter and PMT response. Experimentally, sequences of scans with different Δt's were recorded simultaneously in such a way that any long term drifts in the experimental conditions affected each spectrum equally. Typically, spectra with Δt=100ns, 200ns, 300ns, 400ns, 500ns and 100μs were recorded. This procedure was as follows:

1. The area under the rotational lines was measured for each time delay spectrum. For the thermalised spectrum this quantity was $S_j(t=thermal)$.
2. Next the subtraction procedure was carried out for each rotational line. The integrated OH LIF signal at Δt=100ns was subtracted from each of the signals at later time delays, excluding Δt=100μs. This quantity was labelled $S_j(r=reactive)$.
3. The ratio of the reactive signal, $S_j(r)$, for each line at each difference in time delays to the equivalent signals in the thermalised spectrum was then calculated: $S_j(r) / S_j(t)$. In this way the signal intensities are corrected

for variables within the scan period. This type of calibration is successful in this case because, as with a Boltzmann population plot, most of the nascent OH population is in low rotational levels. Only for the highest levels (N′=8-10) were the Δt=100μs signals too weak for ratios to be reliably estimated. In these cases we smoothly extrapolated the relatively invariant effective detectivity for the last few members of the spectroscopic branch. Figure 4.19 shows the Boltzmann distribution at 298K for the R_1 lines of OH. The Boltzmann population, $P_j(t)$, is calculated using the expression, $P_j(t) = (2J+1)e^{-Ej/kT}$. For the R_1 branch lines, J=N+1/2.

4. The reactive population, $P_j(r)$ can then be calculated using the expression $P_j(r) = S_j(r)/S_j(t) \times P_j(t)$. The sums of these values over all contributing levels were then normalised to unity.
5. The normalised rotational distributions were plotted as a function of the incremental delay, as shown in Figure 4.20 for the OH(v′=0) product of the $O(^3P)$+isobutane reaction. Each point on the x-axis corresponds to a Δt-100ns increment. The desired nascent OH distribution was obtained by linear extrapolation to Δt~100ns (i.e. extrapolation to x=0) from the points at longer delays. Hence we have defined the nascent product as the OH formed in the vanishingly short increment beginning 100ns after the photolysis laser pulse. In this way the effects of secondary collisional rotational relaxation are, to a reasonable approximation, removed. As can be seen from Figure 4.20 the corrections, which were fairly small fractions of the evaluated populations at later times, were upward adjustments for the highest N′ levels and downward for the lowest levels. The lines with intermediate values of N′ remained roughly the same. This is consistent with slight rotational relaxation. The contrast with a thermalised, Boltzmann distribution at ambient temperature (298K) is also illustrated in Figure 4.20.
6. Similar extrapolation procedures were carried out for all the HR reactants and nascent rotational populations obtained. Figure 4.21 shows the OH

$^2\Pi_{3/2}$ (v'=0) rotational distributions (i.e. the populations extrapolated to Δt=100ns) resulting from the reactions of $O(^3P)$ with isobutane, cyclohexane, ethane and methane.

4.5 Results - Fine-Structure Distributions

4.5.1 Λ-Doublets

As discussed in Chapter 3 Section 3.1.1, each of the ground state rotational levels in OH is split into two Λ-doublet components. These Π(A') and Π(A") states can be probed by lines in the P/R and Q branches, respectively[60,61], of the OH $A^2\Sigma^+ \leftarrow X^2\Pi$ transition. In preliminary checks[52], the plane of linear polarisation of the probe laser was varied, establishing that there was no significant laboratory-frame alignment of the OH ground state. Relative populations of rotational lines arising from the same spin doublet, but different Λ-doublets were then compared. This was done by, for example, comparing a Q_1 line and a P_1 line. These measurements were taken at very low probe laser powers to avoid differential optical saturation. We did not find any statistically significant deviations from a Π(A') / Π(A") ratio of unity for any of the reactants at any of the photolysis wavelengths. This analysis is discussed more fully in ref. [52] for photolysis at 337 and 308nm.

4.5.2 Spin-Orbit States

Spin-orbit interactions in OH cause the lower rotational levels of the $X^2\Pi$ ground state to divide into $^2\Pi_{3/2}$ and $^2\Pi_{1/2}$ manifolds, each of which is associated with sets of branches in the $A^2\Sigma^+ \leftarrow X^2\Pi$ spectrum, as explained in detail in Chapter 3 Section 3.1.1. Previous studies on the $O(^3P)$+HR system[11,19] observed a preference for the $OH(^2\Pi_{3/2})$ state to be populated. Spin-orbit state ratios for isobutane were measured at 337nm and 308nm[52],

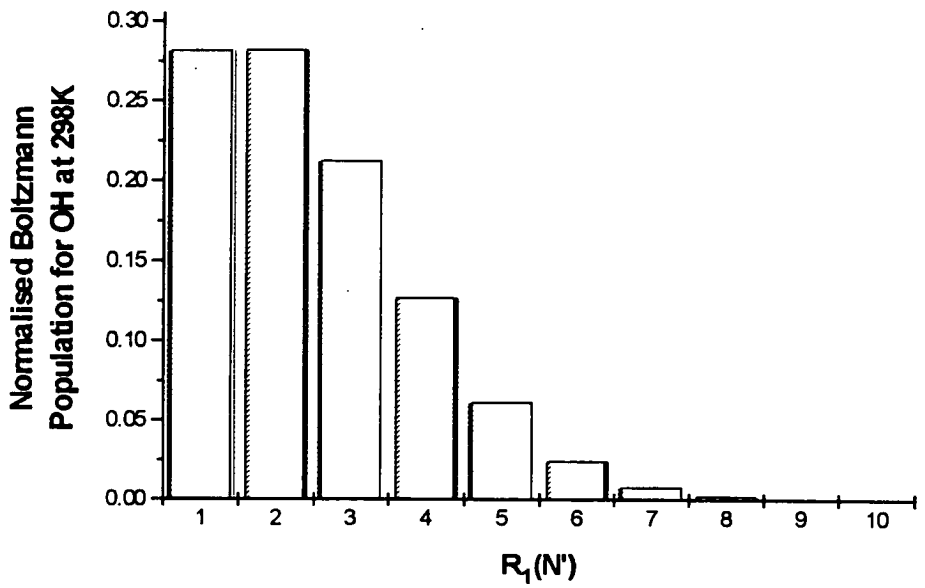

Figure 4.19: The Boltzmann distribution at 298K for the lower levels of the R_1 lines of OH. The Boltzmann population, $P_j(t)$, is calculated using the expression, $P_j(t) = (2J+1)e^{-Ej/kT}$. For the R_1 branch lines, J=N+1/2. E_j is the rotational energy, measured in Joules.

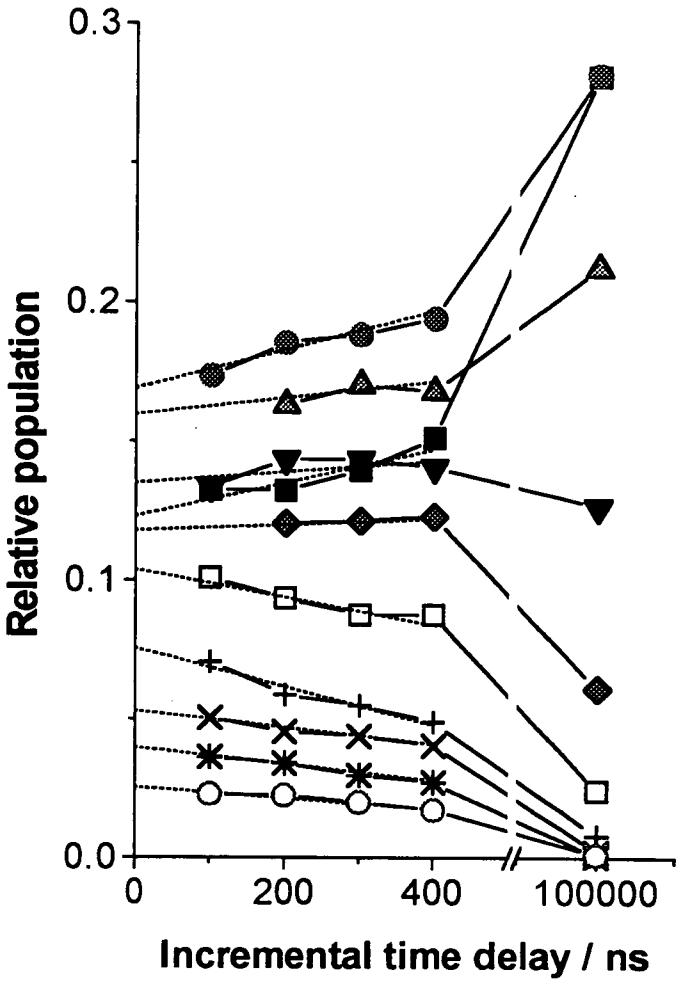

Figure 4.20: Extrapolation of the normalised rotational distributions in the OH $^2\Pi_{3/2}$ (v′=0) product of the O(^{3}P)/isobutane reaction, initiated by 248nm photolysis. The x-axis point were derived by subtracting signals taken at Δt=100ns from those taken at longer delays. Points at 100μs represent a thermalised distribution. The total reactant pressure was 250mTorr.

Rotational levels:

(■) - N′=1 (●) - N′=2 (▲) - N′=3 (▼) - N′=4 (◆) - N′=5

(□) - N′=6 (+) - N′=7 (x) - N′=8 (✳) - N′=9 (O) - N′=10

Extrapolation to Δt=100ns: .....

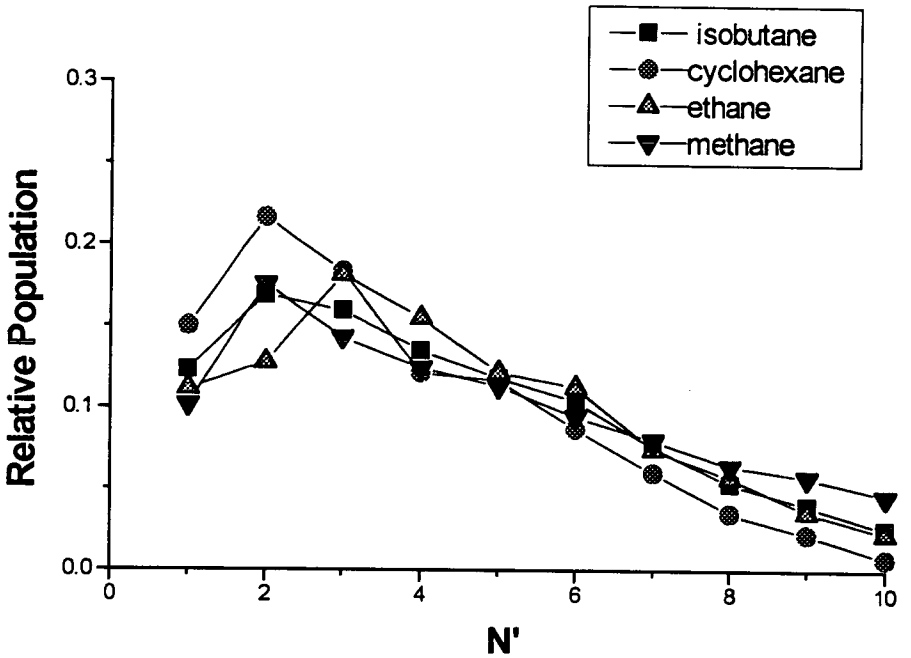

Figure 4.21: Normalised rotational distributions in OH $^2\Pi_{3/2}$ (v'=0) from the reactions of O(^{3}P) with isobutane, cyclohexane, ethane and methane, initiated by 248nm photolysis.

but the work at 248nm has been extended to include all the HR reactants and for all measurable values of N′.

Spin-orbit ratios were obtained by comparing lines associated with the same value of N′ but arising from different spin-orbit states. For example, lines within the R_1 branch originate from $^2\Pi_{3/2}$ and those within the R_2 branch from $^2\Pi_{1/2}$. Both these branches can be seen in Figure 4.10. The reactive population was obtained by:

1. Measuring the area under the rotational lines for each time delay spectrum. Lines originating in each spin doublet were analysed.
2. Subtracting the spectra recorded at shorter time delays from those taken at longer delays.
3. The ratio of the reactive signal, $S_j(r)$, in each subtraction to the equivalent signal in the thermalised spectrum was then calculated: $S_j(r) / S_j(t)$.
4. The reactive population, $P_j(r)$, was then deduced using the expression $P_j(r) = S_j(r)/S_j(t) \times P_j(t)$, where $P_j(t)$ is the Boltzmann population at 298K.

Relative populations were then obtained by evaluating the $P_j(r)^2\Pi_{3/2}$:$P_j(r)^2\Pi_{1/2}$ ratio. By comparing on an individual line basis in this way any propagation of uncertainties, related to the overall normalisation of population within each spin-orbit manifold, was eliminated.

Figure 4.22(a) shows the $^2\Pi_{3/2}$:$^2\Pi_{1/2}$ spin-orbit ratio plotted as a function of N′. This data was obtained by analysing the OH(v′=0) spectra resulting from the reactions between $O(^3P)$ and all HR reactants, initiated by 248nm photolysis. The $^2\Pi_{3/2}$:$^2\Pi_{1/2}$ ratio at each N′ was evaluated from as many sources as possible: for example, by comparing lines within the R_1 and R_2, P_1 and P_2 and Q_1 and Q_2 branches, obtained by excitation of fluorescence on both the (1-0) and (0-0) OH A-X bands.

Figure 3.2 in Chapter 3 shows that states with the same value of N′ have different values of J′, where J′=N′±1/2. The higher degeneracy of the $^2\Pi_{3/2}$

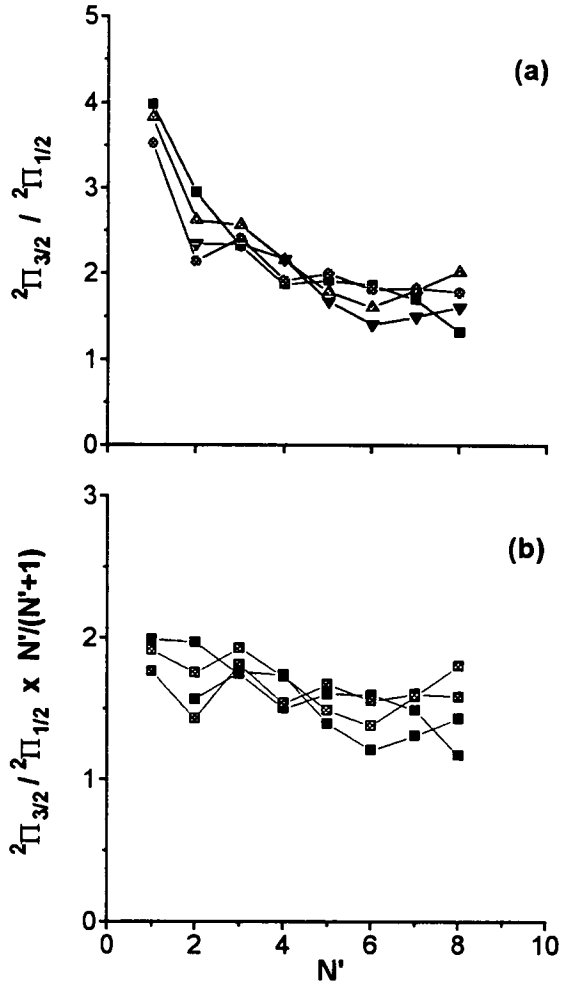

Figure 4.22: (a) The OH(v'=0) $^2\Pi_{3/2}$:$^2\Pi_{1/2}$ spin-orbit population ratios plotted as a function of N'. This data was obtained by analysing the spectra resulting from the reactions between O(^{3}P) and all HR reactants, initiated by 248nm photolysis.

(b) The degeneracy-corrected spin-orbit state ratios for all HR plotted against N'.

(■) - isobutane

(●) - cyclohexane

(▲) - ethane

(▼) - methane

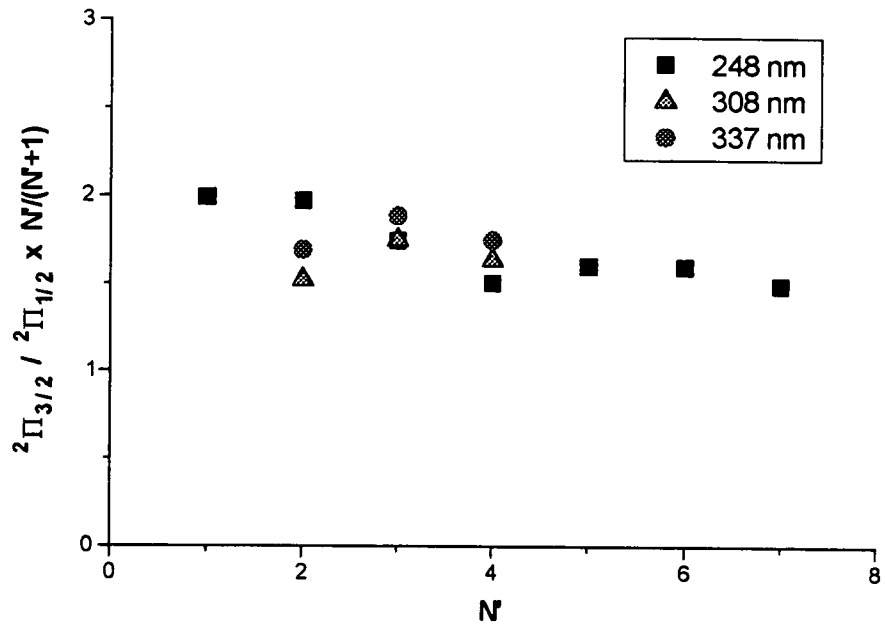

Figure 4.23: The degeneracy corrected OH(v'=0) $^2\Pi_{3/2}$:$^2\Pi_{1/2}$ ratios for the O(^{3}P)+isobutane reaction initiated by 337, 308 and 248nm photolysis. The 337 and 308nm data was collected and analysed as described in previous work[52].

level (which corresponds to J'=N'+1/2) can be compensated for by multiplying the observed $^2\Pi_{3/2}$:$^2\Pi_{1/2}$ ratio by N'/N'+1. Figure 4.22(b) shows the degeneracy-corrected spin-orbit state ratio for all HR plotted against N'.

Although most effort has been concentrated into obtaining spin-orbit state data for the 248nm experiments, ratios were also evaluated in the 337nm and 308nm experiments for the O(^{3}P)+isobutane reaction. The $^2\Pi_{3/2}$:$^2\Pi_{1/2}$ ratio was measured for a few values of N', yielding similar results to those obtained for 248nm[52]. Figure 4.23 shows the degeneracy corrected OH(v'=0) $^2\Pi_{3/2}$:$^2\Pi_{1/2}$ ratios, for selected values of N', at all three photolysis wavelengths. Figures 4.22 and 4.23 illustrate that there is an N'-dependent preference for the OH($^2\Pi_{3/2}$) state to be populated.

4.6 Discussion

4.6.1 Rotational Distributions

It is clearly obvious from examination of both the spectra and the subsequently obtained rotational distributions (Figure 4.3 for 337 and 308nm photolysis and Figure 4.21 for 248nm photolysis) that the OH $^2\Pi_{3/2}$ (v'=0) product is cold, and to the first approximation, irrespective of the precursor identity and collision energy. Comparable results were obtained by Andresen and Luntz[11] for more complex saturated hydrocarbons, and here we confirm that ethane and methane react in a similar fashion.

However closer examination of the results reveal subtle secondary differences in reactivity, superimposed on the general similarity. The rotational distributions in OH $^2\Pi_{3/2}$ (v'=0), first shown in Figure 4.3 for 337 and 308nm photolysis and Figure 4.21 for 248nm photolysis are represented

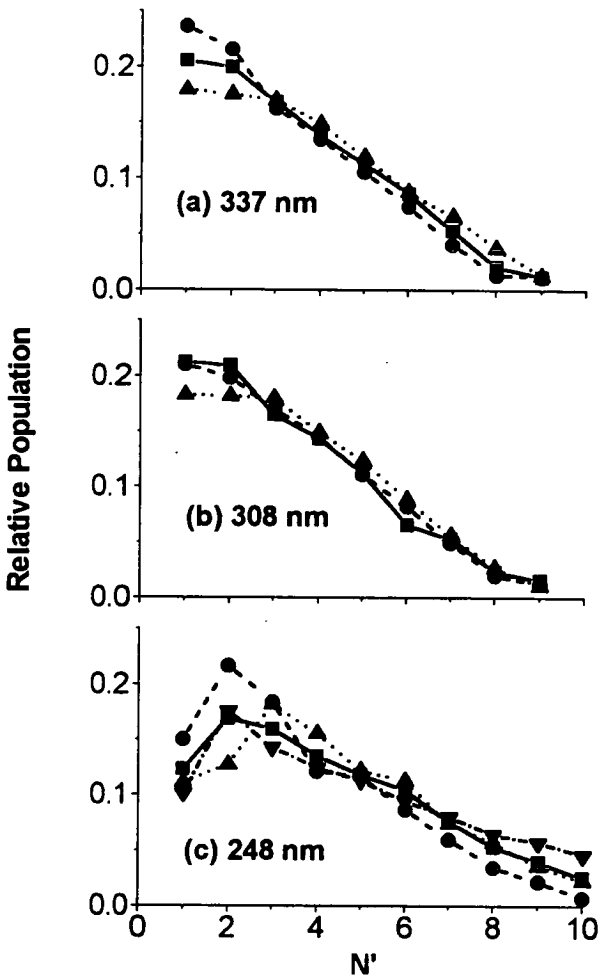

Figure 4.24: Rotational distributions in OH $^2\Pi_{3/2}$ (v'=0) from reaction of O(^{3}P) with HR initiated by NO_2 photolysis at (a) 337nm, (b) 308nm and (c) 248nm.

Hydrocarbon reactants:

(■) - isobutane

(●) - cyclohexane

(▲) - ethane

(▼) - methane

together in Figure 4.24 to facilitate comparison. We believe that there are two slight discernible variations in the distributions shown in Figure 4.24:

1. Independent of the reactant, the distribution becomes slightly hotter as the photolysis wavelength is increased. This difference is particularly noticeable for the large increase in collision energy to 248nm.
2. There are minor systematic differences in the product distributions from the hydrocarbons, most apparent at 248nm.

The best way to determine whether these proposed variations have any quantitative basis is to calculate the average energy in OH rotation, $<E_{rot}>$, for each distribution. This can be simply done by multiplying the nascent rotational population by the energy of each rotational line, and then summing over all the populated levels. These results are collected in Table 4.1. In agreement with proposal 1., the calculated $<E_{rot}>$'s for isobutane, cyclohexane and ethane are larger at 248nm than at the two longer wavelengths. Measurements were not taken for the $O(^3P)$+methane reaction at 337 and 308nm so a comparison cannot be made for this reactant. It is possible that some of this difference could be due to either the experimental strategy or method of analysis at 248nm, but these factors would be unlikely to produce $<E_{rot}>$'s greatly different from those measured at 337 or 308nm.

Generally speaking, all the HR reactants have been shown to produce similar OH rotational distributions, independent of the nature of R, but closer inspection of the distributions in Figure 4.24 and subsequently calculated $<E_{rot}>$'s in Table 4.1 reveal that there are minor differences for each reactant.

Following photolysis of NO_2 at both 337 and 308nm, the resultant OH from the $O(^3P)$+ethane reaction is marginally hotter than from the two other reactant molecules. The $<E_{rot}>$'s for isobutane and cyclohexane cannot be

HR	$\Delta H_0/cm^{-1}$ (a)	λ_{phot}/nm (b)	$<E_{rot}>/cm^{-1}$ (c)	$<E_{av}>/cm^{-1}$ (d)	$<f_{rot}>$ (e)
isobutane	-2200	337	330±30	5150	0.064
		308	330±25	6580	0.050
		248	500±50	10590	0.047
cyclohexane	-1600	337	300±30	4720	0.064
		308	330±20	6250	0.053
		248	390±50	10550	0.037
ethane	-630	337	360±40	3190	0.113
		308	350±25	4370	0.080
		248	510±70	7720	0.066
methane	+700	248	580±90	4890	0.118

(a) Enthalpy change for the reaction at 0K, calculated from the difference in OH and HR bond strengths[62,63]. It is assumed that the tertiary H-C bond is attacked in isobutane. The H-C bond energy in cyclohexane, not quoted explicitly in ref. [63], has been adjusted slightly from an earlier value[29] in line with minor revisions for other secondary H-C bonds.

(b) Wavelength used to initiate reaction by NO_2 photolysis.

(c) $<E_{rot}>$ is the measured average energy in rotation in the $^2\Pi_{3/2}$ spin-orbit manifold of OH(v'=0). The uncertainties quoted are approximate statistical estimates based on the reproducibility of the data.

(d) $<E_{av}>$ is the average total energy available to the products, calculated from Equation (4.2) under the assumptions described in the text.

(e) $<f_{rot}>$ is the ratio $<E_{rot}>$ / $<E_{av}>$. Systematic uncertainties in the estimates of $<E_{av}>$, discussed fully in the text, almost certainly exceed the statistical scatter in $<E_{rot}>$.

Table 4.1: Rotational energy disposal in the OH $^2\Pi_{3/2}$ (v'=0) product of O(^{3}P)+hydrocarbon reactions.

distinguished from one another as their error boundaries overlap. This observation is not dissimilar to the unquantified slight increase in the breadth of the distribution reported by Andresen and Luntz[11] on the sequential abstraction of tertiary, secondary and primary hydrogens.

At 248nm the differences in the rotational distributions from each reactant are more pronounced. The results in Table 4.1 show that $<E_{rot}>$ increases in the order cyclohexane < isobutane ≈ ethane < methane. The positioning of isobutane in this sequence is perhaps surprising but can be explained by re-examining an assumption made earlier. Isobutane is composed of nine primary and one tertiary hydrogen. At the longer photolysis wavelengths it has been assumed, from the isotopic labelling experiments carried out by Andresen and Luntz[11], that only the tertiary hydrogen is abstracted. However, primary abstraction becomes more feasible as the photolysis energy, and hence collision energy is increased. It is suspected that at 248nm the contribution from the primary C-H's become competitive with the single tertiary C-H.

To thoroughly quantify the $O(^3P)$+HR reaction it is instructive to correlate the variations in $<E_{rot}>$ with photolysis wavelength and nature of HR to the corresponding variation in the energy available for distribution amongst product modes, $<E_{av}>$. In our experiments the collision energy has been crudely altered by varying the photolysis wavelength of NO_2. This is not perhaps the best way to select unique $O(^3P)$+HR collision energies since the NO co-product of the photodissociation will be formed in a range of internal states. Hence it is not straightforward to accurately specify $<E_{av}>$ in these experiments. However, despite these problems, approximate values for $<E_{av}>$ were evaluated in the following way.

First, it is assumed that $O(^3P)$ atoms are formed in conjunction with internally cold NO fragments. This assumption may seem rather drastic, and sure to result in $<E_{av}>$ being overestimated, but the error in ignoring the energy partitioned to NO is considerably compensated for by the substantial thermal broadening of the collision energy distribution[64]. In hot atom dynamics experiments the thermal motions of the reagents leads to a spread in the relative collision energy: plots of the collision energy distribution for each $O(^3P)$+HR reaction at 248nm have been generated (using the expressions given in Appendix A of ref. [52]) and are shown in Figure 4.25. Collisions in the high energy tails will contribute with higher weighting to average properties of the products, because of the steep increase in the cross section with energy. This effect will be largest for the reactants with the highest threshold energies.

Applying this assumption, $<E_{av}>$ can be calculated using Equation (4.2). This expressions allows for all the reagents to be moving relative to one another.

$$\left\langle E_{av} \right\rangle = \frac{m_{NO} m_{HR}}{m_{NO_2} m_{OHR}} E_{exc} + \frac{m_O m_{tot}}{m_{NO_2} m_{OHR}} \frac{3}{2} kT - \Delta H_0 + \frac{3}{2} kT \qquad (4.2)$$

The first two terms in Equation (4.2) represent[64] the respective contributions to the average $O(^3P)$+hydrocarbon centre-of-mass collision energy from the excess energy in photolysis, E_{exc}[51], and from the thermal velocities of NO_2 and hydrocarbon. The mass of each reactant is represented with $m_{tot} = m_{NO_2} + m_{HR}$. ΔH_0 is the reaction enthalpy at 0K, calculated from bond strengths [62,63]. The final factor of 3/2 kT accounts for the average energy in hydrocarbon rotation.

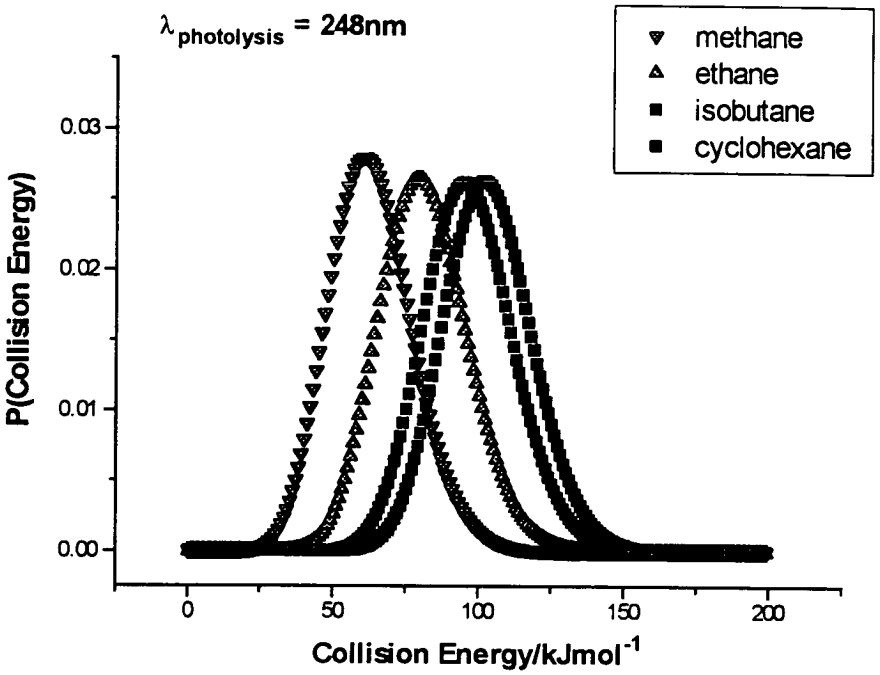

Figure 4.25: The thermal spread in the collision energy distributions for $O(^3P)$+HR reactions, following photolysis of NO_2 at 248nm. These plots were generated using the expressions given in Appendix A of ref. [52] with T=300K. Any additional spread due to the co-production of NO in a range of internal states is neglected.

E_{exc} is calculated using Equation (4.3). In this equation, E_{phot} is the energy available at the photolysis wavelength, D(ON-O) is the energy required to dissociate the ON-O bond and 3/2kT is the average rotational energy in NO_2.

$$E_{exc} = E_{phot} - D(ON - O) + 3/2kT \qquad (4.3)$$

The calculated $<E_{av}>$'s, at each photolysis wavelength and for each HR reactant, are given in Table 4.1. The energy available for distribution amongst product energy modes is naturally always greatest at 248nm and is highly dependent on the C-H bond dissociation energy. The value of $<E_{av}>$ is larger following the removal of tertiary and secondary hydrogens, as compared with primary abstraction.

The average fraction of the available energy appearing as OH rotation, $<f_{rot}> = <E_{rot}> / <E_{av}>$, is also listed in Table 4.1. These values are generally very low, with a maximum at about 10%, thus confirming the qualitative conclusion that only a small amount of the available reaction energy is being channeled into OH rotational modes. Similar results were obtained by Andresen and Luntz[11] and by Whitehead's group for the reaction with cyclohexane[19].

The method of calculation of $<f_{rot}>$ values tends to amplify the distinction between the reactivity of the different hydrocarbons at different photolysis wavelengths. For example, the measured average energy in rotation, $<E_{rot}>$, for isobutane at 248nm in not dissimilar to the value reported for ethane at the same photolysis wavelength, but the $<f_{rot}>$ values are significantly different. This is because there is much more available energy in the $O(^3P)$+isobutane reaction as compared with the $O(^3P)$+ethane system.

Likewise, at 248nm, the $<E_{av}>$ is greater for all HR, leading to lower $<f_{rot}>$ values. Consistently, for a given hydrocarbon, $<f_{rot}>$ drops as $<E_{av}>$ increases: this implies that although some of the extra energy available from higher collision energies is converted to OH rotation, it is less than the amount required to maintain a constant fractional share.

These conclusions should, though, be viewed cautiously because of the difficulty in accurately calculating $<E_{av}>$. However, the low rotational energy release in the OH product is consistent with the expected outcome for the "heavy+light-heavy" kinematic category to which this system belongs, which suggests that the excess translational energy in the reactants should be predominantly converted into translational energy of the products[21-23,65].

4.6.2 The Reaction Mechanism

Following their experimental study of the $O(^3P)$+HR system, Andresen and Luntz[11] proposed that the abstraction mechanism occurs preferentially through a tightly constrained collinear geometry. This conclusion is based on the argument, illustrated in Chapter 1 Figure 1.4, that the geometry of the intermediate determines the degree of rotational excitation. If the intermediate is bent then repulsions between H and R should cause the OH to be ejected with substantial rotational excitation. Conversely, if the intermediate is collinear then repulsive energy release is not converted into rotation and a translationally hot product emerges. The minor trends in the levels of OH rotational excitation, resulting from reaction with the different hydrocarbons, are attributed to a slight relaxation of the collinear constraint in the order tertiary < secondary < primary < methane. Correspondingly, the average fraction of the available energy appearing as OH rotation is greater following primary abstraction. To complement their results Andresen and Luntz subsequently constructed collinear model LEPS surfaces on which

quasiclassical trajectory (QCT) calculations quite successfully reproduced the experimentally obtained data[12].

Since the original work carried out by Andresen and Luntz was published there have been a number of theoretical developments relevant to the $O(^3P)$+HR system. Clary *et al*[66] carried out approximate quantum vibrationally adiabatic distorted wave (VADW) scattering calculations on the LEPS surfaces generated by Andresen and Luntz and successfully reproduced the characteristic cold OH rotational distributions. The significance of this result is essentially that the cold distributions are not an artefact of the classical trajectory methods used in Andresen and Luntz's work.

Walch and Dunning[67] used ab initio methods to calculate the barrier height and transition state geometry for the $O(^3P)$+CH_4 reaction and predicted that the minimum energy path was collinear. Essentially, if there is a loss in collinearity in this system then the degeneracy within the CH_3-H-O intermediate (^3E in C_{3v}) is removed and two surfaces, $^3A'$ and $^3A''$, evolve. These two surfaces differ in the location of π electrons: the unpaired electron is in the plane of the bend in $^3A'$ and perpendicular to the bending plane in $^3A''$. However Walch and Dunning[67] showed that the energy differences between these two states are small, provided that the bending angle (α) does not exceed $\pm 30°$. This degree of bending does cause the barrier height to increase, and the increases agree reasonably well with the values set by the choice of parameters in the LEPS surfaces[12,22]. Hence the proposed collinear reaction geometry is supported by both ab initio and model surface calculations.

As mentioned in Section 4.1 our understanding of the $O(^3P)$+HR system has also been enhanced by recent experimental studies. Suzuki and Hirota[30] detected the CH_3 product resulting from the $O(^3P)$+CH_4 reaction, following

193nm photolysis of SO_2, and reported non-inverted populations in the ν_2 umbrella mode which were hotter than suggested by a prior statistical prediction. The data presented by Suzuki and Hirota can be combined with our results in attempt to rationalise the distribution of all the energy available to products. This type of calculation will determine the amount of energy channeled in product translation.

Suzuki and Hirota[30] didn't explicitly state the average vibrational energy in the ν_2 mode, but it is relatively straightforward to derive this quantity, $\langle E_{vib} \rangle_{CH_3}$ from their results[68]. They also noted that the CH_3 was significantly rotationally excited, at short times following initiation of the reaction, and assigned an approximate temperature of around 730K to its rotational distribution. Assuming that there is no dynamical preference for rotation about different axes, this corresponds to a total average energy in three rotational degrees of freedom, $\langle E_{rot} \rangle_{CH_3} = 3/2kT = 760cm^{-1}$. The approximate $\langle E_{vib} \rangle_{CH_3}$ and $\langle E_{rot} \rangle_{CH_3}$ values are given in Table 4.2.

In this work, for the reaction between $O(^3P)$ and CH_4, the average energy in OH rotation was estimated to be approximately $580cm^{-1}$, with negligible contribution to vibrational modes. The data in Table 4.1 shows that $\langle E_{rot} \rangle_{OH}$ does not vary significantly with changes in the collision energy distribution and hence it is assumed that a comparable low value would apply under Suzuki and Hirota's conditions.

Hence the residual energy partitioned to the centre-of-mass translational recoil, $\langle E_{trans} \rangle$, is given by Equation 4.4:

$$\langle E_{trans} \rangle \approx \langle E_{av} \rangle - \langle E_{rot} \rangle_{OH} - \langle E_{vib} \rangle_{CH_3} - \langle E_{rot} \rangle_{CH_3} \qquad (4.4)$$

Source of $O(^3P)$	193nm photolysis of SO_2 [a]	248nm photolysis of NO_2 [b]
$\langle E_{av} \rangle$ / cm^{-1}	2100	4890
$\langle E_{rot} \rangle_{OH}$ / cm^{-1}	580 [b]	
$\langle E_{vib} \rangle_{CH_3}$ / cm^{-1}	630 [a]	
$\langle E_{rot} \rangle_{CH_3}$ / cm^{-1}	760 [a]	
$\langle E_{trans} \rangle$ / cm^{-1}	130 [c]	2920 [c]

(a) Values given by Suzuki and Hirota[30].

(b) Values previously presented in Table 4.1.

(c) Calculated from the other values via Equation (4.4).

Table 4.2: Distribution of available energy into product rotational, vibrational and translational modes following the reaction between $O(^3P)$ and CH_4.

Unfortunately the most ambiguous factor in Equation (4.4) is the value of $\langle E_{av} \rangle$. Suzuki and Hirota encountered the common problem of quantifying this value in an experimental method based on photolysis of a precursor (in their case SO_2 at 193nm) under bulk conditions. They allowed energy to be partitioned to SO vibration following photolysis but neglected other effects and thus calculated an $\langle E_{av} \rangle$ of 2100cm^{-1}. However, as shown in Table 4.2 using this value leaves only 130cm^{-1} to be channeled into $\langle E_{trans} \rangle$. This extremely low result even neglects any additional partitioning of energy to the unmonitored vibrational modes of CH_3. If this value for $\langle E_{trans} \rangle$ were correct then it would imply that there is virtually no impulsive energy release, following the reaction between $O(^3P)+CH_4$, which subsequently invalidates any conclusions drawn on the collinear mechanism for the reaction from the degree of rotational excitation. This, however, is unlikely because the lack of any repulsive energy release to translation/rotation of the products would imply that there is no barrier to the reverse reaction, which is not consistent with the forward activation energy and the reaction enthalpy.

We do not believe that calculation of $\langle E_{trans} \rangle$, using Suzuki and Hirota's quoted value of $\langle E_{av} \rangle$, exposes any serious flaw in the accepted dynamical picture of the $O(^3P)$+HR reactions. It is more likely that, in this instance, $\langle E_{av} \rangle$ has been calculated using inaccurate assumptions. As has been discussed previously, the reactivity in the $O(^3P)+CH_4$ system is dominated by collisions in the higher energy tail of the collision energy distribution (shown in Figure 4.25). An $\langle E_{av} \rangle$ of 2100cm^{-1} is therefore likely to be an underestimate of the true value and any increases which can be attributed to this quantity will correspondingly augment $\langle E_{trans} \rangle$, as shown in Equation (4.4). Suzuki and Hirota were aware of this discrepancy and noted the appearance of CH_3 ν_2 product levels above their $\langle E_{av} \rangle$.

There are other aspects of Suzuki and Hirota's work[30] which provoke comment. They noted significant CH_3 rotational excitation (but were unable to measure nascent rotational distributions). This observation is surprising because a collinear reaction geometry should cause very little torque to be imparted to CH_3. In fact this fragment should be less rotationally excited than OH because the mutual repulsion within the R-H-O intermediate acts near the light end of the OH rotor but essentially through the centre-of-mass of CH_3. Studies into heavy+light-heavy systems[21-23,65], of which this reaction is an example, suggest efficient conversion of reagent orbital to product orbital angular momentum, rather than to product rotation. Hence an experiment which probed detailed nascent rotational distributions within the CH_3 product of the $O(^3P)+CH_4$ reaction would be extremely useful at this stage.

However, despite some contradictory evidence from Suzuki and Hirota[30], we firmly believe that Andresen and Luntz[11] were correct in their initial proposal that abstraction in $O(^3P)$+HR reactions occurs in near-collinear geometries. Our rotational analysis serves to confirm this conclusion. Nevertheless it ought to be noted that cold rotational distributions should not be overinterpreted in the absence of corroborating measurements such as angular scattering distributions, as witnessed in the closely analogous Cl+HR reactions[32,34-37,39,40] discussed in Section 4.1

4.6.3 Fine-Structure Distributions: Electronic Effects

4.6.3.1 Λ-Doublets

As discussed in Section 4.5.1 no selectivity was observed for one particular OH Λ-doublet level to be preferentially populated over the other. This was the situation for all the different HR reagents and at all photolysis wavelengths. However this isn't such a surprising result since it's only for

high rotational levels that Λ-doublet components can be uniquely associated with directed orbitals[11,60], and, in this experiment it has been established that rotationally cold OH is produced. An additional point irrespective of the OH product state, is that a particular Λ-doublet can only be preferentially populated if the intermediate is **bent**: in the limit of high rotational angular momentum, Λ-doublets in the OH ground state are characterised as having a Π orbital lying either in the plane, Π(A′), or perpendicular to the plane, Π(A″), of rotation. However, for a unique plane to be defined the geometry must be bent, otherwise Π(A′) and Π(A″) are meaningless. Since the cold OH rotational distribution has been concluded to result from a collinearly-constrained intermediate, it is self-consistent that there is no selectivity in the Λ-doublet states.

4.6.3.2 Spin-Orbit States

A preference has been observed, both in this study and in previous work[11,19,52], for the lower OH $^2\Pi_{3/2}$ spin-orbit state to be preferentially populated over the upper $^2\Pi_{1/2}$ state. In their original investigation Andresen and Luntz[11] proposed that this selectivity could be rationalised by linking the reactant to product fine-structure states, and accordingly generated an adiabatic correlation diagram (reproduced in Figure 5.9, Chapter 5). They generated O atoms by microwave discharge of O_2 and assumed thermal populations of the $O(^3P_j)$ reactant states. From comparison of their correlation diagram with the experimental results, Andresen and Luntz concluded that the system did not conform to either a diabatic (full collisional mixing of surfaces) or adiabatic (no mixing) limit. Their measured $^2\Pi_{3/2}$: $^2\Pi_{1/2}$ ratio was closer to their diabatic prediction.

However, although we do agree that the source of the product state selectivity may lie in correlations between reactant and product fine-structure states, we believe that the particular correlations proposed by Andresen and

Luntz are flawed. To justify this argument we have generated correlation models for the $O(^3P)$+HR system. A detailed discussion of this work is presented in Chapter 5.

4.7 Concluding Remarks

We have successfully probed the reactions between $O(^3P)$ and a range of saturated hydrocarbon molecules, and determined quantitatively the partitioning of available energy between rotational and fine-structure states of the $OH(^2\Pi)$ product. Our results, in general, agree with those obtained by Andresen and Luntz[11] who originally studied the system using a different experimental strategy.

$O(^3P)$ was generated by photolysis of NO_2 at 337, 308 and 248nm. In this way the collision energy of the reaction was effectively altered. This was found to have little effect on the observed product distributions, but by photolysing at 248nm we were able to surmount the barrier to the previously unstudied $O(^3P)$+CH_4 reaction.

The observed rotational distributions were found to be virtually insensitive to the nature of the R group: in all cases only a very small proportion of the estimated total available energy was channeled into product rotation. This suggests that the reaction occurs preferentially when the $O(^3P)$ approaches the HR collinearly.

Fine-structure analysis showed that the OH product was preferentially formed in its lower, $^2\Pi_{3/2}$, spin-orbit state. It is thought that the source of this selectivity lies in reactant to product state correlations, as described in Chapter 5.

References

[1] J.T. Herron and R.E. Huie, *J. Phys. Chem.*, **73**, 3327 (1969).

[2] W.K. Stuckey and J. Heicklen, *J. Chem. Phys.*, **46**, 4843 (1967).

[3] R.D.H. Brown and I.W.M. Smith, *Int. J. Chem. Kinet.*, **7**, 301 (1975).

[4] R.D.H. Brown and I.W.M. Smith, *Int. J. Chem. Kinet.*,**10**, 1 (1978).

[5] D.L. Singleton and R.J. Cvetanovic, *Can. J. Phys.*, **56**, 2934 (1978).

[6] R.D.H. Brown, G.P. Glass, I.W.M. Smith, *Chem. Phys. Lett.*, **32**, 517 (1975).

[7] R.G. Macdonald and C.B. Moore, *J. Chem. Phys.*, **68**, 513 (1978).

[8] J.E. Spenser and G.P. Glass, *Int. J. Chem. Kinet.*, **11**, 97 (1977).

[9] B.S. Agrawalla, A.S. Manocha and D.W. Setser, *J. Phys. Chem.*, **85**, 2873 (1981).

[10] A. Miyoshi, K. Ohmori, K. Tsuchiya and H. Matsui, *Chem. Phys. Lett.*, **204**, 241 (1993).

[11] P. Andresen and A.C. Luntz, *J. Chem. Phys.*, **72**, 5842 (1980).

[12] A.C. Luntz and P. Andresen, *J. Chem. Phys.*, **72**, 5851 (1980),

[13] K. Kleinermanns and A.C. Luntz, *J. Chem. Phys.*, **77**, 3533 (1982).

[14] K. Kleinermanns and A.C. Luntz, *J. Chem. Phys.*, **77**, 3774 (1982).

[15] K. Kleinermanns and A.C. Luntz, *J. Chem. Phys.*, **77**, 3537 (1982).

[16] N.J. Dutton, I.W. Fletcher and J.C. Whitehead, *J. Phys. Chem.*, **89**, 569 (1985).

[17] N.J. Barry, I.W. Fletcher and J.C. Whitehead, *J. Phys. Chem.*, **90**, 4911 (1986).

[18] F. Winterbottom and J.C. Whitehead, *Annual Report* (1990) *of the Central Laser Facility*, Rutherford Appleton Lab.

[19] N.J. Dutton, I.W. Fletcher and J.C. Whitehead, *Mol. Phys.*, **52**, 475 (1984).

[20] D.J. Rakestraw, K.G. McKendrick and R.N. Zare, *J. Chem. Phys.*, **87**, 7341 (1987).

[21] K.G. McKendrick, D.J. Rakestraw and R.N. Zare, *Faraday Disc. Chem. Soc.*, **84**, 39 (1987).

[22] K.G. McKendrick, D.J. Rakestraw, R. Zhang and R.N. Zare, *J. Phys. Chem.*, **92**, 5530 (1988).

[23] R. Zhang, W.J. Van Der Zande, M.J. Bronikowski and R.N. Zare, *J.Chem.Phys.*, **94**, 2704 (1991).

[24] C.R. Park, G.D. White and J.R. Wiesenfeld, *J. Phys. Chem.*, **92**, 152 (1988).

[25] C.R. Park and J.R. Wiesenfeld, *J. Phys. Chem.*, **93**, 1365 (1989).

[26] J.C. Whitehead and F. Winterbottom, *Chem. Phys. Lett.*, **177**, 207 (1991).

[27] Y. Rudich, S. Lifson and R. Naaman, *J. Am. Chem. Soc.*, **113**, 7077(1991).

[28] Y. Rudich, Y. Hurwitz, S. Lifson and R. Naaman, *J. Chem. Phys.*, **98**, 2936 (1993).

[29] *CRC Handbook of Chemistry and Physics*, edited by D.R. Lide, (CRC Press, 73rd edition, 1992).

[30] T. Suzuki and E. Hirota, *J. Chem. Phys.*, **98**, 2387 (1993).

[31] K.P. Huber and G. Herzberg, *Molecular Spectra and Molecular Structure. IV. Constants of Diatomic Molecules*, (Van Nostrand Reinhold, New York, 1979).

[32] D.F. Varley and P.J. Dagdigian, *J. Phys. Chem.*, **100**, 4365 (1996).

[33] C.R. Park and J.R. Wiesenfeld, *J. Chem. Phys.*, **95**, 8166 (1991).

[34] W.R. Simpson, A.J. Orr-Ewing and R.N. Zare, *Chem. Phys. Lett.*, **212**, 163 (1993).

[35] W.R. Simpson, A.J. Orr-Ewing S.A. Kandel, T.P. Rakitzis and R.N. Zare, *J. Chem. Phys.*, **103**, 7299 (1995).

[36] W.R. Simpson, T.P. Rakitzis, S.A. Kandel, A.J. Orr-Ewing and R.N. Zare, *J. Chem. Phys.*, **103**, 7313 (1995).

[37] W.R. Simpson, T.P. Rakitzis, S.A. Kandel, T. Lev-On and R.N. Zare, *J. Phys. Chem.*, **100**, 7938 (1996).

[38] Y. -F. Yen, Z. Wang, B. Xue and B. Koplitz, *J. Phys. Chem.*, **98**, 4 (1994).

[39] D.F. Varley and P.J. Dagdigian, *J. Phys. Chem.*, **99**, 9843 (1995).

[40] D.F. Varley and P.J. Dagdigian, *Chem. Phys. Lett.*, **255**, 393 (1996).

[41] H. Okabe, *Photochemistry of Small Molecules*, (Wiley, New York, 1978), p227-235.

[42] T.C. Hall and F.E Blacet, *J. Chem. Phys.*, **20**, 1745 (1952).

[43] G.E. Busch and K.R. Wilson, *J. Chem. Phys.*, **56**, 3626 (1972).

[44] H. Zacharias, M. Geilhaupt, K. Meier and K.H. Welge, *J. Chem. Phys.*, **74**, 218 (1981).

[45] J. Miyawaki, T. Tsuchizawa, K. Yamanouchi and S. Tsuchiya, *Chem. Phys. Lett.*, **165**, 168 (1990).

[46] H.-G. Rubahn, W.J. Van Der Zande, R. Zhang, M.J. Bronikowski and R.N. Zare, *Chem. Phys. Lett.*, **186**, 154 (1991).

[47] N. Changlong, L. Hua and J. Pfab, *J. Phys. Chem.*, **97**, 7458 (1993).

[48] Y.-L. Huang and R.J. Gordon, *J. Chem. Phys.*, **93**, 868 (1990).

[49] A. Miyoshi, K. Tsuchiya, N. Yamauchi and H. Matsui, *J. Phys. Chem.*, **98**, 11452 (1994).

[50] T. Kinugawa, T. Sato, T. Arikawa, Y. Matsumi and M. Kawasaki, *J. Chem. Phys.*, **93**, 3289 (1990).

[51] J. McFarlane, J.C. Polanyi and J.G. Shapter, *J. Photochem. Photobiol. A: Chem.*, **58**, 139 (1991).

[52] A. Watson, *State-Specific Reaction Dynamics*, Ph.D. Thesis, University of Edinburgh, 1994.

[53] Vibrational and rotational levels of the OH product, formed following reaction between $O(^3P)$ and RH are labelled with primes, v′ and N′. This

notation, which is commonly used in reaction dynamics to differentiate between reactant and product energy states, is consistent with the conventions used in Chapters 5 and 6.

[54] G.H. Dieke and H.M. Crosswhite, *J. Quant. Spectrosc. Radiat. Transfer*, **2**, 97 (1962).

[55] I.L. Chidsey and D.R. Crosley, *J. Quant. Spectrosc. Radiat. Transfer*, **23**, 187 (1980).

[56] R.A. Copeland, J.B. Jeffries and D.R. Crosley, *Chem. Phys. Lett.*, **138**, 425 (1987).

[57] C.H. Greene and R.N. Zare, *J. Chem. Phys.*, **78**, 6741 (1983).

[58] C.B. McKendrick, C. Fotakis and R.J. Donovan, *J. Photochem.*, **20**, 175 (1982).

[59] T.G. Slanger, W.K. Bischel and M.J. Dyer, *J. Chem. Phys.*, **79**, 2231 (1983).

[60] P. Andresen and E.W. Rothe, *J. Chem. Phys.*, **82**, 3634 (1985).

[61] M.H. Alexander *et al*, *J. Chem. Phys.*, **89**, 1749 (1988).

[62] K.P Huber and G. Herzberg, *Molecular Spectra and Molecular Structure. Vol 4: Constants of Diatomic Molecules* (Van Nostrand Reinhold, New York, 1979).

[63] J. Berkowitz, G.B. Ellison and D. Gutman, *J. Phys. Chem.*, **98**, 2744 (1994).

[64] W.J. Van Der Zande, R. Zhang, R.N. Zare, K.G. McKendrick and J.J. Valentini, *J. Phys. Chem.*, **95**, 8205 (1991).

[65] C.A. Parr, J.C. Polanyi and W.H. Wong, *J. Chem. Phys.*, **58**, 5 (1973).

[66] D.C. Clary, J.N.L. Connor and W.J.E. Southall, *J. Chem. Phys.*, **84**, 2620 (1986).

[67] S.P. Walch and T.H. Dunning Jr., *J. Chem. Phys.*, **72**, 3221 (1980).

[68] Derived from Figure 10 of ref. [30].

Chapter 5

Spin-Orbit Effects in the Dynamics of $O(^3P_j)$ + Hydrocarbon Reactions

5.1 Introduction

In Chapter 4 an experimental investigation into the dynamics of the reactions between $O(^3P)$ and saturated hydrocarbons (Equation 5.1) was discussed; the partitioning of energy into product rotational and fine structure levels was examined.

$$O(^3P_j) + HR \rightarrow OH(X^2\Pi) + R \qquad (5.1)$$

It was established that reactions of the type specified in Equation (5.1) are characterised by low rotational energy release. This was interpreted as a propensity for the reaction to proceed via collinear intermediates[1,2]. It was also observed that the OH $^2\Pi_{3/2}$ product state was populated preferentially to the OH $^2\Pi_{1/2}$ state. This result was found to be independent of:

- the nature of the R group in HR (representing a saturated hydrocarbon), as shown in Figure 4.25 in Chapter 4.
- the collision energy, as shown in Figure 4.26 in Chapter 4.

Figure 4.25(a) (Chapter 4) shows that the OH $^2\Pi_{3/2}$:OH $^2\Pi_{1/2}$ ratio is typically around 4 for the N′=1 state and declines steadily as N′[3] increases.

One factor which might be expected to affect the observed spin-orbit ratio is the spatial (2J′+1) degeneracy of the states in each spin doublet. Figure 3.2 in Chapter 3 shows that states with the same value of N′ have different

values of J', where J'=N'±1/2. The higher degeneracy of the $^2\Pi_{3/2}$ level (which corresponds to J'=N'+1/2) can be compensated for by multiplying the observed $^2\Pi_{3/2}$:$^2\Pi_{1/2}$ ratio by N'/N'+1. This operation was applied by Andresen and Luntz to their results[2].

Figure 5.1 shows a plot of the degeneracy corrected spin-orbit ratio ((N'/N'+1) × $^2\Pi_{3/2}/^2\Pi_{1/2}$) against N'. This data was obtained following 248nm photolysis of NO_2. The decline in the ratios with N' is now marginal but it is still evident that a non-statistical propensity exists for the $^2\Pi_{3/2}$ state to be populated over the $^2\Pi_{1/2}$ state. The results shown in Figure 5.1 are clarified in Figure 5.2. Since the spin-orbit ratio is independent of the nature of the R group, a combined average value for each N' has been calculated using statistical weights determined by the measured uncertainties[4].

The source of the spin-orbit state selectivity in the O(^{3}P)+HR reactions can perhaps be found by examining the correlations between the reactant and the product states. Both O(^3P_j) and OH($X^2\Pi$) have fine structure states; if these states can be described with good and appropriate quantum numbers and linked via an intermediate, then the outcome of the reaction can be traced back to the initial population of reactant states. Similar approaches have been used to explain the differential reactivities of the fine structure states of reactants and rationalise the preferential yields of fine structure states of products in a variety of chemical systems[5,6].

Reactant to product state correlations for the O(^{3}P)+HR reactions have previously been proposed by Andresen and Luntz[2] but we believe that, in that study, critical errors were made and for this reason we have analysed the system again.

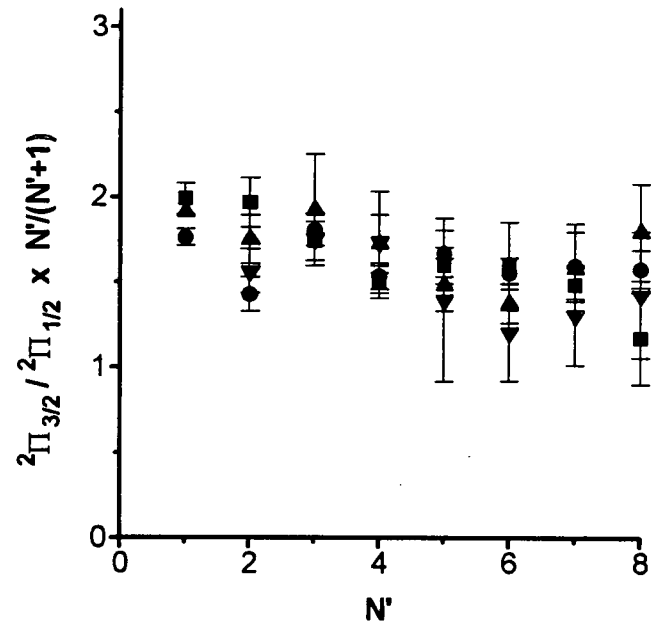

Figure 5.1: Measured $^2\Pi_{3/2}$:$^2\Pi_{1/2}$ ratios for the OH products of O(^{3}P)+HR reactions, corrected for the degeneracy of levels. Error bars represent 1σ uncertainties calculated from the scatter in repeated measurements. The HR reactants were isobutane (■), cyclohexane (●), ethane (▲) and methane (▼).

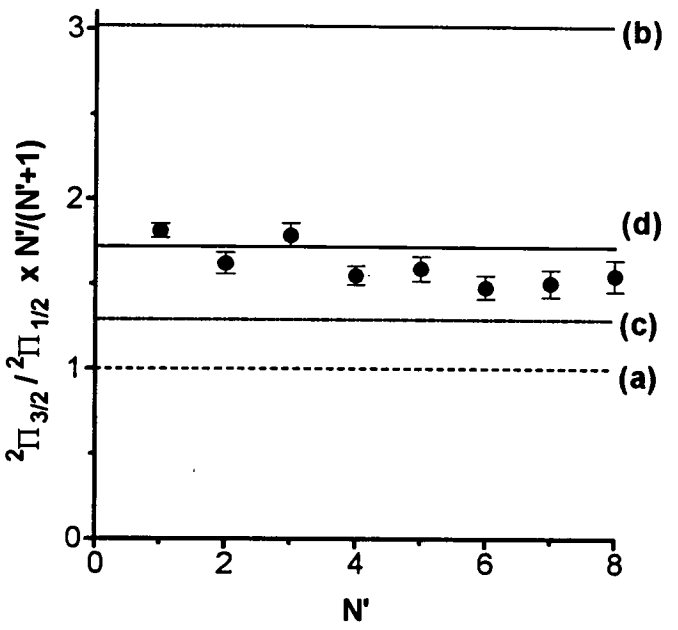

Figure 5.2: Measured OH $^2\Pi_{3/2}$:$^2\Pi_{1/2}$ ratios (●), averaged over all reactants. The predicted limiting values of the spin-orbit state ratio, obtained from Ω-conserving Models 1, 2 and 3, are also shown on this plot:

(a) populations determined only by the relative degeneracy of the levels.

(b) populations obtained by applying Model 1: fully adiabatic correlations.

(c) populations obtained by applying Model 2: selective non-adiabatic mixing in the exit channel.

(d) populations obtained by applying Model 3: selective non-adiabatic mixing in both the entrance and exit channels.

Table 5.1: Universal notation for Chapter 5.

j	=	total electronic angular momentum of $O(^3P_j)$ and, consequently, of whole system
m_j	=	projection onto some axis of j of free $O(^3P_j)$
Ω	=	projection of total electronic angular momentum onto the intermolecular axis
L	=	total orbital angular momentum of electrons
m_L	=	projection of L onto a specified axis in free $O(^3P)$
Λ	=	projection of total electronic orbital angular momentum onto intermolecular axis (whole system)
S	=	total spin of all electrons (when all defined spins are coupled)
m_S	=	projection of S onto a specified axis in free $O(^3P)$
Σ	=	projection of total spin of all electrons onto internuclear axis
S'	=	net spin of OH once separation to products has been established
Σ'	=	projection of OH spin onto its own and, therefore, intermolecular axis
Λ'	=	projection of OH orbital angular momentum onto its own (and hence intermolecular) axis
Ω'	=	combined spin-orbit projection of OH electrons
N'	=	rotational quantum number, excluding spin, associated with the OH product, necessary for labelling experimental product levels.
S''	=	spin of the H/R fragment once separation to the products is established
m_S''	=	projection of S″ onto a specified axis in the H/R fragment
Σ''	=	projection of H/R spin onto intermolecular axis
Λ''	=	projection of H/R orbital angular momentum onto its own (and hence intermolecular) axis

The principal aim in this chapter is to establish the correlations from $O(^3P_j)+HR(^1\Sigma^+)$, via intermediate O-H-R surfaces of well-defined spin and orbital angular momentum, to $OH(^2\Pi)+R(^2\Sigma^+)$. This objective will be achieved in the following stages:

1. Define the $O(^3P_j)$ and $OH(^2\Pi)$ fine structure states and show the surfaces which evolve as a collision partner (HR/R) is introduced.
2. Show how three models were devised, illustrating the reactant to product state correlations. Explain the limits of these models and in which circumstances they would apply.
3. Compare the spin-orbit ratios predicted by each model with the experimental results.

In the subsequent text a range of new notation will be introduced. A definition of these terms will not always be immediately given but can be found in Table 5.1.

Before the reactive system can be defined the geometry must be specified as this will determine the nature of the reactive surfaces. As discussed in Chapter 4 rotationally cold OH products were observed; this was interpreted as evidence that the reaction occurs preferentially when the $O(^3P)$ approaches the HR collinearly. This is supported by theoretical studies[7,8] which have identified a collinear (C_{3v}) geometry for the transition state of the $O(^3P)+CH_4$ reaction. Walch and Dunning[7] characterised the $O(^3P)+CH_4$ reactive surface. They examined the effects of bending in the transition state and found that, energetically, it didn't matter if the O atom moved either towards the H atom in the methyl group (bending angle = $+\alpha$) or between the H atoms ($-\alpha$). This bending is shown in Figure 5.3. The implication is that the system must therefore be approximately cylindrically symmetric and the exact positions of the H atoms are irrelevant. Hence in the following arguments a simple $C_{\infty v}$ approach of the $O(^3P)$ to the C-H bond is assumed.

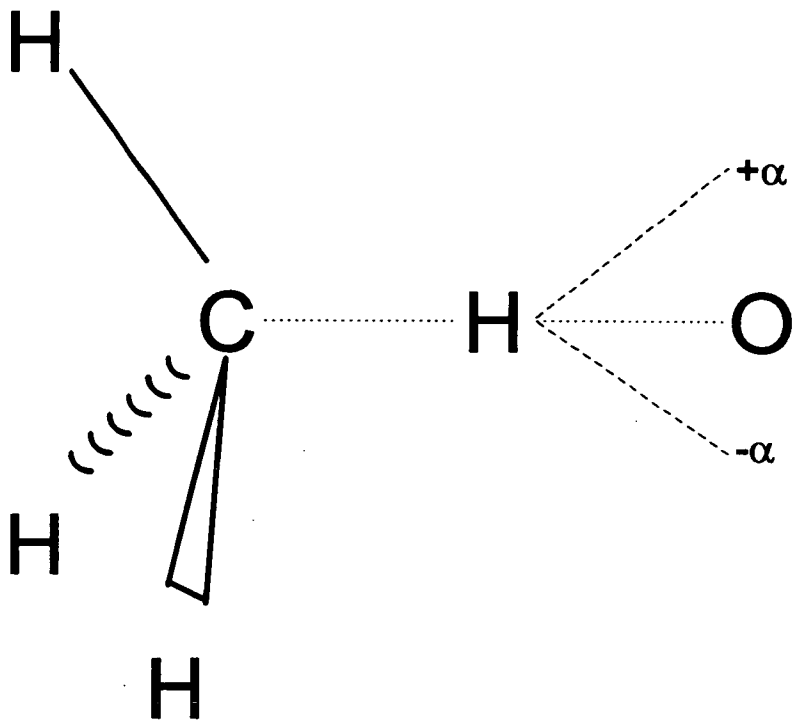

Figure 5.3: This diagram shows the effects of bending in the C_{3v} transition state of the $O(^3P)/CH_4$ reaction. When the O atom moves towards the C-H bond, the bending angle is $+\alpha$. When the O atom moves into the gap between the C-H bonds the bending angle is $-\alpha$. This figure is redrawn from ref. [7].

The hydrocarbon (HR) is treated as a structureless particle with $^1\Sigma^+$ symmetry and the subsequent product organic radical, R, is labelled $^2\Sigma^+$, this being the C_{3v} to $C_{\infty v}$ correlation for the $CH_3(^2A_1)$ product of the $O(^3P)+CH_4$ reaction[7].

5.2 Identification of the Fine Structure States

Two approaches can be used to determine the quantum numbers necessary to define isolated $O(^3P)$ and $OH(X^2\Pi)$; either uncoupled or coupled representations can be used.

The uncoupled representation characterises the reactant and product states in the absence of spin-orbit coupling, and provides a simplistic approach to the subsequent correlations. However in the presence of spin-orbit coupling (a more realistic approach) the description of the system changes and the fine structure states evolve. Each representation requires its own set of quantum numbers.

5.2.1 The Uncoupled Representation

$O(^3P)$ has the electronic configuration ($1s^22s^22p^4$). It has two unpaired electrons and is therefore described as a triplet state. In the uncoupled representation, the quantum numbers which are used to describe $O(^3P)$ are L, S, m_L and m_S. (The notation is explained in Table 5.1). The quantum number j is indeterminate but m_j is defined through the relation $m_j=m_L+m_S$. The ^3P state is nine-fold degenerate with $m_L = -1, 0, +1$, $m_S = -1, 0, +1$.

Ignoring the $1s^22s^2$ electrons in the oxygen atom, the remaining p^4 electrons may be represented pictorially by a set of mutually perpendicular p orbitals of which two lobes are partially filled and the third full. This idea was

illustrated by Walch and Dunning[7] and is reproduced in Figure 5.4. When a closed shell collision partner is brought close to the p orbitals electrostatic interactions cause the three-fold orbital degeneracy to be removed; geometric arguments imply that the $^3\Pi$ and $^3\Sigma^-$ surfaces evolve, a result that can be proved by standard group theoretical methods[9] as shown in Section 5.2.3. The $^3\Sigma^-$ surface is three-fold degenerate and associated with the lone pair in the P_z orbital. The six-fold degenerate $^3\Pi$ surface is split into $^3\Pi^+$ and $^3\Pi^-$ and associated with the lone pairs in the linear combinations, P_x and P_y. When the collision partner contains an abstractable σ-bonded H atom ($^1\Sigma^+$ symmetry) the $^3\Pi$ surface is potentially reactive and correlates with the OH($X^2\Pi$) and R($^2\Sigma^+$) products[7].

For a reactant to product correlation to be successful it must also be possible to access the relevant intermediate surface from the opposite side: it is necessary to define the states and specify the surfaces pertaining to the OH($^2\Pi$)+R($^2\Sigma^+$) reaction.

In a diatomic molecule (OH in this case) the orbital angular momenta of all the electrons are coupled to give L′ and the spin momenta couple to give S′. In the absence of spin-orbit coupling these terms are considered separately. The magnitude of L′, however, is not defined, implying that L′ is not a good quantum number[10]. Instead Λ′, the projection of L′ along the internuclear axis, is used. In the electronic ground state of OH, Λ′=1 making it a doubly degenerate Π state, since all electronic states with Λ>0 are doubly degenerate. S′ is still a good quantum number and the projection of S′ along the molecular axis is Σ′. OH has a spin of 1/2 which means that it's multiplicity (2S′+1) is two. The multiplicity also defines the number of values that Σ′ can take: when S′=1/2 Σ′=±1/2. Hence collating all this data, the electronic ground state of the OH molecule can be defined as a $^2\Pi$ state which is four-fold degenerate with Λ′=±1 and Σ′=±1/2. The isolated R($^2\Sigma^+$) collision partner which contributes a single electron has S″=1/2, m_S″=±1/2

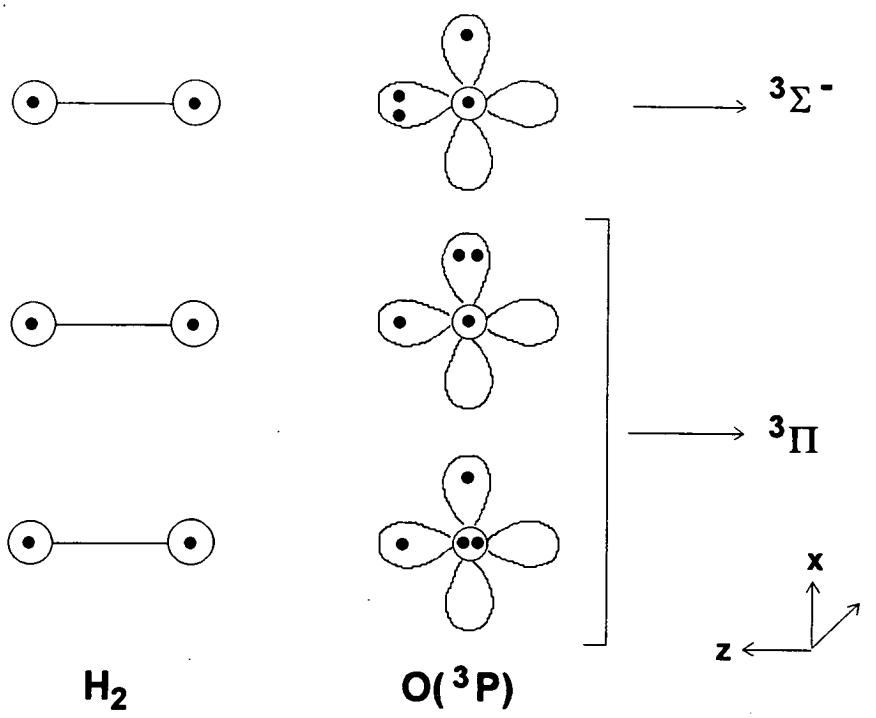

Figure 5.4: The $O(^3P)$ and HR reactants, in Equation (5.1) can be represented pictorially. Ground state oxygen has the electronic configuration $1s^2 2s^2 2p^4$. Ignoring the closed shell, the $O(^3P)$ p^4 configuration can be drawn as a set of mutually perpendicular p orbitals of which two are partially filled and the third is full. In this diagram the closed shell partner (HR) is approximated to be H_2. This approximation is valid because in the $O(^3P)$+HR reaction the outcome of the experiment is irrespective of the nature of the R group. Also H_2 and HR have the same symmetry, $^1\Sigma^+$. The H_2 is drawn here as two H(1s) orbitals. As the reactants approach one another geometric arguments imply that $^3\Pi$ and $^3\Sigma^-$ surfaces evolve. This figure was reproduced from illustrations in ref. [7].

and is two-fold degenerate. The projection of S″ onto the intermolecular axis is $\Sigma''(=\pm 1/2)$. This quantum number becomes important when OH and R are brought together.

In the, rather artificial, uncoupled environment two surfaces, $^1\Pi$ and $^3\Pi$, evolve as the distance between OH and a collision partner with a single electron decreases. The $^3\Pi$ surface is six-fold degenerate, can be labelled either Π^+ or Π^-, and connects to $O(^3P)$ and HR. The two-fold degenerate $^1\Pi$ surface lies to higher energy and correlates with the collinear approach of $O(^1D)$ to HR[11] and hence is unreactive with respect to the $O(^3P)$+HR reaction.

A simplistic uncoupled representation of the correlations in the $O(^3P)+HR \rightarrow OH(X^2\Pi)+R$ reaction is shown in Figure 5.5. In this diagram only electrostatic interactions (which manifest when collision partners are introduced) are considered: all spin-orbit splitting is ignored. It is already evident that connections between the reactants and products are possible via a $^3\Pi$ intermediate. It is also important to note that both the forward ($O(^3P)$+HR) and reverse (OH+R) reactions have pathways which do not connect but should not be neglected in the overall correlations.

5.2.2 The Spin-Orbit Coupled Representation

The picture which has been created so far is relatively straightforward and the inclusion of spin-orbit coupling will undoubtedly complicate the situation. Before the effects of spin-orbit coupling are considered it is perhaps necessary to specify when the coupled and uncoupled representations should be considered. In general terms at long range (i.e. when the collision partners are well separated) spin-orbit coupling is the most important interaction and at short range, electrostatic interactions are the dominant effects. Obviously these two limits are at opposite ends of the scale and the

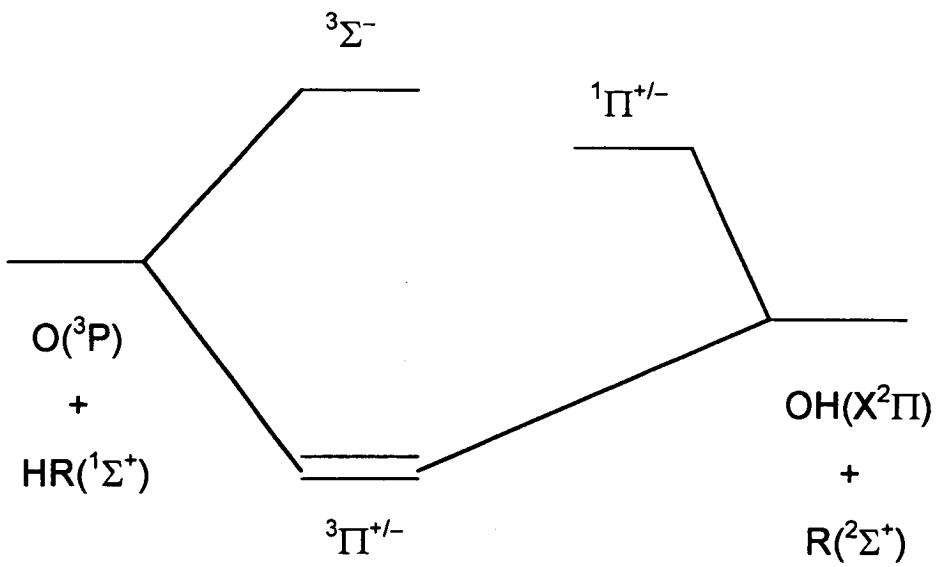

Figure 5.5: A simplistic representation of the correlations in the $O(^3P)+HR \rightarrow OH+R$ reaction, in the absence of spin-orbit coupling. In the forward reaction, on approach of HR with $C_{\infty v}$ geometry the nine-fold degeneracy of the $O(^3P)$ is removed: two surfaces, $^3\Pi$ (six-fold degenerate) and $^3\Sigma^-$ (three fold degenerate) are formed. In the reverse reaction, the $C_{\infty v}$ approach of the collision partners again causes two surfaces to evolve: $^3\Pi$ and $^1\Pi$. This diagram shows that the $^3\Pi$ surface is reactive for both the forward and reverse reactions.

interactions at intermediate range need also to be considered: a more detailed discussion of the important interactions, with respect to distance, will be discussed with each correlation model.

In a spin-orbit coupled representation the quantum numbers which can be used to describe the $O(^3P)$ are L, S, j and m_j. (These terms are defined in Table 5.1). In this instance m_L and m_S are indeterminate. Possible values of j are 2, 1 and 0 leading to the formation of three spin-orbit states:

- $^3P_2$ which is five-fold degenerate; m_j=0, ±1, ±2
- $^3P_1$ which is three-fold degenerate; m_j=0, ±1
- $^3P_0$ which is singly degenerate; m_j=0

In a collinear system, when a collision partner is present, the m_j states become redefined by Ω ($m_j \rightarrow \Omega$): m_j gives the direction of j relative to any chosen quantisation axis, whereas Ω projects j specifically onto the intermolecular axis on approach of a collision partner: all m_j states are degenerate whereas the Ω states are not. The spin-orbit splitting in the isolated $O(^3P)$ atom is illustrated in Figure 5.6. These states transform into reactive ($^3\Pi$) and unreactive ($^3\Sigma^-$) surfaces when a closed shell collision partner approaches the $O(^3P_j)$, as established in Section 5.2.1.

Spin-orbit interactions also affect the intermediate $^3\Pi$ and the product OH ($^2\Pi$) states. As previously mentioned in Section 5.2.1 the projection quantum numbers which can be used to describe the $OH(^2\Pi)$ molecule are Λ' and Σ'. The projection of total (orbital and spin) electronic angular momentum, j, along the internuclear axis is $\Omega=|\Lambda+\Sigma|$. Since $\Lambda'=\pm1$ and $\Sigma'=\pm1/2$ there are four components in $OH(^2\Pi)$ with $\Omega'=\pm3/2$ or $\Omega'=\pm1/2$. Spin-orbit interactions in OH cause the formation of two doubly degenerate $\Pi^{+/-}$ states: $^2\Pi_{\Omega=3/2}$ and $^2\Pi_{\Omega=1/2}$. On approach of the two-fold degenerate R collision partner which has a single electron (and hence $S''=1/2$, $\Sigma''=\pm1/2$) the four components in $OH(^2\Pi)$ split into four pairs of levels corresponding to

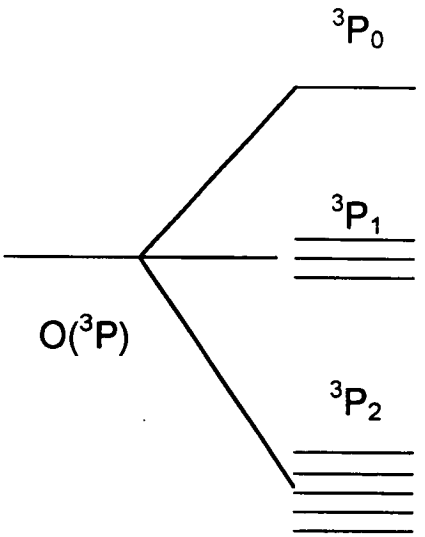

Figure 5.6: This diagram shows the spin-orbit splitting in isolated $O(^3P)$. Energetic separations are not to scale.

- $^3P_2$ is five-fold degenerate; $m_j = \pm 2, \pm 1, 0$
- $^3P_1$ is three-fold degenerate; $m_j = \pm 1, 0$
- $^3P_0$ is singly degenerate; $m_j = 0$

On collinear approach of a closed shell collision partner, $m_j \rightarrow \Omega$:

- $^3P_2 \rightarrow \Omega = \pm 2, \pm 1, 0^+$
- $^3P_1 \rightarrow \Omega = \pm 1, 0^-$
- $^3P_0 \rightarrow 0^+$

The parity restriction for states with Ω=0 is discussed in Section 5.3.1.

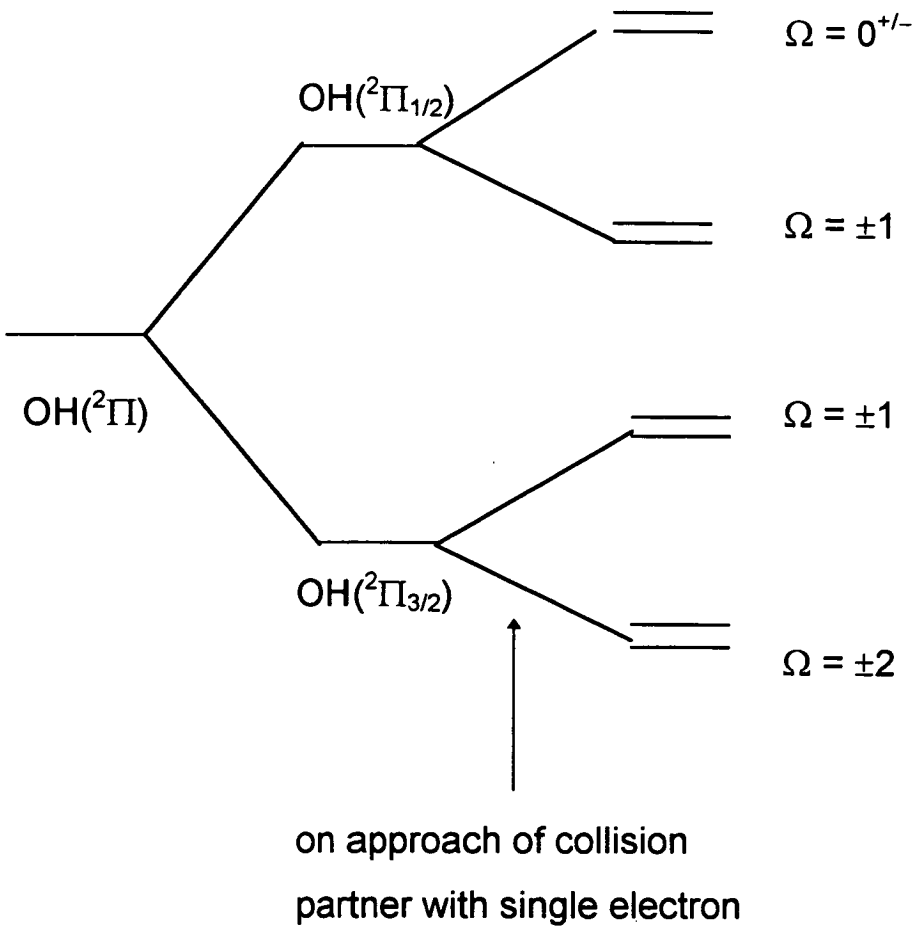

Figure 5.7: This diagram depicts the spin-orbit splitting in OH. In the isolated molecule spin-orbit interactions cause the formation of two spin doublets, $^2\Pi_{3/2}$ and $^2\Pi_{1/2}$. The effect of the approach of the collision partner, with a single electron, is also shown here.

$\Omega'=0$ and ±1 (originating from the $^2\Pi_{1/2}$ level) and $\Omega'=\pm1$ and ±2 (originating from the $^2\Pi_{3/2}$ level). These states arise because now, $\Omega=\Lambda'+\Sigma'+\Sigma''$: there are spin contributions from both OH($^2\Pi$) and R($^2\Sigma^+$) and the different combinations of Λ', Σ' and Σ'' result in four doubly degenerate states. The effect of spin-orbit interactions in the OH+R reaction is illustrated in Figure 5.7.

Then, as explained in Section 5.2.1, as the collision partner with a single electron approaches the OH molecule at shorter range, electrostatic interactions cause two intermediary surfaces, $^3\Pi$ and $^1\Pi$, to emerge. In the $^3\Pi$ state, where $\Lambda=\pm1$ and $\Sigma=1$, 0, -1, spin-orbit interactions cause the formation of three doubly degenerate $\Pi^{+/-}$ states: $^3\Pi_{\Omega=\pm2}$, $^3\Pi_{\Omega=\pm1}$ and $^3\Pi_{\Omega=0+/-}$. Strictly speaking, the $\Omega=0^{+/-}$ states are not quite degenerate[12], but they are very close in energy and can be approximated to be degenerate.

5.2.3 Group Theoretical Proof of the Surfaces Which Evolve in the O(^{3}P)+HR → OH+R Reaction

So far, vector coupling methods have been used to describe the interactions between O(^{3}P) and HR (the forward reaction), and between OH and R (the reverse reaction). It has been established that when a closed shell collision partner is brought close to O(^3P_j) two surfaces, of $^3\Pi$ and $^3\Sigma^-$ symmetry, evolve. In a similar fashion, $^3\Pi$ and $^1\Pi$ surfaces are generated when OH($^2\Pi$) and a partner with a single electron in a σ orbital meet. These results can also be proved by applying standard group theoretical methods[9].

(a) The O(^{3}P)+HR Interaction

The symmetry in O(^{3}P) is broken when a closed shell collision partner (in this case HR) is brought close: the symmetries of the states which evolve, with

$C_{\infty v}$ geometry, are Σ^- and Π[9a]. Obviously these must be triplet states because the collision partner is a closed shell and therefore the spin state of the collision pair is just that of the $O(^3P)$ atom.

Then, the data contained within ref. [9b] can be used to assess the symmetry species of both the spin and orbital functions of each intermediate state:

- The $^3\Pi$ state has a spin function, S=1. In $C_{\infty v}$ this generates Σ^- and Π surfaces.
- The $^3\Pi$ state has an orbital function, Λ=1, generating Π.
- The $^3\Sigma^-$ state also has a spin function, S=1, generating Σ^- and Π.
- For the $^3\Sigma^-$ state Λ=0. Hence its symmetry species is Σ^-.

This information is listed in Table 5.2.

The next step is to determine the symmetry of each spin-orbit level. This is done by taking the direct product of the spin and orbital symmetry species[9c] as shown in Table 5.2. Each resultant symmetry species corresponds exactly to an Ω value, derived on the basis of the vector model, thus proving that the same result can be obtained by applying either group theoretical or vector coupling methods.

(b) The $OH(^2\Pi)$+$R(^2\Sigma^+)$ Interaction

In the absence of spin-orbit splitting, $OH(^2\Pi)$ has S′=1/2, Λ'=1 and $R(^2\Sigma^+)$ has S″=1/2, Λ''=0. Hence the total Λ=1 and the total S=1,0 (yielding respective triplet and singlet multiplicities). Accordingly, when OH interacts with a collision partner with a single electron, $R(^2\Sigma^+)$, $^3\Pi$ and $^1\Pi$ surfaces evolve[9a].

However, the situation is complicated by including the spin-orbit coupling in OH. The symmetry species of the OH S′=1/2 spin function is $E_{1/2}$[9b] and the

$O(^3P)$+HR Interaction: Intermediate Surfaces (i)	Spin Function Symmetry Species[9b](i)	Orbital Function Symmetry Species	Direct Product[9c]	Corresponding Ω value (ii)
$^3\Pi$	Σ^- Π	Π	$\Sigma^-\times\Pi = \Pi$ $\Pi\times\Pi = \Sigma^+$ Σ^- and Δ	$\Pi \rightarrow \Omega=\pm1$ $\Sigma^+ \rightarrow \Omega=0^+$ $\Sigma^- \rightarrow \Omega=0^-$ $\Delta \rightarrow \Omega=\pm2$
$^3\Sigma^-$	Σ^- Π	Σ^-	$\Sigma^-\times\Sigma^- = \Sigma^+$ $\Sigma^-\times\Pi = \Pi$	$\Sigma^+ \rightarrow \Omega=0^+$ $\Pi \rightarrow \Omega=\pm1$

(i) $C_{\infty v}$ geometry

(ii) Ω values derived on the basis of the vector model

Table 5.2: Use of group theory to determine the symmetry of the spin-orbit levels generated when an $O(^3P)$ atom interacts with a closed shell collision partner[9]. The direct product of the spin function symmetry species and the orbital function symmetry species yields the symmetry of each spin-orbit level. Each symmetry state has a corresponding Ω value determined by vector coupling methods: for example, the $^3\Pi$ intermediate state has $\Lambda=\pm1$ and $\Sigma=+1,0,-1$, generating $\Omega=2,=1,0,0,-1,-2$ in possible combinations of $\Lambda+\Sigma$

orbital function is Π since $\Lambda'=1$. The direct product of $E_{1/2} \times \Pi$ yields the symmetry species $E_{1/2}$ and $E_{3/2}$[9c] which correspond to the respective OH $^2\Pi_{1/2}$ and $^2\Pi_{3/2}$ spin-orbit levels. Similarly, the symmetry species of the $R(^2\Sigma^+)$ $S''=1/2$ spin function is also $E_{1/2}$[9b] and the orbital function, with $\Lambda''=0$, is characterised as Σ^+. The direct product of these symmetry species, $E_{1/2} \times \Sigma^+ = E_{1/2}$[9c].

Combining the separate $OH(^2\Pi_{1/2} = E_{1/2})$ and $OH(^2\Pi_{3/2} = E_{3/2})$ fragments with $R(^2\Sigma^+)$ yields[9c]:

- $OH(^2\Pi_{3/2}) + R(^2\Sigma^+) = E_{3/2} \times E_{1/2} = \Pi$ and Δ. These correspond to Ω values of 1 and 2 respectively, as deduced previously from the vector model.
- $OH(^2\Pi_{1/2}) + R(^2\Sigma^+) = E_{1/2} \times E_{1/2} = \Sigma^+$, Σ^- and Π. These correspond to Ω values of $0^{+/-}$ and 1 respectively, as similarly deduced previously.

5.3 Models for Reactant to Product Correlations

The next step is to establish how the $O(^3P_{j=2,1,0})$ and $OH(^2\Pi_{\Omega=3/2,1/2})$ states link to reactive $^3\Pi$ and non-reactive surfaces. Three models (labelled 1, 2 and 3 in the following text) have been devised in an attempt to explain fine-structure effects in the $O(^3P)$+HR reaction[13]. Various connections are possible depending on what approximations are used and the coupling cases defining the system. These factors and influences will be described in detail with each model.

5.3.1 Model 1: Adiabatic, Ω-Conserving Correlations

In this model, as suggested by the title, the reactive system is correlated adiabatically. In general terms this implies that surfaces connect in order of increasing energy and that crossings (between surfaces of the same symmetry, as defined according to some criterion) are not permitted. The

most important consideration in this model is that Ω, the projection of j onto the intermolecular axis, is conserved. This approximation is discussed in greater detail in the following text.

The adiabatic correlations pertaining to the entrance channel ($O(^3P)$+HR reaction) have been described in detail in other contexts[14-21]. First these results will be summarised and then combined with a similar adiabatic treatment of the exit channel ($OH(X^2\Pi)$+R) reaction. This approximation, labelled Model 1, is closely related to the (j,Ω) strong spin-orbit coupling limit defined by Husain[5] for heavy atom-molecule collisions where Hund's case (c) coupling applies.

Aquilanti *et al*[14-17] explained that the interactions to be considered in a colliding system, involving at least one partner with non-zero spin and electronic angular momentum, were:

- spin-orbit coupling
- electrostatic interactions
- and, in the general case of non-collinear approach geometry, the centrifugal energy associated with the orbital motion of the partners about their common centre-of-mass.

The relative strength of these interactions determines which coupling case is best used to describe a system. Transitions between the coupling regimes occur as a result of the individual dependence of each of the aforementioned interactions on the distance between the colliding species: spin-orbit coupling is only weakly distance dependent[14] whereas the electrostatic interaction, reflected in the energy difference between Σ and Π surfaces, increases strongly as the distance between the collision partners lessens.

Hence at each stage of a collision/reaction the principal interactions must be assessed and an appropriate coupling case assigned. In this way the

correlation diagram is split into small regimes which can be linked by a common factor.

The $^3P_2$, $^3P_1$ and $^3P_0$ states of the O atom lie at relative energies of 0, 158 and 226cm^{-1}[6]. At sufficiently long range the spin-orbit coupling outweighs both the centrifugal energy and the electrostatic interaction. Hence the most appropriate long range description of the system is a Hund's case (e), $|jl\rangle$ basis where the good quantum numbers are j, the spin-orbit coupled electronic angular momentum and l, the orbital angular momentum. As the gap between O(^{3}P) and HR shortens the coupling case transforms to Hund's case (c) with a $|j\Omega\rangle$ basis, in which l has been replaced by Ω, the projection of the total electronic angular momentum onto the intermolecular axis. At short range the electrostatic interaction dominates and Hund's case (a), with a $|\Lambda\Sigma\rangle$ basis, defines the coupling. In this description j is replaced by Λ which is the projection of L along the intermolecular axis. The coupling of well defined projections of spin (Σ) and orbital (Λ) momenta determines Ω ($=|\Lambda+\Sigma|$) for each surface.

As the system transforms from Hund's case (e) to (c) to (a) the common factor is Ω. It is normal to impose an Ω-conserving approximation to connect between different coupling regimes[5,15] and justification for this assumption has been discussed in great detail elsewhere[15]. It has also been established that there is a parity restriction for states with $\Omega=0$[14,15,18-22]. In the strong spin-orbit coupling limit, in the presence of a collision partner, there are three O(^3P_j) states with $\Omega=0$. The $|20\rangle$ and $|00\rangle$ $|j\Omega\rangle$ surfaces, which originate from the $m_j=0$ levels of the even asymptotic j states have opposite parity to the $|10\rangle$ surface which connects to j=1. In this work the $|20\rangle$ and $|00\rangle$ levels are labelled $\Omega=0^+$ and the $|10\rangle$ surface, $\Omega=0^-$, following the normal convention for bound molecules[12].

By applying all these assumptions an adiabatic correlation diagram can be drawn for the entrance channel, linking the $O(^3P)+HR(^1\Sigma^+)$ to an intermediate (O-H-R) with collinear geometry. This is illustrated in the left half of Figure 5.8. Similar diagrams were proposed by Ma and Liu[20] and by Kawasaki *et al*[21]. On the entrance side there is only one stage of explicit coupling because the longest range effect is the $m_j \rightarrow \Omega$ correlation which is just a 1:1 mapping because the HR reactant is a closed shell (Λ=0, Σ=0).

It has been mentioned in the preceding text that Andresen and Luntz previously proposed an adiabatic correlation for the $O(^3P)+HR$ reaction[2]. Their diagram is reproduced in Figure 5.9 and exhibits some similar properties to Figure 5.8. However there are some important differences which must be noted. Andresen and Luntz suggested that $O(^3P_1)$ correlates only with the unreactive $^3\Sigma^-$ surface and that $O(^3P_0)$ correlates wholly to reactive $^3\Pi$. We believe that their proposals are flawed because they fail to distinguish correctly between the total electronic angular momentum, j, and its projection onto the intermolecular axis, Ω. In the correlation diagram shown in Figure 5.8 it is implicit that when a collision partner is present, m_j maps onto Ω, which must be conserved in all connections. Take the $^3P_2$ state as an example: $^3P_2$ is five-fold degenerate with m_j values of ±2, ±1, 0. In the presence of HR those states with $m_j=\pm2$ map onto $^3\Pi_{\Omega=\pm2}$, those with $m_j=\pm1$ onto $^3\Pi_{\Omega=\pm1}$ and $m_j=0^+ \rightarrow {}^3\Pi_{\Omega=0+}$. Andresen and Luntz allowed the $^3P_{2,0}$ states to map wholly to $^3\Pi_{2,0}$ thus connecting states using the j quantum number rather than m_j (or Ω). Another problem with their correlation diagram is that the degeneracy of states is not properly conserved.

The next step in creating a complete adiabatic description of the reaction is to examine the reverse reaction, $OH+H \rightarrow O(^3P)+HR$. As discussed in Section 5.2.2 the isolated OH molecule comprises of two spin doublets, $^2\Pi_{3/2}$ and $^2\Pi_{1/2}$. On collinear approach of a $^2\Sigma^+$ collision partner eight surfaces, all

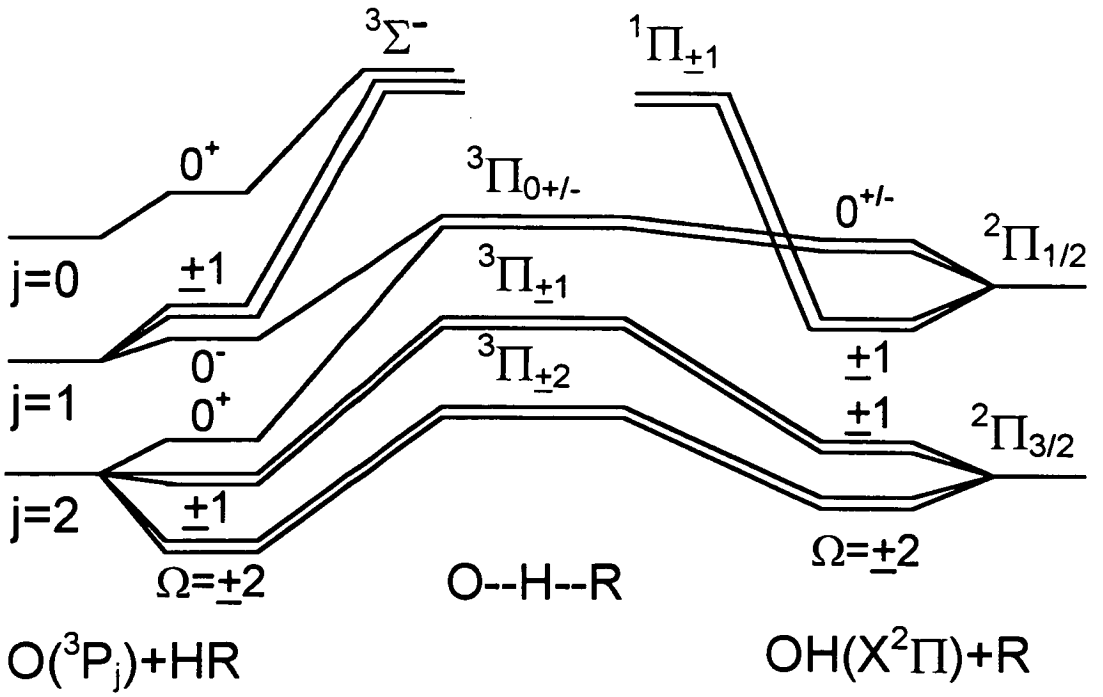

Figure 5.8: Model 1: schematic, fully adiabatic Ω-conserving correlation diagram for collinear $O(^3P_j)$+HR reactions. The energetic separations are not to scale.

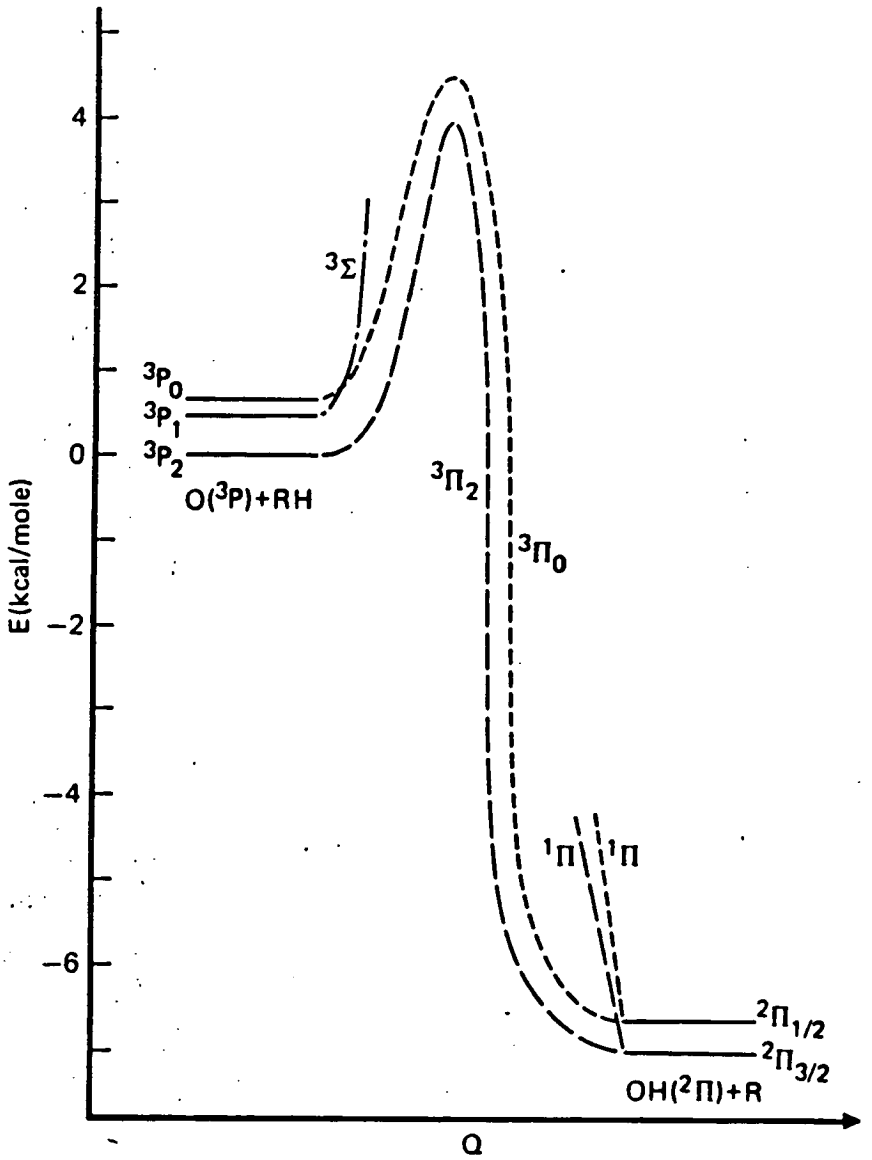

Figure 5.9: The adiabatic reactant to product correlations proposed by Andresen and Luntz for the O(^{3}P)+HR reaction. This diagram is taken from ref. [2].

with Π symmetry, evolve. These surfaces form pairs with Ω=2,1,1 and 0. In the adiabatic strong spin-orbit coupling limit, imposed by Model 1, the six lowest available surfaces of a given Ω connect to the corresponding reactive $^3\Pi$ intermediate surface with the same Ω. The remaining two $\Omega=\pm1$ surfaces, originating from the $^2\Pi_{1/2}$ level, link up with the $^1\Pi$ surface which is unreactive in this context.

The adiabatic correlations for the reverse reaction are also shown in Figure 5.8. This figure shows that, in the strong spin-orbit coupling regime, all the surfaces originating from the $^2\Pi_{3/2}$ level of OH lead to reactive surfaces but those from the $^2\Pi_{1/2}$ level divide between the $^3\Pi$ and $^1\Pi$ surfaces.

Now that Model 1 has been constructed (Figure 5.8) it is possible to predict the OH spin-orbit state distributions under a particular set of reactant conditions. This can be done in two steps:

1. Determine the fraction of the total $O(^3P_j)$ in each j state. (This data can fortunately be obtained from the literature in our case.)
2. Count the relative numbers of reactant surfaces that correlate with particular Ω' ($^2\Pi_{3/2,1/2}$) products and weigh the outcomes with the initial populations from step 1.

These steps can be expressed as an equation:

$$P(\Omega') = \sum_j \omega(j)\, P(j \rightarrow \Omega') \qquad (5.2)$$

In Equation (5.2):

- $P(\Omega')$ = The overall probability of producing OH in a particular spin-orbit state Ω'.
- $\omega(j)$ = The fraction of the total $O(^3P_j)$ population in each j state (normalised to sum to unity).

- $P(j \rightarrow \Omega') =$ The probability of each j state leading to OH(Ω'), as expressed in Equation (5.3).

$$P(j \rightarrow \Omega') = \sum_{m_j} \frac{\delta_{m_j\Omega}}{2j+1} P(|j\Omega> \rightarrow \Omega') \qquad (5.3)$$

The $\delta_{m_j\Omega}$ term in Equation (5.3) is a Kronecker delta which expresses the 1:1 long-to-medium range mapping of m_j states onto surfaces with $\Omega=m_j$. It works in the following way: if $m_j=\Omega$, then $\delta_{m_j\Omega}=1$ but if $m_j\neq\Omega$, then $\delta_{m_j\Omega}=0$. The (2j+1) degeneracy factor maintains the correct normalisation. The probability that a given $|j\Omega>$ entrance channel surface will lead to a particular product, $P(|j\Omega> \rightarrow \Omega')$, must also be determined. This can be done by summing over the Hund's case (a) intermediate (O-H-R) surfaces:

$$P(|j\Omega>\rightarrow\Omega') = \sum_{\Lambda,\Sigma} \delta_{\Omega,\Lambda+\Sigma} P(\varepsilon,0) P(|j\Omega>\rightarrow|\Lambda\Sigma;\Omega>) P(|\Lambda\Sigma;\Omega>\rightarrow\Omega') \qquad (5.4)$$

In Equation (5.4):

- $\delta_{\Omega,\Lambda+\Sigma}$ = In the medium-to-short range, the coupling case transforms from Hund's case (c) with a $|j\Omega>$ basis to Hund's case (a) with a $|\Lambda\Sigma>$ basis. The Kronecker delta imposes conservation of Ω in this transformation.
- $P(\varepsilon,0)$ = This factor accounts for the parity effects for the $\Omega=0$ surfaces. When $\Omega=0$ parity must be conserved.
- $P(|j\Omega> \rightarrow |\Lambda\Sigma;\Omega>)$ = The probability that the reactants, described by Hund's case (c), will map

onto the intermediate, described by Hund's case (a). Within the limits set by Model 1, these terms are either 1 or 0 according to the correlations drawn in Figure 5.8.

- $P(|\Lambda\Sigma;\Omega> \rightarrow \Omega')$ = The probability that the intermediate will map onto a particular product, Ω'.

Equation (5.4) is composed of four terms as shown above; the first three terms describe the correlations from medium to short range in the entrance channel and the last term is the probability that an intermediate surface, described by Hund's case (a), leads to an $OH(\Omega')$ state. This term, which combines the reactive probability, P_r, and the exit channel correlations, is expanded in Equation (5.5):

$$P(|\Lambda\Sigma;\Omega> \rightarrow \Omega') = \delta_{\Lambda 1} P_r(|\Lambda\Sigma;\Omega>) \sum_{\Sigma''} \delta_{\Omega,\Omega'+\Sigma''} P(|\Lambda\Sigma;\Omega> \rightarrow |\Omega'\Sigma'';\Omega>) \quad (5.5)$$

In Equation (5.5):

- $\delta_{\Lambda 1}$ = This term = 0 for $\Lambda \neq 1$. This imposes the condition that Σ surfaces ($\Lambda=0$) are unreactive and that Π surfaces ($\Lambda=1$) are reactive.
- P_r = The reactive probability. This factor will be assumed to be constant for all $^3\Pi$ surfaces and is, conveniently, set to unity if only relative probabilities are required.

$\delta_{\Omega,\Omega'+\Sigma''}$ = This term ensures Ω-conservation from short to medium range in the exit channel. The outcome, imposed by the Kronecker

delta is either 1 or 0 according to the correlations drawn in Figure 5.8.

Equations (5.3)-(5.5) were applied to the reactive system to yield the relative OH spin-orbit state ratio for each $O(^3P_j)$ state. These results are given in Table 5.3. The reactive fraction originating from each j state (i.e. the ratio which tells us how many of the surfaces lead to reaction) is also given here. This table of results reveals how individual j states react. Take the $O(^3P_{j=2})$ state as an example: Table 5.3 shows that all five (5/5) surfaces lead to reaction and the resultant OH $^2\Pi_{3/2}$:$^2\Pi_{1/2}$ ratio is 4:1. In contrast, only one surface originating from $^3P_1$ (1 out of 3) is reactive, yielding an OH $^2\Pi_{3/2}$:$^2\Pi_{1/2}$ ratio of 0:1

Equation (5.2) is used to determine a value for the OH spin-orbit state ratio from a particular distribution of $O(^3P_j)$ states. This is done by applying experimental $O(^3P_j)$ distributions to the data in Table 5.3. $O(^3P_j)$ can be produced in an effusive source, such as that used by Andresen and Luntz[2] and by Whitehead *et al*[23], generating a thermal $O(^3P_j)$ distribution. However in this present work[1], laser photolysis of NO_2 was used to generate the $O(^3P_j)$ reagent. Direct measurements have been made of the $O(^3P_j)$ distributions with several different photolysis wavelengths within the relevant UV band[24,25] and have given consistently similar results. It has therefore been assumed that the same distribution applies for all the photolytically generated $O(^3P_j)$ atoms, regardless of the specific wavelength used. The respective thermal and photolytically produced initial j-state distributions are given in Table 5.4. There is not much difference between the distributions, presumably because the degeneracy and energy factors cooperate for an inverted multiplet like $O(^3P_j)$. Consequently any differences in j-dependent results, following either effusive or photolytic generation of $O(^3P_j)$, are likely to be small.

$O(^3P_j)$	Reactive Fraction Model			$^2\Pi_{3/2}:^2\Pi_{1/2}$ Ratio Model		
	1	2	3	1	2	3
j = 2	5 / 5	5 / 5	3½ / 5	4 : 1	3 : 2	2½ : 1
j = 1	1 / 3	1 / 3	2 / 3	0 : 1	0 : 1	½ : 1½
j = 0	0 / 1	0 / 1	½ / 1	0 : 0	0 : 0	0 : ½

Table 5.3: Predicted relative reactivities (of individual j-states) and subsequent OH $^2\Pi_{3/2}:^2\Pi_{1/2}$ ratios for $O(^3P_j)$+HR correlation Models 1, 2 and 3 described in the text. The reactive fraction determines how many of the available surfaces are reactive. For example for $O(^3P_{j=1})$: for the limits set by Model 1, 1 out of the 3 surfaces is reactive and hence 2 out of 3 are unreactive. The subsequent ratio of product OH $^2\Pi_{3/2}:^2\Pi_{1/2}$ surfaces is 0:1.

Source	$O(^3P_j)$ Distribution			$^2\Pi_{3/2}:^2\Pi_{1/2}$ Ratio			
				Model			Experiment [c]
	j=2	j=1	j=0	1	2	3	
UV Photolysis [a]	0.82	0.16	0.02	3.02	1.29	1.72	1.78 (i-C_4H_{10}) [d] 1.62 (i-C_4H_{10}) [e] 1.75 (i-C_4H_{10}) [f] 1.64 (c-C_6H_{12}) [f] 1.75 (C_2H_6) [f] 1.55 (CH_4) [f]
Thermal [b]	0.72	0.22	0.06	2.65	1.20	1.40	1.68 (c-C_6H_{12}) [g] ~1.4 (c-C_6D_{12}) [h]

(a) Average $O(^3P_j)$ distribution from NO_2 photolysis at 355, 337 and 266nm,[24] very similar to those quoted independently[25] at 355 and 266nm.

(b) Thermal (300 K) distribution, as justified in ref. [2].

(c) Ratios corrected for the (2J'+1) spatial degeneracy, as described in the text. Results are averages over all N', with weightings according to the statistical uncertainties where these were available.

(d) NO_2 photolysis at 337nm.[1]

(e) NO_2 photolysis at 308nm.[1]

(f) NO_2 photolysis at 248nm.[1]

(g) Average of OH(v'=0) data in Fig. 6 of ref. [2].

(h) Value quoted in ref. [2].

Table 5.4: Comparison of the experimentally observed $^2\Pi_{3/2}:^2\Pi_{1/2}$ ratios for OH(v'=0)[3] from $O(^3P_j)$+HR reactions with the predictions obtained from Models 1, 2 and 3, described in the text.

The product OH spin-orbit state ratio for Model 1, obtained using Equation (5.2), is given in Table 5.4. The actual experimental N′-dependent $^2\Pi_{3/2}$:$^2\Pi_{1/2}$ ratios are also shown here. To clarify the comparison between predicted and experimental data, these results are illustrated pictorially in Figure 5.2, where $^2\Pi_{3/2}/^2\Pi_{1/2}\times N'(N'+1)$ is plotted against N′. Clearly the predictions are very different to the experimental results irrespective of the method of $O(^3P_j)$ production. Typically the predicted values are two times greater than the experimental values. Hence Model 1 does not sufficiently explain the experimental observations.

5.3.2 Model 2: Relaxation of Strong Spin-Orbit Coupling in the Exit Channel

Fully adiabatic correlations do not appear to explain the observed OH spin-orbit state ratio. The basis for Model 2 relies on determining where the constraints applied to Model 1 fail on physical grounds. This is most likely to occur in the exit channel as discussed in the following text.

In the OH+R reaction the important interactions at long and short range can be clearly defined. At long range the internal spin-orbit coupling within OH outweighs the (initially) weak interaction between the spin 1/2 of the organic radical fragment and the distant OH molecule. This leads to formation of four doubly degenerate surfaces (Ω=2,1,1 and 0) as described in Section 5.2.2. At very close range the electrostatic interaction dominates. The coupling regime transforms to Hund's case (a) and individual spins couple to form a total resultant S with a well defined projection, Σ, onto the intermolecular axis.

Hence the ambiguous area is the description at intermediate range where electrostatic interaction and spin-orbit coupling are comparable. In Model 1 it was assumed that the long and short range surfaces connected in order of

increasing energy whilst conserving Ω. In Model 2 it is proposed that the strong spin-orbit coupling, (j,Ω), limit no longer applies to the exit channel. The Ω-conserving constraint is still retained but surfaces with the same Ω are allowed to mix. In practice this means that both of the Ω=1 long range surfaces correlate partially, with equally divided probabilities, to the reactive, $^3\Pi$, and unreactive, $^1\Pi$, surfaces as shown in Figure 5.10. The reactant correlations of Model 1 are retained. The limits set by Model 2 suggest that dissociation of the $^3\Pi_1$ intermediate populates both OH $^2\Pi_{3/2}$ and OH $^2\Pi_{1/2}$ equally. This is obviously different to the outcome predicted by Model 1 where dissociation of $^3\Pi_1$ yielded only OH $^2\Pi_{3/2}$. Allowing non-adiabatic mixing in the exit channel has no effect on the unambiguous long range to short range Ω-conserving correlations from the Ω=2 surfaces to $^3\Pi_2$ and from Ω=0 to $^3\Pi_0$.

The relaxation of the strong spin-orbit coupling constraints can be justified in at least two ways. One viewpoint which could explain the non-adiabatic mixing is the effect of Ω-conserving kinetically-induced couplings which are the basis of Model 3, discussed in great detail in Section 5.3.3. Kinetically-induced couplings have been rigorously calculated by Aquilanti *et al*[17] for the entrance channel, but unfortunately no such experimental quantification has been done for the exit channel. Hence the magnitude of the couplings pertaining to the OH+R system is not known. However the O(^{3}P)+HR reaction (except where HR=CH_4) is exothermic and therefore the recoil velocity of the separating products will be higher than the approach velocity of the reactants. The magnitudes of kinetically-induced couplings are dependent on velocity so if couplings occur in the entrance channel then they are also likely to occur (probably with greater probability and strength) in the exit channel because the product fragments are moving rapidly.

Alternatively, the effects of spin conservation could be used to explain the non-adiabatic treatment of the exit channel. The standard Clebsch-Gordan

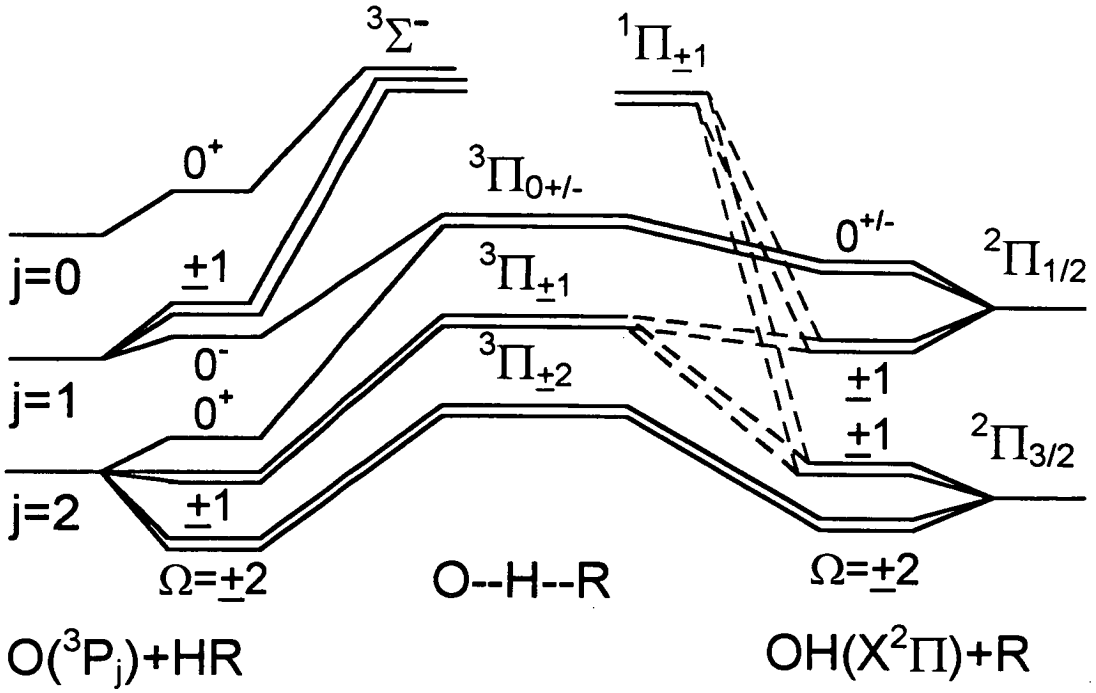

Figure 5.10: Model 2: schematic, Ω-conserving correlation diagram for collinear $O(^3P_j)$+HR reactions. There is selective non-adiabatic mixing in the exit channel. Coupled Ω=1 surfaces are indicated by dashed lines. The energetic separations are not to scale.

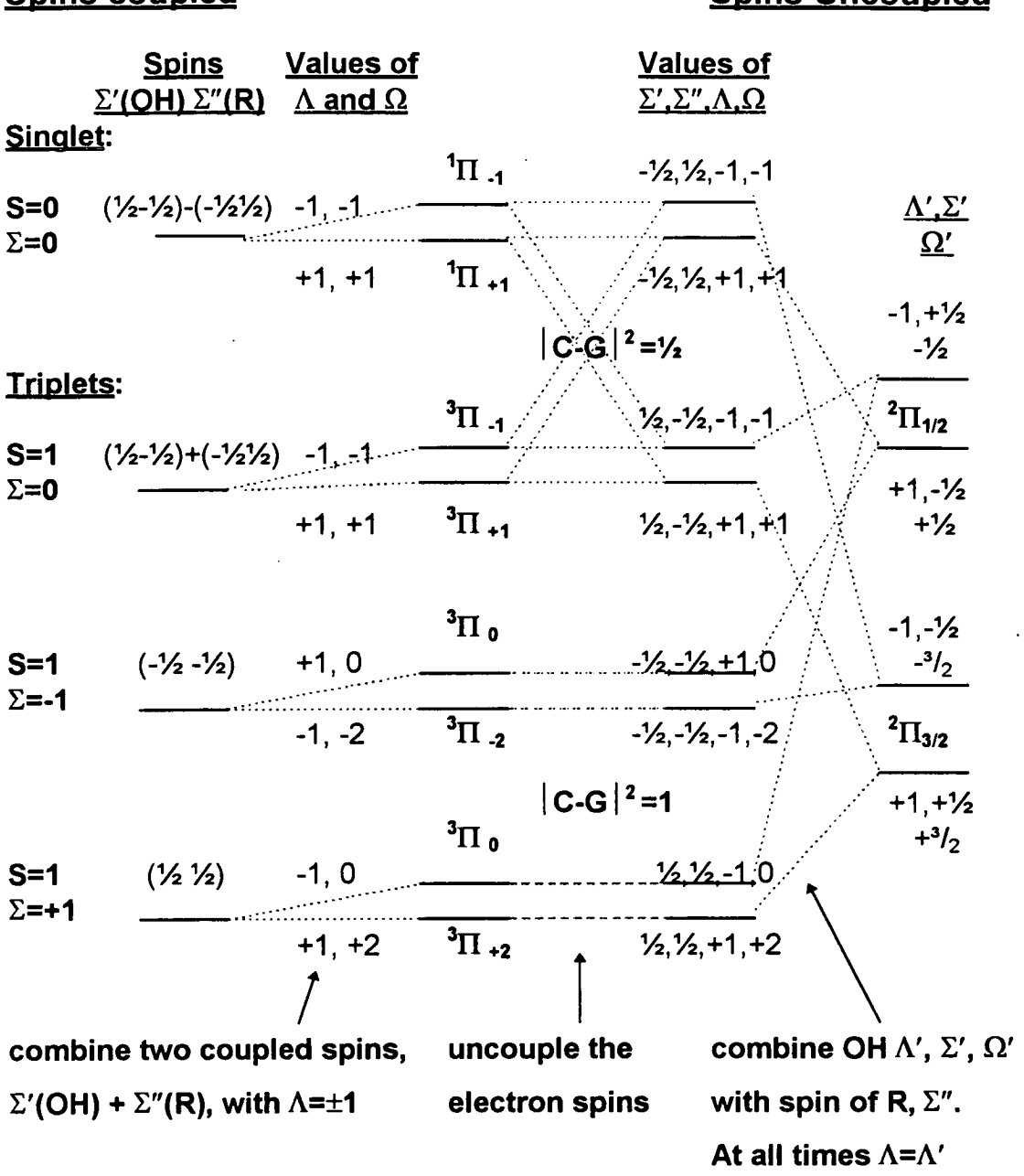

Figure 5.11: Spin coupled (LHS) and uncoupled (RHS) representations for OH($^2\Pi$) and R($^2\Sigma^+$), showing how two spin=1/2 fragments recouple to form $^3\Pi$ and $^1\Pi$, as described in the text. |C-G| is shorthand for the Clebsch-Gordan coefficient; hence $|C\text{-}G|^2$ gives a probability. On the LHS of the diagram only the spins of OH (Σ') and R (Σ'') are considered (no Λ). The RHS shows isolated OH with no R (Λ',Σ').

5.3.3 Model 3: Non-Adiabatic Coupling of Both Entrance and Exit Channel Surfaces

It has been established in the preceding text that neither a fully adiabatic correlation nor partial (exit channel) mixing sufficiently explain the observed OH spin-orbit state ratios. In Model 3 non-adiabatic effects in the entrance channel will be considered.

Aquilanti *et al* have very thoroughly characterised the entrance channel surfaces and the subsequent couplings in $O(^3P_j)+H_2/CH_4$ collisions[17]. In their experiments the spin-orbit dependence of the long range part of the potential energy surface was assessed by molecular beam scattering studies, with preparation of the magnetic sublevels. Adiabatic, Ω-conserving surfaces were derived and it was concluded that an adiabatic description explains the **total** scattering data for the range of collision energies spanned by their experiments.

However, in this work, we are primarily concerned with potentially **reactive collisions** where the activation energy barrier is surmounted. Such low impact parameter collisions must have higher line-of-centres collision energies than those encompassed by Aquilanti *et al*, who effectively only considered the long range interactions associated with **non-reactive collisions**. Hence for the reactive system ($O(^3Pj)$+HR) it is necessary to assess whether an adiabatic description is valid.

A range of different approaches can be used to determine whether the reactive collision between $O(^3P_j)$ and HR, under the reaction conditions specified in Chapters 2 and 4, follows an adiabatic or non-adiabatic pathway.

In their work[17] Aquilanti *et al* presented the Schrödinger equation for the scattering of an O atom by a collision partner as:

$$\left(\frac{-\hbar^2}{2\mu}\left(\mathrm{I}\frac{d}{dR}+P(R)\right)^2+V(R)+\frac{\bar{l}(\bar{l}+1)}{2\mu R^2}\mathrm{I}\right)\overline{\psi}=E\overline{\psi} \qquad (5.6)$$

In Equation (5.6):

- μ = Reduced mass of the system.
- R = Distance between collision partners.
- V(R) = Adiabatic potential energy, measured when the system is stationary. This term contains electrostatic and spin-orbit interactions.
- $\bar{l}$ = Effective orbital angular momentum. l has been averaged to $\bar{l}$ using the centrifugal sudden approximation.
- $\frac{\bar{l}(\bar{l}+1)}{2\mu R^2}$ = Centrifugal potential associated with the orbital motion of one heavy partner around another. In the case of reactive collisions between $O(^3P)$ and HR the centrifugal potential can be neglected because it is assumed that the reaction geometry is near collinear.
- $-\frac{\hbar^2}{2\mu}\left(\mathrm{I}\frac{d}{dR}+P(R)\right)^2$ = Non-adiabatic coupling arises from the $P(R)$ matrix contained within this part of Equation (5.6). This expression may be expanded into several distinct contributions as shown below:

$$\frac{\hbar^2}{2\mu}\left(\frac{d^2\psi}{dR^2}\right)+\frac{\hbar^2}{\mu}\frac{d\psi}{dR}P(R)+\frac{\hbar^2}{2\mu}P(R)^2$$

In this expanded term:

$\frac{\hbar^2}{2\mu}\left(\frac{d^2\psi}{dR^2}\right)$ = Kinetic operator for motion along R.

$P(R)^2$ = One of the terms which contributes to the non-adiabatic coupling. This quantity is independent of velocity.

$\frac{\hbar^2}{\mu}\frac{d\psi}{dR}P(R)$ = This is normally the dominant contribution to the kinetically-induced coupling[27]. The operation of $\frac{d}{dR}$ on the translational wavefunction, ψ, recovers a term proportional to the local reduced momentum, $i\frac{\mu v(R)}{\hbar}$, hence the $\frac{d\psi}{dR}P(R)$ term is velocity dependent.

To determine whether adiabatic or non-adiabatic effects dominate in the O(^{3}P)+HR system it is necessary to assess the value and relevance of non-adiabatic coupling for a particular set of experimental conditions. This procedure has been carried out by Aquilanti *et al*[17] and applied to O(^{3}P)/HR **collisions** (entrance channel of reactive system). The results obtained are here reinterpreted for O(^{3}P)/HR **reactions**.

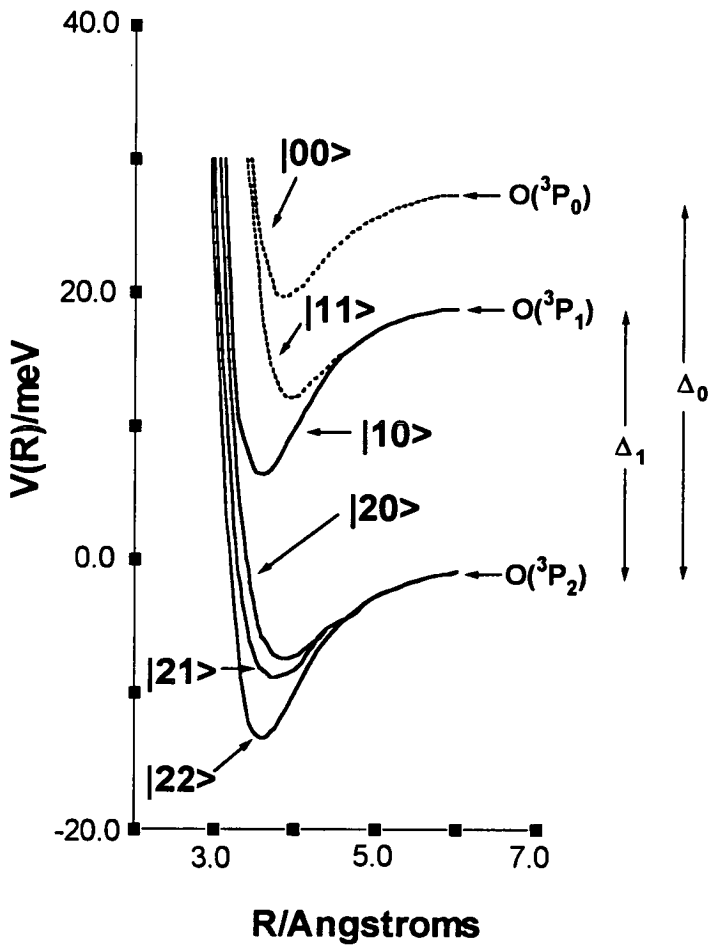

Figure 5.12: Adiabatic potential energy curves for the interaction between $O(^3P_j)$ and CH_4, reproduced from ref. [17]. The curves, which correlate with the different atomic sublevels of $O(^3P_j)$ as shown, are labelled according to the Hund's case (c) $|j\Omega>$ basis described in the text. At short range the dashed curves are of Σ symmetry and the full curves are of Π symmetry.

Aquilanti *et al*[17] established that the strength of the non-adiabatic coupling is $P(R)$, but the probability of coupling between two states depends on the product of $P(R)$ and velocity, as shown in Equation (5.6). This means that even if $P(R)$ is large, transitions will not occur if $v(R)=0$. Figure 5.12 is reproduced from ref. [17] and shows the adiabatic potential energy curves for the $O(^3P_j)+CH_4$ collision, labelled according to a $|j\Omega>$ basis. Coupling is allowed to occur between states with different values of j but Ω must always be conserved. In practice the only non-zero coupling matrix elements ($P(R)$) are between the $|j\Omega>$ pairs $|21> - |11>$ and $|20> - |00>$. These couplings, which are responsible for transfer between $^3P_2 - ^3P_1$ and $^3P_2 - ^3P_0$ respectively, are dependent on the collision velocity. The $|20>$ and $|10>$ states cannot couple due to the different parity of the Ω=0 states.

Aquilanti *et al* identified that the coupling matrix element, $P(R)$, which can also be expressed as $< j\Omega\left|\frac{d}{dR}\right|j'\Omega >$, is dependent on two factors:

1. The asymptotic gaps between the two coupled states ($|21> - |11>$ and $|20> - |00>$). Δ_0 and Δ_1 are the respective energy differences between $^3P_2 - ^3P_0$ and $^3P_2 - ^3P_1$
2. The exact result for the values of $P(R)$ for the $|20> - |00>$ and $|21> - |11>$ couplings are expressed in Equations (5.7a) and (5.7b):

$$\left\langle 20\left|\frac{d}{dR}\right|00\right\rangle = P_{20,00} = \frac{-10/\sqrt{2}}{9\beta_0^2 - 10\beta_0 + 25}\frac{d\beta_0}{dR} \qquad (5.7a)$$

$$\left\langle 21\left|\frac{d}{dR}\right|11\right\rangle = P_{21,11} = \frac{-15/2}{9\beta_1^2 + 25}\frac{d\beta_1}{dR} \qquad (5.7b)$$

In Equations (5.7a) and (5.7b):

$\beta_0 = V_2/\Delta_0$ and $\beta_1 = V_2/\Delta_1$

$V_2=5/3(V_\Sigma-V_\Pi)$

Hence $P(R) \propto \frac{dV_2}{dR}$ which means that $P(R)$ is dependent on the rate at which the Σ and Π surfaces diverge. If these surfaces diverge slowly, relative to the velocity of the system, in the region where the coupled curves are close to one another then the system has time to follow the adiabatic surfaces and accordingly, an adiabatic description applies. Conversely, if they diverge rapidly relative to the velocity of the system then the system won't have time to correctly "choose" adiabatic surfaces and a non-adiabatic description will therefore be applicable

Aquilanti and co-workers calculated the non-adiabatic terms that couple the $|21\rangle - |11\rangle$ and $|20\rangle - |00\rangle$ states for the $O(^3P)/CH_4$ system. Their results, in the form of a plot of P against R, are reproduced in Figure 5.13. Table 5.5, composed from data given in ref. [17], gives the values and locations of the maximum of the $P(R)$ function, P_{max} and R_{max}, for both the $|21\rangle - |11\rangle$ and $|20\rangle - |00\rangle$ couplings. It should be noted that the actual transition probability is $P(R)^2$.

In their work Aquilanti *et al*[17] state that the $P(R)^2$ term is sufficiently small to be ignored. We have inferred from their text that they also disregard any contribution to non-adiabatic effects from the $\frac{d}{dR}P(R)$ term. Accordingly they used adiabatic potentials to describe collisions between $O(^3P_j)$ and CH_4. This approximation is valid for their work where the effects of large impact parameter collisions were being examined. In such collisions the orbital angular momentum, l, is sufficient to reduce the kinetic energy along the line-of-centres, thus making $\frac{d}{dR}P(R)$ small. However in this present work, the behaviour of reactive collisions with small impact parameters is being assessed. In these instances centrifugal effects can be neglected, but the

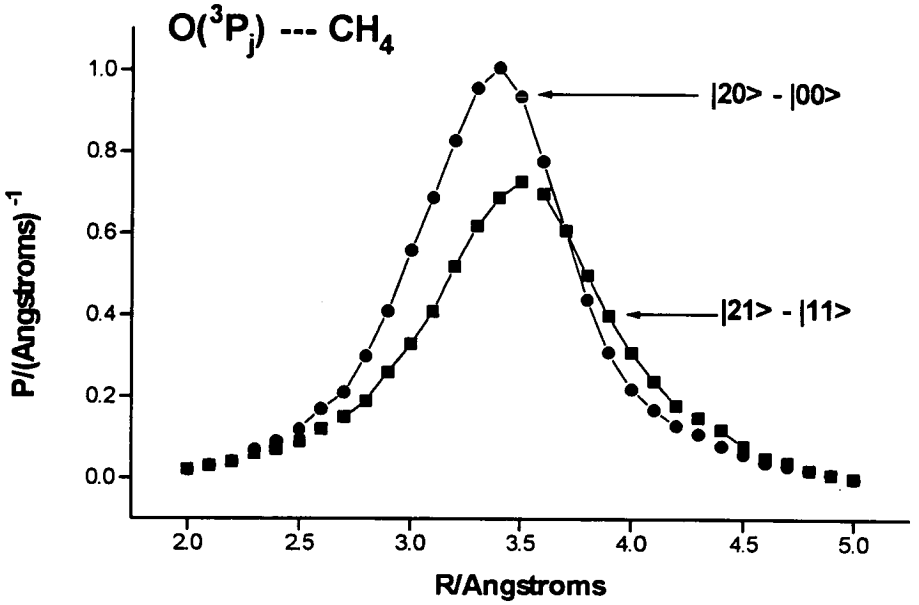

Figure 5.13: Plot of the non-adiabatic coupling terms, P, versus R, the interatomic distance for the coupled states in the $O(^3P_j)+CH_4$ interaction. Reproduced from ref. [17].

(■) represents |20> – |00> transfer

(●) represents |20> – |00> transfer

The plot encompasses the coupling region of 2.0–5.0Å. The maximum of the $P(R)$ function, which occurs at R=3.40Å for $P_{20,00}$ and at R=3.50Å for $P_{21,11}$, marks the point where the coupling case nominally switches from Hund's case (c) to Hund's case (a). This occurs when V_2, the term which is dependent on the distance between the Σ and Π surfaces, is of the order of the fine structure splitting in isolated $O(^3P_j)$.

$O(^3P_j)+CH_4$:	R_{max} / Å	P_{max} / $Å^{-1}$	P_{max}^2 / $Å^{-2}$
$P_{20,00}$	3.40	1.02	1.0404
$P_{21,11}$	3.50	0.73	0.5329

Table 5.5: Location and value of the maximum of the $P(R)$ function for the $O(^3P_j)+CH_4$ interaction. The transition probability at the function maxima, P_{max}^2, is also given. Data taken from ref. [17].

line-of-centres velocity must be sufficient to surmount the activation barrier. Therefore, the velocity dependent $\frac{d}{dR}P(R)$ term is potentially important and its contribution to non-adiabatic coupling must be determined. Time-dependent perturbation theory can be used to assess whether an adiabatic or non-adiabatic description is valid for this type of collision.

First-order perturbation theory allows calculation of transition probabilities. Equation (5.8) can be used to show how a two-level system reacts to a perturbation. In this case the time-dependent perturbation is transfer between two states, i and k. At time=zero, only state i is populated.

$$i\hbar\frac{dc_k^{(1)}}{dt} = \hat{V}_{ki}(t)e^{\frac{i}{\hbar}(E_k - E_i)t} \qquad (5.8)$$

In Equation (5.8):

- $c_k^{(1)}$ = Probability amplitude that state i will transfer to state k.
  $\left|c_k^{(1)}\right|^2$ = probability
- $\frac{dc_k^{(1)}}{dt}$ = Rate at which the population of k changes with time.
- $\hat{V}_{ki}(t)$ = Time-dependent strength of coupling (perturbation) between states i and k. This term has the dimensions of energy.
- E_i and E_k = Energies of states i and k.

If $\hat{V}_{ki}(t)$ is known and integrated over time then $c_k^{(1)}$ is obtained. Squaring this quantity gives the probability of being in state k. We do not know directly the time-dependent function $\hat{V}_{ki}(t)$, but Aquilanti *et al*[17] have

calculated the magnitude of the coupling strength as a function of distance. Hence by using the simple relation, velocity=distance/time, $c_k^{(1)}$ can be expressed explicitly as a function of distance, R , as shown in Equation (5.9):

$$c_k^{(1)}(R') = \int_{\infty}^{R'} \frac{\hat{V}_{ki}(R)}{i\hbar v(R)} e^{\frac{i}{\hbar v(R)}(E_k - E_i)R} dR \qquad (5.9)$$

In Equation (5.9) $v(R)$ is the local velocity along the line-of-centres and is approximated to be constant. This is a good approximation because the depths of the (weakly attractive) potentials, in the region of R in which $P(R)$ is significant, are small compared to a typical collision energy sufficient to cause reaction[17]. It is also assumed that R decreases from infinity at the earliest times. Small differences in the R-dependence of the coupled surfaces are neglected by fixing the $E_k - E_i$ values to the asymptotic spin-orbit splittings, shown in Figure 5.12.

Simple perturbation theory allows calculation of, for example, transition probabilities to higher surfaces than those asymptotically connected to $O(^3P_2)$. States i and k can be identified as entrance channel surfaces in $O(^3P_j)+CH_4$ collisions. As discussed above, we know that the dominant contribution to the coupling between two states is a velocity dependent term, $\frac{\hbar^2}{\mu}\frac{d\psi}{dR}P(R)$. This term can be expanded and substituted for $\hat{V}_{ki}(R)$ in Equation (5.9). Subsequent cancellation of terms yields Equation (5.10):

$$c_k^{(1)}(R') = \int_{\infty}^{R'} P(R) e^{\frac{i}{\hbar v(R)}(E_k - E)R_i} dR \qquad (5.10)$$

Equation (5.10) can be expanded into sin and cos terms and the square modulus taken, yielding the first order transition probabilities as shown in Equation (5.11):

$$\left|c_k^{(1)}(R')\right|^2 = \left|\int_{\infty}^{R'} P(R)\sin\left(\frac{(E_k - E_i)}{\hbar v(R)}R\right)dR\right|^2 + \left|\int_{\infty}^{R'} P(R)\cos\left(\frac{(E_k - E_i)}{\hbar v(R)}R\right)dR\right|^2 \qquad (5.11)$$

This integral (Equation (5.11)) can be used to illustrate what will happen to the transition probability as a function of velocity. Transfer between the $|21\rangle$ and $|11\rangle$ states is taken as an example. The sin and cos functions for a particular velocity can be calculated and plotted as a function of R. These plots can then be superimposed onto a $P_{21,11}(R)$ versus R plot. (The $P_{21,11}(R)$ and $P_{20,00}(R)$ versus R plots are illustrated in Figure 5.13) to show how much the sin and cos functions vary within the coupling region. If the velocity is low with respect to the energy gap, $E_k - E_i$, then the sin and cos functions oscillate rapidly through the coupling region, with positive and negative components, and the total integral of the product of these functions tends to zero. The corresponding transition probability will be low. In contrast, if the velocity is large with respect to the energy gap then the frequencies of the sin and cos functions are much slower and don't vary much in the coupling region. In this instance a finite integral is obtained indicating that transfer is highly probable. Figures 5.14(a) and 5.15(a) show the subsequent plots obtained at $v(R)$=1000 and 3000ms^{-1} respectively. These plots show that a three-fold increase in the velocity causes a three-fold decrease in the frequency of the sin and cos periods. Hence as the collision velocity increases the sin and cos functions oscillate less and the resulting integrals become finite.

The sin and cos functions were each integrated over the coupling region (2.0Å$\leq R \leq$5.0Å, $dR = 0.1$Å), multiplied by $P(R)$, squared and then added

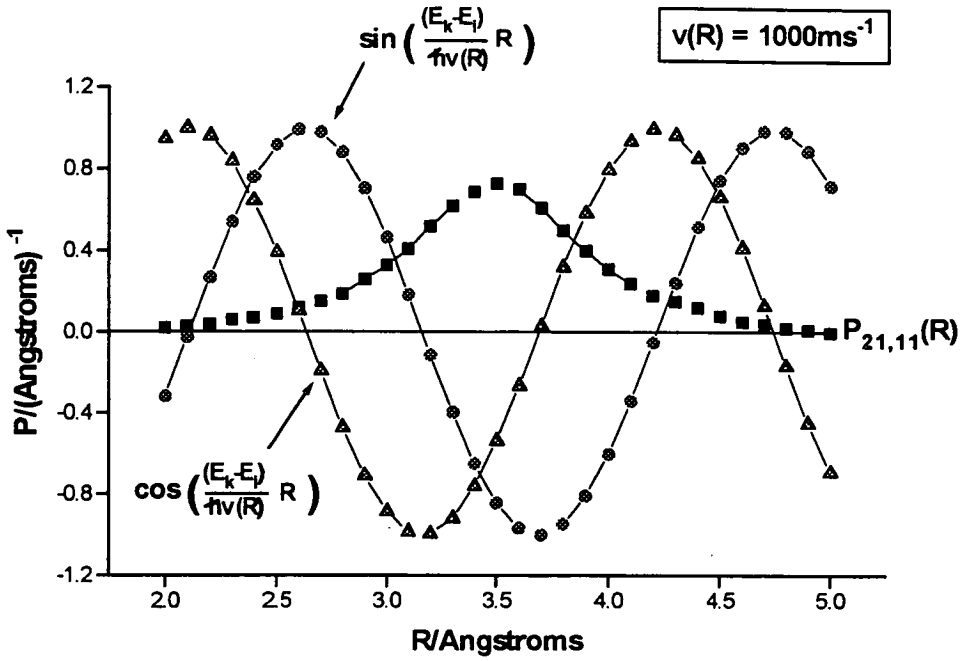

Figure 5.14(a): This figure shows how the coupling strength, $P(R)$, varies with R, the interatomic distance, for inelastic transfer between the |21> and |11> |jΩ> states, in the $O(^3P_j)+CH_4$ interaction. Superimposed over this plot are the sin and cos functions obtained when $v(R)$=1000ms^{-1} using Equation (5.11), thus showing how the sin and cos components of the transition probability vary throughout the coupling region.

(■) - $P_{21,11}(R)$ function from ref. [17]

(●) - sin function

(▲) - cos function

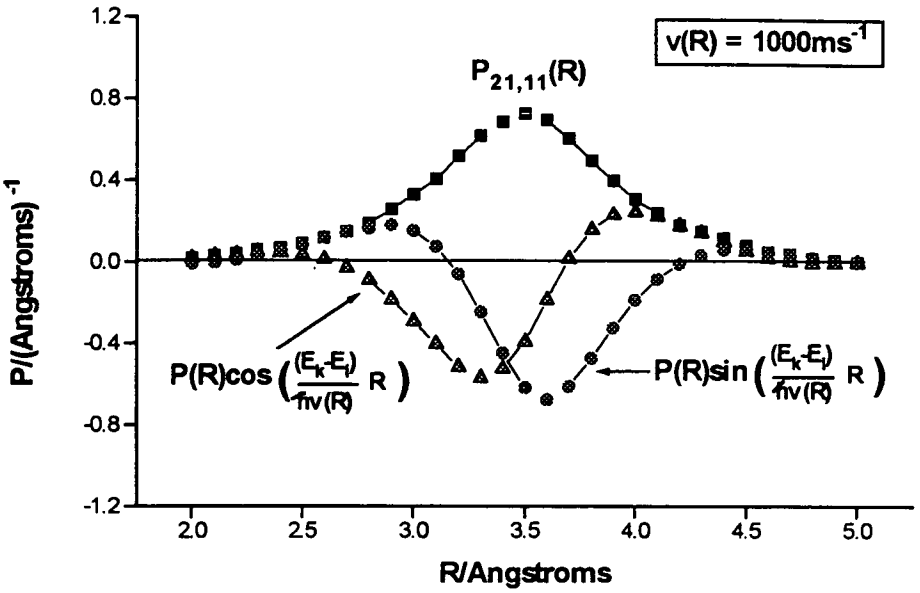

Figure 5.14(b): This figure shows the resultant functions obtained when the sin and cos components, given in Figure 5.14(a), are multiplied by $P(R)$. Taking the sin plot as an example: for a collision velocity of 1000ms^{-1} there are both positive and negative terms in the $P(R)\sin$ function which, when summed, will partially cancel each other. The overall summation will give a small but finite negative number. The cos plot gives a similar (in fact, smaller) result. Squaring and summing together these results yields a small transition probability.

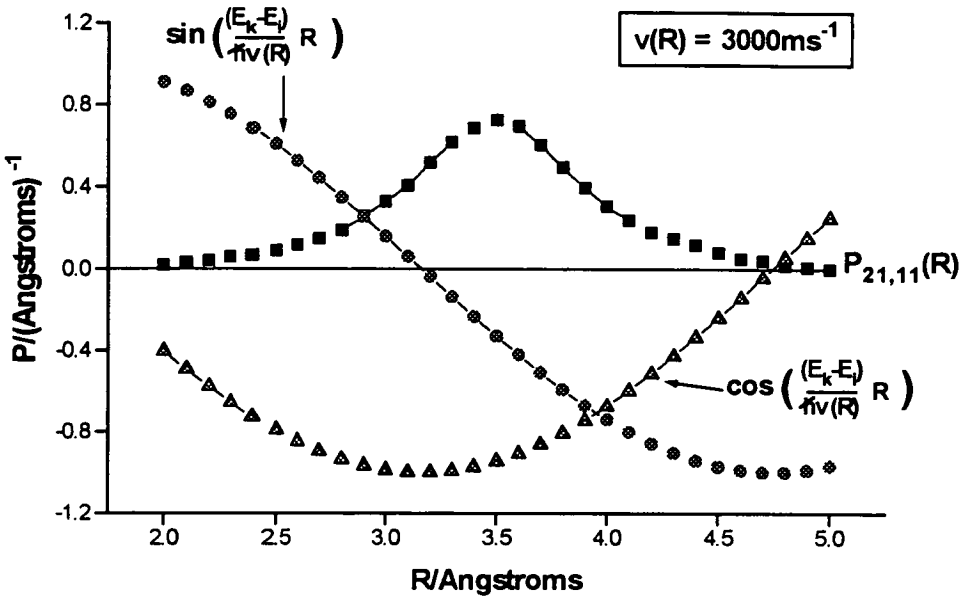

Figure 5.15(a): This figure shows how the coupling strength, $P(R)$, varies with R, the interatomic distance, for inelastic transfer between the |21> and |11> |jΩ> states, in the $O(^3P_j)+CH_4$ interaction. Superimposed over this plot are the sin and cos functions obtained when $v(R)$=3000ms^{-1} using Equation (5.11), thus showing how the sin and cos components of the transition probability vary throughout the coupling region. On comparison with Figure 5.14(a) it is clearly evident that the sin and cos functions oscillate more slowly here; neither of them complete a period in the coupling region. This effect is caused by increasing the collision velocity to 3000ms^{-1}.

(■) - $P_{21,11}$(R) function from ref. [17]

(●) - sin function

(▲) - cos function

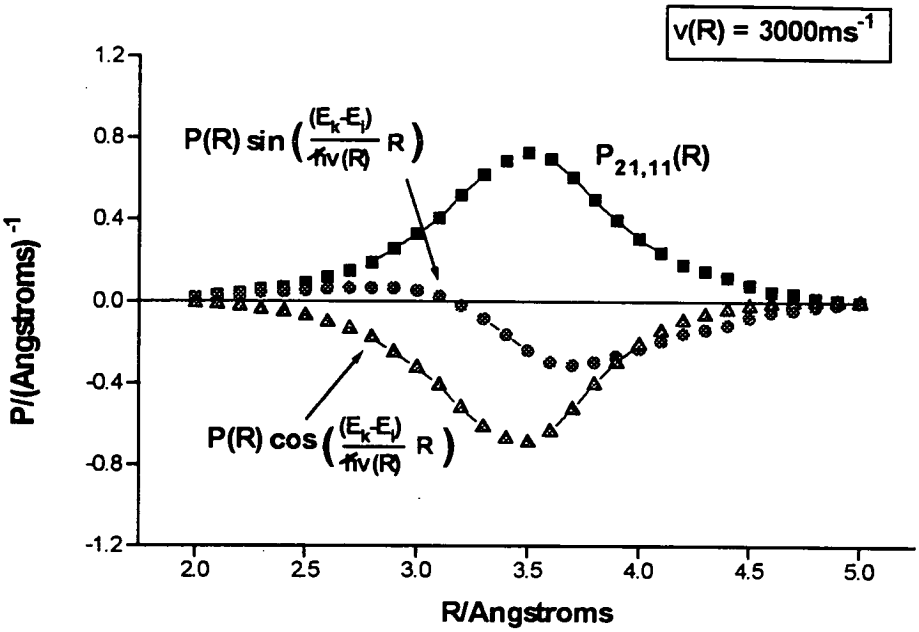

Figure 5.15(b): This figure shows the resultant functions obtained when the sin and cos components, given in Figure 5.15(a), are multiplied by $P(R)$. Taking the cos plot as an example: for a collision velocity of 3000ms^{-1} there are only negative terms in the $P(R)\cos$ function which, when summed, will give a large negative number. The sin plot, which is mostly negative, gives a similar result. Squaring and summing together these results yields a large transition probability.

together to give the final result $\left|c_k^{(1)}(R')\right|^2$, as explained in Equation (5.11). Figures 5.14(b) and 5.15(b) depict the $P_{21,11}(R) \times \sin\left(\frac{(E_k - E_i)}{\hbar v(R)} R\right)$ versus R and $P_{21,11}(R) \times \cos\left(\frac{(E_k - E_i)}{\hbar v(R)} R\right)$ versus R plots, which were used to obtain the transition probabilities at velocities of 1000 and 3000ms^{-1} respectively. This procedure was carried out for a range of collision velocities, 500 to 5000ms^{-1} and for transfer between both $|j\Omega\rangle$ pairs $|20\rangle - |00\rangle$ and $|21\rangle - |11\rangle$.

Figure 5.16 shows a plot of the integrated inelastic transition probabilities, $|c_k^{(1)}|^2$ against collision velocity for $O(^3P_2)$ collisions with CH_4, obtained using Equation (5.11). The velocity dependencies of transfer between both $|20\rangle - |00\rangle$ and $|21\rangle - |11\rangle$ $|j\Omega\rangle$ states are illustrated. Taking a collision velocity of 1000ms^{-1} as an example, this plot shows that for the $|21\rangle - |11\rangle$ coupling approximately 8% of the population will transfer from $O(^3P_{j=2})$ to $O(^3P_{j=1})$. This represents a small perturbation. However, when the collision velocity is 3000ms^{-1} a large perturbation must occur because roughly 50% appears to transfer. This value must only be taken approximately since the perturbation is obviously large and hence no longer in the region where a first order correction applies. The principal conclusion which can be drawn from this figure is that the transfer probability becomes large with velocities well below those needed to surmount the barrier to the reaction. The calculated[7] and kinetically determined[28-30] activation energies for the $O(^3P)+CH_4$ reaction typically exceed 40kJmol^{-1} which is equivalent to a collision velocity of over 3000ms^{-1}. This is far in excess of the velocity at which transfer (between $^3P_2 - {}^3P_1$ and $^3P_2 - {}^3P_0$) becomes feasible. For the other hydrocarbons the reaction barriers are lower but, in general, the centre-of-mass collision velocities were higher, irrespective of the nature of $O(^3P_j)$ production, for purely kinematic reasons[1]. Assuming that the

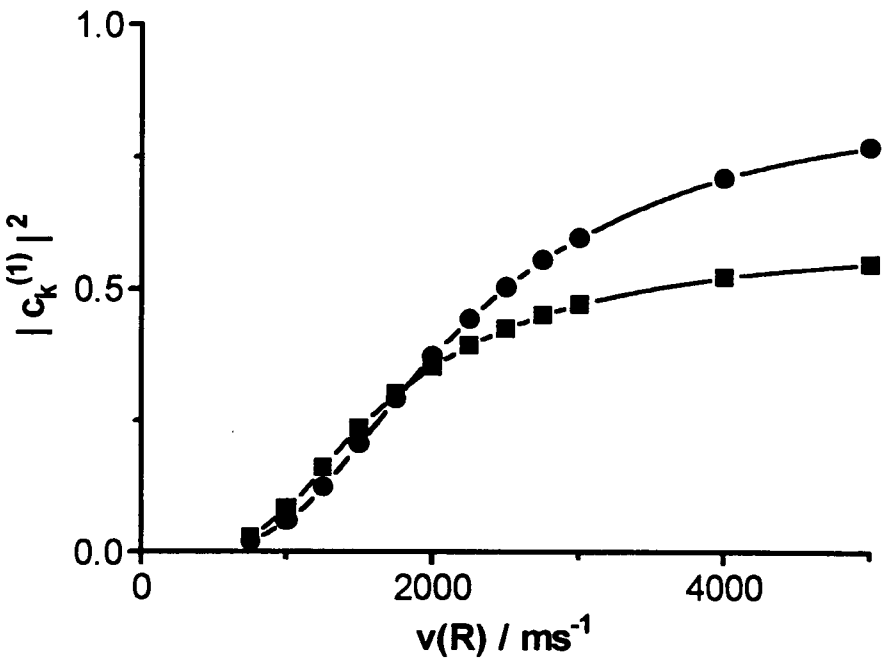

Figure 5.16: Plot of first-order perturbation theory estimates of integrated inelastic transition probabilities, $\left|c_k^{(1)}\right|^2$, against velocity, $v(R)$, for $O(^3P_j)$ collisions with CH_4. This data was generated using Equation (5.11) in the text.

(■) represents $^3P_2 - {}^3P_1$ transfer.

(●)represents $^3P_2 - {}^3P_0$ transfer.

coupling matrix elements for all HR studied are comparable to those for methane it is safe to say that the reactive collisions are substantially affected by non-adiabatic coupling.

An alternative technique which can used to assess whether the reactive collisions are adiabatic or non-adiabatic is to make an estimate using a Massey-type parameter[27] of the type shown in Equation (5.12). The form of this expression can be derived from the relative timescales of electronic and nuclear motion. Non-adiabatic effects can be neglected when:

$$\gamma = \left| \frac{P(R)\hbar v(R)}{E_k - E_i} \right| << 1 \qquad (5.12)$$

In Equation (5.12), v(R) is the collision velocity, E_i and E_k are the energies of the two, in this case, spin-orbit states (for example $O(^3P_2)$ and $O(^3P_1)$) and P(R), the non-adiabatic coupling element, is representative of the strength of the coupling.

However for $O(^3P_2)+CH_4$ collisions, where v(R)=3000ms^{-1}, $\gamma \approx 1$ for either $|21> - |11>$ or $|20> - |00>$ transfer when the respective non-adiabatic coupling elements, P(R), are at their maxima[17]. (This data, P_{max}, is given in Table 5.5.) These values of γ do not satisfy the condition set by Equation (5.12) so it is surmised that non-adiabatic effects cannot be neglected. The Massey parameter is effectively a measure of the ratio of the characteristic time required for distinguishing states to the collision time. If γ is a very small number (<<1) then the spin-orbit states are well defined. If $\gamma \approx 1$ then the states have insufficient time to be correctly defined and mixing occurs.

Finally, separate studies of inelastic j-changing collisions of $O(^3P)$ with hydrocarbons and other simple molecules[18-21] lend support to the conclusion that non-adiabatic mixing occurs in these processes. In fact, attempts to

measure directly the relative reactivities of individual j states have not been successful[30]. These observations are not compatible with the absence of non-adiabatic mixing in the entrance channel, as suggested by Models 1 and 2.

Model 3 has been devised to account for non-adiabatic effects in the entrance channel. This model contains similar concepts to those proposed by Ma and Liu[20] who studied the inelastic conversion between $O(^3P_2)$ and $O(^3P_{1,0})$ following collisions with He and H_2. Aquilanti *et al*[17] provided the coupling strengths, for transfer between $|21\rangle - |11\rangle$ and $|20\rangle - |00\rangle$, as a function of R for the interaction between $O(^3P_j)$ and H_2. Ma and Liu examined these $P_{21,11}(R)$ and $P_{20,00}(R)$ values and concluded that the magnitude of the couplings were approximately equal. However the actual transfer probability depends on $P(R)^2$, not simply P(R). The values of P(R) and $P(R)^2$ at the maxima of the functions for both couplings, $|21\rangle - |11\rangle$ and $|20\rangle - |00\rangle$ are given in Table 5.5. The data in Table 5.5 shows that, at the function maxima, $P_{20,00}^2$ is significantly larger than $P_{21,11}^2$. Fortunately however, this does not alter Ma and Liu's interpretation of Aquilanti *et al*'s results because, as mentioned in the preceding text, the coupling strength is also inversely proportional to the asymptotic energy gap between the two coupled states. As illustrated in Figure 5.12 the energy gap between the $|20\rangle$ and $|00\rangle$ states is larger than the gap between the $|21\rangle$ and $|11\rangle$ states. Somewhat accidentally the opposing effects approximately cancel and the overall transition probabilities between the $|21\rangle - |11\rangle$ and $|20\rangle - |00\rangle$ states are similar.

Ma and Liu[20] observed a non-statistical 2:1 propensity for the $^3P_1$ state to be populated over the $^3P_0$ state which can be rationalised by applying the Ω-conserving approximation. This approach allows transitions to occur between $|21\rangle - |11\rangle$ and $|20\rangle - |00\rangle$ only. Since they had established that the magnitude of the $P_{21,11}(R)$ and $P_{20,00}(R)$ were approximately equal, it

was concluded that a simple count of the relative numbers of product surfaces which are accessible from all the m_j states of $O(^3P_2)$ yields the $^3P_1$: $^3P_0$ branching ratio. Figure 5.12 shows the adiabatic potential energy curves for the $O(^3P_j)$–CH_4 interaction. The $|21\rangle$ and $|11\rangle$ states, which can couple with conservation of Ω, are doubly degenerate because $\Omega=\pm1$. However the coupled $|20\rangle$ and $|00\rangle$ states are only singly degenerate. Hence the 2:1 ratio of $^3P_1$: $^3P_0$ originates in the degeneracy difference for the $\Omega=1$ and $\Omega=0$ states of 2 versus 1.

However it should be noted that Ma and Liu's argument, that the 2:1 ratio of $^3P_1$: $^3P_0$ exists because the transition probabilities of the coupled states are equal, is only valid at low collision energies. Under such conditions the coupling strengths between the $|21\rangle$ – $|11\rangle$ and $|20\rangle$ – $|00\rangle$ states must be similar to yield a $^3P_1$: $^3P_0$ branching ratio of 2:1, otherwise the ratio wouldn't just be proportional to the number of available surfaces. In contrast, at high collision energies, as long as both couplings are sufficiently strong it doesn't matter what the actual coupling strengths are because the coupling process is saturated. Hence in this instance the branching ratio can only be dependent on the number of available surfaces. Ma and Liu show in their results[20] that the coupling becomes saturated above collision energies of approximately 6kJmol^{-1}.

The 2:1 propensity survives clearly in rigorous close-coupled calculations[18,19] for collisions of $O(^3P_j)$ with He and H_2. Both measured[20] and predicted[18,19] $^3P_2$ to $^3P_{1,0}$ cross sections with these collision partners level off at quite moderate collision energies. Assuming similar behaviour for $O(^3P_j)$+hydrocarbon collisions, the equivalent energies at which inelastic transfer becomes probable would lie well below the activation barriers. It is therefore concluded that this plateau region corresponds to the limit in Model 3 in which populations on coupled entrance channel surfaces are completely

scrambled and higher collision velocities do not result in any increase in the net inelastic transfer.

Model 3 assumes that populations on coupled entrance channel surfaces are completely scrambled due to non-adiabatic coupling effects. In practice, states with $\Omega=\pm1$ correlate partially, with equally divided probability, to reactive ($^3\Pi$) and unreactive ($^3\Sigma^-$) surfaces. States with $\Omega=0^+$ behave similarly. The $|22>$ and $|10^->$ surfaces, unaffected by the mixing, link to $^3\Pi_2$ and $^3\Pi_0$ - as in Models 1 and 2.

To complete Model 3 the exit channel correlations must be chosen. For the reasons discussed in the preceding text, those introduced in Model 2 will be most apt for an overall non-adiabatic, Ω-conserving picture. The final correlation diagram is shown in Figure 5.17. The mathematical basis for this model is similar to that proposed in Equations (5.2)-(5.5) but with a few alterations. The $P(|j\Omega>\rightarrow|\Lambda\Sigma;\Omega>)$ term in Equation (5.4) must be amended to equal 1/2 for the entrance channel surfaces with $\Omega=1$ and 0^+. Correspondingly, the $P(|\Lambda\Sigma;\Omega>\rightarrow|\Omega'\Sigma'';\Omega>)$ term in Equation (5.5) must also be altered to equal 1/2 for the exit channel surfaces with $\Omega=1$, as in Model 2.

Now that Model 3 has been fully developed, it is perhaps worthwhile to summarise the dominant interactions at long-medium-short range. Considering the forward reaction, at long range the adiabatic potentials are mixtures of Σ and Π. Here spin-orbit coupling is the dominant interaction and the Λ and Σ quantum numbers are scrambled. These long range interactions are equivalent to those quantified by Aquilanti *et al*[17]. In the intermediate range, where both electrostatic and spin-orbit interactions are important, the non-adiabatic couplings become stronger and cause transitions between states of the same Ω but which are asymptotically associated with different j's. Then at short range electrostatic interactions

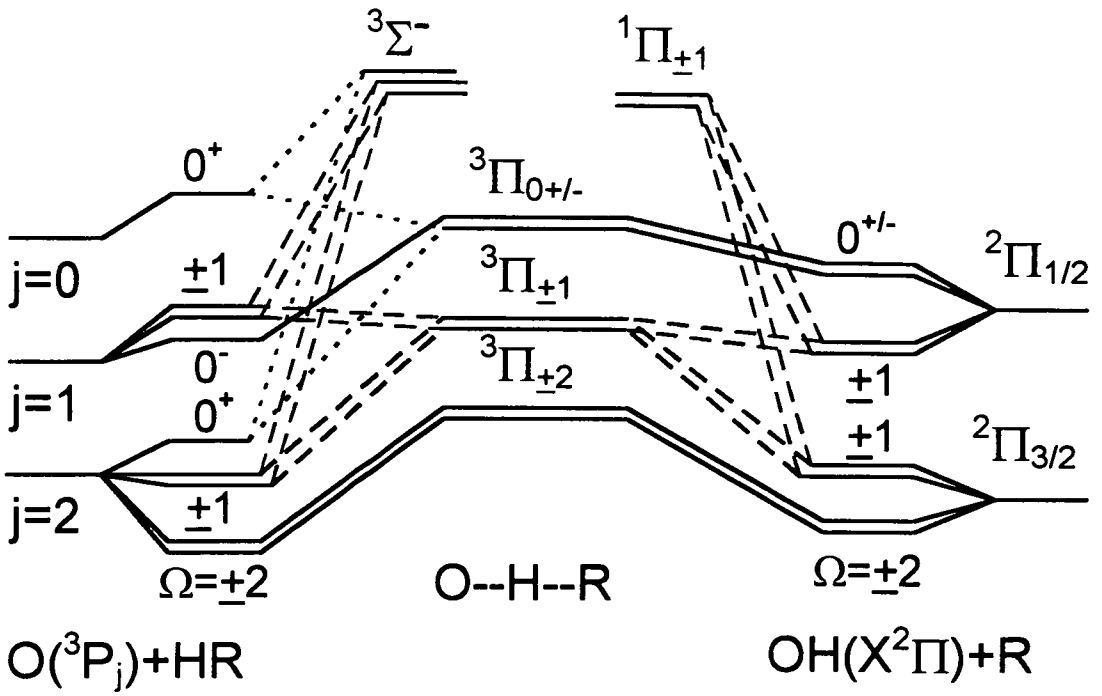

Figure 5.17: Model 3: schematic, Ω-conserving correlation diagram for collinear $O(^3P_j)$+HR reactions. There is selective non-adiabatic mixing in both entrance and exit channels. Coupled Ω=1 and $\Omega=0^+$ surfaces are indicated by dashed and dotted lines respectively. The energetic separations are not to scale.

dominate and the character of the surfaces become defined: they are either Σ or Π, and there are no further non-adiabatic transitions.

The relative reactivity of the $O(^3P_j)$ states and subsequent spin-orbit state ratios of OH predicted by Model 3 are given in Tables 5.3 and 5.4. Figure 5.2 shows pictorially how these predictions compare with the experimental observations and with the other models. There is now **considerably improved agreement** with the experimentally obtained OH spin-orbit state ratios. The data for Model 3, however, does not agree so well with Andresen and Luntz's[2] thermal $O(^3P_j)$+c-C_6H_{12} results although the prediction matches exactly the quoted c-C_6D_{12} value.

It is very reassuring that the predictions obtained using Model 3 match relatively well the experimental observations because this model is expected from all the other independent evidence to be the most probable under the given experimental conditions.

5.3.4 Summarising Models 1, 2 and 3

The common factor in the reactant to product correlations for all models was Ω which was always rigorously conserved. Within this approximation, however, each model had its own set of limits and applications.

In Model 1 the entrance and exit channels were correlated adiabatically. This is the limit where strong spin-orbit coupling is the important interaction, which, in fact, should only be expected to apply at long range. This model does not yield predictions in agreement with the experimental results.

In Model 2 the entrance channel correlations of Model 1 are retained but non-adiabatic mixing is allowed to occur between surfaces of the same Ω in the exit channel. The resulting predicted OH $^2\Pi_{3/2}$:$^2\Pi_{1/2}$ ratio is more in

accord with the experimental results than that predicted by Model 1, but the agreement is still poor.

Model 3 is a wholly non-adiabatic, Ω-conserving correlation. This means that in both the entrance and exit channels surfaces of the same Ω are allowed to mix. This model is most apt, for a reactive system with high collision velocities, because it considers the dominant interactions at all ranges. This approach generates OH spin-orbit state ratios which are in relatively good agreement with the experimental results.

It is, of course, possible that the origin of the spin-orbit state selectivity does not lie in entrance to exit channel correlations. The product state selectivity could perhaps be solely due to some kind of exit channel partitioning not considered here. Such a statistically biased approach would undoubtedly favour the production of the lower lying $^2\Pi_{3/2}$ state as observed experimentally.

The best way to determine which approach (correlation models versus exit channel partitioning) ultimately defines the resulting spin-orbit state ratio would be to radically alter the reactant j-state distribution. The correlation models would be critically affected by such changes whereas exit channel partitioning would not. Unfortunately no methods have yet been devised to create a distinct $O(^3P_j)$ distribution and in the experiments performed so far the photolytically and thermally generated j-state populations are relatively similar.

5.4 Relative Reactivities of the $O(^3P_j)$ States

The principal objective of each correlation model was to make a prediction of the OH spin-orbit state ratio which could be compared with the experimental results. The corresponding relative reactivities of the $O(^3P_j)$ spin-orbit states

emerge as a natural by-product of this analysis. They are assessed by simply counting the ratio of reactive to unreactive surfaces propagating from each asymptotic j-state. These values, given in Table 5.3, are of independent interest[28,29] but as yet remain experimentally undetermined.

The fully adiabatic Model 1 predicts that the reactive $^3\Pi$ surface is populated from the five-fold degenerate $^3P_2$ state and from one state belonging to $^3P_1$. In this limit $^3P_0$ never leads to reaction. The same result is obtained for Model 2 because only the exit channel correlations are altered. The relative reactivities for Models 1 and 2 are 1 : 0.33 : 0 for j=2,1,0 respectively. The non-adiabatic mixing in Model 3 increases the reactivity of the higher j-states at the expense of $^3P_2$. The relative reactivities are now 0.7 : 0.67 : 0.5 for j=2,1,0 respectively. In the preceding text it has been suggested that Model 3 best predicts the product state selectivity. This proposal is based on the assumption that fine structure product populations are influenced by the corresponding fine structure reactant states.

Unfortunately there is no experimental data pertaining to the j dependence of reactivity of atomic oxygen with hydrocarbons. Previous attempts[30] to measure this quantity were unsuccessful due to relaxation, facilitated by the relatively high pressure conditions of the experiments. This problem has also been addressed in transition state theory (TST) calculations[28,29] of rate constants for $O(^3P)$+HR, and for the closely related $O(^3P)+H_2$ reaction[31,32]. Conventional TST calculations are indifferent to which spin-orbit component is reactive; complete diabacity is fundamental to TST[29].

Models 1 and 3 describe two extreme cases which can be used to correlate reactants to products. The strong adiabatic prediction, in which a substantial variation of reactivity with j is implicit, does not appear to be compatible with the experimental spin-orbit partitioning data. However, equal reactivity of the j-states is a proposal that ought to be considered very carefully. If such

a situation arose due to the complete scrambling of populations on all entrance and exit channel surfaces then the OH $^2\Pi_{3/2}$ and $^2\Pi_{1/2}$ states would be equally populated. This clearly does not happen and so the proposal that the j-states react equally due to complete scrambling can be disregarded.

However, there is another way in which equal reactivity can be ascribed to the j-states. Σ and Π entrance channel surfaces are distinguished by the alignment of the paired-electron lobe of the $O(^3P)$ p^4 configuration[7]: the p-orbitals are chosen to be P_x, P_y or P_z (P_x and $P_y \rightarrow \Pi$, $P_z \rightarrow \Sigma$). If there was no further orbital reorientation as the distance between the collision partners is reduced then the Λ values (i.e. Σ or Π) chosen at long range would remain defined. Physically this amounts to switching off (artificially) the spin-orbit coupling in the $O(^3P)$ atom and allowing the electrostatic interactions to dominate. This can be termed an "orbitally frozen" model: the long range spatial projections of the individual atomic states are "frozen" and therefore define the intermediate to short range picture. Scrambling of the populations is not permitted. Effectively, in this approximation the collision distance between the partners reduces almost instantaneously.

In this "orbitally frozen" model the branching factors between surfaces, $P(|j\Omega> \rightarrow |\Lambda\Sigma;\Omega>)$ in Equation (5.4), are the squares of Clebsch-Gordan coefficients[26]. The parity restriction also applies here. The only non-zero coefficients are for connections between those surfaces which were coupled in Model 3 (i.e. the $|21>$ – $|11>$ and $|20>$ – $|00>$ surfaces) but with the distinction that the weightings are no longer necessarily equal. In practice only the $|20>$ – $|00>$ pair is affected; the populations divide in complementary 2/3:1/3 ratios between the $^3\Sigma^-_{0+}$ and $^3\Pi_{0+}$ intermediate surfaces. The correlations between the $O(^3P_j)$ spin-orbit states and the subsequent $^3\Pi$ and $^3\Sigma^-$ intermediate states, obtained by applying this approximation, are shown in Figure 5.18. The exit channel correlations are exactly the same as those drawn for Model 3. In the "orbitally frozen" limit

the reactivities of all the states are the same, irrespective of the value of j. Geometrically this is because 2/3 of collisions will occur on Π (reactive) surfaces and 1/3 on Σ (unreactive) surfaces, as illustrated in Figure 5.18.

The relative reactivity of the $O(^3P_j)$ states and subsequent spin-orbit state ratios of OH predicted by the "orbitally frozen" model are given in Table 5.6. This model predicts very similar OH spin-orbit state ratios to those obtained for the successful Model 3. In fact, even though it is based on completely different assumptions, this model appears to be effectively indistinguishable from Model 3 within the limits of the currently available experimental data, yielding only fractionally different $O(^3P_j)$ reactive fractions and OH spin-orbit-state ratios.

It is also worth noting that the "orbitally frozen" model predicts results consistent with the observations of Ma and Liu[20] who studied the inelastic conversion between $O(^3P_2)$ and $O(^3P_{1,0})$ in collisions with H_2 and He. They reported a 2:1 ratio of $O(^3P_1)$: $O(^3P_0)$, but on closer examination of their data it appears as though they actually obtained an $O(^3P_1)$: $O(^3P_0)$ ratio of around 2¼:1. This exact result is generated by applying the entrance channel correlations contained within the "orbitally frozen" model. If one traces the division of population between the coupled (|21> – |11> and |20> – |00>) surfaces in and then back out of the entrance channel then a ratio of $^3P_1$: $^3P_0$ can be obtained. In Model 3 the population divides equally between the coupled levels thus causing the branching ratio to originate from the degeneracy of the states. However as previously mentioned, the branching factors between the coupled surfaces in the "orbitally frozen" model are the squares of Clebsch-Gordan coefficients. This only affects |20> – |00> pair where the population divides in 2/3:1/3 ratios, as shown in Figure 5.18, generating a $O(^3P_1)$: $O(^3P_0)$ ratio of 2¼:1 rather than the 2:1 ratio predicted by Model 3.

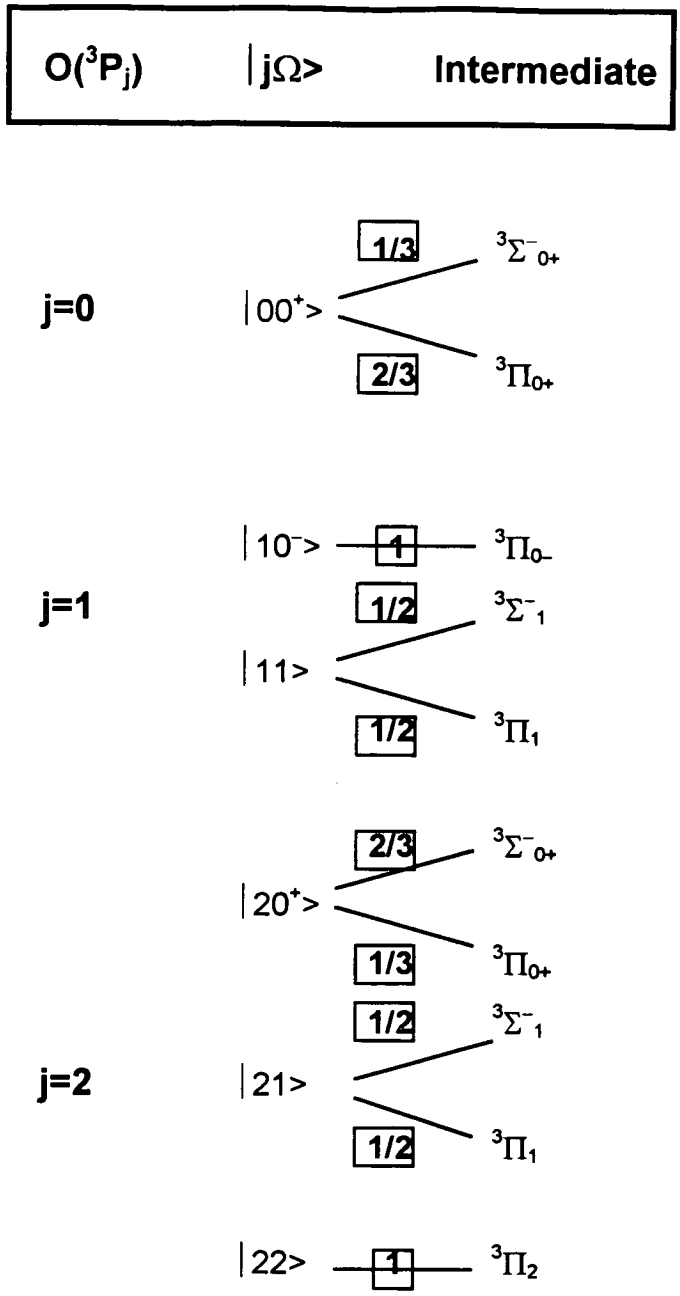

Figure 5.18: This diagram can be used to illustrate the "orbitally frozen" model. In this approximation the branching factors between coupled surfaces are the squares of Clebsch-Gordan coefficients, represented by boxed numbers. Inelastic transfer can only occur between the $|j\Omega>$ pairs $|20>$ – $|00>$ and $|21>$ – $|11>$ because Ω must be conserved. Where there is no transfer (i.e. for $|22>$ – $|10^->$) the surfaces connect wholly to the intermediate. By summing the number of surfaces which lead to $^3\Pi$ and $^3\Sigma^-$ intermediates a ratio of the reactivity of (O^3P_j) states can be obtained. The ratio of reactive to unreactive surfaces = 2/3:1/3.

$O(^3P_j)$	Reactive Fraction	$^2\Pi_{3/2}:^2\Pi_{1/2}$ Ratio	$O(^3P_j)$ Distribution: UV Phot.[a]	Thermal[b]	$^2\Pi_{3/2}:^2\Pi_{1/2}$ UV Phot.: Model	Expt[c]	$^2\Pi_{3/2}:^2\Pi_{1/2}$ Thermal: Model	Expt[c]
j=2	$3\frac{1}{3}/5$	$2\frac{1}{2}:\frac{5}{6}$	0.82	0.72				
j=1	2/3	$\frac{1}{2}:\frac{3}{2}$	0.16	0.22	1.90	1.75 (d)	1.47	1.68 (e)
j=0	$\frac{2}{3}/1$	$0:\frac{2}{3}$	0.02	0.06				

(a) Average $O(^3P_j)$ distribution from NO_2 photolysis at 355, 337 and 266nm,[24] very similar to those quoted independently[25] at 355 and 266nm.

(b) Thermal (300 K) distribution, as justified in ref. [2].

(c) Ratios corrected for the (2J'+1) spatial degeneracy, as described in the text. Results are averages over all N', with weightings according to the statistical uncertainties where these were available.

(d) Experimentally obtained OH spin-orbit state ratio following reaction between $O(^3P)$ and isobutane. $O(^3P)$ was generated by photolysis of NO_2 at 248nm[1].

(e) Average of OH(v'=0) data in Fig. 6 of ref. [2].

Table 5.6: Predicted relative reactivities (of individual j-states) and subsequent OH $^2\Pi_{3/2}:^2\Pi_{1/2}$ ratios for $O(^3P_j)$+HR "orbitally frozen" correlation model described in the text. The reactive fraction determines how many of the available surfaces are reactive. For example for $O(^3P_{j=1})$: 2 out of 3 surfaces are reactive and hence 1 out of 3 is unreactive. The subsequent ratio of $^2\Pi_{3/2}:^2\Pi_{1/2}$ surfaces is ½:1½. This table also compares the experimentally observed $^2\Pi_{3/2}:^2\Pi_{1/2}$ ratios for OH(v'=0)[3] from selected $O(^3P_j)$+HR reactions with the predictions obtained using the "orbitally frozen" model.

However, assuming that Aquilanti *et al's*[17] characterisation of adiabatic surfaces and coupling strengths is valid here, Model 3 is physically more realistic because it considers spin-orbit coupling at all ranges. It also assumes that the collision partner approaches smoothly (rather that suddenly) thus allowing the system time to respond.

5.5 Conclusions

A range of correlation diagrams have been generated in an attempt to rationalise the observed non-statistical product OH spin-orbit state ratios following reactions between $O(^3P_j)$ and saturated hydrocarbon molecules.

It has been established that correlating the reactant and product fine structure states adiabatically, in a strong spin-orbit coupling limit, fails to give good agreement with the experimental results. However, the introduction of non-adiabatic coupling to the entrance and exit channels results in an OH $^2\Pi_{3/2}$:$^2\Pi_{1/2}$ ratio which is close to the experimentally observed value. Ultimately the system could be unambiguously defined if the reactivity of the individual j states in the $O(^3P_j)$ reactant, and the resulting OH spin-orbit state ratios, could be assessed.

References

[1] G. M. Sweeney, A. Watson and K. G. McKendrick, *J. Chem. Phys.*, **106** 9172 (1997).

[2] P. Andresen and A. C. Luntz, *J. Chem. Phys.* **72**, 5842 (1980).

[3] Angular momenta associated with the (spin-orbit coupled) OH molecule are labelled with primes, N′, throughout this chapter to avoid confusion with the same quantities for the system as a whole. Refer to Table 5.1 for definition. Similarly vibrational states of the OH product, formed following reaction between $O(^3P)$ and RH are also labelled with primes, v′. This notation, which is commonly used in reaction dynamics to differentiate between reactant and product energy states, is consistent with the conventions used in Chapters 4 and 6.

[4] P. R. Bevington, *Data Reduction and Error Analysis for the Physical Sciences*, p. 72 (McGraw-Hill, New York, 1969).

[5] D. Husain, *Ber. Bunsenges. Physik. Chem.*, **81**, 168 (1977).

[6] P. J. Dagdigian and M. L. Campbell, *Chem. Rev.*, **87**, 1 (1987).

[7] S. P. Walch and T. H. Dunning, Jr., *J. Chem. Phys.*, **72**, 3221 (1980).

[8] C. Gonzalez, J. J. W. McDouall and H. B. Schlegel, *J. Phys. Chem.*, **94**, 7467 (1990).

[9] G. Herzberg, *Molecular Spectra and Molecular Structure, Vol.III: Electronic Spectra and Electronic Structure of Polyatomic Molecules* (Van Nostrand Rheinhold, New York, 1966).

[a] Appendix IV, Table 58, P.574, [b] Appendix II, Table 56, P.569, [c] Appendix III, Table 57, P.570.

[10] J.M. Hollas, *Modern Spectroscopy*, (John Wiley & Sons, 1987), p.202-205.

[11] G. Durand and X. Chapuisat, *Chem. Phys.*, **96**, 381 (1985).

[12] G. Herzberg, *Molecular Spectra and Molecular Structure, Vol.I: Spectra of Diatomic Molecules* (Van Nostrand Rheinhold, New York, 1950).

[13] G. M. Sweeney and K. G. McKendrick, *J. Chem. Phys.*, **106**, 9182 (1997).

[14] V. Aquilanti and G. Grossi, *J. Chem. Phys.*, **73**, 1165 (1980).

[15] V. Aquilanti, P. Casavecchia, G. Grossi and A. Laganà, *J. Chem. Phys.*, **73**, 1173 (1980).

[16] V. Aquilanti, E. Luzzatti, F. Pirani and G. G. Volpi, *J. Chem. Phys.*, **73**, 1181 (1980).

[17] V. Aquilanti, R. Candori, L. Mariani, F. Pirani and G. Liuti, *J. Phys. Chem.*, **93**, 130 (1989).

[18] T. S. Monteiro and D. R. Flower, *Mon. Not. R. Astron. Soc.*, **228**, 101 (1987).

[19] R. Jaquet, V. Staemmler, M. D. Smith and D. R. Flower, *J. Phys. B: At. Mol. Opt. Phys.*, **25**, 285 (1992).

[20] Z. Ma and K. Liu, *Chem. Phys. Lett.*, **213**, 269 (1993).

[21] M. Abe, Y. Sato, Y. Inagaki, Y. Matsumi and M. Kawasaki, *J. Chem. Phys.*, **101**, 5647 (1994).

[22] M. H. Alexander, T. Orlikowski and J. E. Straub, *Phys. Rev.*, A **28**, 73 (1983).

[23] N. J. Dutton, I. W. Fletcher and J. C. Whitehead, *Mol. Phys.*, **52**, 475 (1984).

[24] J. Miyawaki, T. Tsuchizawa, K. Yamanouchi and S. Tsuchiya, *Chem. Phys. Lett.*, **165**, 168 (1990).

[25] H.-G. Rubahn, W. J. van der Zande, R. Zhang, M. J. Bronikowski and R. N. Zare, *Chem. Phys. Lett.*, **186**, 154 (1991).

[26] see, e.g. P. W. Atkins, *Molecular Quantum Mechanics*, Appendix 9 (Oxford University Press, Oxford, 2nd ed., 1983).

[27] M. S. Child, in *Atom-Molecule Collision Theory: A Guide for the Experimentalist*, edited by R. B. Bernstein, Ch.13, p.435 (Plenum, New York, 1979).

[28] J. V. Michael, D. G. Keil and R. B. Klemm, *Int. J. Chem. Kin.*, **15**, 705 (1983).

[29] N. Cohen and K. R. Westberg, *Int. J. Chem. Kin.*, **18**, 99 (1986).

[30] A. Miyoshi, K. Tsuchiya, N. Yamauchi and H. Matsui, *J. Phys. Chem.*, **98**, 11452 (1994).

[31] B. R. Johnson and N. W. Winter, *J. Chem. Phys.*, **66**, 4116 (1977).

[32] G. C. Schatz, A. F. Wagner, S. P. Walch and J. M. Bowman, *J. Chem. Phys.*, **74**, 4984 (1981).

Chapter 6

The Reactions of $O(^1D)$ with Hydrocarbons

6.1 Introduction

The reactions of $O(^1D)$ play a significant role in initiating much atmospheric chemistry. In particular the reactions of $O(^1D)$ with H_2O, H_2 and simple saturated hydrocarbons are the principal source of OH in the stratosphere which controls the upper boundary of the ozone layer about the Earth[1]. Reaction rates tend to be considerably faster than those of the analogous $O(^3P)$ reactions, with substantial additional chemical activation (approximately 190kJmol^{-1}) to be distributed amongst product degrees of freedom.

The reaction between $O(^1D)$ and saturated hydrocarbons (in particular CH_4) has been studied previously[2-13] and some details relating to the dynamics of the system have been established. However, the full correlation between rovibronic states of the reactants and products is still unknown and thus this reaction makes an interesting candidate for investigation.

An important objective in reaction dynamic studies is to determine from the distribution of energy amongst product modes what the motions of atoms (or groups of atoms) are as they move through their intermediary period, when bonds are broken and formed: for example, if a long-lived intermediate is formed and if all modes of that species participate equally in product formation, then statistical energy partitioning in the product is expected. Non-statistical energy distributions, however, may be due to rapid, direct

processes where one reactive partner plucks an atom from the other without any intermediate being formed[14].

The principal mechanism for the $O(^1D)$+saturated hydrocarbon reactions was identified by Cvetanovic and co-workers[15-18] and later confirmed by others[19]. In these studies N_2O-RH mixtures were photolysed and the composition of the final products monitored as a function of time and initial experimental conditions. It was established that the predominant mechanism is insertion of $O(^1D)$ into a C-H bond to form a vibrationally hot alcohol, as shown in Equation (6.1).

$$O(^1D) + RCH_2H \longrightarrow RCH_2OH^* \qquad (6.1)$$

At high pressure this chemically activated alcohol would be stabilised, but in collision free conditions the complex unimolecularly fragments by either C-O (Equation (6.2)) or C-C (Equation (6.3)) bond cleavage.

$$RCH_2OH^* \longrightarrow RCH_2 + OH \qquad (6.2)$$

$$RCH_2OH^* \longrightarrow R + CH_2OH \qquad (6.3)$$

End-product analysis also indicated that a fraction of the overall reaction proceeded by a mechanism which yielded RCH_2 and OH (as in Equation (6.2)) but which could not be quenched at any attainable pressure of collisional deactivator. This route was ascribed to the direct abstraction of a hydrogen atom by $O(^1D)$ in a single step process that does not involve the formation of a chemically activated intermediate. This is exemplified in Equation (6.4).

$$O(^1D) + RCH_2H \longrightarrow RCH_2 + OH \qquad (6.4)$$

Equation (6.4) is analogous to the corresponding reaction of $O(^3P)$ with simple organic molecules which is known to proceed, exclusively, by a direct abstraction mechanism.

Since the 1980's much effort has been applied to determining the dynamics of the $O(^1D)$+saturated hydrocarbon reaction. OH is very conveniently detected by modern spectroscopic methods such as LIF and for this reason is the fragment most commonly detected in reaction dynamic studies. It is much more difficult to detect and analyse the hydrocarbon moieties, though some level of success has been attained in the detection of CH_3 by REMPI following the reaction between $O(^1D)$ and saturated and chlorinated hydrocarbons[12,13].

Luntz[6] measured the nascent internal state distributions produced in the reactions of $O(^1D)$ with CH_4, C_2H_6, C_3H_8 and $C(CH_3)_4$ by combining laser photolytic generation of $O(^1D)$, from ozone at 266nm, with LIF detection of the OH product. At this wavelength only 3% $O(^3P)$ is produced and hence it's effect on reactivity can be discounted. The OH rotational distributions were found to be bimodal: one component corresponding to population of only the lowest few rotational states whilst the other was a broad rotational distribution representing high rotational excitation. The rotationally hot component was ascribed as being due to an **insertion** mechanism leading to the formation of an ROH collision complex, with subsequent **elimination** of OH, and the rotationally cold component was thought to be the result of a direct hydrogen **abstraction** mechanism. The insertion component was found to be dominant for small RH while the abstraction becomes an increasingly important source of OH as the size of the hydrocarbon increases. Luntz also studied the partitioning of energy into vibrational modes by comparing the relative populations in OH $v'=0$ and $v'=1$[20]. Where the insertion mechanism dominates, the ratio of $v'=1/v'=0$ was found to decrease as the size of R increased. It was also observed that much more

of the available energy for the insertion component was partitioned into OH vibration than predicted by statistics. Vibrational partitioning in the abstraction component was not so well defined, but it appeared that vibrational excitation for this component decreased with increasing RH size.

As discussed in Chapter 3 Section 3.1.1 spin-orbit and orbital-rotation interactions in OH result in spin doubling and Λ-doubling, respectively, for each rovibrational level, (v',N'). Specific fine structure states, $^2\Pi_{3/2}$ (A' and A") and $^2\Pi_{1/2}$ (A' and A"), can be probed to find out whether there is any preference for OH to be formed in a particular Λ-doublet or spin-doublet. Whether or not there is any selectivity provides dynamical information. Luntz found that, for the insertion component, there was a preference for the Π(A') Λ-doublet of OH to be populated which decreased as the size of the R group increased: there was a distinct preference for the Π(A') Λ-doublet to be populated in the $O(^1D)/CH_4$ experiment, but no such selectivity was found with $RH=C_3H_8$ and $C(CH_3)_4$.

Λ-doublets arise because the OH ground state is a Π state and the partially occupied π orbital can lie either in the plane Π(A') or perpendicular to the plane Π(A") of rotation. From adiabatic considerations the OH Π orbital essentially points in the direction of the R-O bond which is broken as the ROH collision complex decays. A Π(A') state is formed if the complex decays in such a fashion that torques are generated in the plane containing the R-O bond whereas the Π(A") component is the result of torques acting about the R-O bond[21]. The preferential population of the Π(A') state, observed by Luntz[6] for reaction of $O(^1D)$ with small hydrocarbons, provides evidence that the ROH complex decays with forces acting in a plane containing the R-O-H bond. This implies that there is a dynamic constraint in the $O(^1D)$/RH reactions, in particular where RH is small and the insertion component dominates. For the abstraction component no selectivity was observed in the Λ-doublets[6]. However this isn't surprising since it's only for

high rotational levels that the Λ-doublets can be uniquely associated with directed orbitals[22] and as the abstraction mechanism produces rotationally cold OH, no selectivity would be expected. This is analogous to the $O(^3P)$ + RH reaction discussed extensively in Chapter 4. However, Luntz reported that there was no preferential population of either of the OH spin-doublets, $^2\Pi_{3/2}$ and $^2\Pi_{1/2}$, which were produced in a statistical ratio.

Luntz's results are best interpreted by considering each mechanism separately. The **insertion/elimination** mechanism for the $O(^1D)$/RH reaction describes the process which occurs when the O atom inserts into the R-H bond to form an ROH collision complex, with approximately 586kJmol^{-1} of vibrational energy. In the absence of stabilising collisions the intermediate must unimolecularly fragment to the products shown in Equations (6.2) and (6.3). The OH produced in this case would have non-statistical partitioning of energy between allowed modes due to the prompt, non-Rice-Ramsperger-Kassel-Marcus (non-RRKM) decomposition of the RCH_2OH^* intermediate. Alternatively, if the lifetime of the complex was sufficiently long the vibrational energy of the complex would be equipartitioned into all modes of the system and the fragmentation becomes a statistical process. Here C-C bond cleavage would be favoured as the more exothermic process. There is an obvious correlation between the lifetimes of the ROH collision complexes and the nature (statistical versus non-statistical) of the decay: the longer the lifetime of the complex, the more time available for internal vibrational redistribution and the greater the likelihood that the system will fragment statistically. Loosely speaking, the larger the R group the longer the lifetime of the ROH complex. The end-product analysis carried out by Cvetanovic *et al*[15-18] pin-pointed that the statistical decay becomes more important for larger RH.

Since Luntz observed rovibrationally hot OH product this infers that the decay of the ROH collision complex cannot be statistical. The insertion

complex is presumed to decay by at least two modes: some of the complex decays promptly to OH+R•, then energy is equipartitioned to all modes of ROH[15-18] which fragments unimolecularly via C-C bond cleavage, excepting where RH=CH_4. In the case where the complex fragments promptly the excess energy, from the O-H stretch and the bend of the complex, is channeled into product OH vibration and rotation. However as the size of RH increases the lifetime of the complex lengthens and this energy is dissipated into other modes of ROH before decay. Hence the degree of rovibrational excitation decreases with increasing RH size.

The insertion component produced some selectivity in the Λ-doublets. This suggests that the reaction geometry is planar. However this selectivity diminishes as RH increases in size and is not evident for R=C_3H_8 and $C(CH_3)_4$. The reduction in selectivity could be accounted for by a variety of reasons. For larger RH there is more time for energy migration within the ROH complex. Some of this energy could be deposited into out-of-plane modes. Also there is more initial orbital angular momentum which can contribute to OH rotation. In addition, for larger RH there is more probability of non-adiabatic transitions between surfaces in the exit channel which will wipe out any selectivity in the Λ-doublets.

A secondary mechanism which has been proposed for the reaction is **abstraction**. Following reaction between $O(^1D)$ and large saturated hydrocarbons Cvetanovic *et al*[15-18] reported that OH formation accounts for 20-30% of the products. It was suggested that these fragments could result from either prompt decay of the ROH collision complex, leading to the formation of rotationally hot OH, or from direct abstraction of H by $O(^1D)$. A third possibility, suggested by Luntz, is that the reaction is induced by a singlet to triplet surface crossing ($^1\Pi \rightarrow {}^3\Pi$), in an assumed pseudo-linear geometry. According to Luntz, the abstraction component, which is

characterised by formation of rotationally cold OH, could be due to either direct abstraction dynamics or a singlet to triplet surface crossing.

In the instance where the reaction occurs directly there will be no complex formation and the $O(^1D)$ approaches the RH collinearly. This geometry ensures that only a minimal torque will be imparted to OH, which will be formed in only low rotational states. However Luntz surmised that it was unlikely that this mechanism accounted for the large abstraction component in the $O(^1D)$/RH reactions due to the strong steric requirement and hence small reaction cross section. He proposed that reaction via a singlet to triplet surface would be a much more probable scenario. This curve crossing is spin-forbidden and it's implication on the reaction dynamics, complicated. The $O(^1D)$ would approach the RH perpendicularly and begin to insert into the C-H bond. There would then be a sudden transformation to the triplet surface whilst still in the entrance channel, and from that point, the dynamics should be analogous to the $O(^3P)$ + RH reaction which also produces rotationally cold OH.

The fraction of OH produced by the proposed abstraction mechanism was found to increase with the size of RH and was accompanied by a decrease in the insertion component. Luntz stated that the number of surface crossings also increases as the R group increases, enhancing the probability for transition to the triplet surface. A factor, however, which contradicts this proposed mechanism is that the reaction rate should decrease when RH=CH_4 and C_2H_6 since both these substrates react less readily with $O(^3P)$. Earlier indirect studies show no evidence to support this conclusion[23]. Luntz also concluded that the decrease in vibrational excitation of OH for the abstraction component is compensated by considerable excitation of internal modes of the R• fragment. This raises a discrepancy with the $O(^3P)$/RH reactions where the dynamics were modeled by treating R• as a structureless particle with no (or little) internal excitation.

No fine structure selectivity was observed for the abstraction component in the $O(^1D)$/RH reactions, but in contrast, the reaction between $O(^3P)$ and hydrocarbons preferentially populates the lower spin-doublet of OH. This additional anomaly raises another question as to the validity of Luntz's proposal that the abstraction is due to a singlet to triplet surface crossing rather than simply direct abstraction dynamics.

Hence the work of A.C. Luntz served to open up the arena for studying the dynamics of the reaction between $O(^1D)$ and saturated hydrocarbons rather than definitively solving all controversy surrounding the reaction. There still remained unanswered questions. The $O(^1D)/CH_4$ system was subsequently studied using pulsed infrared chemiluminescence techniques by Sloan *et al*[7] and via diagonal band LIF of rotationally relaxed OH[24]. The OH vibrational distribution was measured and found to be broad, peaking at $v'=2$. By analogy with the corresponding reaction of F atoms with CH_4[25,26] the relatively high degree of vibrational excitation was interpreted as support for a mechanism where the H is abstracted directly by the $O(^1D)$. In the F atom reactions abstraction mechanisms were found to result in vibrationally hotter products than insertion mechanisms. This clearly contradicts the results of Lin and DeMore[19] and Luntz[6] who proposed that the $O(^1D)+CH_4$ reaction proceeds principally via the CH_3OH^* insertion complex, yielding rotationally hot OH. Sloan *et al* proposed that the vibrational partitioning in the OH product is, to some degree, dependent on the reagent translational energy: if it is assumed that there is a small barrier to abstraction and a negligible barrier to insertion, then the cross section for abstraction is expected to increase as the kinetic energy of the reactants increases. In the experiments carried out by Sloan and co-workers collision energies of ~23kJmol^{-1} were used. Conversely, the reagent translational energy in Luntz's experiment was thermalised to 3/2kT (~3.7kJmol^{-1}). This could account for the differences in vibrational distribution observed by Luntz[6] and Sloan *et al*[7].

Park and Wiesenfeld[8] also made a comprehensive study of the $O(^1D)$/RH reaction. In an experiment similar to Luntz's[6], the OH internal energy distributions arising from the reactions of excited O atoms with CH_4, C_2H_6, C_3H_8 and $C(CH_3)_4$ were determined using LIF. The product distributions reported in this study were in good agreement with Luntz's earlier work. The $O(^1D)/CH_4$ reaction was characterised by a highly excited but unimodal rotational distribution in all vibrational levels, peaking in $v'=2$, whereas with the heavier hydrocarbons the rotational distribution appeared bimodal. This latter class of substrate gave rise to an OH rotational distribution which displayed a prominent maximum at low rotational energy in $v'=0$. The rotationally cold component dominated with the heavier and more complex hydrocarbons. An important feature of this investigation was that OH was probed in $v'=0 \rightarrow v'=4$ and significant population was seen in all 5 vibrational levels for each substrate. It was observed that the OH produced in the reactions of $O(^1D)$ with the heavier hydrocarbons exhibited similar rotational distributions to the $O(^1D)/CH_4$ reaction in the higher vibrational levels, but significant differences in $v'=0$. Park and Wiesenfeld also found, in accordance with Luntz, a preference for the lower Λ-doublet $\Pi(A')$ to be populated for the smaller RH species, thereby providing some support for a mechanism in which the OH is formed following an orientating dissociation which could occur during complex fragmentation.

Wiesenfeld *et al* concluded that the $O(^1D)/CH_4$ reaction proceeds via an insertion/elimination pathway, and for the heavier hydrocarbons parallel mechanisms compete; the dominant process yields rovibrationally cold OH and this channel was attributed to the dissociation of a long-lived collision complex. The highly excited component of OH was concluded to arise from prompt fragmentation of the ROH complex prior to energy equipartition amongst internal product modes. This mechanism also dominates for smaller RH. Any abstraction pathways, including Luntz's proposal that the reaction is facilitated by a singlet to triplet surface crossing, were discounted

on the grounds that abstraction should produce vibrationally excited OH by analogy with F atom[25,26] and $O(^3P)$[22] reactions. It should be noted though, that in the reactions of $O(^3P)$+RH, the degree of vibrational excitation depends markedly on the type of hydrogen being abstracted.

There has also been some attention focused into reaction with hydrocarbon clusters. Naaman *et al*[10] investigated the reactions of $O(^1D)$ with CH_4 and C_3H_8 monomers and clusters via a crossed molecular beam experiment and used LIF to detect the OH product. For the monomeric reactions results in accordance with previous studies were obtained[6,8]. However for the reaction between $O(^1D)$ and propane monomers a preference for OH to be formed in the lower, $^2\Pi_{3/2}$, spin-orbit state was reported, a result which has not been seen in previous flow experiments. No such selectivity was observed with the methane substrate. It was therefore concluded that in the reaction with heavier hydrocarbons $O(^1D)$ crosses to the triplet state and reacts adiabatically producing cold OH. The reaction between $O(^3P)$ and saturated hydrocarbons also results in a preferential population of the OH $^2\Pi_{3/2}$ spin-orbit state[22,27] as discussed extensively in Chapters 4 and 5.

Significant differences were observed between monomeric and clustered reactions for the methane substrate only: OH produced in the cluster reaction was translationally, vibrationally and rotationally cooler than distributions measured for the analogous free reaction. In addition, under clustering conditions, there was an observed propensity for the lower OH spin-doublet to be populated, but a loss in selectivity as regards the Λ-doublets components. These results were explained by a consideration of the nature of a methane cluster, which is thought to resemble a large hydrocarbon, and hence it's reactivity could be expected to be analogous to that of heavier substrates. Naaman and co-workers concluded that, for both monomeric and clustered reactions, the lifetime of the collision complex dictates the mechanism and hence the final energy distribution in the

products: propane monomers and methane clusters will form collision complexes with longer lifetimes than methane monomers, and hence the reaction of $O(^1D)$ with methane clusters mimics the pathways followed with heavier hydrocarbons. Stephenson *et al*[11] also studied the $O(^1D)/CH_4$ cluster system. They reported rotational and vibrational distributions which were cooler than the analogous free reaction, in accordance with Naaman *et al*[10], but observed no measurable spin-orbit state propensity.

In recent years much effort has been focused on determining, solely, the dynamics of the reaction between $O(^1D)$ and CH_4. This system is thought to closely resemble the $O(^1D)/H_2$ reaction which has been studied extensively: experimental[28-34] and theoretical studies[35-42] agree that an insertion mechanism is most probable for this reaction: $O(^1D)$ inserts into the H-H bond yielding a vibrationally excited HOH complex, which subsequently dissociates to give rotationally and vibrationally excited OH. Wiesenfeld *et al*[34] also noted that the OH $\Pi(A')$ Λ-doublet is preferentially populated in the $O(^1D)/H_2$ reaction. This result, which was also observed for the $O(^1D)/CH_4$ system[6,8], was attributed to constraints on the electronic angular momentum during formation of OH.

From the work of Lin and DeMore[19], Luntz[6] and Park and Wiesenfeld[8] it appears that the OH product energies, resulting from the $O(^1D)/CH_4$ reaction, are non-statistical. Non-statistical distributions are usually due to rapid and direct processes where no intermediate is formed, but this reaction is thought to proceed via an insertion mechanism with the formation of a chemically activated collision complex, as illustrated in Equation (6.5). This complex then fragments to yield CH_3 and OH (Equation (6.6)). It is suspected, though, that the intermediate is not particularly long lived which accounts for the non-statistical distribution of product energies.

$$O(^1D) + CH_4 \longrightarrow H_3COH^* \qquad (6.5)$$

$$H_3COH \longrightarrow CH_3 + OH \qquad (6.6)$$

Recently Simons *et al*[4] used polarisation-sensitive, sub-Doppler LIF detection methods to examine correlations between the OH rotation, recoil vectors and the reagent collision velocity. They studied the $O(^1D)+CH_4 \rightarrow OH(^2\Pi_{3/2},v'=0,N'=5)$ reaction and extracted angular scattering and polarisation information from specific selected Λ-doublet levels within the OH product. Observations and subsequent analysis yielded the following conclusions:

- When the OH product is formed in its vibrational ground state the available energy is not channeled into product translation. This characteristic low kinetic energy release, which was also observed for the state-specific channel generating $OH(v'=4,N'=8)$[2], indicates that the reaction exothermicity, ΔH_O, is converted into vibration and rotation of the product fragments. When the channel producing $OH(v'=4,N'=8)$ was selected, the internal energy of OH was comparable with the reaction exothermicity and the internal energy of CH_3 was approximately 0. Conversely, when $OH(v'=0,N'=5)$ was generated, the internal energy of OH was approximately 0 and the internal energy of $CH_3 \approx \Delta H_O$. The low levels of kinetic energy in the product were taken to be indicative that there is no significant barrier in the exit channel of the reaction[43].
- The two Λ-doublet components associated with $OH(^2\Pi_{3/2},v'=0,N'=5)$ yield Doppler-resolved profiles which are indistinguishable from one another. Each have pronounced forward and backward peaks, the backward scattered peak being slightly more dominant. Forward scattering is normally associated with "stripping" mechanisms and backward scattering with direct abstraction (often with a collinear geometry). If a collisional intermediate is formed and its lifetime exceeds a few periods of rotation then, on dissociation, the product fragments will fly apart symmetrically in all directions (i.e. isotropically) and both forward and backward scattering is observed[44]. The presence of a slightly more predominant backward

peak could indicate that two dynamical pathways operate for this reaction; the observed scattering pattern could be the result of both complex formation and abstraction mechanisms as found in the $O(^1D)$+HCl reaction[45]. However it is more probable the collision complex formed has a limited lifetime and that some memory of the initial reactant conditions are retained as the complex dissociates, resulting in slightly asymmetric scattering. This conclusion is consistent with the findings of Luntz[6] and Wiesenfeld *et al*[8].

- Polarisation studies on the system showed that while the $\Pi(A')$ Λ-doublet was formed preferentially in the collision plane, the was no rotational angular momentum alignment in the $\Pi(A'')$ state. To explain this behaviour Simons *et al* proposed that the $O(^1D)+CH_4$ reaction exhibits similar features to the $H+O_2$ reaction studied by Hall *et al*[46]. In both these systems it is assumed that the atom transfer occurs on a single potential energy surface via a CH_3OH/HO_2 insertion intermediate to produce OH $\Pi(A')$. Subsequently the OH $\Pi(A'')$ state is populated by non-adiabatic transitions between the exit channel surfaces associated with the $\Pi(A')$ and $\Pi(A'')$ states, which are very close in energy[47-49].

Most investigations of the $O(^1D)/CH_4$ system have used Laser-Induced Fluorescence (LIF)[2-4,6,8] or pulsed Fourier Transform Infra-Red (FTIR) emission[7] to spectroscopically probe the OH product, and thus any population or polarisation information has been derived for this fragment alone. Obviously it would be highly desirable to examine the ground state populations of the CH_3 fragment, via spectroscopic probing of suitable transitions in this radical. It is suspected that the distribution of energy in the CH_3 fragment will reveal much about what has occurred during the reaction: the OH product results from the bond formation procedure in the reaction and hence it is expected to be excited irrespective of the mechanism. The CH_3 moiety, however, is relatively remote from the reaction site, hence the

migration of energy to this fragment should disclose information pertaining to the formation and lifetime of any transient collision complex.

In the first report of the internal distribution of the "spectator" product fragment, Suzuki and Hirota[5] measured the ν_2 umbrella mode excitation in CH_3 resulting from the reaction between $O(^1D)$ and methane using infra-red diode laser absorption spectroscopy. The measured vibrational distributions were significantly colder than statistically predicted. This is an interesting observation considering that the CH_3 fragment must undergo a significant geometry change from tetrahedral CH_4 to planar CH_3. The spectroscopic bands necessary to establish any potential excitation of other vibrational modes were not scanned and as the experiment was carried out using relatively high pressures, nascent CH_3 rotational distributions were not determined.

Recently, Kleinermanns and his group[12,13] succeeded in detecting the CH_3 product from the reactions of $O(^1D)$ with saturated hydrocarbons, in particular with CH_4. The vibrational distributions in the CH_3 ν_1 symmetric stretch and ν_2 umbrella mode were found to be non-inverted. The ν_2 excitation was much cooler than statistically predicted for the $O(^1D)/CH_4$ and $O(^1D)/C_2H_6$ reactions, a result in agreement with Suzuki and Hirota[5], but nearly statistical for reaction with the heavier hydrocarbons (C_3H_8 and $C(CH_3)_4$). The nascent vibrational distribution measured within the ν_1 mode, for all RH bar C_2H_6, was almost statistical. The $O(^1D)/C_2H_6$ reaction produced a relatively hot (as compared with statistical predictions) ν_1 vibrational distribution. The production of CH_3 in the $O(^1D)$/RH reaction is perhaps of particular dynamical interest because this channel must be the result of the formation of the proposed alcohol insertion intermediate, as shown in Equation (6.3). The CH_3 rotational distribution from the reaction of $O(^1D)$ with CH_4 was also measured by Kleinermanns *et al*[12,13] and observed to be hotter than room temperature.

Hence it appears that in the $O(^1D)$/RH reaction the OH rotational and vibrational distributions are hot and the CH_3 vibrational energy distributions are cold, especially when RH=small Thus, much more of the reaction energy must be partitioned into OH rotation and vibration and less into CH_3 stretch and umbrella mode vibration than predicted by statistics. From a simple Franck-Condon picture of the fragmentation of the CH_3OH^* insertion complex, significant ν_2 excitation would be expected because CH_3 is pyramidal in the reactant but planar in the free radical. However CH_3 appears to be preferentially produced in the ground vibrational state with little excitation of the ν_2 umbrella mode. Kleinermanns *et al*[13] made the obvious proposal that this implies that the transition from pyramidal to planar CH_3 must occur along a minimum energy path with no significant gradient in the direction of the ν_2 normal co-ordinate, thus justifying the low CH_3-ν_2 excitation following decomposition of a vibrationally excited CH_3OH^* complex.

However, despite these conclusions there still remains a great deal of confusion as to the most applicable reaction mechanism. What does seem apparent is that the reaction route followed (insertion and unimolecular decomposition versus abstraction) is heavily dependent on the nature of RH. There is still much scope for studying the $O(^1D)+CH_4$/RH reaction, especially if both the OH and CH_3 products can by spectroscopically probed.

6.2 The $O(^1D)/CH_4$ Reaction: Specific Aims

A series of experiments were designed to investigate the gas phase bimolecular process specified in Equation (6.7), using laser methods for the state-selective preparation of $O(^1D)$ and for the state-specific detection of both the OH and CH_3 product fragments.

$$O(^1D) + CH_4 \longrightarrow OH + CH_3 \qquad (6.7)$$

The OH product of this reaction has been probed in many previous investigations[2-4,6-8,10,11]: the distribution of available energy within this fragment has been well documented and is discussed in Section 6.1. The principal aims of this work were to:

1. Check that the experiment works with the given experimental apparatus, detecting the OH product by LIF. Verify that the results obtained are in agreement with other authors[6,8].
2. Then probe the CH_3 product of the $O(^1D)/CH_4$ reaction by REMPI. Successful detection and subsequent analysis of this fragment is expected to yield important information pertaining to the dynamics of the system. It is only relatively recently that CH_3 has been detected as a product of this reaction[5,12,13] and, so far, the spectra obtained have been only partially resolved and difficult to analyse.

6.3 The $O(^1D)/CH_4$ Reaction: LIF Detection of the OH Product

6.3.1 Experimental Procedure

Nascent OH internal state distributions resulting from the reaction specified in Equation (6.7) were measured using the two-laser photolysis-probe scheme described in Chapter 2 and illustrated in Figure 2.8. $O(^1D)$ was generated by excimer laser photolysis (ArF) of N_2O at 193nm[50,51] and subsequently reacted with CH_4. The time delay between the photolysis and probe lasers was in the range 100-200ns in an attempt to ensure nascent conditions. The OH product was then detected by LIF (as described in Section 2.2.2.4 and illustrated in Figure 2.6) via the $A^2\Sigma^+(v=0,1) \leftarrow X^2\Pi(v=0,1)$ transition. This involved generating laser wavelengths in the region 306-315nm, achieved by doubling the output of the dye laser (DCM dye, Lambda Physik).

To probe OH(v'=0)[20] fluorescence was both excited and observed on the (0-0) band. Similarly OH(v'=1)[20] was probed by both exciting and detecting on the (1-1) band. An Ealing 35-8044 bandpass interference filter, centred at 310nm with a bandwidth of 10nm, was used to transmit light of the desired wavelength to the PMT detector. This filter successfully blocked the scattered light from the photolysis laser whilst, obviously, letting the probe laser light through. Fortunately however, the scattered light from the probe laser was manageable and could be removed, or at least reduced, by attenuating the probe pulse power.

The photolysis beam (~25mJ/pulse) was loosely focused (with a f=50cm lens) to give a spot size of approximately 2mm in the interaction region. The probe beam (~1mJ/pulse) remained unfocused. The typical output energy of the doubled dye beam was far in excess of the energy required to excite fluorescence in OH. Hence to minimise saturation the probe beam was passed through a pair of Glan-Taylor prisms which allowed the laser power to be attenuated whilst still maintaining a fixed (vertical) polarisation axis. The resultant beam entering the reaction chamber typically had pulse energies between 100 and 200μJ.

Non-condensable contaminants were removed from the N_2O (Distillers MG, 99%) and CH_4 (Distillers MG 99.5%) gases by freeze-pump-thaw cycling at liquid N_2 temperatures.

(a) Effusive Experiments

In the initial experiments the reactant gases entered the reaction chamber effusively via a glass injector (hole diameter ~2mm) which was painted black to minimise scattered light. The injector tip was located approximately 10mm from the laser focus. A "steady-state" pressure of around 250mTorr during

the experiment was achieved by partially throttling the reaction chamber diffusion pump.

(b) Jet Experiments

Subsequent experiments investigated the effects of using pulsed molecular beam valves to introduce the gaseous reagents to the reaction chamber. In these instances N_2O and CH_4 entered the reaction chamber via a flange shaped nozzle, painted black, with a 0.5mm diameter hole (illustrated in Figure 2.7(a)). The nozzle to laser distance was approximately 10mm. A 50:50 mixture of N_2O:CH_4 was used with a typical backing pressure of 1 bar above atmosphere. The measured "steady-state" background pressure when the nozzle was firing was relatively constant at 7×10^{-5} mbar. Typically the evacuated reaction chamber pressure was 5×10^{-6} mbar.

6.3.2 Results and Discussion of the LIF Experiments

As discussed in Section 6.2 the object of probing the OH product of the $O(^1D)/CH_4$ reaction was to determine whether the experiment was possible with the given apparatus. Consequently quantitative analysis of the OH LIF spectra was not carried out. Instead the spectra obtained shall be discussed qualitatively and compared with previous work on the system[6,8].

The (0-0) and (1-1) bands of the OH $A^2\Sigma^+ \leftarrow X^2\Pi$ transition were probed by LIF. The resultant excitation spectra are shown in Figures 6.1(a)-(f) and 6.2(a)-(b). Fluorescence was detected on the diagonal, (0-0) and (1-1), bands. Figures 6.1(a)-(f) show the OH(v'=0,1) product resulting from an effusive reactant source. For the jet experiments only the (0-0) band of the A←X transition was probed and the resultant spectra are shown in Figures 6.2(a) and 6.2(b). All spectra were assigned using the data obtained by Dieke and Crosswhite[52].

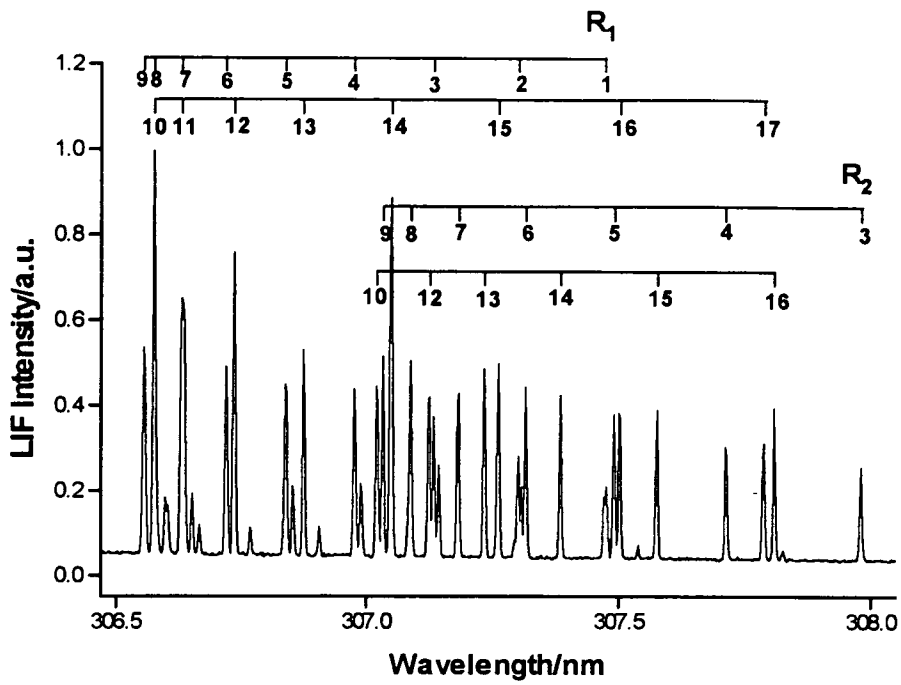

Figure 6.1(a): LIF excitation scan of the OH product resulting from the reaction between $O(^1D)$ and CH_4. $O(^1D)$ was generated by laser photolysis of N_2O at 193nm. The N_2O and CH_4 entered the system effusively and a reaction chamber pressure of 250mTorr was maintained throughout the scan. The beam energies entering the reaction chamber were 25mJ/pulse for the photolysis laser and ~100μJ/pulse for the probe laser. The time delay between the photolysis and probe sequences was 200ns, ensuring that near nascent products were detected. OH was probed by both exciting and observing fluorescence on the A-X (0-0) band. The rotational lines, originating in levels N'[20] of the $X^2\Pi$ ground state, have been assigned[52].

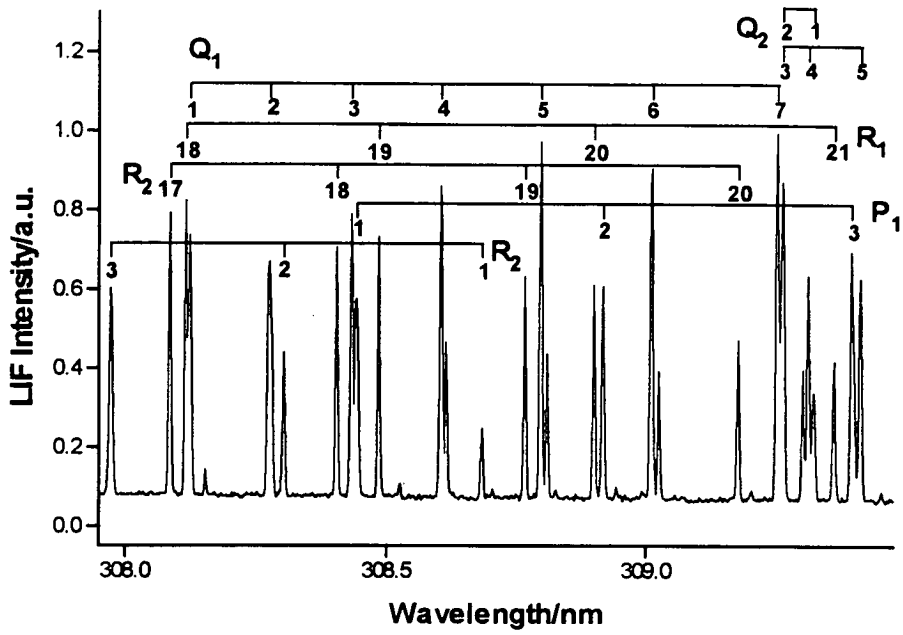

Figure 6.1(b): LIF excitation scan of the OH product resulting from the reaction between $O(^1D)$ and CH_4, continued from Figure 6.1(a). The experimental conditions are the same as for the spectrum shown in Figure 6.1(a).

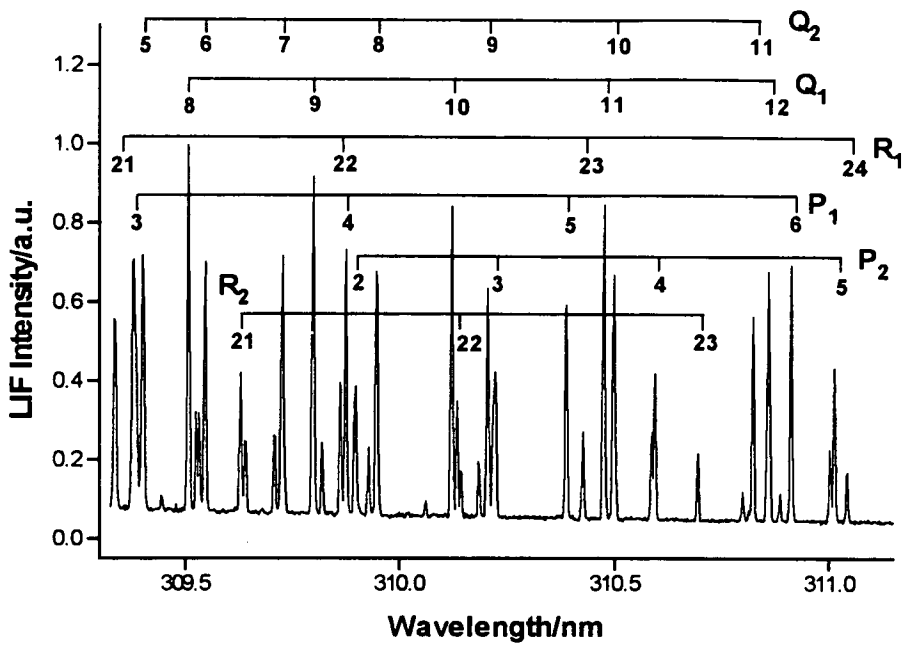

Figure 6.1(c): LIF excitation scan of the OH product resulting from the reaction between $O(^1D)$ and CH_4, continued from Figure 6.1(b). The experimental conditions are the same as for the spectrum shown in Figure 6.1(a).

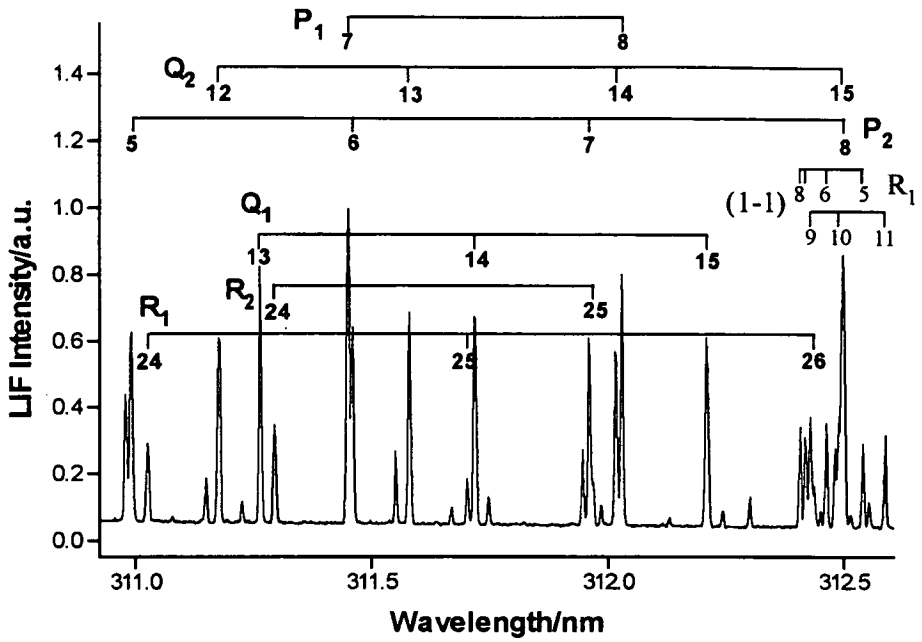

Figure 6.1(d): LIF excitation scan of the OH product resulting from the reaction between $O(^1D)$ and CH_4, continued from Figure 6.1(c). OH(v'=0) was probed by both exciting and detecting fluorescence on the A-X (0-0) band. Similarly, OH(v'=1) was probed by both exciting and detecting fluorescence on the A-X (1-1) band. Lines associated with the (0-0) band are labelled in bold type and lines associated with the (1-1) band are labelled in normal type (and with a different font). The experimental conditions are the same as for the spectrum shown in Figure 6.1(a).

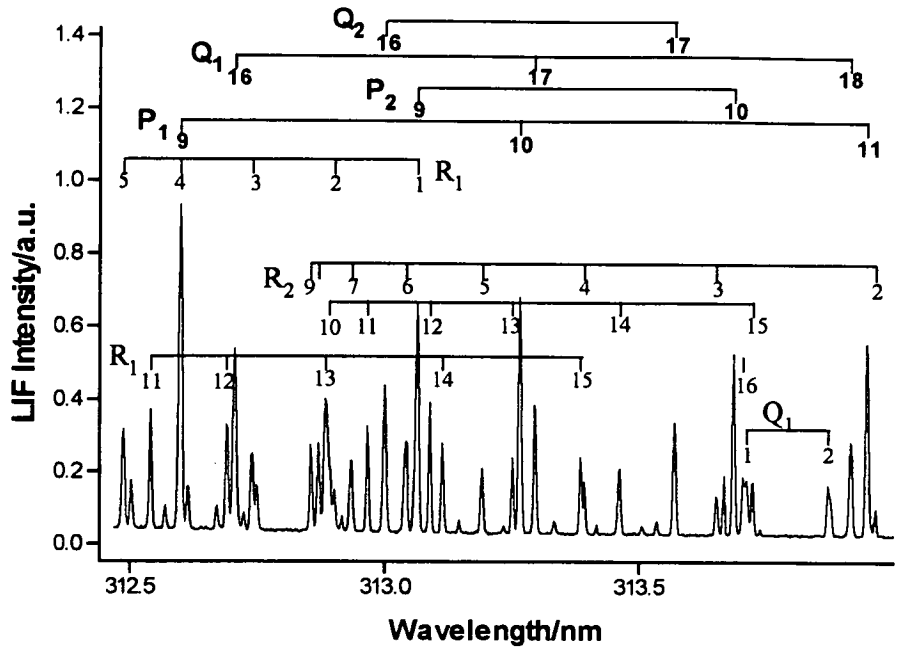

Figure 6.1(e): LIF excitation scan of the OH product resulting from the reaction between $O(^1D)$ and CH_4, continued from Figure 6.1(d). The experimental conditions are the same as for the spectrum shown in Figure 6.1(a).

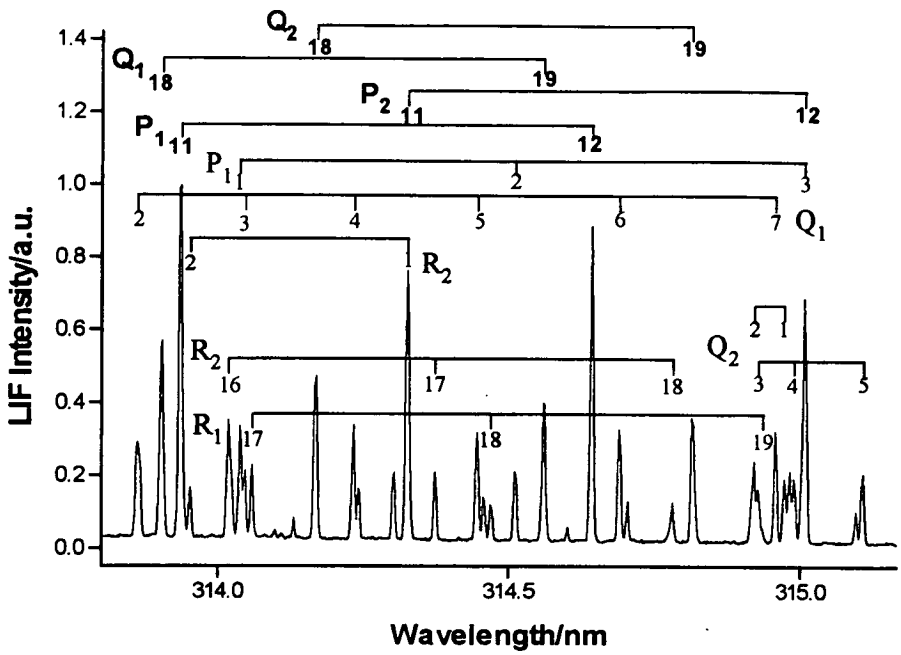

Figure 6.1(f): LIF excitation scan of the OH product resulting from the reaction between $O(^1D)$ and CH_4, continued from Figure 6.1(e). The experimental conditions are the same as for the spectrum shown in Figure 6.1(a).

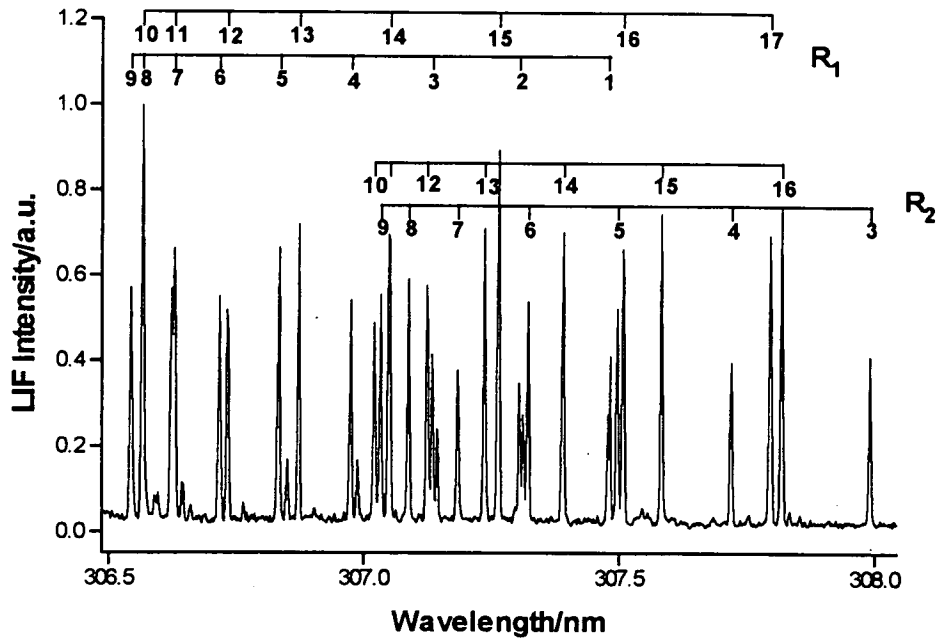

Figure 6.2(a): LIF excitation scan of the OH product resulting from the reaction between $O(^1D)$ and CH_4. $O(^1D)$ was generated by laser photolysis of N_2O at 193nm. The N_2O and CH_4, in a 50:50 mixture, entered the reaction chamber via a pulsed molecular beam valve and a "steady-state" background pressure of 7×10^{-5}mbar was maintained throughout the scan. The backing pressure was 1 bar above atmosphere. The beam energies entering the reaction chamber were 25mJ/pulse for the photolysis laser and ~100μJ/pulse for the probe laser. The time delay between the photolysis and probe sequences was 200ns, ensuring that near nascent products were detected. OH(v'=0) was probed by both exciting and detecting fluorescence on the A-X (0-0) band. The rotational lines, originating in levels N'[20] of the $X^2\Pi$ ground state, have been assigned[52].

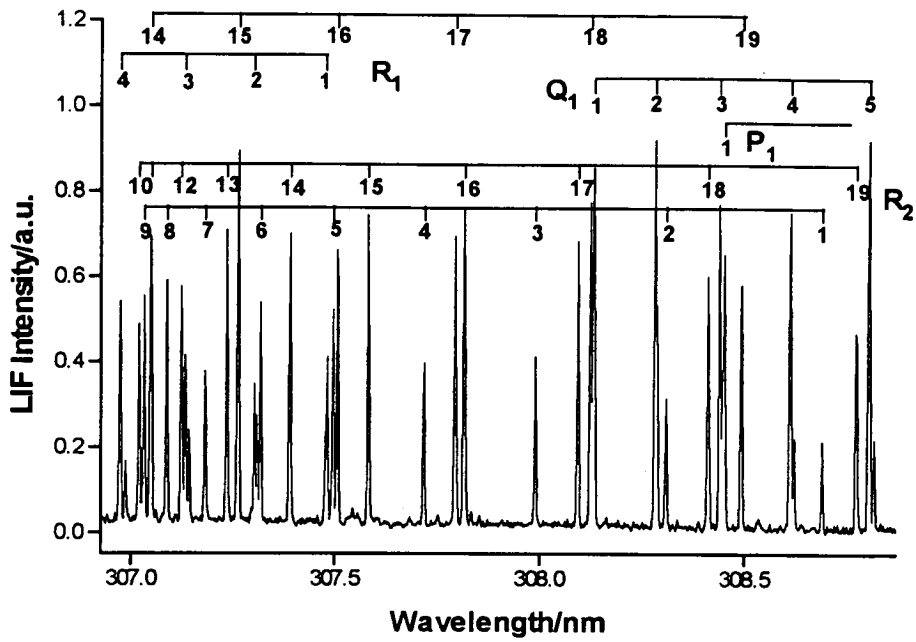

Figure 6.2(b): LIF excitation scan of the OH product resulting from the reaction between $O(^1D)$ and CH_4, continued from Figure 6.2(a). The experimental conditions were the same as for the spectrum in Figure 6.2(a).

Figure	OH(v')	Branches	Gas Source
6.1(a)	0	R_1 and R_2	effusive
6.1(b)	0	R_1, R_2, Q_1, Q_2, and P_1	effusive
6.1(c)	0	R_1, R_2, Q_1, Q_2, P_1 and P_2	effusive
6.1(d)	0 1	R_1, R_2, Q_1, Q_2, P_1 and P_2 R_1	effusive
6.1(e)	0 1	Q_1, Q_2, P_1 and P_2 R_1, R_2, and Q_1	effusive
6.1(f)	0 1	Q_1, Q_2, P_1 and P_2 R_1, R_2, Q_1, Q_2 and P_1	effusive
6.2(a)	0	R_1 and R_2	pulsed nozzle
6.2(b)	0	R_1, R_2, Q_1 and P_1	pulsed nozzle

Table 6.1: Spectral detail within Figures 6.1(a)-(f) and 6.2(a)-(b).

The spectra contained in Figures 6.1(a)-(f) and 6.2(a)-(b) span the OH excitation spectrum from approximately 306-314nm, incorporating bands originating from both v'=0 and v'=1. A breakdown of the spectral detail within each figure is given in Table 6.1.

(a) Effusive Experiments

Qualitative Vibrational Analysis

Cursory examination of the spectra within Figures 6.1(a)-(f) reveals that there is considerable population in both OH(v'=0) and (v'=1)[20]. However it might, at first sight, look as though v'=0 is more significantly populated than v'=1. For example, in Figure 6.1(d) it is clearly evident that the R_1 branch head of the (1-1) band is less intense than the $P_1(7)$ and $P_2(6)$ lines of the (0-0) band. In general terms, the v'=0 lines seem to be greater than the v'=1 lines by a factor of roughly two. This initial observation is at odds with the results of Park and Wiesenfeld[8] who reported roughly similar populations in OH(v'=0) and (v'=1). However this discrepancy can be explained by considering more closely the experimental and spectroscopic details.

The difference in the line intensities of OH(v'=0) and (v'=1) could potentially be attributed to a number of sources. The most obvious answer is that there is more population in v'=0, but before this argument can be accepted other factors must be considered.

Firstly, features of the apparatus used can contribute to the observed spectral intensities of lines. In this experimental study a bandpass interference filter, centred at 310nm with a bandwidth of 10nm, was used to transmit light of the desired wavelength to the PMT detector. This means that v'=0 lines will be favoured since they occur between 306.5 and ~315nm and are thus located well within the transmission limit of the filter, whereas the v'=1 lines only start at 312.5nm and hence never coincide with the region

of maximum transmission. For example, the N′=10 lines of the R_1, Q_1 and P_1 branches of OH(v′=0) (in Figures 6.1(a), (c) and (e) respectively) occur in the region where transmission through the filter is strong whereas only the $R_1(10)$ line of OH(v′=1) (Figure 6.1(d)) is seen in the wavelength region scanned. The corresponding v′=1 $Q_1(10)$ and $P_1(10)$ lines occur outwith the region of transmission of the filter used.

Secondly, Einstein A coefficients, which effectively provide the radiative rates between two states (in this case between specific vibrational levels in the OH $A^2\Sigma^+ \leftarrow X^2\Pi$ transition) can be used to assess the comparative detectivity of states. Examination of the A values reported by Crosley and Lengel[53] provide an insight into the expected relative ratio of the signals obtained by exciting fluorescence on the (0-0) and (1-1) bands. If saturation and quenching are ignored, and if it is assumed that the nascent OH signal is collected with a sufficiently large time gate (i.e. the gate needs to be long enough to collect the fluorescence from all possible levels), then the Einstein A coefficients indicate that the relative ratio of signals in v′=0 to v′=1 should be 1 : ~0.4. This is because the (0-0) band has a large radiative rate and hence a large proportion of molecules excited via this band will transfer to the upper electronic state. In addition, on excitation of the (0-0) band almost all the fluorescence returns on the same band. In contrast, exciting on the (1-1) band, in the first instance, is less favourable (~60% transfers), and secondly, some of the fluorescence returns via alternative bands (in particular, approximately 30% of excited molecules will return via the (1-0) band). This implies that even if the populations in v′=0 and v′=1 were exactly the same, the v′=1 lines should be ~40% of the size of the v′=0 lines.

Hence, the spectra shown in Figures 6.1(a)-(f) show that vibrationally nascent OH product can be detected using the available experimental apparatus: the fact that OH was observed in vibrational levels above v′=0 indicates that this OH resulted from the reaction between $O(^1D)$ and CH_4 and

was not thermalised. Approximate qualitative vibrational analysis of the spectra indicates that the population in OH(v'=0) and (v'=1), probed via the (0-0) and (1-1) bands respectively, is probably roughly similar. This is the anticipated result, previously observed by Luntz[6], Park and Wiesenfeld[8].

Park and Wiesenfeld[8] showed that the OH product from the reaction between $O(^1D)$ and CH_4 is highly vibrationally excited with significant population up to v'=4, with v'=2 being the most populated vibrational level. In this study however, full vibrational analysis has not been carried out; only v'=0 and v'=1 levels of the OH product from the $O(^1D)/CH_4$ reaction were probed. In fact, to measure the vibrational population for v'>2 an alternative detection protocol would have to be used as the diagonal bands ($\Delta v=0$) are efficiently predissociated above v=2 in the $A^2\Sigma^+$ state[8].

The populations in OH(v'=0) and (v'=1) have not been analysed quantitatively because this would require all factors contributing to spectral line intensities to be considered rigorously. This kind of investigation was deemed not to be necessary here as the main objectives of this work were to determine that the $O(^1D)+CH_4$ reaction worked with the available experimental set-up, show that nascent OH product could be detected and check that the vibrational distributions observed were roughly similar to those reported in previous investigations on the system. Rotational distributions, discussed next, are a much better test of the nascent character of populations because rotational relaxation is much more rapid than vibrational relaxation.

Qualitative Rotational Analysis

Park and Wiesenfeld[8] showed that the OH product from the reaction between $O(^1D)$ and CH_4 is highly vibrationally and rotationally excited. Within each vibrational level they observed significant rotational excitation, with levels up to $N'\approx31$ populated for v'=0, decreasing with v to $N'\approx16$ for

v′=4[20]. The rotational distribution in OH(v′=0) and (v′=1) peaked around N′=20(±5). A characteristic of the $O(^1D)/CH_4$ reaction was the essentially similar rotational distributions in all vibrational levels. Park and Wiesenfeld compared this system with the reactions of $O(^1D)$ with heavier hydrocarbons where the rotational distribution in v′=0 was very different to that seen in higher vibrational levels.

It is obvious from the spectra shown in Figures 6.1(a)-(f) that the OH product, in this study, is also highly rotationally excited: Figure 6.1(d) shows that rotational levels up to N′=26 for the R_1 branch of OH(v′=0) are populated and Figure 6.1(f) shows that levels at least up to N′=19 for the R_1 branch of OH(v′=1) are populated. This cut-off (at N′=19) is arbitrary as no further wavelengths were recorded.

To qualitatively analyse the rotational lines a few crude approximations need to be made. Firstly, it is assumed that the rotational linestrengths within any branch change slowly with N′. Secondly, the fact that the detectivity will decline as N′ increases is ignored. Applying these assumptions, in Figure 6.1(a) it can be seen that, for example, the $R_2(15)$ line of OH(v′=0) is greater than $R_2(4)$. This indicates that the returning lines are larger than the incoming lines in the R_2 branch. This also seems to be the case for the OH(v′=0) R_1 branch. Similarly, Figure 6.1(d) shows that the $R_1(11)$ line of OH(v′=1) is greater than $R_1(5)$. Very approximately, the rotational distributions in both v′=0 and v′=1 seem to peak between N′=11 and N′=16. The high N′ lines are likely to be discriminated against because (especially for the P-branch) they fall outwith the peak transmission region of the interference filter, as discussed above for the vibrational distributions. Hence, considering that no quantitative spectral analysis has been carried out, and that the variation in detectivity with wavelength has not been fully

assessed, these figures roughly match the maximum in the OH(v'=0) and (v'=1) rotational distributions observed by Park and Wiesenfeld[8].

These observations indicate that the OH rotational energy distributions are highly excited. At room temperature a Boltzmann distribution would predict that the rotational population in OH(v'=0) would peak in N'=2 and tail off by N'=6. Hence it can be assumed that the OH seen in spectra 6.1(a)-(f) is the at least near nascent product from the reaction between $O(^1D)$ and CH_4, since its rotational distribution is far from thermal.

Concluding Remarks

In conclusion, qualitative vibrational and rotational analysis of the OH (v'=0,1) product have shown that the $O(^1D)+CH_4$ reaction can be studied successfully using the available experimental apparatus and that near nascent OH product is detected. The vibrational and rotational distributions observed were roughly similar to those reported in previous investigations on the system.

(b) Jet Experiments

Figures 6.2(a) and 6.2(b) show the OH(v'=0) product resulting from pulsed molecular beam valve introduction of N_2O/CH_4 to the reaction chamber. Figures 6.1(a) and 6.2(a) are spectra recorded over the same wavelength range but under respective effusive and jet conditions. In these scans the sizes of the rotational lines are comparable, but Figure 6.2(a) was recorded using a significantly lower "steady-state" background pressures. Nozzles can enhance the signal to noise ratio, especially for bimolecular experiments, as they allow a high transient density of reactants at the interaction zone.

However, despite this higher reactant density at the interaction zone, the spectra shown in Figures 6.1(a) and 6.2(a) are remarkably similar, thus implying that there was no substantial relaxation of species in the jet spectra. The main significance of this result is that it shows that nascent products can be detected in a pulsed jet. This experimental condition is not essential for LIF measurements but greatly advantageous for REMPI measurements because of the need to avoid high pressures in the flight tube and at the MCP detector.

6.4 The $O(^1D)/CH_4$ Reaction: REMPI Detection of the CH_3 Product

Before attempts were made to detect the CH_3 fragment resulting from the reaction between $O(^1D)$ and methane, a series of test experiments were implemented in which the photodissociation of CH_3I was studied. This work has been discussed more fully in Chapter 3 (Section 3.2). A brief summary of those parts of the work which are relevant to dynamical studies is included here.

The photolysis of CH_3I using either a one (Section 3.2.3(a)) or two (Section 3.2.3(b)) laser experimental scheme yields CH_3 which can be probed by REMPI. Spectra of both the $3p_z{}^2A_2''(v=0) \leftarrow X^2A_2''(v=0)$[12,13,54-60] and $4p_z{}^2A_2''(v=0) \leftarrow X^2A_2''(v=0)$[61] transitions of the CH_3 radical have been obtained and analysed to gain an insight into the spectroscopy of the system and the relative ease, or difficulty, in detecting CH_3 by REMPI.

These studies highlighted the fact that, with the present experimental apparatus, detection of CH_3 by REMPI, following photodissociation of CH_3I, is not easy. Figure 3.9 (Chapter 3) shows a (2+1) REMPI scan of the $4p_z{}^2A_2'' \leftarrow X^2A_2''$ band origin for CH_3. In this instance CH_3I (seeded in He) was

introduced into the reaction chamber via a pulsed nozzle. The rotational structure is partially resolved. However, this is a relatively easy experiment requiring only one colour (laser) for both the photolysis and probe processes.

In contrast, Figure 3.12 (Chapter 3) shows a power normalised (2+1) REMPI scan of the $3p_z{}^2A_2''(v=0) \leftarrow X^2A_2''(v=0)$ transition of the CH_3 radical. Kleinermanns *et al*[12,13] also used this transition in their study of the $O(^1D)/CH_4$ reaction, where the CH_3 product was probed by REMPI. The type of experiment which yielded the spectrum in Figure 3.12 is more closely related to the bimolecular study of the $O(^1D)/CH_4$ reaction in that two lasers are required: one for photolysis of CH_3I at 248nm and one for the subsequent REMPI of CH_3. In Figure 3.12 the resolution of the rotational branch structure is poor and the spectrum had to be power normalised; the probe power output during the recording of these scans was extremely low, which manifested in signal fluctuations and was corrected by power normalisation. This low probe power output at the wavelengths required for excitation of the $3p_z \leftarrow X$ transition (~315-335nm) is a characteristic of the Spectron dye laser system used in this work; the dye optics do not work well in the extreme red. The only way to solve this problem is to use an alternative laser system.

Hence it is already apparent that obtaining well resolved CH_3 REMPI spectra for relatively easy photodissociation experiments, where the product density is high, is difficult. In the $O(^1D)/CH_4$ experiment there will obviously be much less nascent CH_3 product. In this bimolecular reaction there are a number of factors which will contribute to the possible obtainable product number density:

- N_2O must be efficiently converted into $O(^1D)$
- $O(^1D)$ must react with CH_4
- the CH_3 created then has to be detected.

One positive factor is that the experiment definitely works; the OH product of the reaction has been successfully detected by LIF as illustrated in Section 6.3. However, in hot atom dynamics experiments the concentration of nascent product molecules is dependent on the pressure of the reactants. As discussed in Chapter 3 Section 3.1.5 the pressure constraints set by the MCP detector in a REMPI experiment limits the detection of small quantities of products. In LIF experiments the detector is external to the vacuum system and so higher pressures are used, making it easier to detect nascent products. Obviously it is important to use nozzles rather than effusive flow, in bimolecular experiments coupled with REMPI detection, since they provide a high instantaneous density of reagents for an apparent lower "steady-state" pressure within the entire vacuum system.

6.4.1 Experimental Procedure

Attempts were made to detect the nascent CH_3 product resulting from the reaction between $O(^1D)$ and CH_4 using the experimental arrangement illustrated in Figure 2.9. As this was predicted to be a difficult experiment the following procedure was used:

1. Firstly, CH_3I(20%) seeded in He(80%) entered the reaction chamber via the bullet shaped pulsed molecular beam valve, as shown in Figure 2.7(b). The nozzle housed a 0.5mm diameter hole and was located approximately 10mm from the laser beam. Typically the backing pressure was 3 bar above atmosphere and the "steady-state" reaction and detection chamber pressures were approximately 1.5×10^{-5} and 2.5×10^{-7} mbar respectively.
2. The doubled output of the Nd:YAG pumped dye laser (R590 dye (Exciton) with trace R610 (Exciton)) was then used to photodissociate, at approximately 286nm, the CH_3I and subsequently detect CH_3 by REMPI

via the $4p_z^2A_2'' \leftarrow X^2A_2''$ transition, as described in Chapter 3 Section 3.2.3(a).

3. The CH_3^+ ions formed at the laser focus were extracted, using the ion optic arrangement described in Chapter 2 Section 2.2.2.2(b) and illustrated in Figure 2.5, and detected by the Microchannel Plates housed in the detection chamber. The "top hat" and repeller plate were located 6mm and 8mm from the laser respectively. The reaction and detection chambers were separated by a 10mm×2mm rectangular slot.
4. The CH_3^+ signal was digitised and collected by the PC. A mass spectrum was obtained with a peak at mass 15 corresponding to CH_3. The region of maximum signal intensity (the Q branch of the $4p_z^2A_2'' \leftarrow X^2A_2''$ band origin, as shown in Chapter 3 Figures 3.6-3.9) was then found and the signal optimised. This was achieved by, for example, moving the positions of the lasers (horizontally, vertically, left and right) and fine tuning the ion extraction/detection voltages.
5. Once the optimum signal had been found the source behind the pulsed molecular beam valve was switched from CH_3I/He to a 50:50 mixture of N_2O:CH_4 and attempts were made to detect the nascent CH_3 signal by REMPI using a similar experimental arrangement and conditions. In theory the probe laser should be at the wavelength of the maximum of the $4p_z^2A_2'' \leftarrow X^2A_2''$ band origin, as established by the CH_3I photodissociation control experiment, hence if CH_3 is present in the reaction chamber it should be detectable.

$O(^1D)$ was generated by excimer laser photolysis (ArF) of N_2O at 193nm[50,51] prior to reaction with CH_4. The time delay between the photolysis and probe lasers was kept short (100-200ns) to ensure that collisionally unmodified signal was collected. The nascent signal was probed in exactly the same way as the CH_3 product from the photodissociation experiment, via the $4p_z^2A_2''(v=0) \leftarrow X^2A_2''(v=0)$ transition.

The photolysis beam (ArF, ~25mJ/pulse) was focused into the reaction chamber with a f=50cm lens. The probe beam was tightly focused with a f=30cm to a spot size of ~1-2mm in the interaction region. Doubled dye beam output energies were typically 500μJ-1mJ/pulse.

6.4.2 Results and Discussion of the REMPI Experiments

Unfortunately no nascent CH_3 signal resulting from the reaction between $O(^1D)$ and CH_4 was detected by the probe laser. Perhaps one of the main problems was that the photolysis laser (ArF excimer at 193nm) alone was causing dissociation and ionisation of the reagent gases. This produced huge background signals which could potentially mask any (small) nascent CH_3^+ signal, if present.

Figures 6.3-6.5 are "pictures" of these background signals obtained by signal-averaging a large number of time-of-flight waveforms at a particular wavelength where the signal is maximised. Tests on the system showed that these undesirable signals are excimer-induced: they are present when the probe laser is blocked. This means N_2O and CH_4 are being ionised at 193nm and subsequently ions resulting from these parent molecules are detected and dominate the mass spectrum. Also some degree of photodissociation is occurring and fragment ions are also being seen by the MCP detector. When the nozzle is switched off, and therefore no gas is entering the reaction chamber, but the excimer is firing the mass spectrum consists of oil peaks. Fortunately, the oil peaks were swept out of the probe volume by firing the nozzle.

Figure 6.3 shows the REMPI mass spectrum obtained when only N_2O gas is pulsed into the reaction chamber, with the excimer laser firing and the probe laser blocked. A significant amount of NO is also seen: NO is present either as an impurity in N_2O or has contaminated the gas reservoirs and vacuum

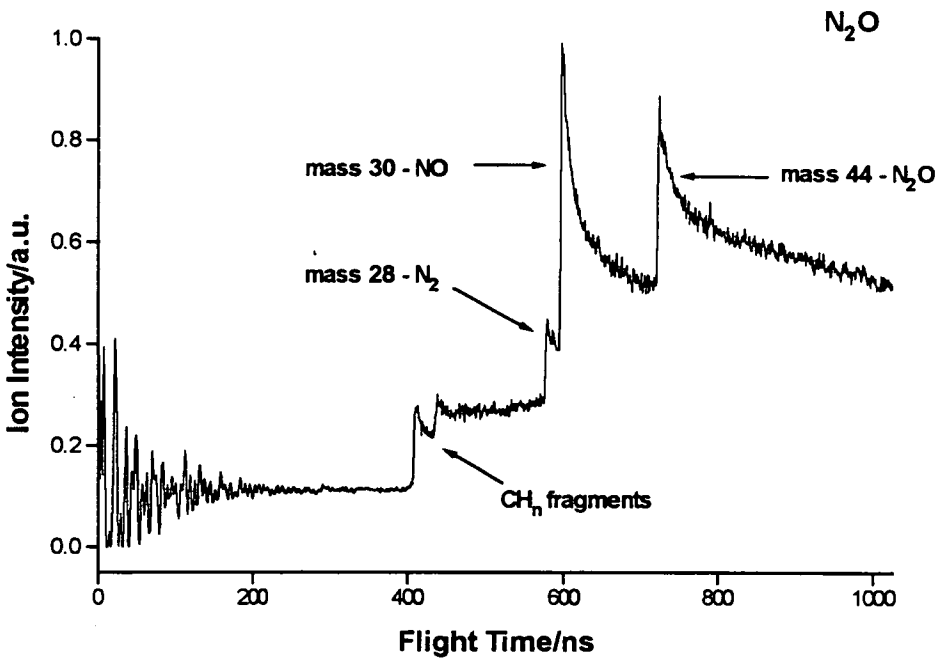

Figure 6.3: The mass spectrum (averaged over 64 shots) resulting from the excimer-induced ionisation (at 193nm) of N_2O. The laser power was 125mJ/pulse. The reagent gases were pulsed into the reaction chamber using a bullet shaped nozzle (Chapter 2 Figure 2.7(b)) with a 0.5mm diameter hole.

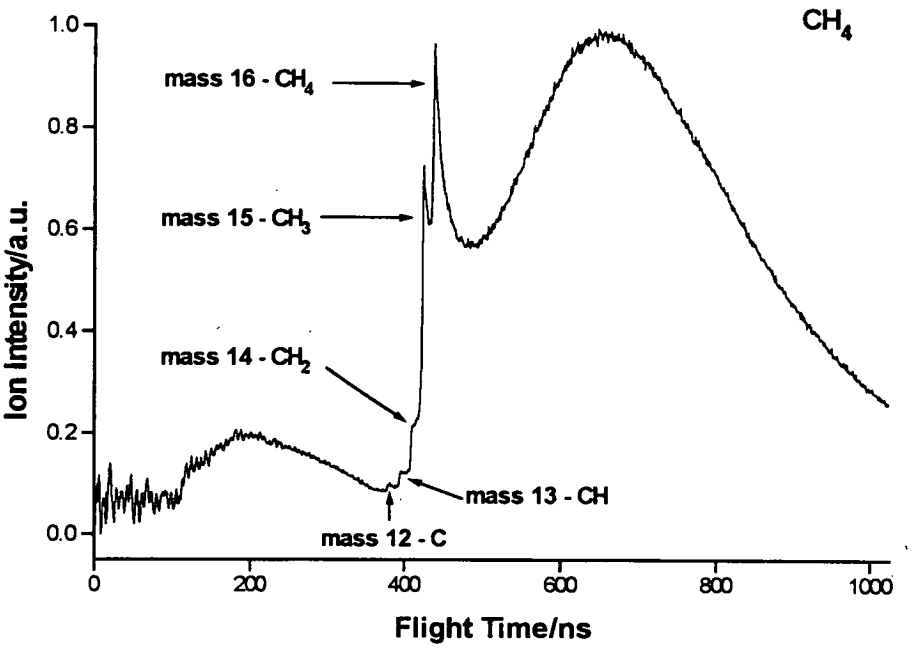

Figure 6.4: The mass spectrum (averaged over 64 shots) resulting from the excimer-induced ionisation (at 193nm) of CH_4. The laser power was 125mJ/pulse. The reagent gases were pulsed into the reaction chamber using a bullet shaped nozzle (Chapter 2 Figure 2.7(b)) with a 0.5mm diameter hole.

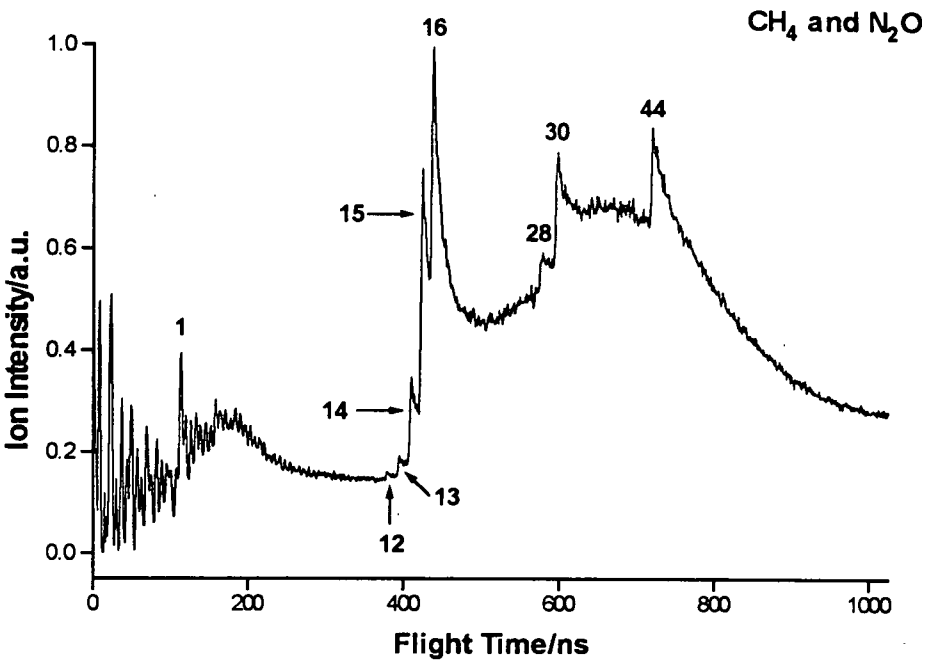

Figure 6.5: The mass spectrum (averaged over 64 shots) resulting from the excimer-induced ionisation (at 193nm) of N_2O and CH_4. The laser power was 125mJ/pulse. The reagent gases were pulsed into the reaction chamber using a bullet shaped nozzle (Chapter 2 Figure 2.7(b)) with a 0.5mm diameter hole.

system from another source (e.g. from the NO_2 used in the experiments described in Chapter 4). The masses of the parent and fragment ions, N_2O, NO and N_2, have been assigned. CH_n fragments are also present. These are presumably due to contaminants within the vacuum system. Figure 6.4 shows the peaks present when only CH_4 is allowed into the system. The signals at masses 12, 13, 14, 15 and 16 have been attributed as being due to different CH_n combinations. For comparison, Figure 6.5 shows the excimer-induced background signals obtained when the N_2O/CH_4 (50:50) mixture is pulsed into the reaction chamber. From these figures it is clearly evident that at mass=15, the region of interest, there are a multitude of background signals which will potentially mask nascent CH_3 resulting from the bimolecular reaction between $O(^1D)$ and CH_4. Hence before any progress can be made these background signals must be removed.

Obviously the spectra shown in Figures 6.3-6.5 look very peculiar and differ greatly from conventional mass spectra. The assigned peaks all appear to have sharp onsets and then exhibit exponential decays, and a huge mass dominates at longer flight times. These odd features could perhaps be due to delayed and secondary ionisation processes, occurring as a consequence of the high gas densities at the laser focus and also because the photolysis laser power is very high (~125mJ/pulse in Figures 6.3-6.5).

One factor which was found to influence greatly the excimer-induced ion signals was the excimer laser power: the size of these signals was found to depend on the power as shown in Figure 6.6. The main picture in this figure shows how the background signal, resulting from excimer-induced ionisation of N_2O and CH_4, reduces as the power is reduced. This result is clarified in the inset figure which shows the signal size at selected laser powers. These results led to the excimer laser power being lowered to 25mJ/pulse in the attempts to detect CH_3 resulting only from the $O(^1D)/CH_4$ reaction. Unfortunately however, the nascent signal still continued to evade detection.

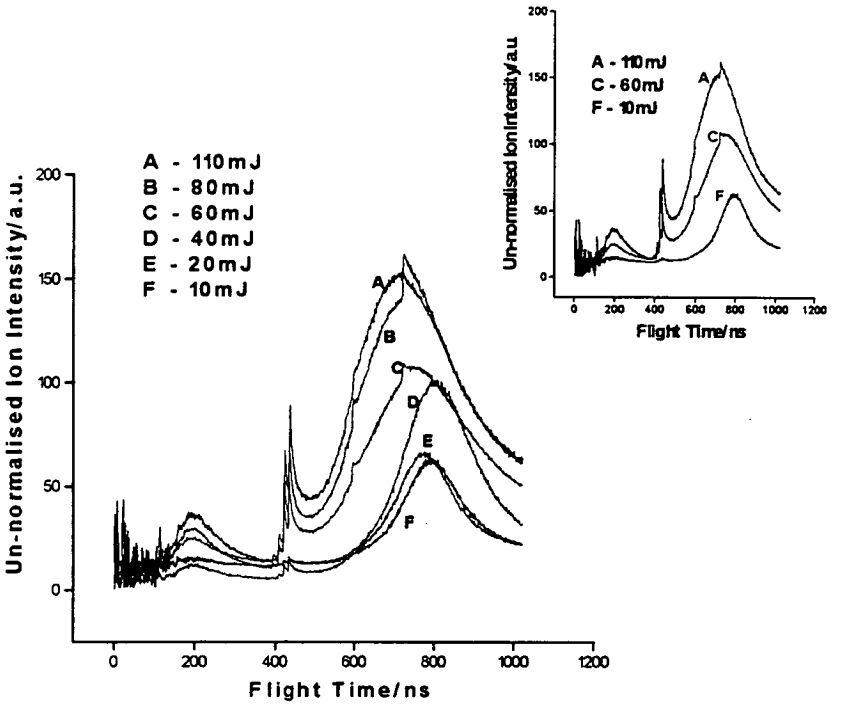

Figure 6.6: The mass spectra (averaged over 64 shots) resulting from the excimer-induced ionisation (at 193nm) of N_2O and CH_4. This figure shows the effect of varying the excimer laser power. The reagent gases were pulsed into the reaction chamber using a bullet shaped nozzle (Chapter 2 Figure 2.7(b)) with a 0.5mm diameter hole. The signal size reduces as the excimer laser power is reduced. This result is clarified in the inset figure which shows the signal size at selected laser powers of 110mJ, 60mJ and 10mJ.

6.5 Concluding Remarks

The OH and CH_3 products of the $O(^1D)$/ CH_4 reaction have been probed spectroscopically. The OH radical was easily detected by LIF and, in agreement with similar studies on the system[6-8,24], found to be rotationally hot. The principal aim in probing this much studied reaction product was to prove that the reaction worked with the given experimental apparatus and then check that the results agreed roughly with previous work on the system.

The distribution of energy in the CH_3 fragment is expected to reveal much about what has occurred during the reaction and thus complement the data obtained from analysis of the OH product. CH_3 does not fluoresce and cannot therefore be detected by LIF. Hence REMPI has been used to probe this fragment in both photodissociation experiments[54-61] and bimolecular reactions[12,13]. However, in this study, the CH_3 resulting from the reaction between $O(^1D)$ and CH_4 was not successfully detected. As discussed in Section 6.4.2 one of the main problems was that any nascent product present was undoubtedly masked by excimer-induced background signals, occurring at the mass of interest. Hence future efforts ought to be directed towards eradicating these undesirable signals.

If nascent CH_3 signals had been seen then the next step would have been to analyse the spectra. If this situation had arisen then it would have been prudent to probe an alternative transition in the methyl radical and to use CD_4 rather than CH_4. The reasoning behind this lies in predissociation, as discussed in Chapter 3 Section 3.2.2. The excited states of CH_3 radical are rapidly predissociated but previous studies have found that the $3p_z{}^2A_2''$ state is more resistant than the $4p_z{}^2A_2''$ state to predissociative effects[12,13,54,61]. Also whilst CD_3 is affected by homogeneous predissociation, rotational level dependent heterogeneous effects dominate in CH_3[61]. Hence, in principle,

probing the $3p_z \leftarrow X$ transition of CD_3, following reaction between $O(^1D)$ and CD_4, should yield potentially resolvable spectra.

References

[1] M. Nicolet, *Can. J. Chem.*, **52**, 1381 (1974).

[2] M. Brouard, S. Duxon, P.A. Enriquez and J. P. Simons, *J. Chem. Soc. Faraday Trans.*, **89**, 1435 (1993).

[3] M. Baba, M. Brouard, S.P. Rayner and J.P. Simons, *Chem. Phys. Lett.*, **220**, 411 (1994).

[4] M. Brouard, H.M. Lambert, J. Short and J.P. Simons, *J. Phys. Chem.*, **99**, 13571 (1995).

[5] T. Suzuki and E. Hirota, *J. Chem. Phys.*, **98**, 2387 (1993).

[6] A.C. Luntz, *J. Chem. Phys.*, **73**, 1143 (1980).

[7] P.M. Aker, J.J.A. O'Brien and J.J. Sloan, *J. Chem. Phys.*, **84**, 745 (1986).

[8] C.R. Park and J. R. Wiesenfeld, *J. Chem. Phys.*, **95**, 8166 (1991).

[9] Y. Matsumi, K. Tonokura, Y. Inagaki and M. Kawasaki, *J. Phys. Chem.*, **97**, 6816 (1993).

[10] Y. Rudich, Y. Hurwitz, G.J. Frost, V. Vaida and R. Naaman, *J. Chem. Phys.*, **99**, 4500 (1993).

[11] R.D. van Zee, J.C. Stephenson and M.P. Casassa, *Chem. Phys. Lett.*, **223**, 167 (1994).

[12] J. Schluetter, R. Schott and K. Kleinermanns, *Chem. Phys. Lett.*, **213**, 262 (1993).

[13] R. Schott, J. Schluetter, M. Olzmann and K. Kleinermanns, *J. Chem. Phys.*, **102**, 8371 (1995).

[14] J.J. Sloan, *J. Phys. Chem.*, **92**, 18 (1988).

[15] H. Yamazaki and R.J. Cvetanovic, *J. Chem. Phys.*, **41**, 3703 (1964).

[16] G. Paraskevopoulos and R.J. Cvetanovic, *J. Chem. Phys.*, **50**, 590 (1969).

[17] G. Paraskevopoulos and R.J. Cvetanovic, *J. Chem. Phys.*, **52**, 5821 (1970).

[18] P.Michaund and R.J. Cvetanovic, *J. Phys. Chem.*, **76**, 1375 (1972).

[19] C.L. Lin and W.B. DeMore, *J. Phys. Chem.*, **77**, 863 (1973).

[20] Vibrational and rotational levels of the OH product, formed following reaction between $O(^1D)$ and RH are labelled with primes, v′ and N′. This notation, which is commonly used in reaction dynamics to differentiate between reactant and product energy states, is consistent with the conventions used in Chapters 4 and 5.

[21] R.P. Mariella Jr. and A.C. Luntz, *J. Chem. Phys.*, **67**, 5388 (1977).

[22] P. Andresen and A.C. Luntz, *J. Chem. Phys.*, **72**, 5842 (1980).

[23] G. Paraskevopoulos and R.J. Cvetanovic, *J. Am. Chem. Soc.*, **91**, 7572 (1969).

[24] S.G. Cheskis, A.A. Iogansen, P.V. Kulakov, I.Y. Razuvaez, O.M. Sarkisov and A.A. Titov, *Chem. Phys. Lett.*, **155**, 37 (1989).

[25] A.S. Manocha, D.W. Setser and M.A. Wickramaaratchi, *Chem. Phys.*, **76**, 129 (1983).

[26] D.J. Smith, D.W. Setser, K.C. Kim and D.J. Bogan, *J. Phys. Chem.*, **81**, 898 (1977).

[27] N.J. Dutton, I.W. Fletcher and J.C. Whitehead, *Mol. Phys.*, **52**, 475 (1984).

[28] A.C. Luntz, R. Schinke, W.A. Lester Jr. and H.H. Gunthard, *J. Chem. Phys.*, **70**, 5908 (1979).

[29] G.K. Smith, J.E. Butler and M.C. Lin, *Chem. Phys. Lett.*, **65**, 115 (1979).

[30] G.K. Smith and N.E. Butler, *J. Chem. Phys.*, **73**, 2243 (1980).

[31] P.M. Aker and J.J. Sloan, *J. Chem. Phys.*, **85**, 1412 (1986).

[32] C.B. Cleveland, G.M. Jursich, M. Trolier and J.R. Wiesenfeld, *J. Chem. Phys.*, **86**, 3253 (1987).

[33] G.M. Jursich and J.R. Wiesenfeld, *Chem. Phys. Lett.*, **119**, 511 (1985).

[34] J.E. Butler, G.M. Jursich, I.A. Watson and J.R. Wiesenfeld, *J. Chem. Phys.*, **84**, 5365 (1986).

[35] E.M. Goldfield and J.R. Wiesenfeld, *J. Chem. Phys.*, **93**, 1030 (1990).

[36] K.S. Sorbie and J.N. Murrell, *Mol. Phys.*, **31**, 905 (1976).

[37] P.A. Whitlock, J.T. Muckermann and E.R. Fisher, *J. Chem. Phys.*, **76**, 4468 (1982).

[38] R. Schinke and W.A. Lester Jr., *J. Chem. Phys.*, **70**, 4893 (1979).

[39] R. Schinke and W.A. Lester Jr., *J. Chem Phys.*, **72**, 3754 (1980).

[40] S.W. Ransome and J.S. Wright, *J. Chem. Phys.*, **77**, 6346 (1982).

[41] L.J. Dunne and J. N. Murrell, *Mol. Phys.*, **50**, 635 (1983).

[42] M.S. Fitzcharles and G.C. Schatz, *J. Phys. Chem.*, **90**, 3634 (1986).

[43] M. Brouard, S.P. Duxon and J.P. Simons, *Isr. J. Chem.*, **34**, 67 (1994).

[44] R.D. Levine and R.B. Bernstein, *Molecular Reaction Dynamics and Chemical Reactivity*, (Oxford University Press, 1987).

[45] N. Balucani, L. Beneventi, P. Casavecchia and G.G. Volpi, *Chem. Phys. Lett.*, **180**, 34 (1991).

[46] H.L. Kim, M.A. Wickramaaratchi, X. Zheng and G.E. Hall, *J. Chem. Phys.*, **101**, 2033 (1994).

[47] P.J. Dagdigian, M.H. Alexander and K. Liu, *J. Chem. Phys.*, **91**, 839 (1989).

[48] M.H. Alexander, *J. Chem. Phys.*, **76**, 5974 (1982).

[49] M.H. Alexander, *Chem. Phys.*, **92**, 337 (1985).

[50] W. A. Noyes and P. A. Leighton, *The Photochemistry of Gases*, (Reinhold Publishing Corp., 1941) p.397.

[51] L. L. Springsteen, S. Satyapal, Y. Matsumi, L. M. Dobeck and P. L. Houston, J. Chem. Phys., 1993 97 7239.

[52] H.M. Crosswhite and G.H. Dieke, *J. Quant. Spectrosc. Radiat. Transfer*, **2**, 97 (1962).

[53] D.R. Crosley and R.K. Lengel, *J. Quant. Spectrosc. Radiat. Transfer*, **15**, 579 (1975).

[54] R. Ogorzalek-Loo, G.E. Hall, H.-P. Haerri and P.L. Houston, *J. Phys. Chem.*, **92**, 5 (1988).

[55] R. Ogorzalek-Loo, G.E. Hall, H.-P. Haerri and P.L. Houston, *J. Chem. Phys.*, **90**, 4222 (1989).

[56] J. Danon, H. Zacharias, H. Rottke and K.H. Welge, *J. Chem. Phys.*, **76**, 2399 (1982).

[57] D.H. Parker, Z.W. Wang, M.H.M. Janssen and D.W. Chandler, *J. Chem. Phys.*, **90**, 60 (1989).

[58] D.W. Chandler, J.W. Thoman Jr., M.H.M. Janssen and D.H. Parker, *Chem. Phys. Lett.*, **156**, 151 (1989).

[59] D.W. Chandler, M.H.M. Janssen, S. Stolte, R.N. Strickland, J.W. Thoman Jr. and D.H. Parker, *J. Phys. Chem.*, **94**, 4839 (1990).

[60] M.H.M. Janssen, D.H. Parker, G.O. Sitz, S. Stolte and D.W. Chandler, *J. Phys. Chem.*, **95**, 8007 (1991).

[61] J.F. Black and I. Powis, *J. Chem. Phys.*, **89**, 3986 (1988).

Appendix A

Courses and Conferences Attended

In accordance with the regulations of the Department of Chemistry, University of Edinburgh, I have attended the following courses during my period of study:

1. Lasers 1 and 2
2. Inelastic and Reactive Scattering Theory
3. Introduction to Computing
4. UNIX 1
5. C Programming
6. Physical Chemistry Postgraduate Lectures

In addition I have attended the Laser Chemistry Research Group meetings, departmental seminars and joint Edinburgh University - Heriot-Watt University Laser Chemistry Group meetings.

I have also participated in the following conferences:

1. 4th Annual Informal Northern Universities Chemical Physics Meeting, University of Nottingham, July 1993.
2. Gas Kinetics Discussion Group, University of Nottingham, November 1993.
3. Annual Northern Universities Meeting on Chemical Physics, University of Northumbria at Newcastle-upon-Tyne, January 1995.
4. 1st Edinburgh University Firbush Physical Chemistry Meeting, Firbush, June 1994.

5. 13th International Symposium on Gas Kinetics, University College Dublin, September 1994.
6. 2nd Edinburgh University Firbush Physical Chemistry Meeting, Firbush, June 1995.
7. 2nd European Meeting of the Molecular Beams and Dynamics Group, University of Kaiserslautern, Germany, July 1995.

Appendix B

Publications

Gillian M. Sweeney, Allister Watson and Kenneth G. McKendrick, "Rotational and Spin-Orbit Effects in the Dynamics of $O(^3P_j)$ + Hydrocarbon Reactions. I. Experimental Results", *J. Chem. Phys.*, **106**, 9172 (1997).

Gillian M. Sweeney and Kenneth G. McKendrick, "Rotational and Spin-Orbit Effects in the Dynamics of $O(^3P_j)$ + Hydrocarbon Reactions. II. Models for Spin-Orbit Propensities", *J. Chem. Phys.*, **106**, 9182 (1997).